On corrections in the Ginzburg–Landau equations associated with the normal component flow in a superfluid Fermi liquid with triplet *p*-wave pairing

A. N. Tarasov

*National Science center ''Kharkov Physicotechnical Institute,'' 310108 Kharkov, Ukraine**
(Submitted October 2, 1996)
Fiz. Nizk. Temp. **23**, 243–248, March (1997)

The Ginzburg–Landau (GL) equation is derived for the spatially inhomogeneous order parameter (OP) of the ^{3}He type superfluid Fermi liquid (SFL) (composed of electrically neutral fermions with triplet p-wave pairing) for a uniform flow of the normal component of the SFL with a velocity $v_n \ll 2T_c/p_F$ (T_c is the temperature of phase transition from the normal to the superfluid state, and p_F is the Fermi momentum). The derivation is based on the integrodifferential equation for OP, which is valid at temperatures near T_c in the absence of strong-coupling effects. The main results are the corrections for the coefficients of the OP gradients in the GL equation (caused by the fact that $v_n \neq 0$), which are calculated in the perturbation theory. These corrections, which indicate the deformation of the OP due to the SFL flow with the velocity v_n, can be not only comparable for $v_n \ll 2T_c/p_F$, but also greater than the so-called nontrivial strong-coupling corrections to these coefficients, depending on the value of v_n, and hence can be of practical importance for describing ^{3}He–B at low pressures, when the strong-coupling effects are weak. © *1997 American Institute of Physics.* [S1063-777X(97)00103-5]

1. INTRODUCTION

In this paper, which is a continuation of our the previous publication,[1] we consider a superfluid Fermi liquid (SFL) consisting of electrically neutral paramagnetic fermions with triplet pairing. Superfluid phases of ^{3}He are examples of such Fermi liquids. We confine our analysis to SFL near the temperature T_c corresponding to the phase transition to the superfluid state. In contrast to Ref. 1, we assume that the external magnetic field is zero, but we have a spatially uniform flow of the normal component of the SFL with a velocity $\mathbf{v}_n$ (the velocity $\mathbf{v}_s$ of the superfluid component is assumed to be zero). The analysis is carried out on the basis of the Landau method of a Fermi-liquid, which is generalized for SFL in Refs. 2–4.

Our aim is to derive the Ginzburg–Landau (GL) equation for a weakly spatially inhomogeneous order parameter (OP) of the SFL with a triplet p-wave pairing taking into account the corrections to the coefficients of OP gradients in the GL equation. These corrections are due to the flow of the SFL normal component, which leads to a deformation of the OP for high values of v_n (a similar effect of an external, moderately strong, magnetic field on the coefficients in the GL equation for the SFL under investigation was studied by us[1] for $v_n = 0$). We disregarded the weak interaction between the magnetic dipole moments of fermions (near ^{3}He atoms)[5,6] and the ''strong-coupling effects'' which are weak in ^{3}He-B under low pressures (see Refs. 7–10 and the literature cited there). Consequently, our approach must be applicable above all to ^{3}He–B under comparatively low pressures.

The effect of external perturbations (such as applied magnetic field and the SFL flow) on the OP deformation in superfluid phases of ^{3}He was reported earlier (see, for example, the monograph[11] and the references cited there).

In the present publication, we will prove that the SFL flow leads to the emergence of correcting terms to the coefficients of the OP gradients in the GL equation even for flow velocities v_n smaller than a certain critical value (namely, for $v_n \ll 2T_c/p_F$, where p_F is the Fermi momentum). As in Ref. 1, we are interested in the corrections to the coefficients of only the terms linear in the OP in the GL equation (without writing explicitly the nonlinear terms). We will compare these corrections with the so-called ''nontrivial'' corrections to the same coefficients associated with the strong-coupling effects.[8]

In Sec. 2, we will write the general integrodifferential (ID) equation for the OP with a small spatial inhomogeneity for a SFL with a triplet pairing (the spin s of a pair is equal to unity and the orbital angular momentum l of the pair can assume any odd value), which is valid at temperatures T close to T_c (in a uniform external field $\mathbf{H}$ and in the case of the normal component flow at a velocity $\mathbf{v}_n$). This ID equation, which is derived in Ref. 1, is transformed in Sec. 2 to a form convenient for deriving the required GL equation, which will be obtained in Sec. 3 in the case of p-wave pairing ($l=1$) for $v_n \ll 2T_c/p_F$ and $H=0$. The results which we obtained will be discussed briefly in the conclusion.

2. INTEGRODIFFERENTIAL EQUATION FOR THE ORDER PARAMETER

We will use for the initial equation the ID equation for the OP of the SFL under investigation of the ^{3}He type [see

Eq. (40) in Ref. 1]. This ID equation is valid in the general case of triplet pairing of fermions ($s=1$ and l is any odd number for a pair) at temperatures T near T_c, i.e., $(T_c-T)/T_c \ll 1$ and has the following form in the limit $V\to\infty$ (V is the system volume):

$$\Delta_\alpha(\mathbf{R},\mathbf{k}) = \frac{1}{(2\pi)^3}\int d^3q L_2(|\mathbf{k}-\mathbf{q}|)\Bigg\{\Delta_\beta(\mathbf{R},\mathbf{q})\,\frac{\Phi_{\alpha\beta}(\mathbf{q},-\mathbf{q})}{D(\mathbf{q},-\mathbf{q})} - i\,\frac{\partial\Delta_\beta(\mathbf{R},\mathbf{q})}{\partial R_l}\int d^3P\,\delta(\mathbf{P})\,\frac{\partial}{\partial P_l}\Bigg[\Phi_{\alpha\beta}\Big(\frac{\mathbf{P}}{2}+\mathbf{q},\,\frac{\mathbf{P}}{2}-\mathbf{q}\Big)D^{-1}\Big(\frac{\mathbf{P}}{2}+\mathbf{q},\,\frac{\mathbf{P}}{2}-\mathbf{q}\Big)\Bigg] - \frac{1}{2}\,\frac{\partial^2\Delta_\beta(\mathbf{R},\mathbf{q})}{\partial R_l\partial R_i}\int d^3P\,\delta(\mathbf{P})\,\frac{\partial^2}{\partial P_l\partial P_i}\Bigg[\Phi_{\alpha\beta}\Big(\frac{\mathbf{P}}{2}+\mathbf{q},\,\frac{\mathbf{P}}{2}-\mathbf{q}\Big)D^{-1}\Big(\frac{\mathbf{P}}{2}+\mathbf{q},\,\frac{\mathbf{P}}{2}-\mathbf{q}\Big)\Bigg] + g_\alpha^{(3)}(\mathbf{R},\mathbf{q})\Bigg\}. \tag{1}$$

Here

$$\Delta_\alpha(\mathbf{R},\mathbf{k}) = \int d^3r\,\exp(-i\mathbf{r}\mathbf{k})\Delta_\alpha(\mathbf{R},\mathbf{r}),$$

where $\Delta_\alpha(\mathbf{R},\mathbf{r})$ is the OP for a SFL with a triplet pairing:

$$\Delta_\alpha(\mathbf{R},\mathbf{r}) = \Delta_\alpha(\mathbf{x}_1,\mathbf{x}_2) = \frac{1}{2i}\,\mathrm{Tr}_s\Delta(\mathbf{x}_1,\mathbf{x}_2)\sigma_2\sigma_\alpha = L_2(|\mathbf{x}_1-\mathbf{x}_2|)g_\alpha(\mathbf{x}_1,\mathbf{x}_2). \tag{2}$$

Here (σ_α are the Pauli matrices (α = 1,2,3); $\mathbf{R}$ = ($\mathbf{x}_1$ + $\mathbf{x}_2$)/2, and $\mathbf{r}=\mathbf{x}_1-\mathbf{x}_2$. The functions g_α appearing in Eqs. (1) and (2) are connected with the anomalous distribution function $g_{s_1s_2}(\mathbf{x}_1,\mathbf{x}_2)$ for quasiparticles in the coordinate representation through the formula

$$g_\alpha(\mathbf{x}_1,\mathbf{x}_2) = (1/2i)\mathrm{Tr}_s\; g(\mathbf{x}_1,\mathbf{x}_2)\sigma_2\sigma_\alpha$$

and the function L_2 is the anomalous Fermi-liquid amplitude of interaction (introduced in Refs. 2–4), which is responsible for triplet pairing of fermions. While deriving Eq. (1), we assumed that $L_2(|\mathbf{r}|)$ has a sharp maximum for $r=0$, and the values of $\Delta_\alpha(\mathbf{R},\mathbf{k})$ change insignificantly over distances of the order of the size $\xi_c\sim\hbar v_F/(\pi k_B T_c)$ of a Cooper pair ($v_F=p_F/m^*$ is the Fermi velocity and m^* the effective mass of a quasiparticle; here $\hbar=1$ and $k_B=1$). Equation (1) also contains the Dirac delta-function $\delta(\mathbf{P})$, and the last term in (1) is a nonlinear term written (without taking into account the gradients of Δ_α) in implicit form since we will be interested here (as in Ref. 1) only in the linear part of the ID equation (see the detailed discussion in the introduction in Ref. 1).

The ID equation (1) contains the following functions:

$$D(\mathbf{p}_1,\mathbf{p}_2) = [\xi_0(\mathbf{p}_1)+\xi_0(\mathbf{p}_2)]^2 - 4\xi^2, \tag{3}$$

$$\Phi_{\alpha\beta}(\mathbf{p}_1,\mathbf{p}_2) = \Phi_{\alpha\beta}(\mathbf{p}_2,\mathbf{p}_1) = [1-N_{(+)}(\mathbf{p}_1)-N_{(+)}\times(\mathbf{p}_2)]\varphi_{\alpha\beta}(\mathbf{p}_1,\mathbf{p}_2) - [N_{(-)}(\mathbf{p}_1)+N_{(-)}\times(\mathbf{p}_2)]\chi_{\alpha\beta}(\mathbf{p}_1,\mathbf{p}_2), \tag{4}$$

where

$$\varphi_{\alpha\beta}(\mathbf{p}_1,\mathbf{p}_2) = -\delta_{\alpha\beta}[\xi_0(\mathbf{p}_i)+\xi_0(\mathbf{p}_2)] + \frac{4\xi_\alpha\xi_\beta}{\xi_0(\mathbf{p}_1)+\xi_0(\mathbf{p}_2)} - i2e_{\alpha\beta\gamma}\xi_\gamma,$$

$$\chi_{\alpha\beta}(\mathbf{p}_1,\mathbf{p}_2) = 2\xi\Big(\delta_{\alpha\beta}-\frac{\xi_\alpha\xi_\beta}{\xi^2}\Big) + ie_{\alpha\beta\gamma}\,\frac{\xi_\gamma}{\xi}\,[\xi_0(\mathbf{p}_1)+\xi_0(\mathbf{p}_2)]$$

($\xi=|\vec{\xi}|$). The functions $N_\pm(\mathbf{p})$ are defined as

$$N_{(\pm)}(\mathbf{p}) \equiv \frac{1}{2}\,[n^{(0)}(\xi_0(\mathbf{p})+|\vec{\xi}(\mathbf{p},H)|) \pm n^{(0)}(\xi_0(\mathbf{p}) - |\vec{\xi}(\mathbf{p},H)|)],$$

$$n^{(0)}(\xi) = [\exp(\xi/T)+1]^{-1}, \tag{5}$$

where $\xi_0(\mathbf{p}) = \varepsilon(\mathbf{p}) - (\mathbf{vp}+\mu)$, and μ is the chemical potential. We assume that the Fermi liquid obeys the isotropic energy–momentum relation $\varepsilon(\mathbf{p})=\varepsilon(p)=p^2/2m^*$. The quantities ξ_α appearing in Eqs. (4) and (5) differ from zero only in the presence of the applied magnetic field $\mathbf{H}$ and depend on the Fermi-liquid exchange interactions (see Sec. 4 in Ref. 1 for details).

We will assume below that the external magnetic field $\mathbf{H}$ is zero, and hence $\xi_\alpha\equiv 0$. In this case (for $v_n\neq 0$, $v_s=0$, and $\xi_\alpha\equiv 0$), the ID equation (1) combined with Eqs. (3)–(5) can be transformed to

$$\Delta_\alpha(\mathbf{R},\mathbf{k}) = -\frac{1}{2(2\pi)^3}\int d^3q L_2(|\mathbf{k}-\mathbf{q}|)\Delta_\alpha(\mathbf{R},\mathbf{q})G(\mathbf{q}) - \frac{i}{4(2\pi)^3}\int d^3q L_2(|\mathbf{k}-\mathbf{q}|)\,\frac{\partial\Delta_\alpha(\mathbf{R},\mathbf{q})}{\partial R_l}\Bigg\{\frac{q_l}{m^*}\times\Bigg[\frac{(\mathbf{v}_n\mathbf{q})}{\varepsilon(\mathbf{q})-\mu}\,\frac{d\tau(\mathbf{q})}{d\xi_0}-\frac{\rho(\mathbf{q})}{\varepsilon(q)-\mu}-\frac{d\rho(\mathbf{q})}{d\xi_0}\Bigg] + v_{nl}\Bigg[\frac{d\tau(\mathbf{q})}{d\xi_0}+\frac{(\mathbf{v}_n\mathbf{q})}{\varepsilon(q)-\mu}\Big(\frac{\rho(\mathbf{q})}{\varepsilon(q)-\mu}-\frac{d\rho(\mathbf{q})}{d\xi_0}\Big)\Bigg]\Bigg\} + \frac{1}{2m^*(4\pi)^3}\int d^3q L_2(|\mathbf{k}-\mathbf{q}|)\,\frac{\partial^2\Delta_\alpha(\mathbf{R},\mathbf{q})}{\partial R_l\partial R_i}\Bigg\{\delta_{il}\Bigg[\frac{d\tau(\mathbf{q})}{d\xi_0} + \frac{(\mathbf{v}_n\mathbf{q})}{\varepsilon(q)-\mu}\Big(\frac{\rho(\mathbf{q})}{\varepsilon(q)-\mu}-\frac{d\rho(\mathbf{q})}{d\xi_0}\Big)\Bigg] + \frac{q_iq_l}{m^*}\Bigg[\frac{d^2\tau(\mathbf{q})}{d\xi_0^2}+\frac{2}{\varepsilon(q)-\mu}\,\frac{d\tau(\mathbf{q})}{d\xi_0} - \frac{(\mathbf{v}_n\mathbf{q})}{\varepsilon(q)-\mu}\,\frac{d^2\rho(\mathbf{q})}{d\xi_0^2}\Bigg] + m^*v_{ni}v_{nl}\Bigg[\frac{d^2\tau(\mathbf{q})}{d\xi_0^2} - \frac{2(\mathbf{v}_n\mathbf{q})}{(\varepsilon(q)-\mu)^2}\Big(\frac{\rho(\mathbf{q})}{\varepsilon(q)-\mu}-\frac{d\rho(\mathbf{q})}{d\xi_0}\Big)$$

$$-\frac{(\mathbf{v}_n\mathbf{q})}{\varepsilon(q)-\mu}\frac{d^2\rho(\mathbf{q})}{d\xi_0^2}\Bigg]$$
$$+(v_{ni}q_l+v_{nl}q_i)\Bigg[\frac{(\mathbf{v}_n\mathbf{q})}{\varepsilon(q)-\mu}\left(\frac{d^2\tau(\mathbf{q})}{d\xi_0^2}-\frac{1}{\varepsilon(q)-\mu}\frac{d\tau(\mathbf{q})}{d\xi_0}\right)+\frac{1}{\varepsilon(q)-\mu}\left(\frac{\rho(\mathbf{q})}{\varepsilon(q)-\mu}-\frac{d\rho(\mathbf{q})}{d\xi_0}\right)-\frac{d^2\rho(\mathbf{q})}{d\xi_0^2}\Bigg]\Bigg\}$$
$$+\frac{1}{(2\pi)^3}\int d^3qL_2(|\mathbf{k}-\mathbf{q}|)g_\alpha^{(3)}(\mathbf{R},\mathbf{q}) \tag{6}$$

[cf. with the ID equation (42) in Ref. 1, where $v_n=0$ but $H\neq 0$].

Equation (6) contains the functions $G(\mathbf{q})$, $\tau(\mathbf{q})$, and $\rho(\mathbf{q})$ defined by the formulas

$$G(\mathbf{q})\equiv\frac{\tanh(\xi_0(\mathbf{q})/2T)+\tanh(\xi_0(-\mathbf{q})/2T)}{\xi_0(\mathbf{q})+\xi_0(-\mathbf{q})},$$
$$\tau(\mathbf{q})\equiv\frac{1}{2}\left[\frac{\tanh(\xi_0(\mathbf{q})/2T)}{\xi_0(\mathbf{q})}+\frac{\tanh(\xi_0(-\mathbf{q})/2T)}{\xi_0(-\mathbf{q})}\right],$$
$$\rho(\mathbf{q})\equiv\frac{1}{2}\left[\frac{\tanh(\xi_0(\mathbf{q})/2T)}{\xi_0(\mathbf{q})}-\frac{\tanh(\xi_0(-\mathbf{q})/2T)}{\xi_0(-\mathbf{q})}\right]. \tag{7}$$

It should be noted that for $v_n=0$, the ID equation (6) is transformed into the equation derived in Refs. 12, 13 since $\xi_0(\mathbf{q})=\xi_0(-\mathbf{q})=\varepsilon(\mathbf{q})-\mu, \rho(\mathbf{q})\equiv 0, G(\mathbf{q})\equiv\tau(\mathbf{q})$.

3. GINZBURG–LANDAU EQUATION FOR A SUPERFLUID FERMI LIQUID WITH *p*-PAIRING FOR $\mathbf{v_N}\neq 0$

Proceeding from the general ID equation (6) for a SFL, we derive the GL equation for a triplet p-wave pairing ($s=1$, $l=1$) for $v_n\neq 0$ in zero magnetic field. For this purpose, we introduce the SFL order parameter, i.e., the complex 3×3 matrix $A_{\alpha j}(\mathbf{R})$ by the formula[5,6,14]

$$\Delta_\alpha(\mathbf{R},\mathbf{k})=A_{\alpha j}(\mathbf{R})\frac{k_j}{k}. \tag{8}$$

Using the approximate equality (see Ref. 1)

$$L_2(|\mathbf{k}-\mathbf{q}|)\approx a-b|\mathbf{k}-\mathbf{q}|^2, \tag{9}$$

where

$$a=4\pi\int_0^\infty drr^2L_2(r),\quad b=\frac{2\pi}{3}\int_0^\infty drr^4L_2(r), \tag{10}$$

we obtain from (6) the equation for the matrix $A_{\alpha j}(\mathbf{R})$

$$A_{\alpha j}(\mathbf{R})\frac{k_j}{k}=-\frac{bk_i}{(2\pi)^3}\int_0^{2\pi}d\varphi\int_{-1}^1 d(\cos\theta)n_in_j\times\int_0^\infty dqq^3\Bigg\{G(\mathbf{q})A_{\alpha j}(\mathbf{R})+\frac{i}{2}\frac{\partial A_{\alpha j}(\mathbf{R})}{\partial R_l}\Bigg[\frac{qn_l}{m^*}\left(\frac{qv_n\cos\theta}{\varepsilon(q)-\mu}\frac{d\tau(\mathbf{q})}{d\xi_0}-\frac{\rho(\mathbf{q})}{\varepsilon(q)-\mu}-\frac{d\rho(\mathbf{q})}{d\xi_0}\right)+v_{nl}\Bigg(\frac{d\tau(\mathbf{q})}{d\xi_0}+\frac{qv_n\cos\theta}{\varepsilon(q)-\mu}\left(\frac{\rho(\mathbf{q})}{\varepsilon(q)-\mu}-\frac{d\rho(\mathbf{q})}{d\xi_0}\right)\Bigg)\Bigg]-\frac{1}{8m^*}\frac{\partial^2A_{\alpha j}(\mathbf{R})}{\partial R_l\partial R_k}\Bigg[\delta_{kl}\Bigg(\frac{d\tau(\mathbf{q})}{d\xi_0}+\frac{qv_n\cos\theta}{\varepsilon(q)-\mu}\left(\frac{\rho(\mathbf{q})}{\varepsilon(q)-\mu}-\frac{d\rho(\mathbf{q})}{d\xi_0}\right)\Bigg)+\frac{q^2n_kn_l}{m^*}\left(\frac{d^2\tau(\mathbf{q})}{d\xi_0^2}+\frac{2}{\varepsilon(q)-\mu}\frac{d\tau(\mathbf{q})}{d\xi_0}-\frac{qv_n\cos\theta}{\varepsilon(q)-\mu}\frac{d^2\rho(\mathbf{q})}{d\xi_0^2}\right)+m^*v_{nk}v_{nl}\Bigg(\frac{d^2\tau(\mathbf{q})}{d\xi_0^2}-\frac{2qv_n\cos\theta}{(\varepsilon(q)-\mu)^2}\left(\frac{\rho(\mathbf{q})}{\varepsilon(q)-\mu}-\frac{d\rho(\mathbf{q})}{d\xi_0}\right)-\frac{qv_n\cos\theta}{\varepsilon(q)-\mu}\frac{d^2\rho(\mathbf{q})}{d\xi_0^2}\Bigg)+q(v_{nk}n_l+v_{nl}n_k)\Bigg(\frac{qv_n\cos\theta}{\varepsilon(q)-\mu}\left(\frac{d^2\tau(\mathbf{q})}{d\xi_0^2}-\frac{1}{\varepsilon(q)-\mu}\frac{d\tau(\mathbf{q})}{d\xi_0}\right)+\frac{1}{\varepsilon(q)-\mu}\left(\frac{\rho(\mathbf{q})}{\varepsilon(q)-\mu}-\frac{d\rho(\mathbf{q})}{d\xi_0}\right)-\frac{d^2\rho(\mathbf{q})}{d\xi_0^2}\Bigg)\Bigg]\Bigg\}+[O(A^3(\mathbf{R}))]_\alpha \tag{11}$$

[cf. the ID equation (45) in Ref. 1, where $v_n=0$, but $H\neq 0$].

At temperatures close to T_c, we can expand the function $G(\mathbf{q})=G(\mathbf{q},T)$ [see (7)] into a power series in $T-T_c$:

$$G(\mathbf{q},T)\approx G(\mathbf{q},T_c)+(T-T_c)\left.\frac{\partial G(\mathbf{q},T)}{\partial T}\right|_{T=T_c}+\frac{(T-T_c)^2}{2}\left.\frac{\partial^2G(\mathbf{q},T)}{\partial T^2}\right|_{\substack{T=T_c\\ v_n=0}}. \tag{12}$$

The value of T_c depends on L_2 and is determined from the linearized integral equation for a spatially homogeneous OP [see Eqs. (6) and (8) for $\partial A_{\alpha j}/\partial R_l=0$, $\partial^2A_{\alpha j}/\partial R_l\partial R_i=0$].

Thus, assuming that $v_n\ll 2T_c/p_F$ and retaining the principal terms, we obtain from (7), (11), and (12) as a result of analytical calculations in the perturbation theory the following GL equation for a SFL liquid with the p-wave pairing (of the ^{3}He type) with corrections to coefficients of gradients of $A_{\alpha j}(\mathbf{R})$:

$$\left[\frac{T_c-T}{T_c}+\frac{1}{2}\left(\frac{T_c-T}{T_c}\right)^2\right]A_{\alpha j}-\frac{m^*v_n^2}{2\varepsilon_F}\left(\frac{\varepsilon_F}{T_c}\right)^2\frac{7\zeta(3)}{5\pi^2}\left[1+2\frac{T_c-T}{T_c}-\frac{i}{\varepsilon_F}\left(\frac{\varepsilon_F}{T_c}\right)^2\frac{93\zeta(5)}{49\pi^2\zeta(3)}\left(v_{nk}\frac{\partial}{\partial R_k}\right)\right]\Bigg(A_{\alpha j}$$

$$+\frac{2v_{nj}v_{nl}}{v_n^2}A_{\alpha l}\Bigg)-\frac{i}{\varepsilon_F}\left(\frac{\varepsilon_F}{T_c}\right)^2\frac{7\zeta(3)}{10\pi^2}\Bigg[\Bigg(1$$

$$-\frac{186\zeta(5)}{49\pi^2\zeta(3)}\frac{m^*v_n^2}{2\varepsilon_F}\left(\frac{\varepsilon_F}{T_c}\right)^2\Bigg)\left(v_{nl}\frac{\partial A_{\alpha l}}{\partial R_j}+v_{nj}\frac{\partial A_{\alpha l}}{\partial R_l}\right)$$

$$+v_{nl}\frac{\partial A_{\alpha j}}{\partial R_l}\Bigg]+\frac{7\zeta(3)v_F^2}{80\pi^2T_c^2}\left[1-\frac{930\zeta(5)}{49\pi^2\zeta(3)}\frac{m^*v_n^2}{2\varepsilon_F}\left(\frac{\varepsilon_F}{T_c}\right)^2\right]$$

$$\times\left(\frac{\partial^2 A_{\alpha j}}{\partial\mathbf{R}^2}+2\frac{\partial^2 A_{\alpha l}}{\partial R_j\partial R_l}\right)+[O(A^3)]_{\alpha j}=0. \qquad (13)$$

where $\zeta(x)$ is the Riemann zeta function. In Eq. (13), we assume that the chemical potential $\mu(T)\approx\varepsilon_F$ for $T\approx T_c\ll\varepsilon_F=p_F^2/(2m^*)$. For $v_n=0$, Eq. (13) coincides with the GL equation from Refs. 5, 6, 12, 13, and 15, while for $v_n\sim 2T_c/p_F$ the perturbation theory is not applicable, and the obtained corrections become of the same order of magnitude as the initial coefficients in the GL equations (for $v_n=0$).

4. CONCLUSIONS

We have disregarded strong-coupling effects which are known to stabilize (see, for example, Refs. 6, 10, 14, and 16) ^{3}He-A under pressures $P>P_{PCP}\approx 21.2$ bar (the pressure at the polycritical point of ^{3}He for $H=0$) and are weak in ^{3}He-B under low pressures. It should be emphasized in this connection that the main results obtained by us are the corrections to the coefficients of the OP gradients in the GL equation (13), which are associated with the effect of a uniform flow (with the velocity v_n) of the normal component of the SFL of the ^{3}He type with the p-wave pairing. These corrections are not reduced only to ''elongation'' of the spatial derivatives $\partial/\partial R_l\to\partial/\partial R_l - i2m^*v_{nl}/\hbar$ in the GL equations in the second-order perturbation of OP gradient (see Ref. 8), but contain an additional contribution. The corrections in Eq. (13), which are additional as compared to Ref. 8, can attain $\sim$10% of the value of the coefficients for $v_n=0$ even for $v_n\ll 2T_c/p_F$, and hence can be not only comparable with, but also larger than ''nontrivial'' corrections[8] (depending on the value of v_n) to the same coefficients, which are due to strong coupling effects in ^{3}He. Consequently, the inclusion of the corrections determined by us in the GL equation can be important above all for ^{3}He$-B$ and indicates the OP deformation for $v_n\neq 0$.

Finally, it should be noted that the ID equation derived by us in the form (1) and (6) is valid in the general case of triplet pairing ($s=1$ and l is any odd number) and hence cannot be used for deriving the GL equation not only in the case of p-wave pairing, but also when the effects of f-pairing ($l=3$), which can play a significant role in superfluid phases of ^{3}He (see, for example, Ref. 17), are taken into account.

The author is grateful to S. V. Peletminskii for his attention to this research and for fruitful discussions.

*E-mail: kfti@rocket.kharkov.ua

[1] A. N. Tarasov, Fiz. Nizk. Temp. **21**, 24 (1995) [Low Temp. Phys. **21**, 17 (1995)].
[2] V. V. Krasil'nikov, S. V. Peletminskii, A. A. Yatsenko, and A. A. Rozhkov, Fiz. Élem. Chast. At. Yadra **19**, 1440 (1988) [*sic*].
[3] V. V. Krasil'nikov, S. V. Peletminskii, and A. A. Yatsenko, Physica A **162**, 513 (1990).
[4] A. I. Akhiezer, V. V. Krasil'nikov, S. V. Peletminskii, and A. A. Yatsenko, Usp. Phys. Nauk **163**, 1 (1993) [Phys. Usp **36**, 63 (1993)].
[5] A. J. Leggett, Rev. Mod. Phys. **47**, 331 (1975)].
[6] V. P. Mineev, Usp. Phys. Nauk **139**, 303 (1983) [Sov. Phys. Uspekhi **26**, 160 (1983)].
[7] D. Rainer and J. W. Serene, Phys. Rev. B **13**, 4745 (1976).
[8] J. W. Serene and D. Rainer, Phys. Rev. B **17**, 2901 (1978).
[9] J. W. Serene and D. Rainer, Phys. Rep **101**, 221 (1983).
[10] D. Vollhardt and P. Wölfe, *The Superfluid Phases of Helium 3*, Taylor and Francis, London (1990).
[11] P. N. Brusov and V. N. Popov, *Superfluidity and Collective Properties of Quantum Liquids* [in Russian], Nauka. Moscow (1988).
[12] A. N. Tarasov, Preprint of Kharkov Physicotechnical Inst. No. 982-29, Kharkov (1992).
[13] A. N. Tarasov, Vopr. Atom. Nauki Tekh., Ser. Yad.-Fiz. Issled. (Teor. Éksp.), **3(24)**, 176 (1992).
[14] I. M. Khalatnikov (Ed.), *Superfluidity of Helium 3* [Russian transl.], Mir, Moscow (1977).
[15] V. Ambegaokar, P. G. de Gennes, and D. Rainer, Phys. Rev. A **9**, 2676 (1974).
[16] W. F. Brinkman, J. W. Serene, and P. W. Anderson, Phys. Rev. A **10**, 2386 (1974).
[17] J. A. Sauls, Phys. Rev. B **34**, 4861 (1986).

Translated by R. S. Wadhwa

Scattering theory of superconductive tunneling in quantum junctions

V. S. Shumeiko[1,2] and E. N. Bratus,[1,2]

[1]*Department of Applied Physics, Chalmers University of Technology and Göteborg University, S-41296 Göteborg, Sweden and* [2]*B. Verkin Institute for Low Temperature Physics and Engineering, 47 Lenin Ave., 310164 Kharkov, Ukraine*

G. Wendin[1]

Department of Applied Physics, Chalmers University of Technology and Göteborg University, S-41296 Göteborg, Sweden

(Submitted September 11, 1996; revised September 27, 1996)
Fiz. Nizk. Temp. **23**, 249–270 (March 1993)

A consistent theory of superconductive tunneling in single-mode junctions within a scattering formulation of Bogolyubov-de Gennes quantum mechanics is presented. The dc Josephson effect and the dc quasiparticle transport in the voltage-biased junctions are considered. Elastic quasiparticle scattering by the junction determines the equilibrium Josephson current. The origin of Andreev bound states in tunnel junctions and their role in equilibrium Josephson transport are discussed. In contrast, quasiparticle tunneling in voltage-biased junctions is determined by inelastic scattering. A general expression for inelastic scattering amplitudes is derived and the quasiparticle current is calculated at all voltages with emphasis on a discussion of the properties of subgap tunnel current and the nature of subharmonic gap structure.
 [S1063-777X(97)00203-X]

1. INTRODUCTION

The tunnel Hamiltonian model[1] has for many years been a main theoretical tool for investigation of tunneling phenomena in superconductors.[2] However, interpretation of recent experiments on transmissive tunnel junctions[3–5] and complex superconductor-semiconductor structures[6,7] requires more detailed knowledge of the mechanisms of the superconductive tunneling than the tunnel model is able to provide. Particularly informative are experiments on superconducting quantum point contacts with controlled number of transport modes and transparency, such as controllable superconducting break junctions[8] and gate-controlled superconductor-semiconductor devices.[9] Since only a few transport modes with controlled transparency are involved in the tunnel transport; the experiments provide precise and detailed information which can be directly compared with theory.

The first attempts to develop a theory of superconductive tunneling beyond the tunnel Hamiltonian model[10–13] were made in generalization of methods applied to *SNS* junctions[14,15] and superconducting constrictions[16,17] based on the Green's function methods. In these theories, the junction Green's functions are directly found from the Green's function equations which are supplemented by special boundary conditions representing the tunnel barrier or by matching the superconductor and insulator Green's functions at the superconductor-insulator boundaries.

In the first studies of the Josephson effect in *SNS* junctions[18,19] another method of calculation, based on expansion over eigenstates of the Bogolyubov-de Gennes (BdG) equation, has been used.[20] A similar method has been also applied to *SIS* tunnel junctions[21] and superconductor-semiconductor junctions.[22] In the absence of inelastic scattering the method of using the BdG equation gives the same results as the Green's function method.[21] One might then expect that the Josephson effects in superconducting junctions can be explained on a rather simple quantum-mechanical level. Following this idea, the quantum-mechanical approach has been successfully applied to calculation of the direct Josephson current in different kinds of mesoscopic weak links[24–28] and tunnel junctions.[29–31] This method was applied for the first time to voltage-biased junctions by Blonder, Tinkham, and Klapwijk, who considered quasiparticle tunneling in *SIN* junctions as a scattering problem in BdG quantum mechanics.[23] Later, the quantum-mechanical approach has been found helpful in investigations of more complex phenomena of quasiparticle transport and ac Josephson effect in voltage-biased *SNS* junctions,[32] mesoscopic *SIS* tunnel junctions[33] and mesoscopic constrictions.[34]

The quantum-mechanical approach based on the BdG equation is adequate for describing the physical situation in mesoscopic junctions, where the inelastic scattering effects are weak and most important is the coherent electron dynamics. Because of the quantization of transverse electron modes in mesoscopic junctions,[24,35] $1D$ models for the current transport through the junction may be appropriate.

In this paper we present a consistent quantum-mechanical theory of superconductive tunneling in a one-mode quantum constriction (Fig. 1). We consider the dc Josephson effect and also dc quasiparticle tunneling in the voltage-biased junctions. In the latter case we focus attention

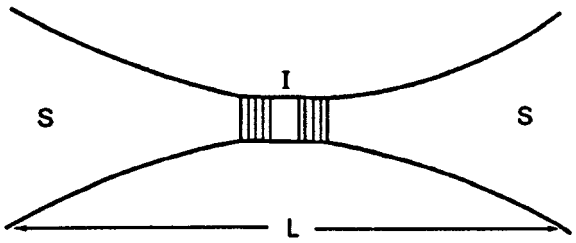

FIG. 1. *SIS* tunnel constriction.

on a detailed calculation of the subharmonic gap structure (SGS) of the tunnel current.[33]

Following the Landauer approach,[36] we consider superconducting electrodes as equilibrium reservoirs which emit quasiparticles into the constriction. Scattering by the junction goes into two channels; (i) the normal channel in which the outgoing quasiparticles remain in the same branch of the quasiparticle spectrum, and (ii) the Andreev channel in which quasiparticles change branch due to electron-hole conversions. The current in such a picture results from the imbalance of currents carried by scattering states originating from the left and the right reservoirs. Here the magnitude of the current is proportional to the transmission coefficient D of the tunnel barrier.

The imbalance of currents in superconducting junctions can be created in two ways: by establishing a difference in the phases of the order parameters in the left and right electrodes or by applying a voltage bias. The basic fact concerning the flow of equilibrium current in the presence of a phase difference, which was established by Furusaki and Tsukada,[29] is that a bulk supercurrent is, upon approaching the tunnel interface, transformed into a current that flows through the superconducting bound states which appear at the tunnel interface in the presence of the phase difference[37] and which provide transmission of the Cooper pairs through the tunnel barrier. The balance among currents of different scattering states is not violated, although the scattering amplitudes depend strongly on the phase difference.

Application of a voltage bias gives rise to more far-reaching consequences than just the imbalance of the elastic scattering modes: the scattering states themselves are modified in a nontrivial way. This follows from the fact that the scattering amplitudes, which are phase-dependent at equilibrium, become time-dependent in accordance with the Josephson relation,[38] $d\varphi/dt=2eV$, when voltage is applied. Thus, in the presence of a constant voltage the superconducting junction behaves as an effective nonstationary scatterer, whose transmissivity oscillates. This property of the superconducting junctions gives rise to ac Josephson effect; however, it is also significant for dc quasiparticle transport, because the quasiparticle transmission through such a scatterer is *inelastic*.

The physical mechanism of inelastic quasiparticle transmission through voltage-biased superconducting junctions has been first considered in *SNS* junctions,[32] where it has been explained in terms of multiple Andreev reflections (MAR): the normal quasiparticles, which are confined between superconducting walls, are permanently accelerated by the static electric field due to sequential electron-hole conversions at the *NS* interfaces, similarly to acceleration of the electrons in an ordinary potential well by a time-dependent electric field. Similar arguments can be extended to the tunnel junctions.[39] However, in tunnel junctions the scattering theory approach is more appropriate because of the quantum nature of quasiparticle transmission through the atomic-size tunnel barrier. This introduces a side band spectrum of scattered waves where the side band energies are shifted with respect to the energy of the incident wave by integer number of quanta of the scatterer frequency.[33] Such an approach is familiar in the theory of quantum scattering by oscillating potential barriers in normal tunnel junctions (see, e.g., Refs. 40 and 41 and the references cited there).

The tunneling through all the inelastic channels (normal and Andreev channels) constitutes a complete picture of superconductive tunneling in biased Josephson junctions—the incoherent part of the side band currents, which correspond to the direct quasiparticle current, and the side band interference currents, which correspond to the alternating Josephson current. An important aspect of this picture is that the Andreev bound states are involved in the current transport together with the extended side band states, which give a multiparticle character to the superconductive tunneling in the subgap voltage region. This multiparticle origin of the subgap tunnel current was first pointed out by Schrieffer and Wilkins.[42]

The structure of the paper is as follows. After formulation of the problem and discussion of the quasiclassical approximation in Sec. 2, we consider the problem of elastic scattering in Sec. 3 as a starting point for construction of inelastic scattering states in biased junctions. The solution of the elastic scattering problem allows us to calculate the dc Josephson current, which is done for completeness in Sec. 4. In Sec. 5 we construct inelastic scattering states and derive a continued-fraction representation for the scattering amplitudes. In Sec. 6 we derive the nonequilibrium current. In Sec. 7 we discuss the origin of the excess tunnel current in the large bias limit. In Sec. 8 we present a general analysis of the subgap tunnel current. Finally, the *SGS* is analyzed in Sec. 9.

2. FORMULATION OF THE MODEL

We consider a superconducting quantum constriction with adiabatic geometry[43]: the cross section varies smoothly with the coordinate x on the scale of the Fermi electron wavelength $1/p_F$, and the size of the cross section is comparable with the Fermi electron wavelength (Fig. 1). The length L of the constriction is assumed to be smaller than the superconducting coherence length ξ_0:

$$1/p_F \ll L \ll \xi_0 . \tag{2.1}$$

The Hamiltonian of the constriction is assumed to have the form

$$\hat{H}=\left[\frac{(\hat{p}-\sigma_z e\mathbf{A}(\mathbf{r},t))^2}{2m}+U(r)-\mu\right]\sigma_z$$
$$+[V(x)+e\varphi(\mathbf{r},t)]\sigma_z+\hat{\Delta}(\mathbf{r},t), \tag{2.2}$$

where $U(\mathbf{r})$ is the potential which confines the electrons within the constriction; $V(x)$ is the potential of the tunnel barrier; $\mathbf{A}(\mathbf{r},t)$ and $\varphi(\mathbf{r},t)$ are electro-magnetic potentials; $\hat{\Delta}(\mathbf{r},t)$ is the off-diagonal superconducting order parameter given by the matrix

$$\hat{\Delta}=\begin{pmatrix} 0 & \Delta e^{i\chi/2} \\ \Delta e^{-i\chi/2} & 0 \end{pmatrix}. \tag{2.3}$$

We assume that the junction is symmetric. The choice of the units corresponds to $c=\hbar=1$.

It is convenient to eliminate the phase of the superconducting order parameter $\chi(\mathbf{r},t)$ in Eq. (2.3) by means of a gauge transformation:

$$\exp(i\sigma_z\chi/2)\hat{H}\ \exp(-i\sigma_z\chi/2)\to\hat{H}, \tag{2.4}$$

which allows us to introduce a gauge-invariant superfluid momentum, $\mathbf{p}_s=\nabla\chi/2-e\mathbf{A}$, and an electric potential $\Phi=\dot{\chi}/2+e\varphi$.

There are different scales of change of potentials in Eq. (2.2): one is an atomic scale over which the confining potential $U(r_\perp)$ and the potential of the tunnel barrier $V(x)$ change. Other scales are related to the changes in the superconducting order parameter, the electromagnetic field penetration lengths and the length of the contact: all these lengths are large in comparison with the atomic length. It is convenient to separate these two scales by introducing quasiclassical wave functions,[44] which vary slowly on an atomic scale, and by including rapidly varying potentials in a boundary condition for quasiclassical wave functions. To this end, we assume that the solution $\Psi(\mathbf{r},t)$ of the Bogolyubov-de Gennes equation[20]

$$i\dot{\Psi}(t)=\hat{H}\Psi(t), \tag{2.5}$$

with the Hamiltonian of Eq. (2.2), has a quasiclassical form

$$\Psi(\mathbf{r},t)=\sum_\beta\ \psi_\perp(\mathbf{r}_\perp,x)\ \frac{1}{\sqrt{v}}\exp\left(i\beta\int p\,dx\right)\psi^\beta(x,t), \tag{2.6}$$

where $\psi_\perp$ is the normalized wave function of the quantized transverse electron motion with the energy $E_\perp$,

$$\left(\frac{\hat{\mathbf{p}}_\perp}{2m}+V(\mathbf{r}_\perp,x)\right)\psi_\perp=E_\perp(x)\psi_\perp,$$

$$\psi_\perp(r_\perp=\infty,x)=0,$$

and p is the longitudinal momentum of the quasiclassical electron, $p(x)=[2m(\mu-E_\perp(x))]^{1/2}$; $\beta=\pm$ indicates the direction of the electron motion. We assume that the constriction has only one transport mode; an extension to the case of several unmixed modes consists of additional summation over all transport modes in the equation for the current. The coefficients ψ^β in Eq. (2.6) describe the wave functions which vary slowly in the x direction and which satisfy the reduced BdG equation

$$i\dot{\psi}^\beta_{L,R}=(\beta v\hat{p}\sigma_z+\Phi_{L,R}\sigma_z+vp_{sL,R}+\Delta\sigma_x)\psi^\beta_{L,R} \tag{2.7}$$

in the left (L) and the right (R) electrodes; $v=p/m$. The potentials $\mathbf{p}_s$ and Φ describe the distributions of the electromagnetic field and supercurrent in the electrodes. In the point contact geometry these quantities are small due to the effect of spreading out of the current.[16,45] We will therefore omit them, $\mathbf{p}_s=\Phi=0$. For the same reason, deviation of the spatial distribution of the module of the order parameter Δ from constant value is small in the point contacts; we will therefore ignore it, $\Delta=$ const.

The functions $\psi^\beta_{L,R}$ are matched at the constriction by the boundary condition[31] (see also Appendix A):

$$\begin{pmatrix}\psi^-_L\\ \psi^+_R\end{pmatrix}=\hat{V}\begin{pmatrix}\psi^+_L\\ \psi^-_R\end{pmatrix}\quad\text{at } x=0, \tag{2.8}$$

with a matching matrix $\hat{V}$

$$\hat{V}=\begin{pmatrix} r & de^{i\sigma_z\varphi/2} \\ de^{-i\sigma_z\varphi/2} & r\end{pmatrix}. \tag{2.9}$$

The quantities d and r are the normal electron transmission and reflection amplitudes due to the barrier. Here and further φ is a gauge-invariant difference in the superconducting phases of the right and left electrodes: $\varphi=\chi_R(0)-\chi_L(0)$. The matching matrix in Eq. (2.9) satisfies the unitarity condition

$$\hat{V}\hat{V}^+=1. \tag{2.10}$$

The boundary condition in Eqs. (2.8) and (2.9) is analogous to the boundary condition used in the quasiclassical Green's function methods (see, e.g., Refs. 11 and 46). This is a very simple equation for coupling of superconducting electrodes, while retaining the main features of the Josephson effect, except for effects of the resonant tunneling.[30,47,48]

3. ELASTIC SCATTERING

In the absence of time dependence in the phase difference at the junction, $\dot{\varphi}=0$, Eqs. (2.7) and (2.8) describe elastic scattering of quasi-particles. The scattering states can be constructed by using stationary solutions of Eq. (2.7), which correspond to elementary propagating waves with energy $|E|>\Delta$:

$$\psi^{\beta\alpha}_E=\exp(-iEt+i\beta\alpha(\xi/v)x)u^\delta_E, \tag{3.1a}$$

$$u^\delta_E=(2\cosh\ \gamma)^{-1/2}\begin{pmatrix}e^{\delta\gamma/2}\\ \sigma e^{-\delta\gamma/2}\end{pmatrix}, \tag{3.1b}$$

where

$$\xi=\sqrt{E^2-\Delta^2},\quad e^\gamma=\frac{|E|+\xi}{\Delta},$$

$$\sigma=\text{sign } E,\quad \alpha=\pm,\quad \text{and}\quad \delta=\alpha\sigma. \tag{3.2}$$

The vector function μ_E is normalized, $(u,u)=1$; the brackets mean that the scalar product is in the electron-hole space. In Eq. (3.1) there are four elementary waves, which correspond to the same energy, as illustrated in Fig. 2, and which are labeled by quantum numbers β (direction of the Fermi electron momentum) and $\alpha=\text{sign}(|p|-p_F)$ (the electron or

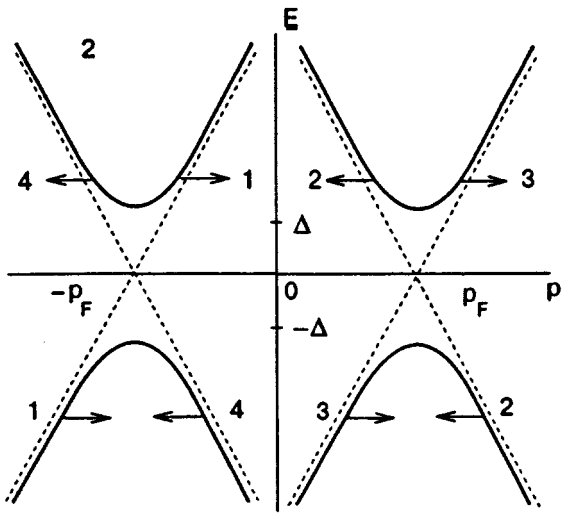

FIG. 2. Quasiparticle spectrum and position of the incoming states: 1(3)—hole (electron)-like quasiparticle incident from left; 2(4)—hole (electron)-like quasiparticle incident from right.

hole-like branch of the quasiparticle spectrum). The direction of propagation of each elementary wave is determined by the sign of the probability current. The probability current density j_p, which is defined by the conservation law (the continuity equation) $\partial|\psi|^2/\partial t+\partial j_p/\partial x=0$ for the BdG equation [Eq. (2.7)], has the form $j_p=(\psi,\sigma_z\psi)$. For the elementary waves in Eq. (3.1), we obtain the explicit result $j_p=\beta\delta\tanh\gamma$. According to this formula, the relation $\delta=\beta$ is satisfied for the waves propagating from left to right, and the relation $\delta=-\beta$ is satisfied for the waves propagating from right to left. Therefore, the incoming waves from the left (L) and the right (R) have the form

$$\text{L:}\exp(i\sigma(\xi/v)x)u_E^{\beta},\quad \text{R:}\exp(-i\sigma(\xi/v)x)u_E^{-\beta},\quad (3.3)$$

while the outgoing waves have the form

$$\text{L:}\exp(-i\sigma(\xi/v)x)u_E^{-\beta},\quad \text{R:}\exp(i\sigma(\xi/v)x)u_E^{\beta}.\quad (3.4)$$

Correspondingly, the incoming quasiparticle can be scattered into four outgoing states: two forward-scattering states and two backscattering states. One of the reflected waves belongs to the same (electron-like or hole-like) branch of the quasiparticle spectrum as the incoming wave and constitutes the normal scattering channel, while the other reflected wave changes the spectrum branch and constitutes the Andreev channel. In a similar way, transmitted waves constitute normal and Andreev channels. The structure of the scattering states then becomes

$$\begin{pmatrix}\psi_L^-\\ \psi_R^+\end{pmatrix}=\begin{pmatrix}\delta_{j,1}\\ \delta_{j,2}\end{pmatrix}e^{i\sigma(\xi/v)x}u_E^-+\begin{pmatrix}a\\ b\end{pmatrix}_j e^{-i\sigma(\xi/v)x}u_E^+,\quad (3.5a)$$

$$\begin{pmatrix}\psi_L^+\\ \psi_R^-\end{pmatrix}=\begin{pmatrix}\delta_{j,3}\\ \delta_{j,4}\end{pmatrix}e^{i\sigma(\xi/v)x}u_E^+ +\begin{pmatrix}c\\ f\end{pmatrix}_j e^{-i\sigma(\xi/v)x}u_E^-,\quad (3.5b)$$

(for brevity we have omitted the time-dependent factors $\exp(-iEt)$). In Eqs. (3.5) the index $j=1(2)$ corresponds to a hole-like quasiparticle that comes from the left(right), while the index $j=3(4)$ corresponds to an electron-like quasiparticle that comes from the left (right). According to the structure of the matching matrix [Eq. (2.9)], the symmetry between the scattering states $j=1$ and 2 is

$$\begin{pmatrix}a\\ b\end{pmatrix}_2(\varphi)=\begin{pmatrix}b\\ a\end{pmatrix}_1(-\varphi),\quad \begin{pmatrix}c\\ f\end{pmatrix}_2(\varphi)=\begin{pmatrix}f\\ c\end{pmatrix}_1(-\varphi).\quad (3.6)$$

Analogous symmetry exists also for the scattering states $j=3,4$. Using the unitarity of the matching matrix [Eq. (2.9)], we can find the following relation between the scattering states $j=3$ and 1:

$$\begin{pmatrix}a\\ b\end{pmatrix}_3(\gamma,r,d)=\begin{pmatrix}c\\ f\end{pmatrix}_1(-\gamma,r^*,d^*),$$

$$\begin{pmatrix}c\\ f\end{pmatrix}_3(\gamma,r,d)=\begin{pmatrix}a\\ b\end{pmatrix}_1(-\gamma,r^*,d^*).\quad (3.7)$$

These symmetry relations allow us to find all the scattering amplitudes if one of the scattering states is known.

Let us find the explicit scattering amplitudes for the scattering state $j=1$. After substituting Eqs. (3.5) into Eq. (2.8), it is convenient to split the resulting equation, using the orthogonality condition, $(u^+,\sigma_z u^-)=0$, into two independent equations for the normal scattering amplitudes c,f and for the Andreev scattering amplitudes a,b:

$$(u^-,\sigma_z u^-)\begin{pmatrix}1\\ 0\end{pmatrix}=(u^-,\sigma_z\hat{V}u^-)\begin{pmatrix}c\\ f\end{pmatrix}_1,\quad (3.8a)$$

$$(u^+,\sigma_z u^+)\begin{pmatrix}a\\ b\end{pmatrix}_1=(u^+,\sigma_z\hat{V}u^-)\begin{pmatrix}c\\ f\end{pmatrix}_1.\quad (3.8b)$$

Calculating the scalar products in Eqs. (3.8), we find the explicit expression for the Andreev amplitudes in terms of the normal amplitudes,

$$\begin{pmatrix}a\\ b\end{pmatrix}_1=\frac{id\,\sin(\varphi/2)}{\sinh\,\gamma}\begin{pmatrix}f\\ -c\end{pmatrix}_1.\quad (3.9)$$

The solution of the first equation in Eq. (3.8) is given by

$$c_1=\frac{r\,\sinh^2\,\gamma}{Z},\quad f_1=-\frac{d\,\sinh\,\gamma\,\sinh(\gamma+i\varphi/2)}{Z},\quad (3.10)$$

where

$$Z=-\frac{d}{d^*}(R\,\sinh^2\,\gamma+D\,\sinh(\gamma+i\varphi/2)\times\sinh(\gamma-i\varphi/2)),\quad (3.11)$$

$D=|d|^2$ is the normal electron transmission coefficient of the tunnel junction, and $R=|r|^2=1-D$ is the normal electron reflection coefficient. It follows from Eqs. (3.9) and (3.10) that if there is no phase difference across the junction, $\varphi=0$, the Andreev scattering channel is closed: $a=b=0$. It is worth mentioning that the Andreev reflection is also absent if the normal transparency of the junction is equal to zero, $D=0$. If, on the other hand, the junction is completely transparent for normal electrons, $D=1$, there is no Andreev forward scattering, $b=c=0$.

In the presence of a phase difference at the junction the quasiparticle scattering is accompanied by the appearance of

superconducting bound states.[37] One can establish the existence of bound states by investigating the poles of the scattering amplitudes, Eq. (3.10), at imaginary γ corresponding to energies lying inside the gap $|E|<\Delta$. Assuming $\gamma \to i\gamma$ in Eq. (3.11), we have the dispersion equation $Z(i\gamma)=0$ or

$$\sin^2 \gamma = D \sin^2 \varphi/2. \tag{3.12}$$

The bound states correspond to a positive value of $\sin \gamma$: $\Delta \sin \gamma = \mathrm{Im}\, \xi > 0$. This condition has two roots:

$$\gamma = \gamma_0 = \arccos(\sqrt{D} \sin \varphi/2), \quad \gamma = \pi - \gamma_0 \tag{3.13}$$

or

$$E(\varphi) = \pm \Delta \sqrt{1 - D \sin^2 \varphi/2}. \tag{3.14}$$

The wave functions of the bound states can be constructed from elementary solutions of Eq. (2.7) with $|E|<\Delta$, which decay at $x=\pm\infty$:

$$\varphi^{\beta}_{E,R} = \exp(-iEt - \zeta x/v) u^{\nu}_{E}, \tag{3.15a}$$

$$\varphi^{\beta}_{E,L} = \exp(-iEt + \zeta x/v) u^{-\nu}_{E}, \tag{3.15b}$$

where

$$u^{\nu}_{E} = \frac{1}{\sqrt{2}} \begin{pmatrix} e^{i\nu\gamma/2} \\ \sigma e^{-i\nu\gamma/2} \end{pmatrix},$$

$$e^{i\gamma} = \frac{|E| + i\zeta}{\Delta}, \quad \zeta = \sqrt{\Delta^2 - E^2}, \quad \nu = \beta\sigma. \tag{3.16}$$

The bound state ansatz has a form similar to the outgoing part of the scattering states [Eq. (3.5)] with the coefficients satisfying the homogeneous equations in (3.8). These coefficients are

$$f = -\frac{d \sin(\gamma + \varphi/2)}{r \sin \gamma} c, \tag{3.17a}$$

$$\begin{pmatrix} a \\ b \end{pmatrix} = \frac{d \sin(\varphi/2)}{\sin \gamma} \begin{pmatrix} f \\ -c \end{pmatrix}, \tag{3.17b}$$

where γ is given by Eq. (3.12). We note that the bound state spectrum is nondegenerate. The coefficient c in Eqs. (3.17) is obtained from the normalization condition for the bound state wave function,

$$\int d^2 r_{\perp} \int_{-\infty}^{\infty} dx |\Psi|^2 = \frac{1}{\zeta} (|a|^2 + |b|^2 + |c|^2 + |f|^2) = 1,$$

which yields

$$|c|^2 = \Delta \sin \gamma \left(1 + \frac{D}{R} \frac{\sin^2(\gamma + \varphi/2)}{\sin^2 \gamma} \right)^{-1}. \tag{3.18}$$

What is the origin of the bound states in a tunnel junction? According to Eq. (3.8), one can regard these states as resulting from hybridization of the bound states in the short ballistic constriction[24] due to the normal electron reflection by the barrier (cf. effect of impurities in the *SNS* junction[25,26]). Let us consider a smooth constriction with the length exceeding the coherence length, $L \gg \xi_0$. In such a constriction the supercurrent density and the superfluid momentum are related by the local equation, $J_s(x) = (e/m) N_s p_s(x)$, and they are both enhanced in the neck of the constriction due to current concentration (for simplicity we disregard the effect of suppression of the superfluid electron density N_s by the supercurrent). The local quasiparticle spectrum in the presence of supercurrent has an additional contribution $\pm v_F p_s(x)$,[20] which gives rise to a shift of the local energy gap (Fig. 3). The spatial bending of the gap edges forms the potential wells at $E<0 (E>0)$ for quasiparticles with electron velocities directed along (opposite) the current. The bound states in these potential wells are similar to the Andreev bound states in the *SNS* junctions.[49] The difference is that here the bound states are caused by the spatial inhomogeneity of the *phase* of the order parameter, while the original Andreev states are caused by the spatial inhomogeneity of the modulus of the order parameter. With decreasing length of the constriction, the number of the bound states in the well decreases. The short Josephson constriction corresponds to an infinitely narrow and deep δ-potential well which contains only one Andreev level.[24]

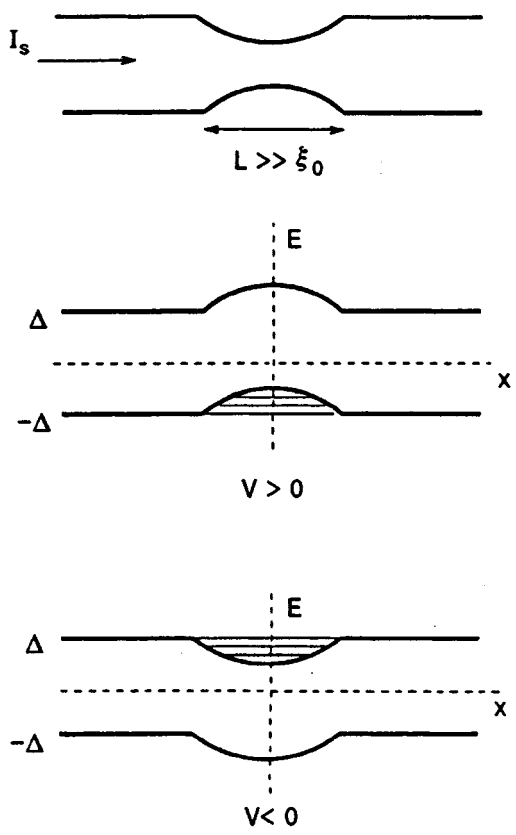

FIG. 3. Spatial configuration of the edges of the superconducting energy bands in a long constriction: $E_{\min}$, $E_{\max} = \pm\Delta + p_s(x)v$. A potential well appears in upper (lower) band for electrons moving in a direction opposite to (along) the supercurrent.

4. DIRECT JOSEPHSON CURRENT

A convenient expression for the tunnel current results from statistical averaging of the current operator written in the Nambu representation[50]:

$$I(x,t)=\frac{e}{2m}\left\{(\hat{p}-\hat{p}')\int d^2r_\perp \times[\delta(\mathbf{r}-\mathbf{r}')\mathbf{Tr}\langle\hat{\Psi}(\mathbf{r},t)\hat{\Psi}^+(\mathbf{r}',t)\rangle]\right\}_{\mathbf{r}=\mathbf{r}'}, \quad (4.1)$$

where $\hat{\Psi}$ is a two-component field operator

$$\hat{\Psi}(\mathbf{r},t)=\begin{pmatrix}\hat{\psi}_\uparrow(\mathbf{r},t)\\ \hat{\psi}_\downarrow^+(\mathbf{r},t)\end{pmatrix}, \quad (4.2)$$

and **Tr** is a trace in electron-hole space. The angular brackets in Eq. (4.1) denote a thermal average of the one-particle density matrix of the superconductor.[51] At equilibrium this matrix has the form

$$\langle\hat{\Psi}(\mathbf{r})\hat{\Psi}^+(\mathbf{r})\rangle=\sum_\lambda \Psi_\lambda(\mathbf{r})n_F(-E_\lambda)\Psi_\lambda^+(\mathbf{r}'), \quad (4.3)$$

where $\Psi_\lambda(\mathbf{r})$ are the eigenstates of the steady-state BdG equation [Eq. (2.5)] with the quantum numbers λ. We note that the definition of Fermi distribution function n_F here corresponds to the distribution of holes in the normal metal: in the ground state all energy levels above the Fermi level ($E>0$) are occupied, while energy levels below the Fermi level ($E<0$) are empty (see also the discussion in the next section). In the quasiclassical approximation [Eq. (2.6)] the average tunnel current calculated at the middle of the junction has the form

$$I=-e\sum_\lambda n_F(-E_\lambda)\sum_\beta \beta|\psi_\lambda^\beta(0)|^2. \quad (4.4)$$

The current in Eq. (4.4) can be calculated either at the left or the right side of the junction, because the equality

$$|\psi_L^+|^2-|\psi_L^-|^2=|\psi_R^+|^2-|\psi_R^-|^2, \quad (4.5)$$

due to the unitarity of the matching matrix $\hat{V}$ in Eq. (2.10), holds for each eigenstate. The current in Eq. (4.4) consists of contributions from the scattering states and the bound states:

$$I=-\int_{|E|>\Delta}\frac{dE|E|}{2\pi\xi}n_F(-E)\sum_j I_j(E)-\sum_{|E|<\Delta} n_F \times(-E)I_{\text{bound}}(E),\ I(E)$$
$$=e\sum_\beta \beta|\psi^\beta(E)|^2. \quad (4.6)$$

When calculating the contribution from the scattering states, it is convenient to consider the transmitted current of each scattering mode:

$$I_j(E)=\begin{cases}e(|b_j|^2-|f_j|^2) & j=1,3,\\ e(|c_j|^2-|a_j|^2) & j=2,4.\end{cases} \quad (4.7)$$

The symmetry relations [Eqs. (3.6) and (3.7)] yield

$$I_1(E)=I_4(E),\ I_2(E)=I_3(E),\ I_2(E)=-I_1(E). \quad (4.8)$$

The currents of all the scattering states with a given energy therefore cancel each other at equilibrium.[52] Substituting Eqs. (3.17) and (3.18) into Eq. (4.6), for, e.g., the right electrode, we obtain the following expression for the current of the bound state:

$$I_{\text{bound}}(E)=e(|b|^2-|f|^2)=-\frac{e\Delta^2}{2E}D\ \sin\ \varphi. \quad (4.9)$$

A useful formula for the current of the single bound state, which allows direct evaluation of the current from the bound state spectrum, is given by equation

$$I(E)=2e\frac{dE(\varphi)}{d\varphi}, \quad (4.10)$$

where $E(\varphi)$ is the bound state energy band [Eq. (3.14)]. This formula is derived in Appendix B. Taking into account Eqs. (4.9) and (4.6), we write the total current in the form[10–12,53]

$$I=\frac{e\Delta D\ \sin\ \varphi}{2\sqrt{1-D\ \sin^2(\varphi/2)}}\tanh\frac{\Delta\sqrt{1-D\ \sin^2(\varphi/2)}}{2T}. \quad (4.11)$$

Thus, the Josephson direct current in tunnel junctions is carried only by the bound states, which is similar to the situation found in the other kinds of short weak links.[24–26,28,30] It follows from Eqs. (4.6) and (4.9) that the nonvanishing total current results from the imbalance of the bound state currents due to a difference in the equilibrium population numbers. Creation of a nonequilibrium population makes it possible to control the Josephson transport.[28,31,48]

5. INELASTIC SCATTERING

Let us now discuss inelastic scattering in voltage-biased junctions. According to our assumption $\Phi=0$, which is explained in Sec. 2, the applied voltage drop V is confined to the constriction; in order not to complicate the problem, we have also disregarded a small time-dependent voltage induced across the junction by the ac Josephson current (self-coupling effect[54]). This implies the following dependence on time of the phase difference:

$$\varphi=\varphi_0+2eVt. \quad (5.1)$$

The appearance of factors with periodic time dependence in the boundary condition [Eqs. (2.8) and (2.9)] gives rise to a more complex structure of the scattering states than in Eq. (3.5). In order to satisfy the boundary condition, the outgoing part of the scattering states in Eq. (3.5) is to be constructed from the eigenstates of Eq. (2.7) with different energies $E_n=E-neV$ shifted with respect to the energy E of the incoming wave with an integer $-\infty<n<\infty$ (side band structure)

$$\begin{pmatrix}\psi_L^-\\ \psi_R^+\end{pmatrix}(0)=\begin{pmatrix}\delta_{j,1}\\ \delta_{j,2}\end{pmatrix}u_E^-e^{-iEt}+\sum_n\begin{pmatrix}a\\ b\end{pmatrix}_{j,n}u_{E_n}^+e^{-iE_nt}, \quad (5.2a)$$

$$\begin{pmatrix}\psi_L^+\\ \psi_R^-\end{pmatrix}(0)=\begin{pmatrix}\delta_{j,3}\\ \delta_{j,4}\end{pmatrix}u_E^+e^{-iEt}+\sum_n\begin{pmatrix}c\\ f\end{pmatrix}_{j,n}u_{E_n}^-e^{-iE_nt}. \quad (5.2b)$$

For brevity we use the notation $u_n=u_{E_n}$. While the incoming state is itinerant, the outgoing states can be either itinerant

[Eq. (3.1) if $|E_n| > \Delta$] or bound [Eq. (3.16) if $|E_n| < \Delta$]. It is convenient to combine the two equations for the functions u_n in a single analytical form:

$$u_n^{\pm} = \frac{1}{\sqrt{2\cosh \Gamma_n}} \begin{pmatrix} e^{\pm \gamma_n/2} \\ \sigma_n e^{\mp \gamma_n/2} \end{pmatrix}, \tag{5.3}$$

$$e^{\gamma_n} = \frac{|E_n| + \xi_n}{\Delta}, \ \Gamma_n = \mathrm{Re}\ \gamma_n,$$

$$\xi_n = \begin{cases} \sqrt{E_n^2 - \Delta^2}, & |E_n| > \Delta, \\ i\sigma_n \sqrt{\Delta^2 - E_n^2}, & |E_n| < \Delta. \end{cases} \tag{5.4}$$

To find the scattering amplitudes in Eq. (5.2) we consider the boundary condition Eq. (2.8). It is important to mention that this boundary condition was derived without regard for the energy dispersion of the normal electron scattering amplitudes d and r, which means that now this assumption should be valid for the entire interval of relevant energies E_n. Let us first discuss $j=1$ (hole-like quasi-particle coming from the left):

$$\begin{pmatrix} 1 \\ 0 \end{pmatrix} u_n^- \delta_{n,0} + \begin{pmatrix} a \\ b \end{pmatrix}_{1,n} u_n^+ = r \begin{pmatrix} c \\ f \end{pmatrix}_{1,n} u_n^- + \frac{d}{2} \begin{pmatrix} 1+\sigma_z & 0 \\ 0 & 1-\sigma_z \end{pmatrix} \begin{pmatrix} f \\ c \end{pmatrix}_{1,n-1} u_{n-1}^- + \frac{d}{2} \begin{pmatrix} 1-\sigma_z & 0 \\ 0 & 1+\sigma_z \end{pmatrix} \begin{pmatrix} f \\ c \end{pmatrix}_{1,n+1} u_{n+1}^-. \tag{5.5}$$

It is convenient to separate the equations for normal and Andreev scattering amplitudes in Eq. (5.5) using a procedure similar to Eq. (3.8). The equation for the normal scattering amplitudes then becomes

$$r c_{1,n} + (d/2)(V_{nn+1}^- f_{1,n+1} + V_{nn-1}^+ f_{1,n-1}) = \delta_{n0},$$

$$r f_{1,n} + (d/2)(V_{nn+1}^+ c_{1,n+1} + V_{nn-1}^- c_{1,n-1}) = 0, \tag{5.6}$$

where the coefficients

$$V_{nm}^{\pm} = \frac{(u_n^{-*}, \sigma_z \pm 1, u_m^-)}{(u_n^{-*}, \sigma_z u_n^-)} \tag{5.7}$$

have the explicit form

$$V_{nm}^+ = -\frac{\exp(-(\gamma_n + \gamma_m)/2)}{\sinh \gamma_n} \left(\frac{\cosh \Gamma_n}{\cosh \Gamma_m} \right)^{1/2}, \tag{5.8a}$$

$$V_{nm}^- = \sigma_n \sigma_m \frac{\exp((\gamma_n + \gamma_m)/2)}{\sinh \gamma_n} \left(\frac{\cosh \Gamma_n}{\cosh \Gamma_m} \right)^{1/2}. \tag{5.8b}$$

The equation for the Andreev scattering amplitudes is

$$a_{1,n} = (d/2)(U_{nn+1}^- f_{1,n+1} + U_{nn-1}^+ f_{1,n-1}^+),$$

$$b_{1,n} = (d/2)(U_{nn+1}^+ c_{1,n+1} + U_{nn-1}^- c_{1,n-1}), \tag{5.9}$$

where the coefficients are defined as

$$U_{nm}^{\pm} = \frac{(u_n^{+*}, \sigma_z \pm 1, u_m^-)}{(u_n^{+*}, \sigma_z u_n^+)}, \tag{5.10}$$

and have the explicit forms

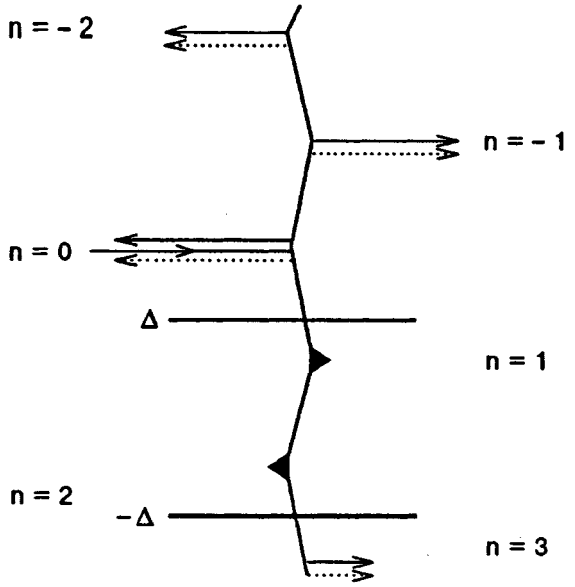

FIG. 4. Scattering diagram of voltage-biased superconducting tunnel junctions. Solid (dotted) arrows indicate scattering in the normal (Andreev) channel. Filled triangles indicate superconducting bound states. Transmission (reflection) occurs into side bands with odd (even) indices.

$$U_{nm}^+ = \frac{\exp((\gamma_n - \gamma_m)/2)}{\sinh \gamma_n} \left(\frac{\cosh \Gamma_n}{\cosh \Gamma_m} \right)^{1/2}, \tag{5.11a}$$

$$U_{nm}^- = -\sigma_n \sigma_m \frac{\exp(-(\gamma_n - \gamma_m)/2)}{\sinh \gamma_n} \left(\frac{\cosh \Gamma_n}{\cosh \Gamma_m} \right)^{1/2}. \tag{5.11b}$$

As can be seen from Eqs. (5.6) and (5.9), the inelastic scattering possesses a specific asymmetry: the forward scattered waves have odd side band indices and backward scattered waves have even side band indices, as illustrated in Fig. 4. Correspondingly, bound states with odd or even side band indices are induced either in the right or in the left electrode. We note that the scattering to any side band consists of normal and Andreev components.

It is instructive to compare the superconducting scattering diagram in Fig. 4 with the scattering diagram of normal junctions. In the normal limit $\Delta = 0$, all the Andreev amplitudes in Eq. (5.9) vanish [$U_n^{\pm} = 0$ in Eq. (5.11)] and Eq. (5.6) split because $V^+ = 0$ in Eq. (5.8), which yields $f_n = c_{n-1} = 0$ for all $n \neq 1$. Thus, the side band diagram in Fig. 4 reduces to the elementary fragment shown in Fig. 5a. This fragment corresponds to the scattering of a *true hole*, meaning a particle with spectrum $E_h = -(p^2/2m - \mu)$, according to the BdG equations (2.2) and (2.5). In the ground state, $T = 0$, these holes fill all positive energy states $E > 0$, while the negative energy states are empty. For the electrons, the corresponding diagram is sketched in Fig. 5b. In this diagram the chemical potentials in both electrodes are equal, while the energies of the incident and transmitted states are shifted by eV. This difference from the conventional diagram of normal electron tunneling in Fig. 5c (where the chemical potentials in the electrodes are shifted relative to each other, while the scattering is elastic) appears after separating out the superconducting phase in Eq. (2.4); the con-

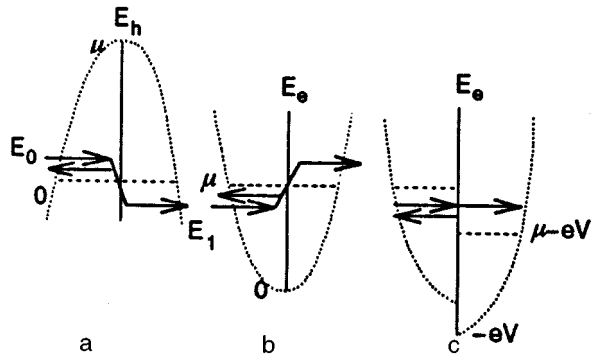

FIG. 5. Scattering diagrams of voltage-biased normal tunnel junctions: scattering of normal holes with spectrum $E_h = \mu - (p^2/2m)$; represents an elementary fragment of the diagram in Fig. 4 for $j = 1$ (a); scattering of the normal electrons with spectrum $E_e = p^2/2m$ (c); conventional diagram of elastic electron scattering in biased tunnel junctions; the local chemical potentials in the electrodes are then shifted by eV (c).

ventional picture with shifted chemical potential can be restored by means of the gauge transformation of the normal electron wave function $\psi \to \exp(-ieVt)\psi$.

When superconductivity is switched on, $\Delta \neq 0$, the incoming quasi-particle consists of both electron and hole components, and therefore the scattering diagram is a combination of the diagrams in Figs. 5,a and 5,b. The electron-hole conversion, which leads to the appearance of electron and hole components in the upper and lower transmitted states, must also be taken into account. Continuation of this process creates the whole superconducting scattering diagram in Fig. 4.

From a mathematical point of view, Eqs. (5.6) and (5.9) for the scattering amplitudes are second-order difference equations which cannot be solved exactly, except in special cases, e.g., a fully transparent constriction ($r=0$), where Eq. (5.6) reduces to a binary relation.[34] In general, it is possible to find asymptotic solutions using a small parameter. In the present case of a tunnel junction, there is a natural small parameter—the transparency of the tunnel barrier: $D \ll 1$. However, a straightforward perturbation expansion with respect to this parameter gives rise to divergences, which are similar to the difficulties encountered in of the multiparticle tunneling theory (MPT).[42,57,58] In order to formulate an improved perturbation procedure, it is convenient to rewrite Eqs. (5.6) and (5.9) in terms of the parameter $\lambda = D/4R$, the true small parameter of the theory, as will be seen later. Accordingly, we introduce new scattering amplitudes

$$c_{1,\pm 2k} = \frac{\lambda^k}{r}\, c_{\pm 2k}, \quad f_{1,\pm(2k+1)} = \frac{\lambda^k d^*}{2R}\, f_{\pm(2k+1)},$$

$$a_{1,\pm 2k} = \lambda^k a_{\pm 2k}, \quad b_{1,\pm(2k+1)} = \frac{\lambda^k d}{2r}\, b_{\pm(2k+1)}, \qquad (5.12)$$

which satisfy equations

$$\begin{aligned} &c_n + \lambda V^{-1}_{nn+1} f_{n+1} + V^{+}_{nn-1} f_{n-1} = 0, \\ &f_n - \lambda V^{+}_{nn+1} c_{n+1} - V^{-}_{nn-1} c_{n-1} = 0, \qquad (5.13a) \\ &a_n = \lambda U^{-}_{nn+1} f_{n+1} + U^{+}_{nn-1} f_{n-1}, \end{aligned}$$

$$b_n = \lambda U^{+}_{nn+1} c_{n+1} + U^{-}_{nn-1} c_{n-1} \qquad (5.13b)$$

for $n>0$. For $n<0$ it is necessary to make the change $V^{\pm}_{nm} \to V^{\mp}_{-n-m}$, $U^{\pm}_{nm} \to U^{\mp}_{-n-m}$, $(n, m>0)$ in the above equations. The equation for $n = 0$ can then be written as

$$c_0 + \lambda(V^{-}_{01} f_1 + V^{+}_{0-1} f_{-1}) = 1. \qquad (5.13c)$$

Let us now turn to the second scattering case in Eq. (5.2), $j=2$ (hole-like quasi-particle incoming from the right). According to the symmetry relations of Eq. (3.6), the scattering amplitudes $j=2$ differ from the scattering amplitudes $j=1$ by $\varphi \to -\varphi$, which in our time-dependent case means that $n \pm 1 \to n \mp 1$. Taking into account this symmetry and also the property of the scattering amplitudes in Eq. (3.6), we introduce new scattering amplitudes

$$f_{2,\pm 2k} = \frac{\lambda^k}{r}\, \overline{c}_{\pm 2k},$$

$$c_{2,\pm(2k+1)} = \frac{\lambda^k d^*}{2R}\, \overline{f}_{\pm(2k+1)}, \quad b_{2,\pm 2k} = \lambda^k \overline{a}_{\pm 2k}, \qquad (5.14)$$

which satisfy the following equations (for $n > 0$):

$$\begin{aligned} &\overline{c_n} + \lambda V^{+}_{nn+1} \overline{f}_{n+1} + V^{-}_{nn-1} \overline{f}_{n-1} = 0, \\ &\overline{f_n} - \lambda V^{-}_{nn+1} \overline{c}_{n+1} - V^{+}_{nn-1} \overline{c}_{n-1} = 0, \qquad (5.15a) \\ &\overline{a_n} = \lambda U^{+}_{nn+1} \overline{f}_{n+1} + U^{-}_{nn-1} \overline{f}_{n-1}, \end{aligned}$$

$$\overline{b_n} = \lambda U^{-}_{nn+1} \overline{c}_{n+1} + U^{+}_{nn-1} \overline{c}_{n-1}, \qquad (5.15b)$$

$$\overline{c_0} + \lambda(V^{+}_{01} \overline{f_1} + V^{-}_{0-1} \overline{f}_{-1}) = 1. \qquad (5.15c)$$

Equations (5.15) differ from Eqs. (5.13) by

$$V^{\pm} \to V^{\mp}, U^{\pm} \to U^{\mp}. \qquad (5.16)$$

In the case of electron-like quasi-particles incoming from the left, $j=3$, the symmetry of Eq. (3.7) involves transformation $\gamma \to -\gamma$, which means transformation of the coefficients $V^{\pm} \to -\sigma_n \sigma_m V^{\mp}$, $U^{\pm} \to -\sigma_n \sigma_m U^{\mp}$ in Eqs. (5.6) and (5.9). This transformation allows us to relate the scattering amplitudes of this case to the solutions of Eqs. (5.5):

$$a_{3,\pm 2k} = \frac{\lambda^k}{r^*}\, \sigma_{\pm 2k} \overline{c}_{\pm 2k},$$

$$b_{3,\pm(2k+1)} = -\frac{\lambda^k d}{2R}\, \sigma_{\pm(2k+1)} \overline{f}_{\pm(2k+1)},$$

$$c_{3,\pm 2k} = \lambda^k \sigma_{\pm 2k} \overline{a}_{\pm 2k}, \qquad (5.17)$$

$$f_{3,\pm(2k+1)} = -\frac{\lambda^k d^*}{2r^*}\, \sigma_{\pm(2k+1)} \overline{b}_{\pm(2k+1)}.$$

In a similar way the scattering amplitudes of electron-like quasi-particles incoming from the right, $j=4$, are related to the solutions of Eqs. (5.13):

$$b_{4,\pm 2k} = \frac{\lambda^k}{r^*}\, \sigma_{\pm 2k} c_{\pm 2k},$$

$$a_{4,\pm(2k+1)} = -\frac{\lambda^k d}{2R}\, \sigma_{\pm(2k+1)} f_{\pm(2k+1)},$$

$$f_{4,\pm 2k}=\lambda_k \sigma_{\pm 2k} a_{\pm 2k},$$

$$c_{4,\pm(2k+1)}=-\frac{\lambda^k d^*}{2r^*}\,\sigma_{\pm(2k+1)} b_{\pm(2k+1)}. \tag{5.18}$$

According to the symmetry of the coefficients in Eqs. (5.13) and (5.15),

$$V^{\pm}_{nm}(-E)=V^{\pm *}_{-n-m}(E), \quad U^{\pm}_{nm}(-E)=U^{\pm *}_{-n-m}(E), \tag{5.19}$$

all scattering amplitudes with positive and negative incoming energies are related by the relation

$$a_n(-E)=\overline{a}_{-n}{}^*(E), \tag{5.20}$$

and similarly for the other amplitudes.

Let us now formally solve Eq. (5.13) for $n>0$ in the form[55]

$$f_{2k+1}=(-1)^k \prod_{i=0}^{2k+1} S_l c_0, \tag{5.21}$$

where the quantities S_l are defined as

$$S_{2k}=-\frac{c_{2k}}{f_{2k-1}}, \quad S_{2k+1}=\frac{f_{2k+1}}{c_{2k}}, \tag{5.22}$$

and satisfy the recurrence relations

$$S_{2k}=\frac{V^{+}_{2k,2k-1}}{1+\lambda V^{-}_{2k,2k+1} S_{2k+1}},$$

$$S_{2k+1}=\frac{V^{-}_{2k+1,2k}}{1+\lambda V^{+}_{2k+1,2k+2} S_{2k+2}}. \tag{5.23}$$

The quantity c_0 in Eq. (5.27) is given by

$$c_0=\frac{1}{1+\lambda(V^{-}_{01}S_1+V^{+}_{0-1}S_{-1})}. \tag{5.24}$$

It is convenient to express the functions S_n in Eq. (5.23) in terms of the relation $S_n=V^{\pm}_{n,n+1}/Z_n$, where the denominators $Z_n(n\neq 0)$ satisfy the recurrence relation

$$Z_n=1+\lambda\,\frac{a^{\pm}_n a^{\pm}_{n+1}}{Z_{n+1}}, \quad a^{\pm}_n=\frac{e^{\pm\gamma} n}{\sinh\,\gamma_n}, \tag{5.25}$$

($\pm$ corresponds to even/odd n), and to define Z_0 as the denominator of c_0, Eq. (5.24):

$$Z_0=1+\lambda\,\frac{a^{+}_0 a^{+}_1}{Z_1}+\lambda\,\frac{a^{-}_0 a^{-}_{-1}}{Z_{-1}}. \tag{5.26}$$

Using the above notation, we can express the coefficients of the normal forward scattering, $|f_n|^2$, in the form

$$|f_n|^2=\frac{e^{\gamma_0}}{\cosh\,\gamma_0|Z_0|^2}\,e^{\Gamma_n}\cosh\,\Gamma_n \prod_{l=1}^{n}\,\frac{1}{|Z_l\sinh\,\gamma_l|^2}. \tag{5.27}$$

The equation for the coefficients of the normal backward scattering, $|c_n|^2$, differs from Eq. (5.27) by $\exp(\Gamma_n)\rightarrow\exp(-\Gamma_n)$. The relation between the amplitudes of the Andreev and normal forward scattering in Eq. (5.13) taking into account Eqs. (5.22), (5.23), and (5.25), has the form

$$b_n=-e^{-\gamma_n}\left(1-\lambda\,\frac{2e^{-\gamma_{n+1}}}{\sinh\,\gamma_{n+1}Z_{n+1}}\right)f_n. \tag{5.28}$$

In a similar way, one can express the solution of Eq. (5.15) for $n>0$ in the form

$$|\overline{f_n}|^2=\frac{e^{-\gamma_0}}{\cosh\,\gamma_0|\overline{Z_0}|^2}\,e^{-\Gamma_n}\cosh\,\Gamma_n \prod_{l=1}^{n}\,\frac{1}{|\overline{Z_l}\sinh\,\gamma_l|^2},$$

$$\overline{b_n}=-e^{\gamma_n}\left(1+\lambda\,\frac{2e^{\gamma_{n+1}}}{\sinh\,\gamma_{n+1}\overline{Z_{n+1}}}\right)\overline{f_n}, \tag{5.29}$$

where

$$\overline{Z_n}=1+\lambda\,\frac{a^{\mp}_n a^{\mp}_{n+1}}{\overline{Z_{n+1}}},$$

$$\overline{Z_0}=1+\lambda\,\frac{a^{-}_0 a^{-}_1}{\overline{Z_1}}+\lambda\,\frac{a^{+}_0 a^{+}_{-1}}{\overline{Z_{-1}}}. \tag{5.30}$$

We note that Eqs. (5.29) and (5.30) differ from Eqs. (5.27) and (5.28) by $\gamma_n\rightarrow-\gamma_n$ everywhere.

Equations for the scattering amplitudes with negative side band indices, $n<0$, can be derived in a similar way, and the result differs from the above equations for positive side band indices [Eqs. (5.25)–(5.30)] by the substitution

$$\gamma_n\rightarrow-\gamma_{-|n|}, \quad n\neq 0, \tag{5.31}$$

which is introduced everywhere except in Z_0 and $\overline{Z_0}$.

6. QUASIPARTICLE CURRENT

In the nonstationary problem under consideration, the density matrix determining the current [Eq. (4.1)] is time dependent, and its dynamic evolution can be described by an equation similar to Eq. (4.3),

$$\langle\hat{\Psi}(\mathbf{r},t)\hat{\Psi}^{+}(\mathbf{r},t)\rangle=\sum_{\lambda}\,\Psi_\lambda(\mathbf{r},t) f_\lambda \Psi^{+}_\lambda(\mathbf{r},t), \tag{6.1}$$

Ψ_λ are now solutions of the time-dependent problem, Eq. (2.5), whose initial conditions correspond to the eigenstates of the initial Hamiltonian with the eigenvalues λ, and occupation numbers f_λ of these initial states. We consider the inelastic scattering states, [Eqs. (2.6) and (5.2)] as the propagators $\Psi_\lambda(t)$ in Eq. (6.1) with λ corresponding to the complete set of the incoming states $\lambda=(E,j)$; according to the assumption about local equilibrium within the electrodes, the incoming states possess the Fermi distribution of occupation numbers, $f_{Ej}=n_F(-E)$. Thus the current [Eq. (4.1)] takes the form

$$I(t)=-e\int_{|E|>\Delta}\frac{dE|E|}{2\pi\xi}\,n_F(-E)\sum_{N=-\infty}^{\infty} e^{iNeVt} \times\sum_{n=-\infty}^{\infty}\sum_{j\beta}\,\beta(\psi^{\beta}_j(E,n),\psi^{\beta}_j(E,N+n)). \tag{6.2}$$

The current in Eq. (6.2) consists of a time-independent part, $N=0$, which is formed by incoherent contributions from all the side bands (the quasiparticle current) and from a time-dependent part, $N\neq 0$, which results from interference among

the different side bands (Josephson alternating current). The difference between the side band indices N is an even number since the side band index is either even or odd, depending on the electrode; therefore, the time-dependent current oscillates with the Josephson frequency $\omega = 2eV$.

In this paper we concentrate on an analysis of the time-dependent quasiparticle current. By analogy with Eq. (4.7), we calculate the current using the transmitted states,

$$I = \frac{1}{2}\frac{e}{\pi}\int_{|E|>\Delta} dE\,\frac{|E|}{\xi}\,n_F(-E)\sum_{n=-\infty}^{\infty} \times\left[\sum_{j=1,3}(|f_{jn}|^2-|b_{jn}|^2)+\sum_{j=2,4}(|a_{jn}|^2-|c_{jn}|^2)\right]. \tag{6.3}$$

Using the scattering amplitudes introduced in the previous section through Eqs. (5.12), (5.14), (5.17), and (5.18), we express the current in Eq. (6.3) in the form

$$I = \frac{e}{\pi}\int_{|E|>\Delta} dE\,\frac{|E|}{\xi}\,n_F(-E)\sum_{\text{odd}}(K_n - \overline{K_n}), \tag{6.4}$$

where

$$K_n = \lambda^{|n|}(R^{-1}|f_n|^2-|b_n|^2),$$
$$\overline{K_n} = \lambda^{|n|}(R^{-1}|\overline{f_n}|^2-|\overline{b_n}|^2) = K_n(-\gamma). \tag{6.5}$$

The factor of 2 appears in Eq. (6.4) because of equality of the currents I_1 and I_4 and the currents I_2 and I_3 in Eq. (4.8), which hold also in the nonstationary case. However, there is no balance between the currents of these two pairs any more. The symmetry of Eq. (5.20) allows us to reduce the interval of integration in Eq. (6.4) to the semiaxis $E > 0$,

$$I = \frac{e}{\pi}\int_{\Delta}^{\infty} dE\,\frac{E}{\xi}\tanh\frac{E}{2T}\sum_{\text{odd}}(K_n - \overline{K_n}). \tag{6.6}$$

The side band currents K_n in Eq. (6.5) are proportional to the powers of the small parameter λ, $K_n \sim \lambda^{|n|}$. Therefore, Eqs. (6.6) and (6.5) present a perturbative expansion of the current, which is convenient for analysis in the limit of low barrier transparency. In the following sections we carry out such an analysis of the structure of the current in Eq. (6.6).

7. EXCESS CURRENT AT LARGE BIAS

To make some useful observations for analysis of the subgap current, it is instructive first to discuss the simpler case of large bias $eV \gg \Delta$, which has been studied extensively in literature.[11,12,17,23] We derive at the same time the explicit analytical expression for the current in this limit, which is valid in the whole range of the junction transparency, $0 < D < 1$. The asymptotic expansion of the current with respect to the small parameter Δ/eV has the form[17]

$$I = \frac{e^2 DV}{\pi} + I_{\text{exc}}(D) + O\left(\frac{\Delta}{eV}\right), \tag{7.1}$$

where the first term is the tunnel current of the normal junction and the second term is a voltage-independent excess current which represents the leading superconducting correction.

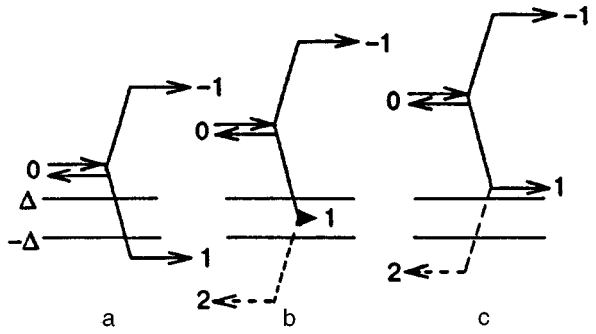

FIG. 6. Three kinds of processes that contribute to the tunnel current at large bias $eV \gg \Delta$: creation of a real excitation across the gap by forward scattering (a); excitation of the Andreev bound state due to creation of a real excitation via backward scattering (dashed arrow) (b); imbalance of ground state modes due to creation of a real excitation via backward scattering (c). Excess current is caused by processes b) and c).

A main simplification in this case is that the side band currents K_n and $\overline{K_n}$, $|n| > 1$ diminish when the bias voltage increases. This follows from an estimate of the transmission amplitudes in Eqs. (5.27)–(5.29), which contain products of factors $|\sinh\gamma_k|^{-2}$ which are small at large voltages, $|\sinh\gamma_k|^{-2} \sim (\Delta/eV)^2$, because of the large interval of involved energies, $E \sim eV$. Furthermore, inspection of the amplitudes f_{-1} and f_1 shows that they are also small due to the factors $\exp(-\gamma_0 - \gamma_1)$; therefore, the nonvanishing part of the current [Eq. (6.6)] in the limit $eV \gg \Delta$ becomes

$$I = \frac{e}{\pi}\int_{\Delta}^{\infty} dE\,\frac{E}{\xi}\tanh\frac{E}{2T}(K_1 - \overline{K_{-1}}). \tag{7.2}$$

The essential fragments of the scattering diagram in the large bias limit are shown in Fig. 6.

The structure of the current in Eq. (7.2) is essentially determined by the presence of a gap in the spectrum of the side band $n=1$; this causes different analytical forms of the current K_1 in the regions $|E| < \Delta$ and $|E| > \Delta$. We note that the spectrum of the side band $n=-1$ possesses no gap: $E_{-1} > \Delta$ for $E > \Delta$. Accordingly, we divide the integral in Eq. (7.2) into three parts:

$$I = I_< + I_\Delta + I_> .$$

The first part corresponds to the current of the states in the side band $n = 1$, which lie below the gap, $E_1 < -\Delta$. The second part corresponds to the current of the states of the same side band which lie in the gap, $-\Delta < E_1 < \Delta$. The third part combines contributions from the remaining states of the side band $n = 1$, $\Delta < E_1$, and from all the states of the side band $n = -1$. Making use of the approximations

$$|Z_0|^2 = |\overline{Z_0}|^2 \approx |1 + 2\lambda(E+\xi)/\xi|^2,$$
$$|Z_{-1}|^2 = |\overline{Z_1}|^2 = |Z_2|^2 = |\overline{Z_{-2}}|^2 \approx 1, \tag{7.3}$$
$$|Z_1|^2 = |\overline{Z_{-1}}|^2 = |Z_{-2}|^2 = |\overline{Z_2}|^2 \approx 1/R^2,$$

it is possible to express the integral $I_<$ in the form (we restrict the analysis to the limit $T=0$):

$$I_<=\frac{e}{\pi}\int_\Delta^{eV-\Delta} dE\,\frac{E}{\xi}\,K_1=\frac{8e\lambda}{\pi R}\int_\Delta^{eV/2} dE\,\frac{E}{\xi Z_0^2}$$
$$-\frac{2e\lambda}{\pi R}\int_\Delta^{\infty} dE\,\frac{(E-\xi)}{\xi Z_0^2}\left(1-4\lambda R\,\frac{E}{\xi}\right), \qquad (7.4)$$

where the limit of integration in the last term is extended to infinity since the main contribution to this integral comes from the energies $E \sim \Delta \ll eV$. Separating out the normal junction current, we can express Eq. (7.4) in the form

$$I_<=\frac{e^2DV}{\pi}-\frac{8e\lambda^2}{\pi}\int_\Delta^{\infty}\frac{dE}{Z_0^2\xi}\left[4\lambda R\,\frac{E\Delta^2}{\xi^2}\right.$$
$$\left.+(2R+1)\,\frac{E(E-\xi)}{\xi}+\frac{E-\xi}{4\lambda R}\right]. \qquad (7.5)$$

We note that this current is always smaller than the normal current. It is convenient to express the integral I_Δ as

$$I_\Delta=\frac{e}{\pi}\int_{eV-\Delta}^{eV+\Delta} dE\,\frac{E}{\xi}\,K_1=\frac{16e\lambda^2}{\pi}\int_0^{\Delta} dE\,\frac{\Delta^2}{|\xi Z_0|^2}, \qquad (7.6)$$

which is found from the relations between the functions Z_n [which result from their definition in Eq. (5.25)]

$$Z_n(E+eV)=\overline{Z_{n-1}}(E),$$
$$Z_0(E+eV)Z_1(E+eV)=\overline{Z_0}(E)\overline{Z_{-1}}(E). \qquad (7.7)$$

Inspection of the equation for $I_>$,

$$I_>=\frac{e}{\pi}\int_{eV+\Delta}^{\infty} dE\,\frac{E}{\xi}\,K_1-\frac{e}{\pi}\int_\Delta^{\infty} dE\,\frac{E}{\xi}\,\overline{K_{-1}}, \qquad (7.8)$$

shows that the two integrals diverge at the upper limit $E=\infty$, which means that the states lying far from the Fermi level formally contribute to the current, while the quasiclassical approximation of Eq. (2.6) assumes that all relevant states lie close to the Fermi level. To eliminate this formal divergence, the variable is commonly shifted by eV in the first integral in Eq. (7.8). Using again the relations (7.7) we express this integral in the form

$$\frac{4e\lambda}{\pi R}\int_\Delta^{\infty} dE\,\frac{E}{\xi Z_0 Z_{-1}}+\frac{8e\lambda^2}{\pi}\int_\Delta^{\infty} dE\,\frac{E(E-\xi)}{\xi^2 Z_0^2},$$

where the first term has the same analytical form but the opposite sign compared to the divergent term in the second integral in Eq. (7.8),

$$-\frac{4e\lambda}{\pi R}\int_\Delta^{\infty} dE\,\frac{E}{\xi Z_0 Z_{-1}}+\frac{2e\lambda}{\pi R}\int_\Delta^{\infty} dE\,\frac{(E-\xi)}{\xi Z_0^2}.$$

After elimination of the divergent terms, the integral in Eq. (7.8) takes the form

$$I_>=\frac{2e\lambda}{\pi R}\int_\Delta^{\infty} dE\,\frac{(E-\xi)}{\xi Z_0^2}\left(1+4\lambda R\,\frac{E}{\xi}\right). \qquad (7.9)$$

The positive currents in Eq. (7.9) and Eq. (7.6) overcompensate the missing part of the current in Eq. (7.5). Collecting Eqs. (7.5), (7.6), and (7.9), we find after some algebra the following explicit equation for the excess current in Eq. (7.1):

$$I_{\rm exc}=\frac{16e\Delta\lambda^2 R}{\pi}\left[1-\frac{D^2}{2(1+R)\sqrt{R}}\ln\frac{1+\sqrt{R}}{1-\sqrt{R}}\right], \qquad (7.10)$$

which is valid in the whole interval of junction transparency $0<D\leqslant 1$. Asymptotics of this expression coincide with the results presented in literature,[11,23] both in the limit of fully transparent ($D=1$) constrictions, $I_{\rm exc}=8e\Delta/3\pi$, and in the limit of low-transparency ($D\ll 1$) tunnel junctions, $I_{\rm exc}=e\Delta D^2/\pi$.

The above calculation reveals an important difference between the structure of the current in normal and superconducting junctions. In normal junctions, the current, e.g., in the right electrode (see Fig. 5c) results from scattering states that lie above the local chemical potential, $E>\mu-eV$, while contribution from the energy interval $E<\mu-eV$ is equal to zero due to mutual cancellation of currents of the scattering states incident from the left and from the right (in Fig. 5a the current-carrying energy region corresponds to negative energies, $E_h<0$). Thus, the total current coincides with the current of real excitations emitted from the contact, which is consistent with the nonequilibrium origin of the current in the voltage-biased junctions. In superconducting junctions, only ''across-the-gap'' current $I_<$ is clearly related to the real excitations emitted at the right side of the junction where the current is calculated (Fig. 6a): the dissipative character of the currents, I_Δ and $I_>$, is not obvious. However, the creation of real excitations at the left side of the junction via backscattering into the side band $n=2$ should be taken into account (Figs. 6b and 6c). Although the current of this side band exists only at the left side of the scattering diagram, it should have an effect at the right side due to continuity of the current at the interface [Eq. (4.5)] and therefore it should be distributed among the states of the side band $n=1$. As our calculations show, this ''kick'' current partially flows through the Andreev bound states, which involve the current I_Δ (Fig. 6b) and which convert this current into a supercurrent outside the junction. It is also partially distributed among the scattering states with positive energies (current $I_>$, Fig. 6c) in the form of imbalanced ground state currents.

8. SUBGAP CURRENT

In this section we discuss the tunnel current in the subgap region, $eV<2\Delta$. A basic property of the subgap current is the presence of temperature-independent structures on the I-V characteristics—the subharmonic gap structure (SGS). The SGS in tunnel junctions was discovered in experiments by Taylor and Burstein[56] and the first theoretical explanation was given by Schrieffer and Wilkins[42] in terms of multiparticle tunneling (MPT). Recently, the SGS has been observed in many experiments on transmissive tunnel junctions.[3–5] Although SGS in planar junctions can be attributed to normal shorts, the observation of SGS in superconducting controllable break junctions[8] provided convincing confirmation of the existence of SGS in the true tunnel regime.

The existence of SGS in tunnel current can be established within the MPT theory by means of rather simple perturbative arguments.[42,57–59] Assuming a small perturbative coupling between electrodes, we can calculate, on the

basis of the tunnel Hamiltonian model, the probability of tunneling in nth order of perturbation theory. Such a probability is proportional to a product of filling factors of the initial and the final states: $n_F(E)[1 - n_F(E - neV)]$. At zero temperature this factor is equal to zero outside the interval $\Delta < E < neV - \Delta$, which selects the quasiparticle transitions across the gap, i.e., the processes of creation of real excitations relevant for the tunnel current. Such a restriction places the threshold of the nth order current at $eV = 2\Delta/n$, and a sequence of current onsets of $\sim D^n$ at the voltages $eV = 2\Delta/n$ forms the SGS of the tunnel current.[58,59]

In our approach, the filling factors of final states do not enter the equation for the current Eq. (6.6), and the existence of SGS is therefore not obvious, although the side band currents [Eq. (6.5)] gradually decrease with increasing side band index. However, attribution of the nonequilibrium tunnel current in biased junctions to the current of real excitations is a general physical argument which should be automatically met in any correct theory. In fact, the true tunnel current, as we can see from the discussion of the previous section, is hidden in Eq. (6.6): it results from partial cancellation of large contribution of different scattering modes. The cancellation is nontrivial because of mixture of currents of different side bands, the odd side bands containing information about the currents of the even side bands and vice versa. This means that a finite perturbation expansion of Eq. (6.6) is not satisfactory and will not adequately correspond to the perturbative structure of the true tunnel current. To reveal such a structure one must rearrange the series in Eq. (6.6).

To this end, we consider a general term K_n, $n > 0$ in Eq. (6.6). It follows immediately from the explicit form of the normal and Andreev transmission coefficients [Eqs. (5.27) and (5.28)] that the leading term with respect to λ in K_n is proportional to a factor $[(1 - \exp(2\Gamma_n)]$, which is equal to zero if $|E_n| < \Delta$. Having made this observation, we express the quantity K_n in the form

$$K_n = \frac{2}{R}\,\lambda^n \theta(E_n^2 - \Delta^2) e^{-\gamma_n} \sinh\,\gamma_n |f_n|^2 + 4\lambda^{n+1} e^{-2\Gamma_n} \left|\frac{f_n}{Z_{n+1}}\right|^2 F_{n+1}, \tag{8.1a}$$

$$F_{n+1} = |Z_{n+1}|^2 + \mathrm{Re}\left(\frac{e^{-\gamma_{n+1}} Z_{n+1}^*}{\sinh\,\gamma_{n+1}}\right) - \lambda \left|\frac{e^{-\gamma_{n+1}}}{\sinh\,\gamma_{n+1}}\right|^2. \tag{8.1b}$$

In Eq. (8.1a) the first term represents the main contribution of the nth side band to the current: it is proportional to the probability of normal scattering to the nth side band and it does not contain the contribution of the side band states lying inside the gap $|E_n| < \Delta$. Using the recurrence relation (5.25) and recalling that $\lambda = D/4R$, after some algebra the function F_n in Eq. (8.1b) becomes

$$F_n = \frac{1}{R}\,\theta(E_n^2 - \Delta^2)\,\frac{1}{\tanh\,\gamma_n} - \lambda \left|\frac{e^{\gamma_n}}{\sinh\,\gamma_n Z_{n+1}}\right|^2 G_{n+1}, \tag{8.2a}$$

$$G_{n+1} = |Z_{n+1}|^2 - \mathrm{Re}\left(\frac{e^{\gamma_{n+1}} Z_{n+1}^*}{\sinh\,\gamma_{n+1}}\right) - \lambda \left|\frac{e^{\gamma_{n+1}}}{\sinh\,\gamma_{n+1}}\right|^2. \tag{8.2b}$$

Substituting Eq. (8.2) into Eq. (8.1a), we find that the second term in the equation for K_n, which is proportional to λ^{n+1}, has analytical structure similar to the first term in the same equation, proportional to λ^n, namely, it consists of the probability of normal scattering to the $(n + 1)$th side band [cf. Eq. (5.22)] and it does not include the contribution of the side band states that lie inside the gap, $|E_{n+1}| < \Delta$. This allows us to associate this term with the effective contribution of the nearest *even* side band.

A similar transformation of the function G_{n+1} in Eq. (8.2) yields the recurrence relation

$$G_{n+1} = -\frac{1}{R}\,\theta(E_{n+1}^2 - \Delta^2)\,\frac{1}{\tanh\,\gamma_{n+1}} - \lambda \left|\frac{\exp(-\gamma_{n+1})}{\sinh\,\gamma_{n+1} Z_{n+2}}\right|^2 F_{n+2}. \tag{8.3}$$

Combining of Eqs. (8.1a)–(8.3) shows that the next term of the current K_n, which is proportional to λ^{n+2}, has the same analytical structure as the leading term in the current K_{n+2} of the next odd side band, and therefore it can be regarded as a renormalization of that current.

Continuing this procedure by systematic use of the recurrence relations (8.2) and (8.3), we obtain the following expansion for the current K_n in Eq. (6.5):

$$\begin{aligned} K_n = {} & \frac{2\lambda^n}{R}\,\theta(E_n^2 - \Delta^2) Q_n + \frac{4\lambda^{n+1}}{R}\,\theta(E_{n+1}^2 - \Delta^2) \\ & \times e^{-\Gamma_n} \cosh\,\Gamma_n Q_{n+1} + \frac{4\lambda^{n+2}}{R}\,\theta(E_{n+2}^2 - \Delta^2) \\ & \times \exp(-\Gamma_n + 2\Gamma_{n+1}) \cosh\,\Gamma_n Q_{n+2} + \frac{4\lambda^{n+3}}{R} \\ & \times \theta(E_{n+3}^2 - \Delta^2) \exp(-\Gamma_n + 2\Gamma_{n+1} - 2\Gamma_{n+2}) \cosh \\ & \times\, \Gamma_n Q_{n+3} + \ldots, \end{aligned} \tag{8.4}$$

where we have introduced the quantity Q_n defined for all n as

$$Q_n = \frac{e^{\gamma_0}}{\cosh\,\gamma_0 |Z_0|^2}\,\sinh\,\gamma_n \cosh\,\Gamma_n \prod_{l=1}^{n} \frac{1}{|Z_l \sinh\,\gamma_l|^2}. \tag{8.5}$$

Similar expansions can be derived for the currents $\overline{K_n}$ and for the currents of the side bands with negative $n < 0$. Expanding each term of the series in Eq. (6.6) with use of Eq. (8.4) and collecting the terms with the same factor λ^n, we can finally express the series in the form

$$\sum_{\mathrm{odd}} (K_n - \overline{K_n}) = \sum_{n \neq 0} (\tilde{K}_n - \tilde{\bar{K}}_n). \tag{8.6}$$

The last summation is done over all odd *and even* integer n, and the renormalized coefficients have the form

$$\tilde{K}_n=\lambda^n\theta(E_n^2-\Delta^2)(4Q_n/R)[(1/2)+\cosh\Gamma_{n-2}$$
$$\times\exp(-\Gamma_{n-2}+2\Gamma_{n-1})+\cosh\Gamma_{n-4}$$
$$\times\exp(-\Gamma_{n-4}+2\Gamma_{n-3}-2\Gamma_{n-2}+2\Gamma_{n-1})$$
$$+\ldots+\cosh\Gamma_1\exp(-\Gamma_1+2\Gamma_2-2\Gamma_3+\ldots$$
$$+2\Gamma_{n-1})] \tag{8.7a}$$

for odd $n>0$ and the form

$$\tilde{K}_n=\lambda^n\theta(E_n^2-\Delta^2)(4Q_n/R)[\cosh\Gamma_{n-1}e^{-\Gamma_{n-1}}$$
$$+\cosh\Gamma_{n-3}\exp(-\Gamma_{n-3}+2\Gamma_{n-2}-2\Gamma_{n-1})+\ldots$$
$$+\cosh\Gamma_1\exp(-\Gamma_1+2\Gamma_2-2\Gamma_3+\ldots-2\Gamma_{n-1})] \tag{8.7b}$$

for even $n>0$.

The representation of Eqs. (8.6) and (8.7) is exact. A general term of the series can be regarded as an effective renormalized current of the nth side band. In fact, this effective current consists of the contributions of all side bands with odd indices smaller than n. An important feature of this representation is the presence of the θ-function in the general term, which allows us to separate out in Eq. (6.6) that part of the current which is obviously responsible for the SGS,

$$I_{\rm SGS}=\sum_{n=1}^{\infty}\frac{e}{\pi}\int_{\Delta}^{neV-\Delta}dE\,\frac{E}{\xi}\tanh\frac{E}{2T}\,(\tilde{K}_n-\tilde{\bar{K}}_n). \tag{8.8}$$

One might expect (cf. Ref. 55) that Eq. (8.8) represents the subgap tunnel current at zero temperature and that the remaining part of the current in Eq. (6.6),

$$I_r=I-I_{\rm SGS}=\sum_{n=1}^{\infty}\frac{e}{\pi}\left[\int_{neV+\Delta}^{\infty}dE\,\frac{E}{\xi}\tanh\frac{E}{2T}\,(\tilde{K}_n-\tilde{\bar{K}}_n)\right.$$
$$\left.+\int_{\Delta}^{\infty}dE\,\frac{E}{\xi}\tanh\frac{E}{2T}\,(\tilde{K}_{-n}-\tilde{\bar{K}}_n)\right], \tag{8.9}$$

corresponds to the current of thermal excitations. However, this separation is not exact. An analysis shows that the current in Eq. (8.9) does not vanish completely at $T=0$, but contributes a small residual part. An important property of this residual current is that it does not contain any structureless component but demonstrates behavior similar to the current $I_{\rm SGS}$ in Eq. (8.8), thus resulting in a small correction to Eq. (8.8).

9. SUBHARMONIC GAP STRUCTURE

The explicit analytical expressions (8.8) and (8.9) provide a basis for numerical calculation of the subgap current for small λ (low transparency) with any desirable accuracy. However, they are also convenient for qualitative discussion of the SGS. In this section we will analyze the SGS at zero temperature on the basis of Eq. (8.8).

The current-voltage characteristic $I_{\rm SGS}(V)$ in Eq. (8.8) has a complex form consisting of a sum of renormalized side band currents $I_n(V,\lambda)$:

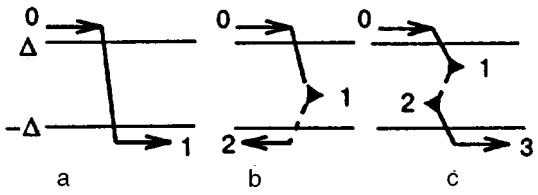

FIG. 7. Scattering processes that contribute to the subgap current: single-particle scattering into the side band $n=1$ gives the main contribution at $eV>2\Delta$ (a); excitation of the Andreev bound state ($n=1$) due to backward scattering into the side band $n=2$ gives the main contribution at $eV>\Delta$ (b); single-particle scattering into the side band $n=3$ and simultaneous excitation of the Andreev bound state in the side band $n=1$ gives the main contribution at $eV>2\Delta/3$ (c).

$$I_{\rm SGS}(V,\lambda)=\sum_{n=1}^{\infty}I_n(V,\lambda),$$
$$I_n(V,\lambda)=\frac{e}{\pi}\int_{\Delta}^{neV-\Delta}dE\,\frac{E}{\xi}\,(\tilde{K}_n-\tilde{\bar{K}}_n). \tag{9.1}$$

The partial current-voltage characteristics $I_n(V,\lambda)$ are similar to each other, and it is convenient to analyze them independently.

According to Eq. (9.1) the partial current I_n starts with an onset at the threshold voltage $V_n=2\Delta/en$. In the limit $\lambda\to0$ the onset is infinitely sharp and its magnitude is

$$I_n(V_n,\lambda\to0)=e\Delta D^n\,\frac{2n}{4^{2n-1}}\,\frac{n^{2n}}{(n!)^2}. \tag{9.2}$$

The jumps of the current at the thresholds result from the singular denominators in Eqs. (5.27) and (5.29), which are related to the singular density of states at the side band energy gap edges, $\sinh\gamma_k=0$. Accumulation of these singularities in the high-order scattering amplitudes leads to a huge increase of the partial currents well above the corresponding thresholds—this causes the failure of multiparticle tunneling theory.[57–59] In our theory, the singularities are regularized by the factors

$$P_n=\prod_{k=0}^{n}|Z_k|^2 \tag{9.3}$$

in the denominators of the scattering amplitudes, Eq. (5.27). These factors are expressed in terms of the continued fractions Z_n [Eq. (5.25)], which therefore should be calculated with sufficient accuracy to preserve the singular parts of Z_n which provide regularization of the integrals.

The first-order current I_1 in Eq. (9.1) corresponds to direct one-particle scattering to the side band $n=1$ (Fig. 7a). The explicit form of the current I_1 is

$$I_1=\frac{2e\lambda}{\pi R}\int_{\Delta}^{eV-\Delta}dE\,\frac{|E_1|}{\xi\xi_1}\left(\frac{E+\xi}{P_1}+\frac{E-\xi}{\bar{P}_1}\right). \tag{9.4}$$

In the limit $\lambda\to0$ this current coincides with the quasiparticle current of the tunnel Hamiltonian model.[54,60] At finite λ the threshold onset of the current at $V=V_1$ is washed out. To evaluate the width of the onset we truncate the continued fraction in P_1 assuming $Z_{-1}=Z_2=1$, which yields

$$P_1 \approx |(1+\lambda a_0^- a_{-1}^-)(1+\lambda a_1^- a_2^-)+\lambda a_0^+ a_1^+|^2. \qquad (9.5)$$

The function $\overline{P_1}$ has a similar form. The regularization effect of the threshold singularity is provided by the most singular term $\lambda a_0^+ a_1^+$ in Eq. (9.5). Keeping this term, we obtain in the vicinity of the threshold, $e(V-V_1) \ll \Delta$, the result

$$I_1(V)=\frac{2e\Delta\lambda}{\pi R} f\left(\frac{eV-eV_1}{\Delta\lambda}\right),$$

$$f(z)=\int_0^\pi d\theta \frac{\sin^2\theta}{(\sin\theta+1/z)^2}. \qquad (9.6)$$

According to this formula the onset width is $e(V-V_1) \sim \lambda\Delta$.

The second-order current I_2 corresponds to the creation of a real excitation during quasiparticle backscattering into the side band $n=2$ (Fig. 7b) and appears as the current of transmitted states of the side band $n=1$ (cf. the excess current in Sec. 7). In the vicinity of the threshold, $V_2 < V < V_1$, this current exists only in the form of currents through the bound states and therefore it is completely converted into a supercurrent far away from the junction. At larger voltages, $V > V_1$, the side band $n=1$ extends outside the energy gap (see Fig. 8a), which also makes the current I_2 partially consist of contributions from extended states. The explicit expression for the second-order current is

$$I_2=\frac{4e\Delta^3\lambda^2}{\pi R}\int_\Delta^{2eV-\Delta} dE \frac{|E_2|}{\xi\xi_2|\xi_1|^2} \times \cosh\Gamma_1\left(\frac{e^{-\gamma_0+\Gamma_1}}{P_2}+\frac{e^{\gamma_0-\Gamma_1}}{\overline{P_2}}\right). \qquad (9.7)$$

Omitting the λ-dependence of P_2 in Eq. (9.7), we obtain the two-particle tunnel current of Schrieffer and Wilkins.[42,57] To keep the singular terms in P_2 one has to truncate the continued fractions in Eq. (5.25) assuming $Z_{-1}=Z_3=1$, which yields

$$P_2 \approx |(1+\lambda a_{-1}^- a_0^-)(1+\lambda a_1^- a_2^-) + \lambda a_0^+ a_1^+(1+\lambda a_2^+ a_3^+)|^2. \qquad (9.8)$$

The threshold singularity results from the small product $\xi\xi_2$ in the denominator of Eq. (9.7). However, in Eq. (9.8) there are no singular terms proportional to $a_0 a_2$ among the terms linear in λ. Such terms are quadratic in λ and they provide, along with the terms λa_0 and λa_2, the width of the onset: $e(V-V_2) \sim \lambda^2\Delta$. This onset is sharper than the onset of the current I_1.

The threshold singularity in the current I_2 is typical of all higher-order currents $n > 1$. The appearance of the first side band outside the energy gap at $V=V_1$ is manifested through a spike in the current I_2. Indeed, if $V \approx V_1$, the nodes of ξ_1 overlap the nodes of ξ and ξ_2 at the lower ($E=\Delta$) and the upper ($E=3\Delta$) limits of integration in Eq. (9.7), respectively (see Fig. 8a). This singularity yields an increase of the current I_2 when the voltage approaches V_1,

$$I_2 \sim e\Delta\lambda^2\left(\frac{\Delta}{e(V_1-V)}\right)^{1/2}.$$

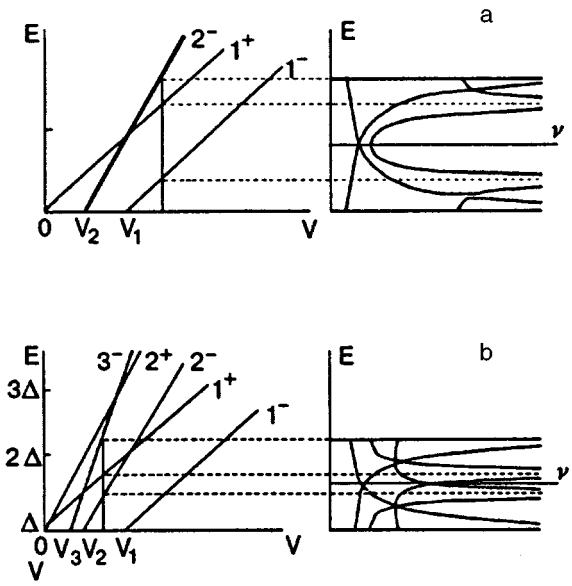

FIG. 8. a) Density of states $\nu(E)=|E_n/\xi_n|$ of the side bands and E_0, E_1, and E_2 at applied voltage $V > V_1$ (right), position of singularities of the side-band density of states plotted as function of the applied voltage for the current I_2 (left), $1^\pm$:$E_1=\pm\Delta$, 2^-:$E_2=-\Delta$. b) Density of states of the side bands E_0, E_1, E_2, and E_3 at applied voltage $V_2 < V < V_1$ (right), position of singularities of the side-band density of states plotted as a function of the applied voltage for the current I_3 (left), $1^\pm$:$E_1=\pm\Delta$, $2^\pm$:$E_2=\pm\Delta$, 3^-:$E_3=-\Delta$.

Regularization of the integral, which is provided by the singular terms $\lambda a_1 a_0$ and $\lambda a_1 a_2$ in Eq. (9.8) at the lower and the upper integration limits, respectively, yields

$$\frac{I_2(V_1)}{I_2(V_2)} \sim \frac{1}{\sqrt{\lambda}}.$$

Further analysis shows that the current reaches a maximum value slightly above $V=V_1$, after which it rapidly decreases (see Fig. 9). At voltages $V > V_1$ the singular point $\xi_1=0$ remains within the integration region, which increases the current by a logarithmic factor in comparison with the value of the current near the threshold V_2,

$$I_2(V>V_1) \sim \frac{e\Delta\lambda^2 \ln\lambda}{R}. \qquad (9.9)$$

At large voltage $V \gg V_1$ the current I_2 forms the excess current [Eq. (7.10)]. It is interesting to note that in this limit the logarithmic factor is compensated for by the current I_r [Eq. (8.9)], which yields the λ^2-dependence of the excess current.

The third-order current I_3 at voltages close to the threshold V_3 results from the combination of one-particle tunneling into the side band $n=3$ and excitation of the transmitted Andreev bound states of the side band $n=1$ (Fig. 7c). The probabilities of these two processes are related as 1:2 at threshold [Eq. (8.7)]. A gradual emergence of the bound states of the side bands $n=1$ and 2 outside the energy gap at $V=V_2$ and $V=V_1$ (Fig. 8b) gives rise to the current peaks. The current I_3 has the explicit form:

$$I_3=\frac{2e\Delta^5\lambda^3}{\pi R}\int_{\Delta}^{3eV-\Delta}dE\,\frac{|E_3|}{\xi\xi_3|\xi_1\xi_2|^2}\times\left[\frac{e^{\gamma_0}(1+2\cosh\Gamma_1 e^{-\Gamma_1+2\Gamma_2})}{P_3}+\frac{e^{-\gamma_0}(1+2\cosh\Gamma_1 e^{\Gamma_1-2\Gamma_2})}{\overline{P_3}}\right] \tag{9.10}$$

with the regularization factor

$$P_3\approx|(1+\lambda a_{-1}^- a_0^-)(1+\lambda a_1^- a_2^-)(1+\lambda a_3^- a_4^-)+\lambda a_0^+ a_1^+(1+\lambda a_2^+ a_3^+)|^2. \tag{9.11}$$

The current peak at $V=V_2$ results from the overlap of nodes of ξ and ξ_2 at $E=\Delta$ and nodes of ξ_1 and ξ_3 at $E=2\Delta$, similarly to the peak of the current I_2. These singularities yield again an increase in the current inversely proportional to the square root of the departure from the voltage V_2: $I_3 - e\Delta^{3/2}\lambda^3/[e(V_2 - V)]^{1/2}$. However, since the factor P_3 [Eq. (9.11)] contains neither the term $\lambda a_0 a_2$ nor the term $\lambda a_1 a_3$, regularization of the singularity is provided, e.g., at $E = \Delta$, by the terms λa_0 or λa_2, which gives rise to a more pronounced peak with magnitude

$$\frac{I_3(V_2)}{I_3(V_3)}\sim\frac{1}{\lambda}. \tag{9.12}$$

We note that the magnitude of this peak is comparable to the magnitude of the onset of the current I_2. The second peak at $V=V_1$ results from the overlap of the nodes of ξ_2 and ξ_3 at $E=3\Delta$, which increases the current I_3 near the voltage $V = V_1$ which is inversely proportional to the first power of the distance to this voltage: $I_3\sim\lambda^3\Delta^2/(V_1 - V)$. The divergence is regularized by the term $\lambda a_2 a_3$ in Eq. (9.11), which results in a peak of magnitude

$$\frac{I_3(V_1)}{I_3(V_3)}\sim\frac{1}{\lambda}. \tag{9.13}$$

Thus the heights of the two peaks of the current I_3 are of the same order in λ, although the peak at $V \approx V_1$ is sharper.

In a similar way, all of the high-order currents in the vicinity of their thresholds are attributable either to the Andreev bound state currents (even n) or to a combination of Andreev bound state currents and the current of a single real excitation (odd n). The number of excited Andreev states is correspondingly $n/2$ or $(n - 1)/2$. Singularities similar to the singularity of the current I_3 at the voltage $V \approx V_1$ exist in all high-order currents, where they cause even more pronounced current peaks because of the absence of terms $\lambda a_k a_{k+1}$ in the corresponding smearing functions P_n. Because of this property, the heights of such peaks exceed the threshold value of the corresponding current by two orders of λ: $(I_n)_{\max}-e\Delta\lambda^{n-2}/R$.

The above discussion reveals the current peaks to be essential features of the SGS of tunnel current in addition to the current onsets (Fig. 9) (these peaks are seen also in the numerical results of Refs. 34 and 39). It allows us to establish a general classification of singularities that cause peaks

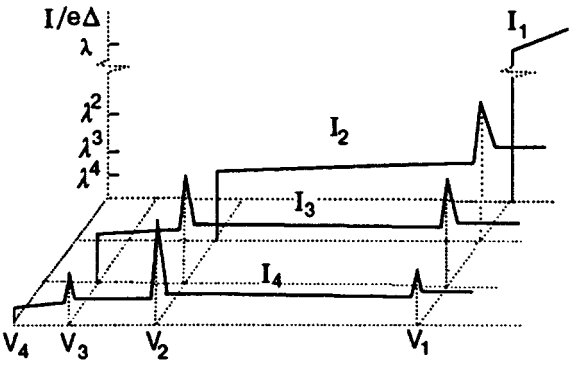

FIG. 9. Schematic diagram of the partial $I_n - V$ characteristics.

in partial currents I_n. They result from the overlap of singularities of the side band density of states. It is easy to see that the singularities of only two side bands can overlap. The condition of the overlap for mth and kth side bands have the form

$$E-keV=\Delta,\quad E-meV=-\Delta. \tag{9.14}$$

This condition is met at voltages $eV=2\Delta/(m - k)$ for all integer $0 \leqslant k < m \leqslant n$. The magnitude of the current peaks depends on whether the overlapping side bands are neighbors or not, and whether the side band index is inside or at the edge of the interval $(0, n)$.

I. $m - k=1$, $m=n$ or $k=0$: edge-type singularity, neighbor side bands. This type of singularity forms the peak of the current I_2 at the main threshold V_1. The magnitude of the current peak is $(I_2)_{\max}\sim e\Delta\sqrt{\lambda}/R$.

II. $m - k > 1$, $m=n$ or $k=0$: edge-type singularity, nonneighbor side bands. This type of singularity forms the first peak of the current I_n, $n > 2$ at voltage V_{n-1}. The magnitude of the current peak is $(I_n)_{\max}\sim e\Delta\lambda^{n-1}/R$.

III. $m - k = 1, m < n, k > 0$: internal singularity, neighbor side bands. This type of singularity forms the last peak of each current I_n, $n > 2$ at voltage V_1. The magnitude of the current peak is $(I_n)_{\max}\sim e\Delta\lambda^{n-1}/R$.

IV. $m - k > 1$, $m < n$, $k > 0$: internal singularity, nonneighbor side bands. This type of singularity forms all intermediate peaks of each current I_n, $n > 3$. The magnitude of the current peaks are $(I_n)_{\max}\sim e\Delta\lambda^{n-2}/R$.

CONCLUSION

In this paper we have considered superconductive tunneling as a scattering problem within the framework of Bogolyubov-de Gennes (BdG) quantum mechanics. An essential aspect of this problem is that the scatterer consists not only of the potential of the tunnel barrier but also of the discontinuity of the phase of the order parameter. At equilibrium (zero bias, Josephson direct current) the scattering problem is *elastic*. The peculiar feature of the elastic scattering problem in short junctions, which is considered here, is that the balance of currents of the scattering modes is not violated: the supercurrent flows only through the superconducting bound states (for a more general discussion, see Ref. 48). In the presence of voltage bias the scattering is *inelastic*,

because the time dependence of the component of the scatterer is related to the superconducting phase difference. In general, the currents of all inelastic channels, taken collectively, constitute the components of the tunnel current that flows through the biased junction. The quasiparticle current corresponds to the incoherent part of the inelastic side band contributions, and the Josephson alternating current corresponds to the interference of the side band contributions.

There are three distinct components of the quasiparticle tunnel current at zero temperature: (i) the current of quasiparticles excited above the ground state, (ii) the current trough Andreev bound states converted to a supercurrent outside the junction, and (iii) the imbalance current of the ground state modes. At large bias voltage, $eV \gg 2\Delta$, the first component corresponds to a single particle current of the normal junction, while the other components cause excess current. When voltage is decreased, redistribution of current among the components gives rise to subharmonic gap structure (SGS) in the form of current onsets and current peaks. Within the voltage intervals $2\Delta/n < eV < 2\Delta/(n-1)$ with even n, the tunnel current consists entirely of currents through the Andreev bound states [component (ii); e.g., Fig. 7b]; the states of all side bands with odd indices smaller than n contribute to the current. If n is odd, a real excitation current of the side band n [component (i); e.g., Figs. 7a, and 7c] is also present in the tunnel current. Opening of new channels of tunneling of real excitations gives rise to current structures. Thus, SGS reveals the discrete nature of the side band spectrum. The structure becomes more pronounced with decreasing transparency of the junction.

Since each Andreev state provides transfer of one Cooper pair through the junction for every incident quasiparticle, n particles will tunnel in the interval $2\Delta/n < eV < 2\Delta/(n-1)$.

The participation of a large number of bound Andreev states in the current transport at low voltages is surprising: it appears to contradict the fact that subgap current diminishes at zero bias. After all, the probability of the scattering into side bands does not depend on the bias and is proportional to powers of D. This paradox can be solved by increasing the compensation of currents between the normal and Andreev channels in each side band with decreasing voltage, which gives the required voltage dependence of the total current.

ACKNOWLEDGMENT

This work was supported by the Swedish National Science Research Council (NFR), the Swedish National Board for Technical and Industrial Development (NUTEK), and the Swedish Royal Academy of Sciences (KVA).

APPENDIX A: BOUNDARY CONDITIONS

The quasiclassical boundary condition in Eqs. (2.8) and (2.9) has been derived in Ref. 31 by using the method of Ref. 21. Here we present simple arguments which lead to this boundary condition. We consider the more general case of asymmetric junction, using an asymmetric version of the Hamiltonian of Eq. (2.2) with the same restriction imposed on the length of the nonsuperconducting region, $L \ll \xi_0$. We include a contact potential difference in the potential $U(x)$, which implies that this potential may have nonvanishing asymptotic values at infinity: $U(-\infty) \neq U(\infty) \neq 0$. If the junction has more than one transverse transport mode, we assume that these modes are not mixed.

A one-dimensional quasiclassical wave function of a given transverse channel in the right electrode has the form [Eq. (2.6)],

$$\Psi_R(x,t) = \sum_\beta \frac{1}{\sqrt{v_R}} \exp\left(i\beta \int p_R dx \right) \times \exp(i\sigma_z \chi_R/2)\, \psi_R^\beta(x,t), \tag{A1}$$

with a similar expression for the left electrode. The quantities ψ_R^β are slowly varying two-component wave functions on the scale of $1/p_R$, where $p_R(x) = [2m_R(\mu - U_R - E_{\perp R}(x))]^{1/2}$. This equation is valid over the distance $x \gg 1/p_R$ from the junction, and in the spatial region $1/p_R \ll x \ll \xi_0$ the functions ψ_R^β are almost constant.

From another point of view, at large distance from the junction, $|x| \gg 1/p_{R,L}$, the function Ψ can be expressed in the form of a linear combination of the scattering states at the Fermi level,

$$\Psi = C_1\chi_1 + C_2\chi_2 \tag{A2}$$

$$\chi_1 = \begin{cases} (1/\sqrt{v_L})[e^{ip_L x} + re^{-ip_L x}], & x<0, \\ (1/\sqrt{v_R})\, d e^{ip_R x}, & x>0, \end{cases} \tag{A3a}$$

$$\chi_2 = \begin{cases} (1/\sqrt{v_R})[e^{-ip_L x} + \tilde{r} e^{-ip_R x}], & x>0, \\ (1/\sqrt{v_L})\, \tilde{d} e^{-ip_L x}, & x<0. \end{cases} \tag{A3b}$$

Comparing Eqs. (A2) and (A3) with Eq. (A1) in the region $1/p_F \ll |x| \ll \xi_0$, we have

$$C_1 = e^{i\sigma_z \chi_L/2}\psi_L^+, \quad C_2 = e^{i\sigma_z \chi_R/2}\psi_R^-,$$
$$rC_1 + \tilde{d}C_2 = e^{i\sigma_z \chi_L/2}\psi_L^-,$$
$$dC_1 + \tilde{r}C_2 = e^{i\sigma_z \chi_R/2}\psi_R^+, \tag{A4}$$

which yields the boundary condition

$$\begin{pmatrix} \psi^- \\ \psi^+ \end{pmatrix} = \hat{V} \begin{pmatrix} \psi^+ \\ \psi^- \end{pmatrix}, \tag{A5}$$

with the matching matrix

$$\hat{V} = \begin{pmatrix} r & \tilde{d} e^{i\sigma_z \varphi/2} \\ d e^{-i\sigma_z \varphi/2} & \tilde{r} \end{pmatrix}, \tag{A6}$$

where $\varphi = \chi_R(0) - \chi_L(0)$. The matrix $\hat{V}$ satisfies the unitarity condition $\hat{V}\hat{V}^+ = 1$, provided by the relations among the normal electron scattering amplitudes in Eq. (A3): $\tilde{r} = -\tilde{d}(r/d)^*$, $|d|^2 = |\tilde{d}|^2 = D$, $|r|^2 = |\tilde{r}|^2 = R = 1 - D$.

APPENDIX B: BOUND STATE CURRENT

Equation (4.10) for the current of a single bound state can be derived directly[61] from the Bogolyubov-de Gennes equations (2.5) and (2.2). The derivation is valid for junctions with an arbitrary nonsuperconducting region between the superconducting electrodes. We assume for simplicity

that the phase of the order parameter [Eq. (2.3)] in the electrodes is constant and equal to $\pm\ \varphi/2$ in the right and left electrodes, respectively. Let $\Psi(\mathbf{r},E)$ be a normalized wave function of the Andreev bound state with energy E,

$$\hat{H}\Psi - E\Psi = 0, \quad \Psi(x = \pm\infty) = 0. \tag{B1}$$

The energy and the wave function of the bound state depend on the phase difference φ. Using the derivative with respect to φ in Eq. (B1) and a scalar product of the resulting equation with the function Ψ, we obtain

$$\int d^3r \left(\Psi, \frac{d}{d\varphi} (\hat{H} - E)\Psi \right) = 0, \tag{B2}$$

where the brackets denote a scalar product in the electron-hole space, similar to Eq. (3.8). In this equation the derivative of the Hamiltonian has the form

$$\frac{d\hat{H}}{d\varphi} = \frac{d\hat{\Delta}}{d\varphi} = \frac{i\ \text{sign}\ x}{2}\ \sigma_z \hat{\Delta}, \tag{B3}$$

in accordance with Eqs. (2.2) and (2.3). Substituting relation (B3) into Eq. (B2) and taking into account that the function Ψ is normalized, we obtain

$$\frac{dE}{d\varphi} = \int d^3r \left(\Psi, \frac{d\hat{\Delta}}{d\varphi}\ \Psi \right). \tag{B4}$$

The continuity equation for the charge current,

$$I(x,E) = \frac{e}{2m}\ (\hat{p}_x - \hat{p}'_x) \int d^2r_\perp (\Psi(x'), \Psi(x))_{x=x'}, \tag{B5}$$

in accordance with Eq. (B1), has the form

$$i\ \frac{d}{dx}\ I(x,E) = e \int d^2r_\perp (\Psi(x), [\sigma_z, \hat{\Delta}]\Psi(x)). \tag{B6}$$

Substituting relation (B3) into Eq. (B6) and integrating this equation over the entire x axis, we obtain

$$I(0,E) = 2e \int d^3r \left(\Psi, \frac{d\hat{\Delta}}{d\varphi}\ \Psi \right). \tag{B7}$$

In Eq. (B7) the current at infinity drops out because of decay of the bound state wave function, $I(\pm\infty) = 0$. The current $I(0)$ is formally taken in the middle of the junction; however, the current has the same value in the whole nonsuperconducting region, according to the conservation equation (B6). Comparison of Eqs. (B4) and (B7) finally yields

$$I(E) = 2e\ \frac{dE}{d\varphi}. \tag{B8}$$

[1] J. Bardeen, Phys. Rev. Lett. **6**, 57 (1961).
[2] A. Barone and G. Paterno, Physics and Applications of the Josephson Effect, Wiley, New York (1982).
[3] C. L. Foden, R. Rando, A. van Dordrecht, A. Peacock, J. Lumley, and C. Pereira, Phys. Rev. B**47**, 3316 (1993).
[4] R. Cristiano, I. Frenzio, R. Monaco, C. Nappi, and S. Pagano, Phys. Rev. B**49**, 429 (1994).
[5] A. W. Kleinsasser, R. E. Miller, W. H. Mallison, and G. B. Arnold, Phys. Rev. Lett. **72**, 1738 (1994).
[6] H. Takayanagi and T. Kawakami, Phys. Rev. Lett. **54**, 2449 (1985).
[7] A. Frydman and Z. Ovadyahu, Solid State Commun. **95**, 79 (1995).
[8] N. van der Post, E. T. Peters, I. K. Yanson, and J. M. van Ruitenbeek, Phys. Rev. Lett. **73**, 2611 (1994).
[9] H. Takayanagi, T. Akazaki, and J. Nitta, Phys. Rev. Lett. **75**, 3533 (1995).
[10] W. Haberkorn, H. Knauer, and S. Richter, Phys. Status Solidi **47**, K161 (1978).
[11] A. V. Zaitsev, Zh. Éksp. Teor. Fiz. **86**, 1742 (1983) [Sov. Phys. JETP **59**, 1015 (1984)].
[12] G. B. Arnold, J. Low Temp. Phys. **59**, 143 (1985).
[13] L. G. Aslamasov and B. Fistul', Zh. Éksp. Teor. Fiz. **83**, 1170 (1982) [Sov. Phys. JETP **56**, 666 (1982)].
[14] C. Ishii, Prog. Theor. Phys. **44**, 1525 (1970).
[15] A. V. Svidzinsky, T. N. Anzygina, and E. N. Bratus', J. Low Temp. Phys. **10**, 131 (1973).
[16] I. O. Kulik and A. N. Omel'yanchuk, Fiz. Nisk. Temp. **3**, 945 (1977); **4**, 296 (1978) [Sov. J. Low Temp. Phys. **3**, 459 (1977); **4**, 142 (1978)].
[17] S. N. Artemenko, A. F. Volkov, and A. V. Zaitsev, Zh. Éksp. Teor. Fiz. **76**, 1816 (1979) [Sov. Phys. JETP **49**, 924 (1979)].
[18] I. O. Kulik, Zh. Éksp. Teor. Fiz. **57**, 1745 (1969) [Sov. Phys. JETP **30**, 944 (1970)].
[19] J. Bardeen and J. L. Jonson, Phys. Rev. B**5**, 72 (1972).
[20] P. G. de Gennes, Superconductivity of Metals and Alloys, Addison-Wesley, New York (1989).
[21] A. V. Svidzinsky, Spatial Inhomogeneity Problems in the Theory of Superconductivity, Nauka, Moscow (1982) (in Russian).
[22] I. F. Itskovich and R. I. Shekhter, Fiz. Nizk. Temp. **7**, 863 (1981) [Sov. J. Low Temp. Phys. **7**, 418 (1981)].
[23] G. E. Blonder, T. M. Klapwijk, and M. Tinkham, Phys. Rev. B**25**, 4515 (1982).
[24] C. W. J. Beenakker and H. van Houten, Phys. Rev. Lett. **66**, 3056 (1991).
[25] P. F. Bagwell, Phys. Rev. B**46**, 12573 (1992).
[26] C. W. J. Beenakker, Phys. Rev. Lett. **67**, 3836 (1991).
[27] M. Hurd and G. Wendin, Phys. Rev. B**49**, 15258 (1994).
[28] L. Y. Gorelik, V. S. Shumelko, R. I. Shekhter, G. Wendin, and M. Jonson, Phys. Rev. Lett. **75**, 1162 (1995).
[29] A. Furusaki and M. Tsukada, Physica B**165–166**, 967 (1990); Phys. Rev. B**43**, 10164 (1991).
[30] C. W. J. Beenakker and H. van Houten, in Single Electron Tunneling and Mesoscopic Devices, Springer, Berlin (1991).
[31] V. S. Shumeiko, E. N. Bratus', and G. Wendin, Phys. Rev. B**48**, 13129 (1993).
[32] T. M. Klapwijk, G. E. Blonder, and M. Tinkham, Physica B+C **109–110**, 1657 (1982).
[33] E. N. Bratus', V. S. Shumeiko, and G. Wendin, Phys. Rev. Lett. **74**, 2110 (1995).
[34] D. Averin and A. Bardas, Phys. Rev. Lett. **75**, 1831 (1995).
[35] B. J. van Wees, H. van Houten, C. W. J. Beenakker, J. G. Williamson, L. P. Kouwenhoven, D. van der Marel, and C. T. Foxon, Phys. Rev. Lett. **60**, 848 (1988).
[36] R. Landauer, IBM J. Res. Dev. **1**, 223 (1957).
[37] S. V. Kuplevakhskii and I. I. Fal'ko, Fiz. Nizk. Temp. **17**, 961 (1991) [Sov. J. Low Temp. Phys. **17**, 501 (1991)].
[38] B. D. Josephson, Adv. Phys. **14**, 419 (1965).
[39] G. B. Arnold, J. Low Temp. Phys. **68**, 1 (1987).
[40] A. D. Stone, M. Ya. Azbel, and P. A. Lee, Phys. Rev. B**31**, 1707 (1985).
[41] P. F. Bagwell and R. K. Lake, Phys. Rev. B**46**, 15329 (1992).
[42] J. R. Schrieffer and J. W. Wilkins, Phys. Rev. Lett. **10**, 17 (1963).
[43] L. I. Glazman, G. B. Lesovik, D. E. Khmel'nitskii, and R. I. Shekhter, Pis'ma Zh. Éksp. Teor. Fiz. **48**, 218 (1988) [JETP Lett. **48**, 238 (1988)].
[44] J. Bardeen, R. Kümmel, A. E. Jacobs, and L. Tewordt, Phys. Rev. **187**, 556 (1969).
[45] I. O. Kulik, R. I., Shekhter, and A. N. Omel'yanchouk, Solid State Commun. **23**, 301 (1977).
[46] M. Yu. Kupriyanov and V. F. Lukichev, Zh. Éksp. Teor. Fiz. **94**, 139 (1988) [Sov. Phys. JETP **67**, 1163 (1988)].
[47] I. A. Devyatov and M. Yu. Kupriyanov, Pis'ma Zh. Éksp. Teor. Fiz. **59**, 187 (1994) [JETP Lett. **59**, 200 (1994)].
[48] G. Wendin and V. S. Shumelko, Phys. Rev. B**53**, R6006 (1996).
[49] A. F. Andreev, Zh. Éksp. Teor. Fiz. **46**, 1823 (1964) [Sov. Phys. JETP **19**, 1228 (1964)].
[50] J. R. Schrieffer, Theory of Superconductivity, Benjamin, New York (1964).
[51] V. P. Galaiko, Zh. Éksp. Teor. Fiz. **61**, 382 (1971) [Sov. Phys. JETP **34**, 203 (1972)].

[52] The contribution from the continuum does not vanish if there is imbalance of populations of electron-like and hole-like branches of the quasiparticle spectrum in one of the electrodes.
[53] V. Ambegaokar and A. Baratoff, Phys. Rev. Lett. **10**, 468 (1963).
[54] N. R. Werthamer, Phys. Rev. **147**, 255 (1966).
[55] E. N. Bratus' and V. S. Shumelko, Fiz. Tverd. Tela **21**, 2821 (1979) [Sov. Phys. Solid State **21**, 1506 (1979)].
[56] B. N. Taylor and E. Burstein, Phys. Rev. Lett. **10**, 14 (1963).
[57] J. W. Wilkins, in Tunneling Phenomena in Solids, Plenum, New York (1963).
[58] L. E. Hasselberg, J. Phys. F**3**, 1438 (1973); L. E. Hasselberg, M. T. Levinsen, and M. R. Samuelsen, Phys. Rev. B**9** 3757 (1974).
[59] E. L. Wolf, Principles of Electron Tunnel Spectroscopy, Oxford University, New York (1985).
[60] M. H. Cohen, L. H. Fallcov, and J. C. Phillips, Phys. Rev. Lett. **8**, 316 (1962).
[61] L. Y. Gorelik, unpublished.

This article was published in English in the original Russian journal. It was edited by S. J. Amoretty.

The effect of pressure and silver impurity on the superconducting properties of the HTS $YBa_2Cu_4O_8$

V. Z. Kleĭner, O. N. Ovcharenko, A. A. San'kov, N. S. Tereshina, and V. A. Finkel'

*National Science Center, Kharkov Physicotechnical Institute, 310108 Kharkov, Ukraine**

(Submitted June 12, 1996; revised September 24, 1996)
Fiz. Nizk. Temp. **23**, 271–277 (March 1997)

The effect of uniform compression is studied on the superconducting transition temperature of the HTS ceramics $YBa_2(Cu_{1-x}Ag_x)_4O_{8\pm\delta}$($x=0$, 0.05, 0.1, 0.15). It is shown that the pressure effect in these compounds differs considerably from that in the system $YBa_2(Cu_{1-x}Ag_x)_3O_{7-\delta}$. The observed peculiarities are discussed on the basis of the van Hove anomaly in the electron energy spectrum of oxide cuprates. The correspondence of the superconducting properties of the 1–2–4 and 1–2–3 systems under pressure with certain models of high-temperature superconductivity is discussed. The nature of nonlinearity of the temperature dependence of the electrical resistance of the 1–2–4 system in the normal state and the effect of substitution of silver for copper on it are studied. The corresponding phase diagram is constructed. The correspondence of the observed increase in crossover temperature with the Nagaoza–Lee theory is discussed. © *1997 American Institute of Physics.*
[S1063-777X(97)00303-4]

INTRODUCTION

Several investigations of high-temperature superconducting cuprate oxides have shown that different atomic substitutions in them affect significantly the sign and the magnitude of the pressure derivative of T_c. This quantity is usually found to be a nonlinear function of the concentration x of the substituting element even for small values of x. For example, a partial replacement of Y^{3+} ions by Pr^{3+} ions in the compound $YBa_2Cu_3O_{7-\delta}$ results not only in a monotonic decrease in T_c with increasing praseodymium concentration x, but also in a strong variation in the nonlinear dependence of T_c on pressure in the interval[1] $0\leqslant x\leqslant 0.5$. An identical nonlinear effect in the dependence $(dT_c/dP)(x)$ was observed in the compound $YBa_2Cu_4O_{8\pm\delta}$ upon a partial replacement of Y^{3+} ions by Ca^{2+} ions ($0\leqslant x\leqslant 0.3$). The superconducting transition temperature increased and attained a maximum value[2] in contrast to the compound $Y_{1-x}Pr_xBa_2Cu_3O_{7-\delta}$. In both cases, the nonlinear dependence of dT_c/dP on x was treated as a manifestation of the singularity in the electron density of states caused by a change in the number of carriers as a result of substitution of yttrium. These results serve as an important argument in favor of the recently established concepts associated with the van Hove approach to the high-temperature superconductivity.[3] On the other hand, it is known that substitution of copper by its close chemical analog silver in the 1–2–3 structure leads to a slight change in the transition temperature and a different type of the dependence $(dT_c/dP)(x)$.[2] The well-known difference in the pressure effects in 1–2–3 and 1–2–4 systems is attributed to the singularity of the 1–2–4 crystal structure, viz., the presence of double copper–oxygen chains rather than single chains in 1–2–3 crystals. Hence it should also be interesting to compare the effects of substitution of silver for copper in both structural modifications.

Studies of the peculiarities of normal properties of HTS compounds also serve as an important source of information about the nature of high-temperature superconductivity. This explains the rising interest in certain peculiar properties of the 1–2–4 system above the superconducting transition temperature. It is well known that the temperature dependence of the resistance of $YBa_2Cu_4O_{8\pm\delta}$ reveals departures from the linear $R(T)$ dependence in the normal region which is typical of high-temperature superconductors.[4,5] According to the results obtained by a number of authors, these properties may throw light on the very nature of the high- temperature supreconductivity mechanism. Hence it is extremely interesting to find out whether atomic substitutions affect the peculiarities of normal conductivity of 1–2–4 compounds.

EXPERIMENT

1. We studied the superconducting and normal states of the ceramic samples $YBa_2(Cu_{1-x}Ag_x)_4O_{8\pm\delta}$ in the concentration range $0\leqslant x\leqslant 0.15$ by using the following technique. Compounds of nominal composition $YBa_2(Cu_{1-4/3x}Ag_{4/3x})_3O_{7-\delta}$ ($x=0$; 0.05 ;0.1; 0.15) were first synthesized by using the standard ceramic technology, then powdered to a grain size of 1μm and mixed with equimolecular amounts of copper oxide CuO. Parallelepiped samples of size $3\times2\times20$ mm were compressed from the obtained mixture, fritted in air at a temperature of 950 °C for several hours, and then cooled with the furnace. The samples were then placed in a high-pressure chamber and annealed in oxygen amosphere near the upper limit of stability of the 1–2–4 phase for about one hundred hours at a temperature of 800 °C under a pressure $P=16$ atm, and then cooled slowly. Silver contacts were formed on the samples for measuring electrical resistance.

The x-ray diffraction studies of the obtained samples revealed them to be single-phase 1–2–4 structures in the entire range of variation of x. The magnitude of orthorhombic distortion $(b-a)/(b+a)$ decreased slightly with increasing

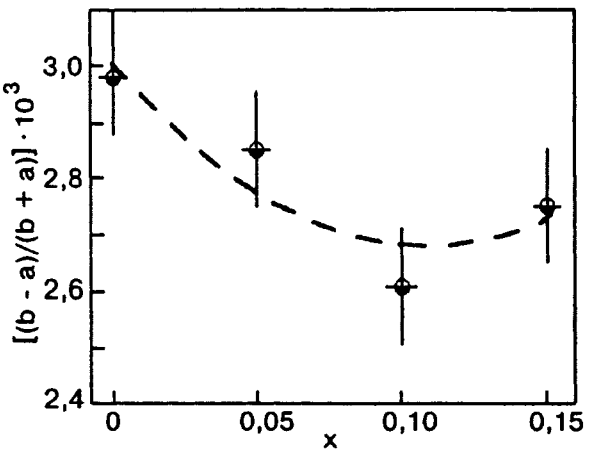

FIG. 1. Dependence of the orthorhombicity distortion parameter on silver concentration.

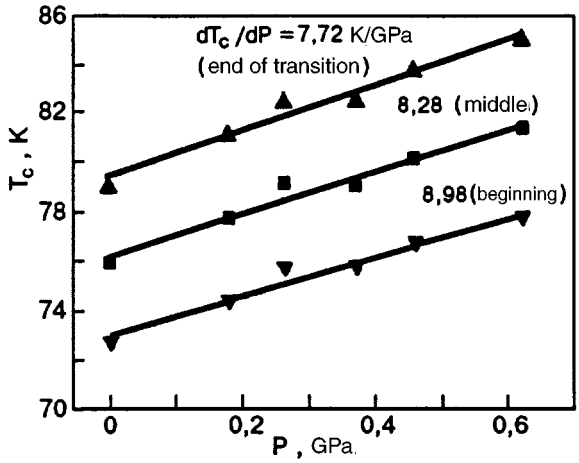

FIG. 3. Dependence of the superconducting transition temperature of a $YBa_2(Cu_{0.95}Ag_{0.05})_4O_{8\pm\delta}$ polycrystal on temperature.

concentration of Ag (Fig. 1). Note that this dependence of the distortion parameter on x is stronger[2] than for the compound $YBa_2(Cu_{1-x}Ag_x)_3O_{7-\delta}$ and the region of its significant variation is displaced towards lower values of x.

The samples were subjected to hydrostatic compression in a beryllium–bronze bomb up to 0.7 GPa in the superconducting transition region. The pressure in the bomb was determined by measuring the electrical resistance of a manganin probe, while the temperature in the cryostat was determined from the reading of a standard germanium resistance thermometer. The superconducting transition was recorded from the temperature dependence of the electrical resistance which was measured by the four-probe technique by passing constant current of 1 and 5 mA through the sample. The superconducting transition temperature corresponded to a twofold decrease in the electrical resistance in the transition region.

2. All investigated samples revealed a metal-like temperature dependence of electrical resistivity before the onset of the superconducting transition (Fig. 2); the resistivity decreased monotonically with increasing silver concentration.

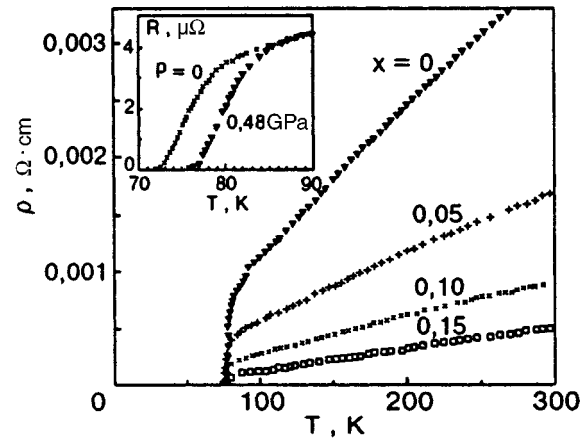

FIG. 2. Temperature dependence of the electrical resistivity ρ of $YBa_2(Cu_{1-x}Ag_x)_4O_{8\pm\delta}$. The inset shows the displacement of the superconducting transition curve under pressure.

The inset in Fig. 2 shows the typical superconducting transition curves for a $YBa_2(Cu_{0.95}Ag_{0.05})_4O_{8\pm\delta}$ sample without pressure and at $P=0.48$ GPa. The transition width remained nearly constant with pressure and amounted to about 7–8 K.

Under pressure up to 0.7 GPa, the transition temperature increased linearly in the entire range of variation of x. By way of an example, Fig. 3 shows the displacement of T_c with pressure for the same sample. The indicated values of the slope of the straight lines correspond to the onset, middle, and end of the transition. It can be seen that the quantity dT_c/dP does not depend significantly on the method by which T_c is determined.

DISCUSSION

1. The data obtained from the measurement of T_c of $YBa_2(Cu_{1-x}Ag_x)_4O_{8\pm\delta}$ under pressure and for $P=0$ are shown in Fig. 4 together with the values of $R(T)$ in normal state for various degrees x of substitution of copper by silver. It can be seen that the effect of replacement of copper in this system differs significantly from that in the 1–2–3 system.[2] In the first place, the initial descent in the $T_c(x)$ dependence becomes much steeper as a result of substitution (curve *1*). This correlates with the difference in the nature of variation of the distortion parameter in 1–2–3 and 1–2–4 systems in the same range. Second, the difference is manifested in the nonmonotonic dependence $T_c(x)$ in the 1–2–4 systems, which is not observed in the 1–2–3 system. The difference in the properties of two structural modifications and in experiments under pressure is equally significant. Indeed, the dependence $(dT_c/dP)(x)$ in the 1–2–4 system is nonlinear and has a peak at $x=0.1$ (curve *2* in Fig. 4), and the variation of the quantity $(dT_c/dP)(x)$ is about an order of magnitude larger than the corresponding variation in $YBa_2(Cu_{1-x}Ag_x)_3O_{7-\delta}$. On the other hand, this also reveals a qualitative resemblance with the pressure effect in the same structure 1–2–4 in which Y is replaced by Ca, and the $(dT_c/dP)(x)$ dependence shows a minimum.[2] It can be assumed that the observed peak is a consequence of the electron-topological transition (van Hove anomaly in the en-

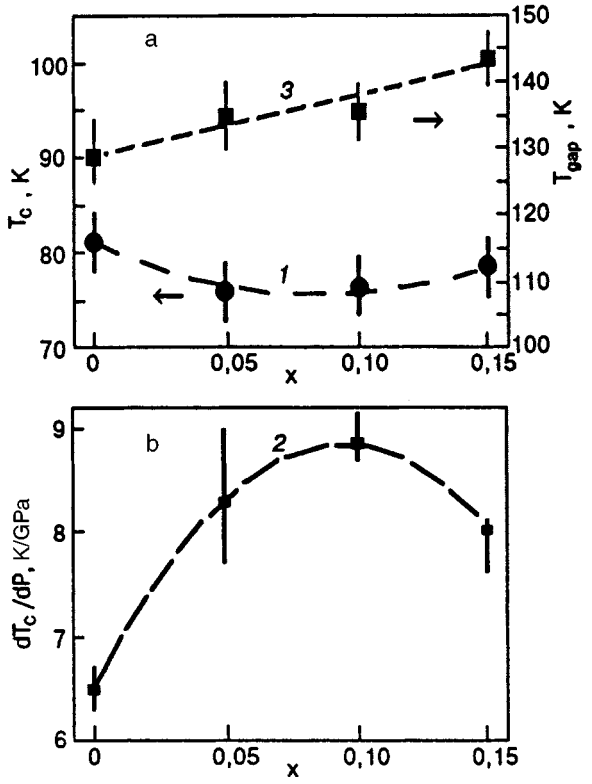

FIG. 4. Dependences $T_c(x)$ and $T_{gap}(x)$(a), and the dependence $(dT_c/dP)(x)$(b).

ergy spectrum of electrons) due to a change in the number of carriers upon replacement of yttrium or copper.[1)] The electron transition may be caused directly by the change in the number density of carriers associated with the valency of the substituent element or, which is less likely, by a distortion of the crystal lattice as a result of substitution or an external mechanical agency affecting the electron energy spectrum, or by both these factors simultaneously.

The effect of pressure on the superconductivity of systems of various compositions can be analyzed conveniently by studying the T_c vs. $d\ln T_c/d\ln V$ dependence. For the system investigated by us, this dependence is shown in Fig. 5 (we use the value $B=142$ GPa for the bulk modulus of the 1–2–4 system).[14] The same figure also shows the data corresponding to the 1–2–4 structure of $Y_{1-x}Ca_xBa_2Cu_4O_{8\pm\delta}$ (Ref. 2) as well as the results for the 1–2–3 structure of $YBa_2(Cu_{1-x}Ag_x)_3O_{7-\delta}$ (Ref. 2) and $Y_{1-x}Pr_xBa_2Cu_3O_{7-\delta}$ (Ref. 1). A considerable difference is observed between the diagrams for the systems 1–2–3 and 1–2–4. The decrease in T_c with increasing $d\ln T_c/d\ln V$ is much slower for the 1–2–4 structures whose composition is far from optimal as shown by the diagram. Strictly speaking, however, the actual value of this difference cannot be determined in the absence of data on the effect of substitution on the compressibility in 1–2–4 systems.

The existing models of high-temperature superconductivity allow a quantitative analysis of the correlation between the values of T_c and $d\ln T_c/d\ln V$ for different atomic substitutions. For the structure 1–2–3, this dependence with a T_c peak is in good agreement with Cyrot's model.[15] Using

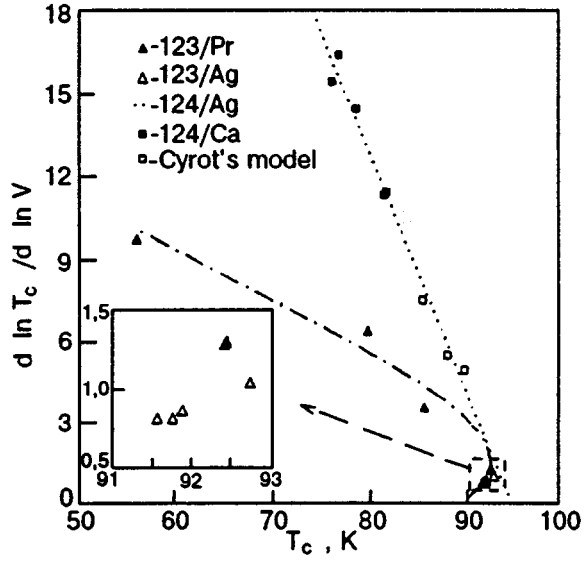

FIG. 5. T_c vs. $d\ln T_c/d\ln V$ diagram for 1–2–3 and 1–2–4 systems with different substituent impurities.

the expression obtained in this model for the transition temperature

$$T_c = t\delta\exp\left(-\frac{U}{t}\delta\right),$$

where t is the hopping integral, δ is the number density of carriers, and U is the Coulomb repulsion energy, neglecting the volume dependence of U, we can obtain for the abovementioned set of data for $YBa_2(Cu_{1-x}Ag_x)_3O_{7-\delta}$ and $Y_{1-x}Pr_xBa_2Cu_3O_{7-\delta}$ quite reasonable values of the derivatives $d\ln t/d\ln V=-0.77$ and $d\ln\delta/d\ln V=5.5$ (corresponding to $\sim 3\%$/GPa). However, the same model gives for the 1–2–4 system [$Y_{1-x}Ca_xBa_2Cu_4O_{8\pm\delta}$ and $YBa_2(Cu_{1-x}Ag_x)_4O_{8\pm\delta}$] a positive(!) value of $d\ln t/d\ln V=+1.5$ and a very large value of the derivative $d\ln\delta/d\ln V=27(\simeq 19\%$/GPa), which apparently suggests a lack of agreement.

Another property of the volume dependence of T_c is obtained from the Labbe–Bok model of a two-dimensional superconducting lattice.[11,12] In this BCS-type model, which explicitly takes into consideration the contribution of the logarithmic singularity to the density of states of the half-filled band, the superconducting transition temperature is defined by the expression

$$T_c = D\exp(-1/\sqrt{\lambda}),$$

where D is the ''width'' of the singularity. The expression for the volume dependence of T_c has the form

$$\frac{d\ln T_c}{d\ln V}=\frac{d\ln D}{d\ln V}+\frac{1}{2\sqrt{\lambda}}\frac{d\ln\lambda}{d\ln V}.$$

The linear relation between $d\ln T_c/d\ln V$ and $\ln T_c$, which follows from these relations

$$\frac{d\ln T_c}{d\ln V}=a_1\ln T_c+a_2;$$

$$a_1 = -\frac{1}{2}\frac{d\ \ln \lambda}{d\ ln\ V}; \quad a_2 = \frac{d\ \ln D}{d\ \ln V} - a_1\ \ln D,$$

holds reasonably well for $YBa_2(Cu_{1-x}Ag_x)_4O_{8\pm\delta}$ and $Y_{1-x}Ca_xBa_2Cu_4O_{8\pm\delta}$ (Fig. 5). However, the very steep slope of the straight line accounts for an extremely strong dependence of the interaction parameter on the volume, which corresponds to $d\ \ln \lambda / d\ \ln V \simeq -(112-143)$ (the spread in this quantity is associated with the choice of the value of the bulk modulus for 1–2–4 between 110 and 142 GPa by different authors.

The linear relation between $d\ \ln T_c / d\ \ln V$ and $\ln T_c$ mentioned above follows from the expression for the transition temperature obtained by Abrikosov *et al.*:[13]

$$T_c = \frac{E}{\mathbf{n}^2}\ \exp(-1/\lambda n),$$

where E is the characteristic electron energy ~ 1 eV; $\mathbf{n} = \nu/\nu_0$, ν is the density of electron states associated with the contribution from the van Hove anomaly, and ν_0 is the ''background'' density of states. Neglecting the volume dependence of E, we obtain the relation $d\ \ln n/d\ \ln V + d\ \ln \lambda / d\ \ln V \simeq (60-70)$ for the relative derivatives which characterize the corresponding volume dependences. Assuming that the main contribution comes from the first component, the large value of $d\ \ln n/d\ \ln V$ could be treated as the result of a very sharp change in the density of states near the singular point. In any case, such an assumption seems to be more justified than the strong dependence of the interaction parameter λ on volume following from a comparison with the Labbe–Bok model. Another indication of the importance of variation of the density of electron states is provided by the above-mentioned correlation between $T_c(x)$ and the distortion parameter. It is known that orthorhombic distortion of a two-dimensional lattice splits the van Hove critical point. The gap between the critical energies, and hence the density of states, becomes extremely sensitive to factors affecting the distortion parameter.[2)] According to our results (Fig. 1), the orthorhombic distortion parameter indeed varies significantly upon replacement of copper in the 1–2–4 system (this was observed earlier also upon replacement of yttrium by calcium[2]). Apparently, this leads to an effective variation in the density of states at the Fermi level. An analogous effect for the case of uniaxial compression of HTS single crystals was observed, for example, in Ref. 8.

Nevertheless, the obtained values of these parameters are hard to explain physically and the quantitative agreement between the above models and the superconducting properties of the 1–2–4 system can hardly be treated as satisfactory.

2. Let us now consider the normal properties of the system under consideration. The curves of the temperature dependence of the normal state resistivity $\rho(T)$ presented in Fig. 2 show that the departure from linearity observed in $YBa_2Cu_4O_{8\pm\delta}$ (Ref. 4) is also preserved in $YBa_2(Cu_{1-x}Ag_x)_4O_{8\pm\delta}$ ($x \leqslant 0.15$). This nonlinearity can be seen clearly upon a numerical differentiation of the data on $\rho(T)$ (Fig. 6). All the $(d\rho/dT)(T)$ curves shown in the figure are characterized by the presence of three well-defined segments corresponding to the rise in the value of $d\rho/dT$ with increasing temperature up to values indicated by arrows in Fig. 6, followed by a region of almost constant value of the derivative and a region of subsequent decrease in $d\rho/dT$ with increasing temperature.

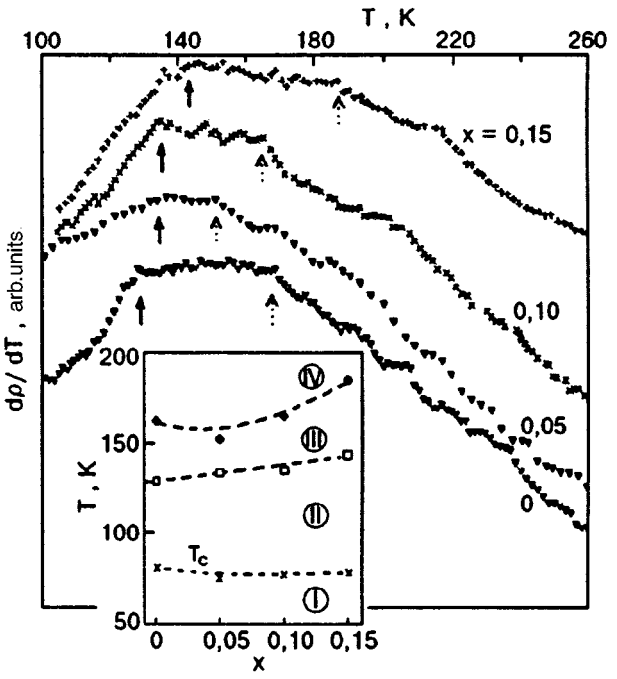

FIG. 6. Temperature dependence of the derivative $d\rho/dT$ of the system $YBa_2(Cu_{1-x}Ag_x)_4O_{8\pm\delta}$. The inset shows the $T-x$ phase diagram.

The existence of kinks (crossover points) on the dependence $\rho(T)$ in the normal conductivity region has already attracted the attention of many researchers. According to the theory proposed by Nagaosa and Lee[6] and based on resonant valence bonds,[9] a spin gap appears in the elementary excitation spectrum of the 1–2–4 system upon a decrease in temperature. This must lead to a decrease in the contribution to the resistance from electron scattering at spin fluctuations and hence to a more rapid decrease in resistance as the temperature falls below the crossover point. The existence of the spin gap is also confirmed by the NMR data.[10] It can be seen clearly from the $d\rho/dT$ curves in Fig. 6 that at the points $T_{gap}(x)$ marked by dark arrows, the regions with increasing derivative are replaced by regions with a nearly constant value of $d\rho/dT$, as indeed must be observed during crossover between states with a spin gap and the region of linear dependence $\rho(T)$ typical of oxide cuprates. Thus it can be assumed that the indicated points correspond to the crossover line in temperature-vs.-carrier density coordinates. According to Ref. 6, the shape of the $T_{gap}(n)$ curve must be related quite definitely to the variation of the superconducting transition temperature $T_c(n)$ as a result of doping, and this correlation must also exist on the T-vs.-x diagram to the same extent to which the number n of charge carriers depends on the degree x of substitution of silver ions for copper. In other words, the increase in T_{gap} with varying x (Fig. 4a) must correspond to a decrease in T_c and vice versa. It can be seen

from Fig. 6 that the value of the crossover temperature increases upon an increase in the silver concentration in samples, and hence the above-mentioned correlation between $T_c(x)$ and $T_{gap}(x)$ is indeed observed, at least for $x \leqslant 0.1$ (see curves *1* and *3* in Fig. 4). Hence the behavior of $T_c(x)$ and $T_{gap}(x)$ in the system $YBa_2(Cu_{1-x}Ag_x)_4O_{8\pm\delta}$ is in accord with the Nagaosa–Lee theory[6] for very low concentration of silver ions.

Finally, it should be mentioned that the linear dependence $\rho(T)$ for $YBa_2Cu_4O_{8\pm\delta}$ (Fig. 6, curve corresponding to $x=0$) is transformed into a dependence with saturated resistance at temperatures above 170 K (these points are indicated by dashed arrows). Such a region of negative curvature was observed in 1–2–4 systems by other authors also (see, for example, Ref. 5). For $x>0$, the $d\rho/dT$ curves in Fig. 6 show that the saturation region for $\rho(T)$ is preserved even as copper is replaced by silver. It should be emphasized that as shown by the $d\rho/dT$ curves, a transition to saturation region from the linear dependence region occurs over a very narrow temperature interval which thus determines the boundary between the linear growth region (III) and $\rho(T)$ saturation region (IV) on the $T-x$ phase diagram (see the inset in Fig. 6, which also shows the superconductivity region (I) and the spin gap region (II)).

CONCLUSIONS

(1) The nonlinear variation of the superconducting transition temperature and its volume derivative observed in the system $YBa_2(Cu_{1-x}Ag_x)_4O_{8\pm\delta}$ is in qualitative accord with the concept that the properties of HTS cuprates are linked with the electronic and topological peculiarities of their spectrum (van Hove anomaly). However, a quantitative comparison of the experimental data on $T_c(x)$ and $(d\ln T_c/d\ln V)(x)$ with the results of a number of calculations of the superconducting properties indicates, unlike the results obtained earlier for the 1–2–3 structure, the absence of any agreement between these experimental results and the models considered.

(2) The nature of nonlinearity of the temperature dependence of the electrical resistivity in the normal state of the 1–2–4 system does not change significantly upon a replacement of copper ions by silver. However, an increase in the temperature of crossover corresponding to the emergence of a spin gap in the system is observed. For a very low degree of substitution, there exists a correlation between the superconducting transition temperature and crossover temperature, as predicted by the Nagaosa–Lee model on the basis of the resonant valence bond model.

(3) Like pure $YBa_2Cu_4O_{8\pm\delta}$, $YBa_2(Cu_{1-x}Ag_x)_4O_{8\pm\delta}$ also displays a transition from linear temperature dependence of resistance to its saturation upon an increase in temperature. This corresponds to the phase diagram in which the region of linear growth of $\rho(T)$ separates the regions of spin gap and resistance saturation.

This research was supported by Grants from the Soros Foundation and INTAS.

*E-mail: kfti@rocket.kharkov.ua

[1)]The spectroscopic data obtained in a recent publication[6] point towards the existence of a van Hove anomaly in the 1–2–4 electron spectrum corresponding to the saddle point on the Fermi surface.

[2)]Naturally, the irregularity in the arrangement of Ag atoms at crystallographic positions Cu1 and Cu2 must cause a blurring of the van Hove singularity. Apparently, this explains the nonlinearity in the dependence $T_c(x)$ even for small values of x.

[1] J. J. Neumeier, M. B. Maple, and M. S. Torikachvili, Physica **C156**, 574 (1988).
[2] V. I. Makarov, V. Z. Kleiner, O. N. Ovcharenko *et al.*, Physica **C219**, 273 (1994).
[3] D. M. Newns, H. R. Krishnamurthy, P. C. Pattnaik *et al.*, Physica **B186–188**, 801 (1993).
[4] B. Bucher, J. Karpinski, E. Kaldis, and P. Wachter, Physica **C167**, 324 (1990).
[5] B. M. Andersson, B. Sundqvist, J. Niska *et al.*, Physica **C170**, 521 (1990).
[6] N. Nagaosa and P. A. Lee, Phys. Rev. **B45**, 966 (1992).
[7] B. Bucher, P. Steiner, J. Karpinski *et al.*, Phys. Rev. Lett. **70**, 2012 (1993).
[8] V. M. Gvozdikov, Fiz. Nizk. Temp. **19**, 1285 (1993) [Low Temp. Phys. **19**, 914 (1993)].
[9] P. W. Anderson, Science **235**, 1196 (1987).
[10] H. Zimmermann, M. Mali, I. Mangelshots *et al.*, J. Less-Common Met. **164–165**, 138 (1990); H. Zimmermann, M. Mali, D. Brinkmann *et al.*, Physica **C159**, 681 (1989).
[11] J. Labbe and J. Bok, Europhys. Lett. **3**, 1225 (1987).
[12] R. Griessen, Phys. Rev. **B36**, 5284 (1987).
[13] A. A. Abrikosov, J. C. Campuzano, and K. Gofron, Physica **C214**, 73 (1993).
[14] J. J. Scholtz, E. N. van Eenige, R. J. Wijngaarden, and R. Griessen, Phys. Rev. **B45**, 3077 (1992).
[15] M. Cyrot, Solid State Commun. **62**, 821 (1987).

Translated by R. S. Wadhwa

Thermal conductivity of anisotropic HTS crystals $YBa_2Cu_3O_{7-x}$ and $Bi_2Sr_2CaCu_2O_{8+y}$

V. B. Efimov and L. P. Mezhov-Deglin

*Institute of Solid State Physics, Russian Academy of Sciences, Chernogolovka, Moscow District, 142432 Russia**

(Submitted April 3, 1995; revised July 9, 1996)
Fiz. Nizk. Temp. **23**, 278–289 (March 1997)

The results of measurements of thermal conductivity κ and resistivity ρ of some superconducting crystals of $YBa_2Cu_3O_{7-x}$ and $Bi_2Sr_2CaCu_2O_{8+y}$ in the ab plane (κ^{ab} and ρ^{ab}) and along the c axis (κ^c and ρ^c) are presented. The magnitudes and temperature dependences of the thermal conductivity of Y- and Bi-crystals are found to be close and to vary less significantly than the resistance of samples of the same composition. In contrast to the predictions of the electron heat transport theory in HTS cuprate crystals, the relative height of the peaks in $\kappa^{ab}(T)/\kappa^{ab}(T_c)$ curves becomes equal to two in highly anisotropic Bi-samples, and the peak is displaced toward lower temperatures $T_m<0.4T_c$ with increasing value of this ratio, as well as in Y-crystals which have a lower anisotropy. All these facts indicate that in theoretical calculations of the thermal conductivity of layered HTS crystals in the ab plane at temperatures below T_c, the possibility of an increase in the electron and the phonon components of thermal conductivity must be taken into consideration, as in calculations of thermal conductivity of perfect crystals of conventional metallic superconductors. In the direction perpendicular to the layers, the thermal conductivity $\kappa^c \ll \kappa^{ab}$ and decreases monotonically with temperature. The contribution from the electron component to κ^c can be disregarded.
 [S1063-777X(97)00403-9]

1. INTRODUCTION

As a superconductor undergoes a transition from the normal state to the superconducting state, the thermal conductivity κ of the sample remains finite, in contrast with, say, the electrical resistivity ρ or thermo-emf. Hence, by measuring the thermal and electrical conductivities, we can estimate the contribution κ_e of the electron component and κ_p of the lattice (phonon) component to the total thermal conductivity of the sample

$$\kappa=\kappa_e+\kappa_p \tag{1}$$

in the normal and the superconducting state. The latter is especially interesting for the case of high-T_c superconductors, since the mechanism of interaction between quasiparticles leading to pairing of charge carriers in HTS materials has not been established unambiguously so far.

The value of κ_e in the normal state, and hence the relation between κ_e and κ_p for $T\geqslant T_c$, can be estimated from the measured value of the electrical resistivity ρ by using the Wiedemann–Franz law:

$$\kappa_e=LT/\rho, \tag{2}$$

where $L=L_0=2.4\times10^{-8}$ W·Ω/K^2 the (Lorentz number) if the electrical and thermal resistance in the electron system are determined by the same elastic scattering of carriers in the bulk. In the case of inelastic scattering, for example, the inelastic electron–phonon scattering or scattering at freshly introduced defects at low temperatures, the coefficient is $L<L_0$ and depends on temperature (see, for example, Ref. 1).

According to Coleman *et al.*,[2] at least two different transport relaxation times associated with electron excitations are observed in HTS cuprates at $T\sim T_c$: the electrical current attenuation is dominated by rapid relaxation processes, while ''neutral currents'' like Hall current and thermal flux are controlled by slow processes. Hence the estimate (2) cannot claim a higher than order-of-magnitude accuracy.

If the relation between κ_e and κ_p in the normal state at $T\geqslant T_c$ is known, a comparison of the experimental dependence $\kappa(T)$ in the superconducting state with the temperature dependences following from various theoretical models of heat transport in HTS crystals can lead to definite conclusions about the applicability of a certain model, and hence about the peculiarities in the interaction between quasiparticles in HTS cuprates.

We shall discuss the results of our measurements of the thermal and electrical conductivities of some relatively perfect crystals of $YBa_2Cu_3O_{7-x}$ and $Bi_2Sr_2CaCu_2O_{8+y}$ with a

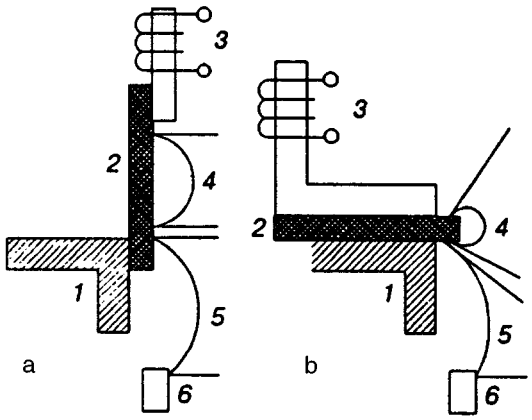

FIG. 1. Schematic diagram for measurements of the thermal conductivity of crystals in the ab plane (a) and in the c-direction (b); sample (*1*), heater (*2*), copper cold duct (*3*), thermocouples (*4, 5*), and Ge or Pt reference thermometer (**6**).

TABLE I. Basic parameters of $YBa_2Cu_3O_{7-x}$ samples whose $\kappa(T)$ curves are presented in Figs. 2 and 6.

Sample (curve No.)	Direction of measurements	Characteristic size, mm	T_c, K	ΔT, K	κ(120 K), W/(m·K)	ρ(120 K), mΩ·cm	κ_e(120 K), W/(m·K)
Y-21 (*1*)	*ab*-plane	1.70×0.94×0.030	92.5	0.5	7.3	0.07	4.2
Y-25 (*2*)	*ab*-plane	1.65×1.00×0.135	92.5	2	11.0	0.26	1.1
(2^c)	*c*-axis	-"-	-	-	3.2	10.6	0.027
Y-cer [6] (*3*)		20.0×2.0×2.5	90.5	3	4.3	0.44	0.66
Y [7] (κ^a)	*a*-axis	0.6×0.6×0.025	90.5	~1	10.2	-	-
(κ^b)	*b*-axis	-"-	-	-	14.9	-	-
Y [8] (κ^{ab})	*ab*-plane	10×2×1	90.5	-	10.9	-	-

transition temperature $T_c > 82$ K in the temperature interval 10–150 K. A distinguishing feature of our research is that the entire cycle of measurements of thermal conductivity and resistance in the cuprate *ab*-plane (κ^{ab} and ρ^{ab}) and along the *c*-axis at right angles to it (κ^c and ρ^c) was completed on the same sample, which is quite significant in view of the large spread in the values of electrical conductivity of HTS crystals even for samples taken from the same batch. The directions of the heat flux and electrical current coincided during measurements of κ and ρ, thus enabling us to eliminate systematic errors in estimates of the relation between κ_e to κ_p which creep because of a strong anisotropy of the crystals and are unavoidable in measurements of κ and ρ in different samples.

Crystals of $YBa_2Cu_3O_{7-x}$ were grown at the Institute of Solid State Physics, Russian Academy of Sciences.[3] The $Bi_2Sr_2CaCu_2O_{8+y}$ crystals were grown at the Moscow Institute of Steel and Alloys.[4] Some of the results of measurements of the properties of Bi crystals in the *ab*-plane were reported in our earlier publication.[5]

2. EXPERIMENTAL PROCEDURE

The measuring technique for thermal conductivity of crystals in the *ab* plane and along the *c* axis is shown schematically in Fig. 1. The resistance measurements were carried out by using the standard four-point potentiometer technique in a constant current. The contact areas were formed on the sample by applying silver paste, and copper leads 50 μm in diameter were attached to them.

The thermal conductivity was measured by the steady-state heat flux technique. The temperature difference along the crystal was measured by a chromel–constantan thermocouple. An identical thermocouple was used for measuring the temperature difference between the sample and the platinum or germanium thermometers attached to the sample. The use of chromel–constantan thermocouples with a wire 12 μm in diameter set a lower limit $T > 10$ K on the range of thermal conductivity measurements. The thermocouples and the heater were attached to the sample by IBM lacquer which has a very high thermal conductivity and can be easily removed in a solution consisting of equal amounts of methanol and toluene. The same adhesive was used for attaching the sample to the cold finger. This made it possible to remount the sample during investigations and to carry out the entire cycle of measurements on the same sample.

Initially, we measured the resistance in the *ab*-plane and determined the superconducting transition temperature T_c. After this, the temperature dependence of the resistivity ρ^c along the *c* axis was measured in some samples. The sample was then remounted for measuring thermal conductivity in the *ab* plane. Finally, the setup was changed for measuring thermal conductivity along the *c*-direction. As a rule, the sample could not be removed without damage after all these measurements.

3. RESULTS OF MEASUREMENTS

Tables I and Tables II show the main parameters characterizing the properties of the investigated samples.

The temperature dependences of the thermal conductivity κ of the samples studied by us are presented in Figs. 2 and 3 on logarithmic scale. The insets show the same dependences on linear scale. The results of measurements of the resistivity $\rho(T)$ of the same samples are presented in Figs. 4 and 5.

The light triangles *1* and squares *2* in Fig. 2 show the dependences $\kappa^{ab}(T)$ of Y-21 and Y-25 crystals (see Table I)

TABLE II. Basic parameters of $Bi_2Sr_2CaCu_2O_{8+y}$ samples whose $\kappa(T)$ curves are presented in Figs. 3 and 7.

Sample (curve No.)	Direction of measurements	Characteristic size, mm	T_c, K	ΔT, K	κ(120 K), W/(m·K)	ρ(120 K), mΩ·cm	κ_e(120 K), W/(m·K)
Bi-6 (*1*)	*ab*-plane	0.96×0.58×0.016	89	3.5	15	0.63	0.47
Bi-4 (*2*)	*ab*-plane	2.00×0.59×0.050	86	1.5	10.5	0.22	1.3
(2^c)	*c*-axis	-"-	-	-	1.25	-	-
Bi-3 (*3*)	*ab*-plane	2.3×1.20×0.020	82	4	5.4	0.28	1.05
(3^c)	*c*-axis	-"-	-	-	1.08	-	-
Bi-cer [10] (*6*)		20.0×2.0×2.5	105	3	1.52	1.47	0.16
Bi [12] (*4*)	*ab*-plane	-	-	-	~5.1	~0.11	~2.6
Bi [11] (*5*)	*ab*-plane	2×1×0.01	89	-	~5.5	~0.18	~1.6

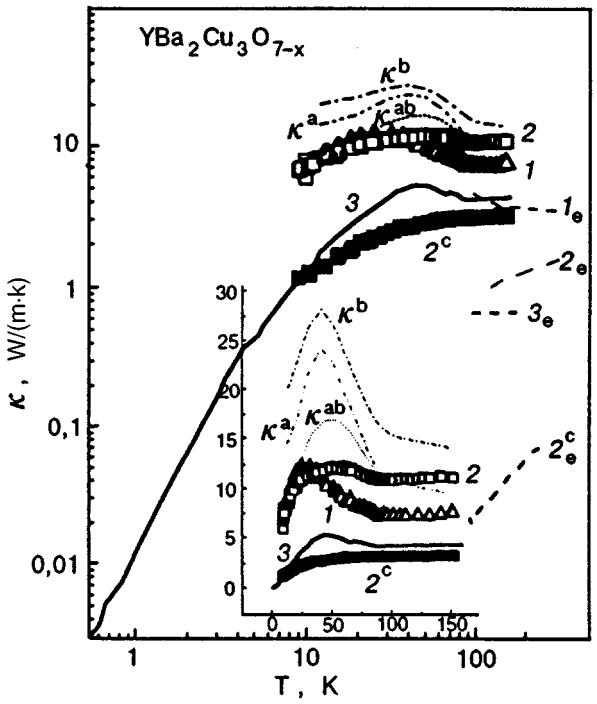

FIG. 2. Temperature dependences of thermal conductivity of $YBa_2Cu_3O_{7-x}$: samples Y-21 (curve *1*) and Y-25 (curve *2*) in the ab-plane and Y-25 (curve 2^c) in the c-direction. The curves κ^a, κ^b, and κ^{ab} are plotted according to the results obtained in Refs. 7, 8, curve *3* corresponds to the results of measurements for the ceramic.[6] Dashed curves 1_e, 2_e, 2_e^c, and 3_e correspond to contributions to the thermal conductivity of the electron component for Y-21 and Y-25 crystals and the ceramic, calculated from the results of electrical conductivity measurements.

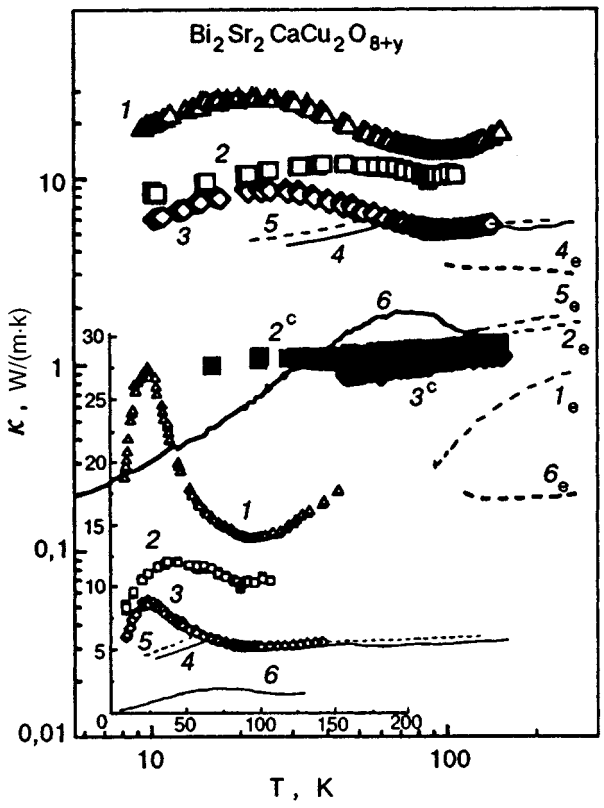

FIG. 3. Temperature dependences of thermal conductivity of $Bi_2Sr_2CaCu_2O_{8+y}$: samples Bi-6 (curve *1*), Bi-4 (curve *2*), and Bi-3 (curve *3*) in the ab-plane, and Bi-4 (curve 2^c) and Bi-3 (curve 3^c) in the c-direction. Curves *4* and *5* are plotted according to the results obtained in Refs. 11, 12, curve *6* corresponds to the results of measurements for the ceramic,[10] dashed curves 1_e, 2_e, 4_e, 5_e, and 6_e correspond to contributions to the thermal conductivity of the electron component for *1, 2, 4,* and *5* crystals and the ceramic respectively, calculated from the results of electrical conductivity measurements.

in the ab plane. The thermal conductivity $\kappa^c(T)$ of the sample Y-25 at right angles to the ab plane is shown by dark squares 2^c. The solid curve *3* was plotted for a ceramic sample from the data of Ref. 6. The dashed curves 1_e, 2_e, 2_e^c, and 3_e describe the electron component contribution to the measured thermal conductivity of the samples, determined from the known value of the electrical conductivity of samples along the same direction as per formula (2).

To complete the picture, the data available in literature on the thermal conductivity of samples with maximum values of κ^{ab} below T_c are also presented in Fig. 2. The dot-dashed curves show the temperature dependence of the thermal conductivity of a crystal studied in Ref. 7 along the directions a (curve κ^a) and b (curve κ^b) in the ab plane. The dotted curve below these curves describes the thermal conductivity κ^{ab} of the sample, as studied in Ref. 8. It can be seen that in the normal state at $T>T_c$, the thermal conductivity of our samples is close to that of the best crystals investigated earlier. However, the maximum value of the thermal conductivity of our samples is slightly lower, and the peaks T_m are displaced toward lower temperatures.

The spread in the values and thermal conductivities $\kappa^{ab}(T)$ of our samples is much smaller than the difference in the behavior of their resistivity $\rho^{ab}(T)$ (Fig. 4), and hence of the electron component $\kappa_e^{ab}(T)$ of thermal conductivity, described by Eq. (2). Unfortunately, it is not possible to compare the relation between the total thermal conductivity and the contribution from the electron component for crystals at $T>T_c$ obtained by other authors[7,8] since no information is available about the magnitude and temperature dependence of the electrical resistance of these samples in the same direction.

The behavior of the thermal conductivity of the Y-25 crystal along the c axis (curve 2^c) is in accord with the available data in the literature.[9] It should be also observed that the temperature dependence of the thermal conductivity κ^{cer} of the molten ceramic (curve *3*) is close to the dependence $\kappa^{ab}(T)$ of crystalline samples. Consequently, the main contribution to the thermal conductivity in a homogeneous molten ceramic consisting of arbitrarily oriented microcrystals comes from heat transport in the ab plane.

Figure 3 shows the temperature dependence of the thermal conductivity of Bi samples in the ab plane (curves *1- 3* for samples Bi-6, Bi-4 and Bi-3, respectively) and along the c axis (curves 2^c and 3^c for samples Bi-4 and Bi-3, respectively). The solid curve *6* is reproduced from our earlier publication[10] and describes the thermal conductivity of a molten ceramic Bi sample with $T_c=105$ K. The dashed curves 1_e, 2_e and 6_e correspond to theoretical dependences of the electron thermal conductivity component $\kappa_e(T)$ for the same sample.

The data on thermal conductivity of Bi crystals are much

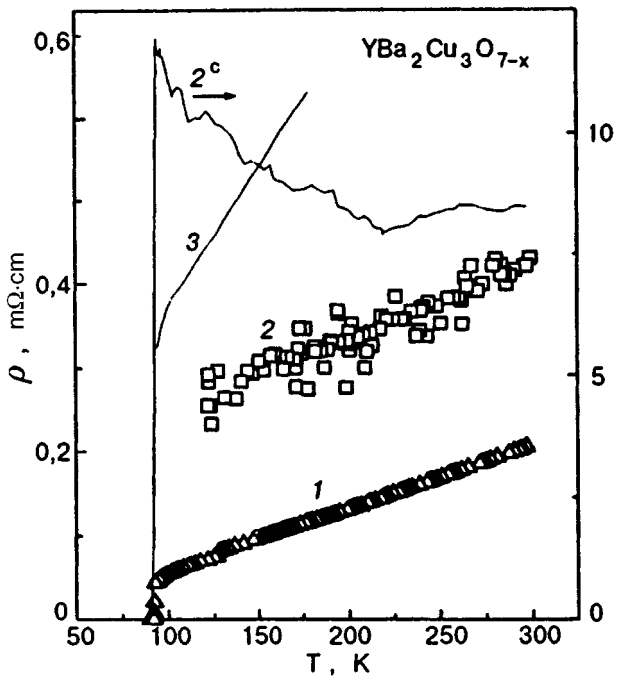

FIG. 4. Temperature dependences of resistivity of Y-samples. Notation is the same as in Fig. 2 and in Table I.

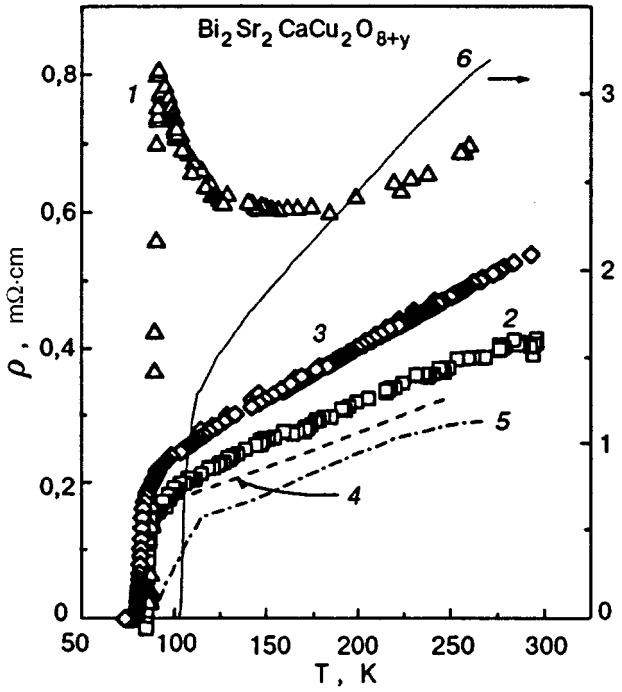

FIG. 5. Temperature dependences of resistivity of Bi-samples. Notation is the same as in Fig. 3 and in Table II.

more scarce in the literature. Hence, to complete the picture, Fig. 3 shows the dependences $\kappa^{ab}(T)$ for crystals investigated in Refs. 11 and 12 (curves *4* and *5*, respectively). The electron component $\kappa_e^{ab}(T)$ of thermal conductivity of the same crystals, calculated by us from the data presented in the same works, are shown by dashed curves 4_e and 5_e, respectively.

The temperature dependences of the electrical resistivity of Y- and Bi-samples in ab plane and along the c axis are shown in Figs. 4 and 5, respectively. The notation on the plots is the same as in Figs. 2 and 3 and in Tables I and II. The large spread in the magnitude and temperature dependences $\rho^{ab}(T)$ of crystals having the same composition may be due to a slight difference in the degree of doping of samples with oxygen (the spread in the values of T_c does not exceed a few degrees) or to different degrees of perfection of crystals. As a rule, thinner crystals are found to be more perfect. The temperature dependence of the resistivity ρ^{ab} of perfect HTS crystals at $T>T_c$ is close to metallic dependence: $\rho^{ab}(T) \propto T$. The resistance of the less perfect crystals depends weakly on temperature, or even increases in the vicinity of T_c (semiconductor-type conductivity).

The lack of correlation between the dependences $\rho^{ab}(T)$ and $\kappa^{ab}(T)$ for samples of the same composition may be due to a change in the electron structure of the crystal as a result of uncontrollable variation in the oxygen concentration, or to different efficiencies of scattering of normal electron excitations and phonons at the same microscopic defects like charged impurities in the bulk of the sample. The difference in the anisotropy of thermal and electrical conductivities along the a and b axes in the ab plane may turn out to be quite significant in different samples. Hence, while discussing the peculiarities in the behavior of the electron (κ_e) and lattice (κ_p) components of thermal conductivity and comparing theoretical predictions with the experimental results, care must be taken to ensure that the experimental data pertain to the same sample and even have the same direction of heat flux and electric current in highly anisotropic crystals.

4. DISCUSSION OF EXPERIMENTAL RESULTS

4.1. Thermal conductivity of crystals in the *ab* plane

As the HTS samples undergo a transition from the normal state to the superconducting state, the slope of the curve $\kappa^{ab}(T)$ changes abruptly: below T_c, the thermal conductivity increases with decreasing temperature and passes through a maximum. This can be seen quite clearly in Figs. 6 and 7, in which the temperature dependence of thermal conductivity is plotted in normalized coordinates $\mathrm{K}^{ab}(t) = \kappa^{ab}(t)/\kappa^{ab}(T_c)$, where $t=T/T_c$. The curve numbers and notation of the points are the same as in Figs. 2 and 3. The dashed curves 1_e–4_e show the relative contribution from the electron component to the total thermal conductivity above T_c, i.e, the ratio

$$\mathrm{K}_e(t)=\kappa_e(T)/\kappa(T_c)=L_0T/\rho\kappa(T_c). \tag{3}$$

Normalized coordinates are used frequently for comparing theoretical results with the results of measurements. A transition to normalized coordinates makes it possible to eliminate systematic errors in the absolute values of κ and ρ which inevitably creep in during experiments with small samples, as well as in estimates of numerical factors in theoretical computations of the kinetic coefficients of crystals.

It can be seen from Figs. 6 and 7 that in all Y-samples, the electron component $\mathrm{K}_e(t) \leqslant 0.5\mathrm{K}(t)$ in the normal state

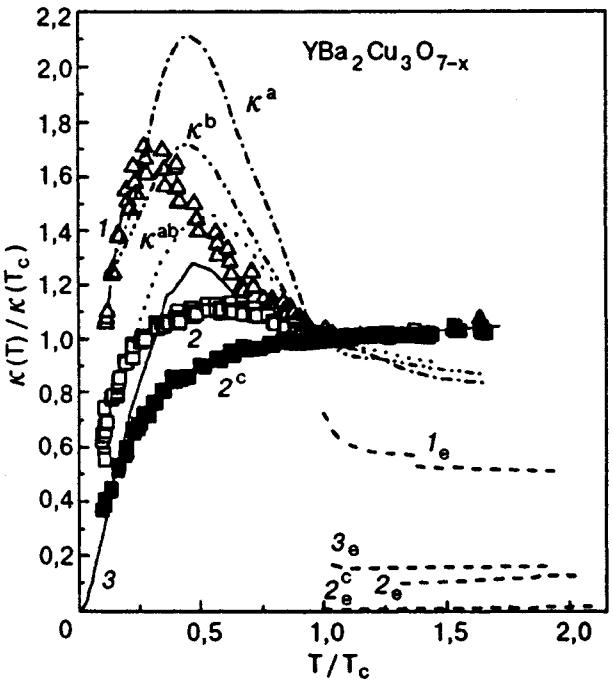

FIG. 6. Temperature dependences of thermal conductivity of Y-samples in reduced coordinates. Notation is the same as in Fig. 2.

for $t>1$. In other words, the lattice component $K_p(t) \geqslant K_e(t)$ for $t>1$. With the exception of sample 4 from Ref. 11, $K_p \gg K_e$ for all Bi crystals. By analogy with the known behavior of thermal conductivity of superconducting crystals of ''dirty'' metals or alloys (see, for example, Refs. 13 and 14), it could be naturally expected that the observed increase in the thermal conductivity $K(t)$ below T_c is associated with the increase in the lattice component: the effective phonon mean free path λ_p increases as a result of

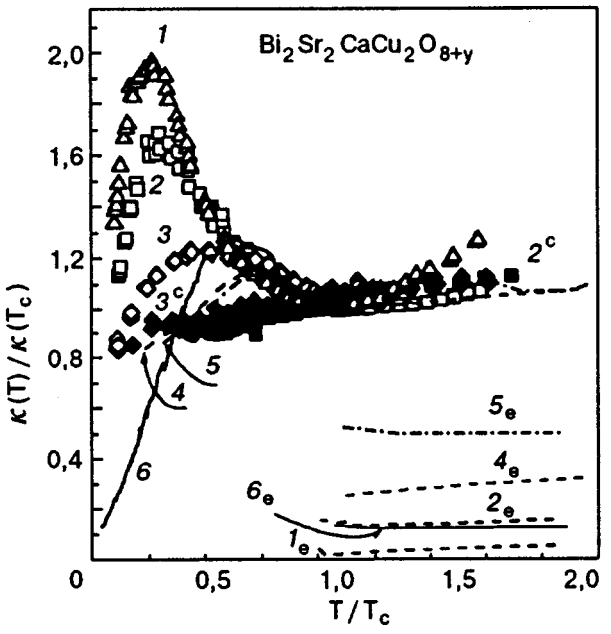

FIG. 7. Temperature dependence of thermal conductivity of Bi-samples in reduced coordinates. Notation is the same as in Fig. 3.

''freezing out'' of normal electron excitations for $t<1$, which confine the largest phonon mean free paths in the bulk of the sample at temperatures above the maximum thermal conductivity point T_m. The electron component K_e of thermal conductivity of dirty metals decreases nearly exponentially for $t<1$.

Such a ''phonon'' approach for explaining the nature of peaks on the $\kappa^{ab}(T)$ curves was used in the review by Uher[9] and has been applied for discussing the experimental results in several current publications (see, for example, Ref. 8).

An alternative (''electron'') approach for explaining the nature of the peaks was first proposed in Ref. 7 following the discovery of a manifold increase in the rf conductivity $\sigma_{\rm rf}$ of a gas of normal electron excitations below T_c in studies of the absorption of electromagnetic microwave radiation in HTS cuprates.

It was assumed in Ref. 7 that the increase in thermal conductivity in the superconducting state is due to a manifold increase in the electron component

$$\kappa_e(T)=\sigma_{\rm rf}L_0T \quad \text{at} \quad T<T_c. \tag{4}$$

Hence it was concluded in Ref. 7, and later in Refs. 12 and 15 also, that the electronic properties of HTS cuprates differ considerably from those of conventional metallic superconductors described by the familiar BCS model.[1,13,14] In addition, the strong electron–electron interaction (D-wave pairing) mechanism is more suitable for describing the behavior of $K_e(t)$ and $\sigma_{\rm rf}(t)$ in the superconducting state.

The fundamental difference in the approach used for explaining the nature of peaks in Refs. 7 and 9 shows that a detailed investigation of the relation between phonon and electron components of the thermal conductivity of a crystal in the normal and superconducting states is essential for a proper choice of the model describing correctly the behavior of the kinetic coefficients of HTS crystals. We shall consider this approach in greater detail.

4.1.1. The phonon hypothesis

As was done earlier in Ref. 9, we assume that the thermal conductivity of a sample is defined as $\kappa=\kappa_p+\kappa_e$. The thermal resistivity $W_p \equiv \kappa_p^{-1}$ for the phonon subsystem and $W_e \equiv \kappa_e^{-1}$ for the electron subsystem is the result of scattering of quasiparticles by one another, impurities, and defects in the bulk, as well as by the grains on the surface of the polycrystalline sample[1]:

$$W_p=\kappa_{pp}^{-1}+\kappa_{pe}^{-1}+\kappa_{pi}^{-1}; \tag{5}$$

$$W_e=\kappa_{ee}^{-1}+\kappa_{ep}^{-1}+\kappa_{ei}^{-1}. \tag{6}$$

The dual indices in these formulas point toward the type of quasiparticle and the scattering mechanism (pp stands for phonon–phonon scattering, pe and pi represent phonon scattering by electrons and impurities of various types, respectively, and so on). Upon a transition from normal to superconducting state, the relative concentration n_e of normal electron excitations in the sample decreases rapidly. This leads to a decrease in the second term in (5) and a change in all three terms in (6). In the framework of the BCS model (electron–phonon pairing),[13,14] the thermal conductivity of a ''dirty'' or imperfect metallic superconducting crystal at $T<T_c$ decreases with temperature in proportion to the den-

sity n_e of normal electron excitations, since the heat capacity of a gas of normal excitations $C_e \propto Tn_e$, while the effective mean free path of normal excitations in the bulk $\lambda_{ei}=\text{const}$; i.e.,

$$\kappa_{ei} \sim C_e \lambda_{ei} \sim T n_e \lambda_{ei}. \tag{7}$$

In perfect high-purity metallic crystals, mutual electron–phonon scattering dominates in the vicinity of T_c, and hence the effective mean free path λ_{ep} of normal electron excitations depends strongly on temperature below T_c. We shall discuss the behavior of the electron component in perfect metallic crystals below T_c in the following section. It is assumed under the phonon hypothesis[9] that λ_e in the superconducting state is constant, and hence κ_e decreases with temperature.

The thermal resistance of a metallic crystal lattice in the normal state is mainly determined by phonon–electron scattering the [second term in (5)]. The effective phonon mean free path corresponding to it is $\lambda_{pe} \sim T^{-1}$, so that the value of $\kappa_p \sim \kappa_{pe} \sim C_p \lambda_{pe} \sim T^2$ decreases with decreasing temperature of the crystal above T_c (here, $C_p \sim T^3$ is the lattice heat capacity). In the superconducting state at $T \ll T_c$, the effective phonon mean free path λ_{pe}, which is restricted by scattering at normal electron excitations, increases rapidly, and hence the lattice thermal conductivity κ_{pe} also increases with decreasing temperature:

$$\kappa_{pe} \sim T^2/n_e \sim T^2 \exp(\Delta/T) \sim t^2 \exp(g/t), \tag{8}$$

where Δ is the band gap of the superconductor [for $t \ll 1$, $\Delta(0)=gT_c$]. In superconductors with a weak electron–phonon coupling (BCS model), $g=g_{\text{BCS}}=1.76$.

The exponential increase in κ_{pe} predicted by formula (8) was observed most prominently while studying the thermal conductivity of perfect crystals of pure lead,[16] which is a superconductor with a strong electron–phonon (ep) coupling ($g=\chi g_{\text{BCS}}$, where the multiplier $\chi \sim 1.4$).

It was assumed in Refs. 8 and 9 that the increase in thermal conductivity κ^{ab} of Y-samples below T_c is due to an increase in the phonon component $\kappa^{ab}(T) \sim \kappa_{pe}(T)$. It was also assumed that the remaining terms in (5) and (6) vary weakly. Neglecting the contribution of the electron component, we find from Eqs. (5) and (6) that the thermal conductivity in normalized coordinates $\mathrm{K}(t)$ must increase for $t \ll 1$ as follows:

$$\mathrm{K}(t) \approx \mathrm{K}_{pe}(t) \approx \kappa_{pe}(t)\kappa_{pe}(T_c) \sim t^2 n_e \sim t^2 \exp(g/t), \tag{9}$$

i.e., the value of the parameter g can be estimated from the slope of the curve $\mathrm{K}(t)$. It should be recalled that $\chi=1$ in BCS superconductors with a weak coupling, while $\chi=1.2$–1.4 in superconductors like Nb or Pb with a strong electron–phonon coupling, for which $\Delta=\chi\Delta_{\text{BCS}}$ (and hence $g=\chi g_{\text{BCS}}$).[1,14]

It follows from the computations made in Refs. 9 and 10 that the experimental dependences $\mathrm{K}^{ab}(t)$ of perfect HTS crystals $YBa_2Cu_3O_{7-x}$ (like those shown by dot-dashed curves in Fig. 6) and homogeneous ceramics may be described by expressions of the type (9) under the assumption that the value of χ may vary for different samples in the interval 1.4–1.7.

For such a numerical fitting of theoretical curves $\mathrm{K}(t)$ with the experimental dependences presented in Figs. 6 and 7 (disregarding the change in the electron component contribution), the numerical values of the parameter χ for Bi- crystals will be $\geqslant 2$, i.e., slightly higher than the values $\chi \sim 1.7$ obtained earlier for the best Y-crystals. A separate theoretical analysis is required to study the possibility of a nearly 1.5-fold increase in the cofactor χ as compared to metals with a strong electron–phonon coupling in the electron–phonon pairing model for carriers.

While discussing the peculiarities of the behavior of lattice component, mention must also be made of the article by Bondarenko *et al.*,[17] in which they discuss the effect of phonon spectrum peculiarities in layered superconductors on the temperature dependence $\kappa_p(t)$ in a wide temperature range.

The maximum values of the normalized thermal conductivity $\mathrm{K}(t)$ of the best Y-crystal investigated by us (curve *1* in Fig. 6) are close to the thermal conductivity of the crystal[7] in the *a*-direction, or of the sample studied in Ref. 8. However, the peak is displaced toward lower temperatures. In the phonon approximation, this can be attributed to a higher concentration of point defects in our crystals.

In contrast, the maximum values of thermal conductivity of the Bi-crystals investigated by us are several times the values available in the literature,[11,12] and the position of the peak T_m is displaced toward lower temperatures with increasing relative height of the peak $\mathrm{K}(t)$ (Fig. 7). This may be due to a lower concentration of extended defects like dislocations or twin boundaries in our samples, which might confine the maximum values of the phonon mean free path in the bulk for small values of n_e.

4.1.2. The electron hypothesis

Let us first discuss the behavior of thermal conductivity of Y-crystals. It is assumed in Ref. 7 that peaks on the κ^{ab} curves emerge as a result of multiple increase in the electron component below T_c. It is significant that while constructing the ''experimental curves'' $\kappa_e(T)/\kappa_e(T_c)$ by measuring the thermal conductivity of Y-crystals along the directions *a* and *b* in the *ab* plane, the authors of Ref. 7 assumed that below T_c, the phonon component κ_p is nearly constant, or decreases monotonically like the thermal conductivity of crystals in the *c*-direction (see curves with index *c* in Fig. 3 and 4). The values of $\kappa_e^a(T_c)$ and $\kappa_p^b(T_c)$ were determined from the difference $\kappa_p(T_c)=\kappa(T_c)-\kappa_e(T_c)$. The electron components $\kappa_e^a(T_c)$ and $\kappa_e^b(T_c)$ were calculated with the help of formula (2) using the data available in literature on the resistivity of perfect Y-crystals along *a* and *b* directions.

The ''experimental curves'' $\kappa_e(T)/\kappa_e(T_c)$ constructed in this way are in fairly good accord with the theoretical dependences $\kappa_e = T\sigma_{\text{hf}}(T)/T_c\sigma_{\text{hf}}(T_c)$, where $\sigma_{\text{hf}}(T)$ is the conductivity of a gas of normal excitations in a given direction in the *ab* plane according to the results of high-frequency measurements.[18] This leads to the conclusion that the electron component κ_e^{ab} in the superconducting state increases manifold upon a decrease in temperature, and hence neither the temperature dependence, $\kappa^{ab}(T) \propto \kappa_e(T)$, nor the

dependence $\sigma_{\rm hf}(T)$, can be described by the BCS model, and the strong electron–electron ($e-e$) interaction (D-wave pairing) is preferred.

However, one cannot be certain about the possibility of neglecting the variation of the phonon component in calculations of $\kappa_e(T)$, as well as the accuracy in the estimation of κ_e from the results of measurements of dc resistance above T_c and rf conductivity below T_c, which were carried out in other samples. It can be seen from Figs. 2 and 6 that the relation between κ_e and κ_p may vary sharply from one sample to another even if they belong to the same batch. For example, $\kappa_e \approx \kappa_p$ below T_c for the sample Y-21, while $\kappa_e \sim 0.1\kappa_p$ for the sample Y-25. If we assume, in accordance with Ref. 7, that $\kappa_p = \text{const}$ below T_c, peaks can emerge on the curves $\kappa^{ab}(T)$ only if the ratio $\kappa_e(T)/\kappa_e(T_c)$ at the peak increases in both samples to about thrice its value, irrespective of the magnitude and temperature dependence of $\rho^{ab}(T)$ in the normal state, which seems to be quite unlikely.

Moreover, the results of measurements of thermal Hall effect made in Ref. 19 on analogous Y-crystals show that $\kappa_e^{ab} \sim 0.1\kappa_p^{ab}$ near T_c as in our sample Y-25. At the thermal conductivity peak ($T_m \sim 0.4T_c$), the ratio $\kappa_e(T_m)/\kappa_e(T_c) \sim 6$, but the phonon component also increases below $T_c[\kappa_p(T_m)/\kappa_p(T_c) \sim 1.3]$. Although the electronic component of thermal conductivity increases much more rapidly that the phonon component, the value of κ_p near T_m is more than twice the value of κ_e. Obviously, the increase in the phonon component cannot be disregarded in calculations of thermal conductivity of Y-crystals in the ab plane under these conditions.

The increase in the electronic component of thermal conductivity of a superconductor below T_c does not contradict the predictions of the BCS model,[13,14] as was assumed in Ref. 7. For example, it was shown in subsequent computations[20] that the ratio $\kappa_{ep}(T)/\kappa_{ep}(T_c)$ in pure metals with a weak electron-phonon coupling increases by a factor of about 2.4 as the temperature decreases to $0.3T_c$. The value of κ_{ep} decreases only as a result of an exponential decrease in the concentration n_e of normal electron excitations. The increase in κ_{ep} in metallic superconductors in the vicinity of T_c indicates that the effective mean free path λ_{ep} of normal electronic excitations, which was restricted in the normal state by scattering of carriers at phonons in the bulk of an ideal crystal and hence increases as $\lambda_{ep} \propto T^{-3}$, increases much more rapidly than n_e^{-1} upon a transition to the superconducting state right up to $T \sim 0.3T_c$ (scattering can occur only at phonons with an energy higher than the superconducting gap).

It was mentioned in the introduction that the effective mean free paths λ_{ep} of carriers in pure metals, which determine the behavior of thermal conductivity (momentum relaxation is significant as well as the energy relaxation), may turn out to be much smaller than the transport mean free paths λ_{ep}, which determine the behavior of electrical conductivity (momentum relaxation[1]). In this case, the parameter L appearing in Eq. (2) is much smaller than L_0 and depends on temperature. For HTS crystals, it is even more important to determine the range of applicability of the Wiedemann–Franz–Lorentz relation for calculating κ_e from resistivity measurements. It was mentioned in Ref. 2 that Y-crystals with a metal-type conductivity $\rho^{ab} \propto T$ above T_c display two different transport relaxation times for charge carriers which differ not only in magnitude, but also in their temperature dependence (in ep scattering in a metal, the relaxation time determining electrical conductivity is smaller than the time characterizing the Hall current or heat flux). The reason behind this phenomenon has not been established unambiguously. The assumption that the relaxation in both cases is determined by the peculiarities of mutual interaction of quasiparticles (ep or ee interaction) raises a whole range of questions: which relaxation time determines the behavior of κ_{ep} (or κ_{ee} in the normal state)? How does the interaction of normal electronic excitations with phonons (or with one another) vary as the superconductor is cooled below T_c? How significantly does the behavior of $\kappa_{ep}(T)$ below T_c depend on the variation of the temperature dependence $\rho^{ab}(T)$ in samples of nearly identical composition for $T > T_c$? The answers to these questions may considerably influence the choice of the model (ep or ee interaction) suitable for describing the observed dependence $\kappa^{ab}(T)$, i.e., the nature of the interaction leading to pairing of carriers below T_c.

A specific mechanism of electronic heat transport in HTS cuprates, viz., heat transport by Bose-type collective electron modes (acoustic plasmons) formed in the crystal below T_c was proposed in Ref. 21. In order to determine the applicability of this model for describing the observed dependences $\kappa^{ab}(T)$ in Y- and Bi-crystals, we must find out how the variations in the magnitude and dependences of $\rho^{ab}(T)$ affect the properties of acoustic plasmons.

The peculiarities of the thermal conductivity of $Bi_2Sr_2CaCu_2O_{8+y}$ crystals have not been studied so intensively. It follows from variational computations[15] of the electronic thermal conductivity of anisotropic HTS crystals (the ee interaction was considered for the case of S- or D-wave pairing) based on the conclusions drawn in Ref. 7 and the results of measurements made in Refs. 11 and 12 that for the same concentration $N \sim 0.05-0.1$ of ionized impurities in the bulk, the maximum values of the ratio $\kappa_e(T)/\kappa_e(T_c)$ must be smaller in Bi-crystals with a higher anisotropy ($\sim 1.5-2.5$) than in Y-crystals ($\sim 5-7$), and the peak T_m in Bi-crystals must be displaced toward higher temperatures ($T_m/T_c \sim 0.6-0.7$) as compared to Y-crystals of the same quality ($T_m/T_c \sim 0.4$). As in Ref. 7, the variation of the lattice component was neglected while calculating the total thermal conductivity of the crystal. In other words, it was assumed that $\kappa(T) = \kappa_e(t) + \kappa_p(T_c)$. Taking into account the contribution of κ_p in normalized coordinates $\mathrm{K}(t) = \kappa(T)/\kappa(T_c)$, the theoretical values of the peaks on the curves $\mathrm{K}(t)$ in Bi-crystals ($\mathrm{K}(t_m) \sim 1.3$) were found to be much smaller than for Y-crystals ($\mathrm{K}(t_m) \sim 2$). The calculated peak positions were also displaced accordingly ($t_m \sim 0.6-0.7$ and 0.4). But this is in contradiction with our measurements (Figs. 3 and 7). Curves *4* and *5* in these figures, describing the results of measurements obtained in Refs. 11 and 12, nearly coincide with curve *3* in Fig. 3 above T_c. Hence it is natural to assume that the difference in the behavior of thermal conductivity of different materials below T_c is associated with the degree of their imperfection;

i.e., measurements in Refs. 11 and 12 were made on less perfect crystals.

Using Eq. (2), we obtain $\kappa_e < 0.1\kappa$ for our samples *1* and *2* in Fig. 3. This means that the lattice component $\kappa_e \ll \kappa_p$ dominates in the vicinity of T_c. At the same time, $\kappa_e \sim 0.4\kappa_p$ in sample *5*, while our estimates show that $\kappa_e \sim \kappa_p$ in sample *4*. Moreover, it can be seen from Figs. 3 and 5 that the electrical conductivity of our samples *1* and *2* is just a fraction of the conductivity of samples *4* and *5*. Hence, in the framework of the ''electron hypothesis,'' the multiple increase in the electrical conductivity of the normal component below T_c must be manifested more strongly just in samples *4* and *5*. In order to attribute the peaks on curves *1* and *2* to the increase in the electron component, it should be assumed that the ratio $\kappa_e(T_m)/\kappa_e(T_c) \sim 10$ in sample *2*, and ~ 100 in sample *1*. Obviously, this is much higher than the theoretical estimates.[15] Such a strong disparity between theory[15] and experiment indicates the dominance of the phonon component below T_c (like in the Y-sample in Ref. 19). All the remarks made above about the applicability of the ''electron hypothesis'' only while discussing the thermal conductivity of Y-crystals remain valid.

4.2. Anisotropy in the thermal conductivity of crystals along and at right angles to the cuprate layers

Our measurements show that the thermal conductivity of the Y-25 crystal varies more weakly than the electrical conductivity upon a transition from the plane ab to the direction of the c axis (see Fig. 2), i.e., $\kappa_p^c \gg \kappa_e^c$, and the contribution of the electron component to κ^c can be disregarded in the working temperature interval.

The electrical conductivity anisotropy of Bi crystals is much higher than the thermal conductivity anisotropy. At $T \sim T_c$, the resistivity ρ^c is several orders of magnitude higher than ρ^{ab} (ρ^c is not shown in the figure). The temperature dependences $\rho^{ab}(T)$ and $\rho^c(T)$ also differ radically, thus pointing toward different mechanisms of charge movement in the crystal (band motion in the ab plane and the hopping diffusion of localized carriers along the c axis). This confirms the assumption[9] that the behavior of the thermal conductivity κ^c of HTS crystals at right angles to the cuprate layers is mainly determined by the lattice component κ_p.

Analyzing the results of measurements of thermal conductivity κ^{ab} in the ab plane of Bi samples, the authors of Refs. 12 and 15 concluded that heat transport in the lattice of Bi crystals in the ab plane and along the c axis occurs through incoherently vibrating atoms (Einstein's model applicable for describing transport of heat in highly disordered structures), and not by traveling sound waves (phonon modes), as in ordinary crystals. In this case, the values of κ_p must be essentially reproduced for all samples, irrespective of the orientation of the crystals. However, the observed multiple increase in the lattice component κ_p^{ab} as we go over from samples *3*, *4*, and *5* to samples *1*, and *2* in Fig. 3, as well as the change in κ_p with the orientation of the heat flux, indicates that heat transport in the lattice of these crystals is carried out by phonons whose effective mean free paths $\lambda_p(T)$ may be restricted by mutual scattering, scattering by charge carriers (normal electron excitations), as well as at the ionized impurities and other defects in the bulk of the crystal under investigation.

The absence of correlation in the values of κ and ρ in the ab plane is quite understandable, since the transport mean free paths λ_p of phonons and λ_e of electrons may be restricted by various scattering mechanisms. For example, electrons are strongly scattered by ionized impurities $\lambda_{ei} = \text{const}/n_i$ (n_i is the impurity concentration) while the phonon mean free paths λ_{pi} increase with decreasing temperature upon scattering by the same impurities (point defects) at temperatures below the Debye temperature Θ_D as $(T/\Theta_D)^{-m}/n_i$, where the exponent m tends to 4 for $(T/\Theta_D) \ll 1$ (Rayleigh scattering).

It is natural to assume that the phonon approximation is applicable for describing heat transport in the lattice along the c axis. in contrast with κ^{ab}, the value of κ^c does not change upon a transition of the sample to the superconducting state; i.e., the contribution of phonon–electron interaction to the thermal resistivity of the lattice in the c-direction can be neglected in comparison with the phonon–phonon scattering and scattering by impurities and defects in the bulk of the sample. In the Debye approximation, the lattice thermal conductivity in the c-direction can be estimated by using the relation:

$$\kappa^c \approx (1/3) C_p v_s^2 \tau_p, \tag{10}$$

where $\tau_p^{-1} = \tau_{pp}^{-1} + \tau_{pe}^{-1} + \tau_{pi}^{-1}$; C_p is the heat capacity, v_s is the velocity of sound in the c-direction, and $\tau_{pp}, \tau_{pi} \ll \tau_{pe}$ are the corresponding relaxation times in the phonon system. While the main contribution to the thermal resistance along and across the layers comes from the same scattering mechanism in the bulk, i.e., $\tau_p^{ab} \approx \tau_p^c$, the anisotropy in the thermal conductivity κ_p is due to the anisotropy of the velocity of sound along and across the cuprate layers [according to the data presented in Ref. 22, the ratio v^{ab}/v^c in Y-crystal was $\approx (5.6/3.1) \sim 1.8$ for longitudinal sound and $\approx (3.6-2.3)/2.2 \sim 1.1-1.6$ for transverse sound]. This does not contradict the observed value of the ratio κ^{ab}/κ^c for Y-samples in the normal state. It can be seen from Figs. 2 and 3 that the anisotropy of the lattice thermal conductivity component κ_p in Bi-samples is higher than in Y-samples of the same quality.

Some conclusions concerning the role of different phonon scattering mechanisms in the c-direction can be drawn by comparing the thermal conductivity κ^c of the crystals and the thermal conductivity κ^{cer} of homogeneous ceramic samples (Figs. 2 and 3).

At temperatures for which the contribution to the thermal resistivity κ^{-1} from mutual scattering or scattering of quasiparticles at point defects in the bulk is much larger than the contribution due to scattering at the grain surface of a fine-crystalline sample, the thermal conductivity of a microcrystalline sample can be estimated from the equation

$$\kappa^{\text{cer}} \approx (\kappa^a \kappa^b \kappa^c)^{1/3}, \tag{11}$$

where $\kappa^a \approx \kappa^b \gg \kappa^c$ is the bulk thermal conductivity of an anisotropic crystal in a-, b- and c-directions. This estimate is in good accord with the results of measurements of $\kappa^{\text{cer}}(T)$

at temperatures higher than, or of the order of, the peak point T_m. Equation (11) is not applicable below T_m, when the transport mean free paths of phonons in ceramics with small-size grains are restricted due to scattering at the grain surface (or, say, at the twin boundaries in grains). It can be seen from Figs. 2 and 3 that the thermal conductivity of a ceramic is higher than κ^c at $T>T_m$ and is comparable with the thermal conductivity in the c-direction only when the temperature decreases to $T\leqslant 0.2T_c\sim 0.06\Theta_D$ ($\Theta_D\simeq 300$ K is the Debye temperature of the crystal). Consequently, the effective phonon transport mean free paths in crystals at these temperatures are much longer than the transport mean free paths in a ceramic in the ab plane and along the c axis. Computations of λ_p from known value of κ^c using Eq. (10) give a lower estimate of λ_p.[17] However, it can be estimated even in this approximation that at $T=10$ K($\sim 1/30\Theta_D$), $\lambda_p\simeq 10^{-5}$ cm is much larger than the separation between planes, i.e., is confined from below by scattering at microscopic defects and, probably, phonon–phonon scattering.

5. CONCLUSIONS

A comparison of the results of measurement of thermal conductivity and electrical resistivity of HTS crystals $YBa_2Cu_3O_{7-x}$ and $Bi_2Sr_2CaCu_2O_{8+y}$ with the results of previous experimental and theoretical studies shows that in contrast to the predictions of the theory of electron heat transport in anisotropic HTS crystals,[15] the magnitude and temperature dependence of the thermal conductivity are close over a wide temperature range above and below T_c.

The absence of correlation in the behavior of the thermal conductivity $\kappa^{ab}(T)$ and electrical resistivity $\rho^{ab}(T)$ of samples in cuprate ab planes indicates that while finding the origin of peaks on the curves $\kappa^{ab}(T)$ in the superconducting state, we must take into account the possibility of an increase in both the electronic (κ_e) and phonon (κ_p) components of thermal conductivity as in conventional metallic superconductors.[14,20] Hence the statement[7,15] that the behavior of thermal conductivity κ^{ab} of HTS cuprate crystals below T_c is described quite well by the theory of $e-e$ interaction (S- or D-wave pairing) does not seem to be justified.

The significant difference between the investigated HTS and metallic superconductor crystals lies in that $\kappa_e\leqslant\kappa_p$ for HTS crystals near T_c, while $\kappa_e\geqslant\kappa_p$ for metals. Hence the most important question in determining the relation between κ_e and κ_p in HTS crystals from experimental results or from computation of their electrical resistivity concerns the applicability of the Wiedemann–Franz–Lorentz relations for evaluating κ_e near T_c, where the temperature $T\sim T_c\sim 0.3\Theta_D$, as well as in the region of maximum thermal conductivity, where $T\leqslant T_m\leqslant 0.4T_c\approx 0.1\Theta_D$ (it should be recalled that in pure metals at $T\leqslant 0.1\Theta_D$, the transport relaxation time τ_{ep} appearing in the electrical conductivity is longer than the energy relaxation time of carriers, which determines the behavior of κ_e).[1]

A comparison of the thermal conductivity of crystals with that of molten ceramics (microcrystalline samples) having an identical composition leads to the conclusion that lattice heat transport in the ab plane as well as along the c axis is carried out predominantly by phonons. The effective phonon mean free paths in crystals at low temperatures $T\leqslant 0.2T_c$ are much larger than the characteristic grain size in ceramics and are apparently restricted by scattering at microscopic defects whose concentration between planes is certainly much higher than in the ab plane. In detailed calculations of $\kappa^c(T)$, we must also take into account the peculiarities of phonon–phonon interaction in layered crystals.[17]

We believe that further experimental studies of transport phenomena in more prefect crystals for $T\leqslant T_c$, as well as theoretical computations of the behavior of electron and lattice components of thermal conductivity, taking into account the $e-e$, $e-p$, and $p-p$ interactions in layered HTS crystals at $T<T_c$, appear to be quite promising.

The authors are indebted to G. A. Emel'chenko and A. S. Nigmatullin for kindly supplying the samples, to N. S. Sidorov for help in sample preparation, and to E. Gmelin, B. Veal, A. A. Abrikosov, and E. A. Pashitskii for their interest and useful discussions.

This research was supported in part by DAAD, ISF Foundation (Grant J4K 100), and the HTS Foundation (project ''Real'').

*E-mail: efimov@issp.ac.ru

[1] A. A. Abrikosov, *Fundamentals of the Theory of Metals*, Elsevier, New York (1988).
[2] P. Coleman, A. J. Schofield, and A. M. Tsvelik, Phys. Rev. Lett. **76**, 1324 (1996).
[3] Yu. A. Ossipjan, V. B. Timofeev, and I. F. Scheglov, Physica C **153–155**, 1133 (1988).
[4] A. M. Balashov, E. A. Antonova, A. S. Nigmatullin, and S. T. Karbashev, Sverkhprovodimost': Fiz., Khim., Tekh. **2**, 57 (1989).
[5] V. B. Efimov and L. P. Mezhov-Deglin, Pis'ma Zh. Éksp. Teor. Fiz. **62**, 934 (1995).
[6] V. B. Efimov, A.A. Levchenko, L. P. Mezhov-Deglin, *et al.*, Sverkhprovodimost': Fiz., Khim., Tekh. **2**, 16 (1989).
[7] R. C. Yu, M. B. Salamon, J. P. Lu, and W. C. Lee, Phys. Rev. Lett. **69**, 1431 (1992).
[8] T. Saki, M. Sawamura, S. Awaji, *et al.*, Physica B **194–196**, 2135 (1994).
[9] C. Uher, J. Supercond. **3**, 337 (1990).
[10] V. B. Efimov, L. P. Mezhov-Deglin, S. A. Shevchenko *et al.*, Sverkhprovodimost': Fiz., Khim., Tekh. **4**, 1114 (1991).
[11] M. F. Crommie and A. Zettl, Phys. Rev. B **41**, 10978 (1990).
[12] P. B. Allen, X. Du, L. Mihaly, and L. Forro, Phys. Rev. B **49**, 9073 (1994).
[13] J. Bardin, G. Rickaysen, and L. Tewordt, Phys. Rev. **113**, 982 (1959).
[14] B. T. Geilikman and V. Z. Kresin, *Kinetic and Nonstationary Phenomena in Superconductors* [in Russian], Nauka, Moscow (1972).
[15] M. Houssa and M. Ausloos, Phys. Rev. B **51**, 9372 (1995); Physica C **257**, 321 (1996).
[16] L. P. Mezhov-Deglin, Zh. Éksp. Teor. Fiz. **77**, 734 (1979) [*sic*].
[17] A. V. Bondarenko, O. A. Gavrenko, B. A. Merisov *et al.*, Fiz. Nizk. Temp. **17**, 318 (1991) [Sov. J. Low Temp. Phys. **17**, 165 (1991)].
[18] Kuan Zhang, D. A. Bonn, S. Kamal, *et al.*, Phys. Rev. Lett. **73**, 2884 (1994).
[19] K. Krishana, J. M. Harris, and N. P. Ong, Phys. Rev. Lett. **75**, 3529 (1995).
[20] B. T. Geilikman, V. R. Chechetkin, and M. I. Dushenat, Zh. Éksp. Teor. Fiz. **73**, 2319 (1977) [Sov. Phys. JETP **46**, 1213 (1977)].
[21] È. A. Pashitskii and V. I. Pentegov, Pis'ma Zh. Éksp. Teor. Phys. **60**, 366 (1994); Zh. Éksp. Teor. Phys. **108**, 652 (1995) [JETP **81**, 353 (1995)].
[22] T. I. Kim, J. Kowalewski, W. Assmus, and W. Grill, Z. Phys. B **78**, 207 (1990).
[23] M. Cassart, J. P. Issi, J. Hejtmanek *et al.*, Physica C **259**, 385 (1996).

Translated by R. S. Wadhwa

Magnetooptical effects in ferroelectric materials

I. E. Chupis

*B. Verkin Institute for Low Temperature Physics and Engineering, National Academy of Sciences of the Ukraine, 310164 Kharkov, Ukraine**

(Submitted June 4, 1996; revised July 9, 1996)
Fiz. Nizk. Temp. **23**, 290–295 (March 1997)

An expression for high-frequency susceptibility of a ferroelectric material in a constant magnetic field $\mathbf{H}_0$ parallel to the direction of spontaneous polarization $\mathbf{P}_0$ has been derived. The reflection and transmission of light through the ferroelectric is considered for the normal incidence at the surface (along the normal $\vec{\nu}$ to the surface). It is shown that the polarization plane in reflected light should be rotated through an angle proportional to the product P_0H_0. For $\mathbf{H}_0 \perp \vec{\nu}$, the angle of rotation of the polarization plane of transmitted light is a periodic function of the optical path, its amplitude being proportional to P_0H_0. In the $\mathbf{H}_0 \| \vec{\nu}$ geometry, a weak gyration effect proportional to P_0H_0 is observed in transmitted light, in addition to the Faraday effect. This effect does not depend on the optical path, and is canceled during backward transmission, in contrast with the Faraday effect. The effect is apparently similar to ''magnetopolarization gyration,'' but the estimates give a much smaller magnitude of the effect. The above magnetooptical effects can be observed not only in ferroelectric crystals of any symmetry, but also in insulators in constant electric and magnetic fields. © *1997 American Institute of Physics.* [S1063-777X(97)00503-3]

Magnetooptics of crystals is a well-developed branch of solid state physics. Nonreciprocal optical phenomena, and especially Faraday's effect, were studied extensively in magnetically ordered media in magnetic as well as in electric fields (see, for example, Ref. 1). However, the optical properties of ferroelectric crystals in a magnetic field have been investigated insufficiently, and their existence has not been accepted generally. For example, in a series of publications[2] the observation of a new ''magnetopolarization'' gyroeffect manifested in the rotation of the polarization plane of light propagating along the magnetic field and the optical axis of the crystal through an angle φ proportional to the product of the first powers of electrical polarization $\mathbf{P}_0$ and the magnetic field $\mathbf{H}_0$($\varphi \propto P_0H_0$) was reported. In contrast to Faraday's effect, the double (forward and backward) passage of light compensated for the above-mentioned ''magnetopolarization'' effect. Pisarev[3] noted the controversial nature of the interpretations of the observed effect proposed in Ref. 2 and stated that ferroelectric crystals can exhibit only second-order effects.

In the present research, the high-frequency susceptibility of a ferroelectric material in a magnetic field parallel to the spontaneous polarization is obtained phenomenologically. We analyze the normal incidence of light in a crystal in the cases where $\mathbf{H}_0$ and $\mathbf{P}_0$ are either normal to the surface of the ferroelectric or lie in the surface plane. The rotation of the polarization plane of the reflected line through an angle $\varphi \propto P_0H_0$ is predicted. The angle of rotation of the polarization plane in transmitted light in the case where $\mathbf{H}_0$ and $\mathbf{P}_0$ are parallel to the surface depends on the periodically traversed optical path with an amplitude proportional to the product P_0H_0. In the case where $\mathbf{H}_0$ and $\mathbf{P}_0$ are normal to the ferroelectric surface for the transmitted light, in addition to the Faraday effect, a much weaker rotation of the polarization plane proportional to the product P_0H_0, which is similar to the effect of ''magnetopolarization gyration'' reported in Ref. 2, was also observed. The predicted effects are more general in nature and are possible not only in ferroelectrics, but also in ordinary insulators to which constant electric $\mathbf{E}_0$ and magnetic $\mathbf{H}_0$ fields are applied simultaneously.

In the optical region of the spectrum, the electric polarizability is mainly created by electrons; for this reason, we will henceforth consider only the electron density of the dipole magnetic moment $\mathbf{P}(\mathbf{r})$, which is due to electrons from outer shells which are bound least strongly to the nucleus. The role of ionic skeleton in our model reduces to the creation of an internal electric field as a result of displacement of ions from positions with a symmetry center during a ferroelectric transition. This field deforms the electron shells and leads to the emergence of an equilibrium electron component of the dipole moment $P_0 \propto E_0$. The electron component of the Hamiltonian of an axial ferroelectric crystal (in which z is an easy axis) in a constant external magnetic field H_0 and a varying electromagnetic field $\mathbf{e}$, $\mathbf{h}$ can be written in the form

$$\hat{H}_e = \int \left\{ \frac{C_1}{2}\hat{P}_z^2 + \frac{C_2}{2}(\hat{P}_x^2 + \hat{P}_y^2) - \mathbf{E}\hat{\mathbf{P}} + \frac{a_1}{2}\left(\frac{\partial \hat{P}_z}{\partial x_i}\right)^2 + \frac{a_2}{2}\left[\left(\frac{\partial \hat{P}_x}{\partial x_i}\right)^2 + \left(\frac{\partial \hat{P}_y}{\partial x_i}\right)^2\right] + \frac{\vec{\hat{\pi}}^2}{2f} - \lambda \mathbf{P}[\vec{\hat{\pi}}\mathbf{H}] \right\} dV,$$

$$\mathbf{E} = \mathbf{E}_0 + \mathbf{e}, \quad \mathbf{H} = \mathbf{H}_0 + \mathbf{h}. \tag{1}$$

Here $\vec{\hat{\pi}} = \vec{\hat{\pi}}(\mathbf{r})$ is the operator of the electron momentum

density, and $\mathbf{E}_0 \propto \mathbf{P}_l$, where $\mathbf{P}_l$ is the dipole moment of the ionic skeleton. We assume that the vectors $\mathbf{P}_l$ and $\mathbf{H}_0$ are directed along the easy axis z. It will be shown below that the constants C_1 and C_2 are proportional to the components of reciprocal electron static susceptibility. The last term in Eq. (1) corresponds to the electron polarization energy in the field created by the motion of electrons under the action of magnetic field. It is well known (see, for example, Ref. 4) that an electron moving at a velocity $\mathbf{v}$ in a magnetic field $\mathbf{H}$ creates an effective electric field of strength $\mathbf{E}=(1/c)\times[\mathbf{v}\times\mathbf{H}]$. For this reason, the interaction constant in Eq. (1) has the form $\lambda = v_0(mc)^{-1}$, where m is the effective electron mass, v_0 is the unit cell volume, and c is the velocity of light. The value of the constant f in (1) is of the order of mv_0^{-1}.

The density operators $\hat{\mathbf{P}}(\mathbf{r})$ and $\hat{\vec{\pi}}(\mathbf{r})$ satisfy the commutation relation

$$[\hat{P}_i(\mathbf{r}), \hat{\pi}_k(\mathbf{r}')] = iq\Delta_{ik}\delta(\mathbf{r}-\mathbf{r}'), \tag{2}$$

where $q = e\hbar v_0^{-1}$, and e is the electron charge.

The equilibrium value of the electron polarization P_0 can be determined from the condition of energy minimum corresponding to the operator (1), $P_0 = C_1^{-1}E_0$.

Small deviations from the equilibrium values of $\hat{\mathbf{P}}$ and $\hat{\vec{\pi}}$, which describe the linear response of the system to the electromagnetic field, satisfy the quantum-mechanical equation of motion for the operators which have the following form in the linear approximation:

$$\begin{aligned}
\dot{\hat{P}}_x &= q\hbar^{-1}[f^{-1}\hat{\pi}_x - \lambda(P_0 h_y - H_0\hat{P}_y)],\\
\dot{\hat{P}}_y &= q\hbar^{-1}[f^{-1}\hat{\pi}_y - \lambda(H_0\hat{P}_x - P_0 h_x)],\\
\dot{\hat{P}}_z &= q\hbar^{-1}f^{-1}\hat{\pi}_\hbar,\\
\dot{\hat{\pi}}_x &= -q\hbar^{-1}(C_2\hat{P}_x - a_2\Delta\hat{P}_x - e_x - \lambda H_0\hat{\pi}_y),\\
\dot{\hat{\pi}}_y &= -q\hbar^{-1}(C_2\hat{P}_y - a_2\Delta\hat{P}_y - e_y + \lambda H_0\hat{\pi}_x),\\
\dot{\hat{\pi}}_z &= -q\hbar^{-1}(C_1\hat{P}_z - a_1\Delta\hat{P}_z - e_z).
\end{aligned} \tag{3}$$

Going over in these expressions to Fourier components, we obtain the expressions for high-frequency electrical χ_{ik}^e and magnetoelectric χ_{ik}^{em} susceptibilities defined as

$$P_i(\mathbf{k},\omega) = \chi_{ik}^e(\mathbf{k},\omega)e_k(\mathbf{k},\omega) + \chi_{ik}^{em}(\mathbf{k},\omega)h_k(\mathbf{k},\omega),$$

where

$$\chi_{xx}^e = \chi_{yy}^e = \frac{\overline{\omega_0^2}(\omega_0^2 - g_0^2H_0^2 - \omega^2)}{(\omega^2-\omega_1^2)(\omega^2-\omega_2^2)},$$

$$\chi_{zz}^e = \frac{\overline{\omega_0^2}}{\omega_e^2-\omega^2},$$

$$\chi_{xy}^e = \chi_{yx}^{*e} = -\frac{2i\omega\overline{\omega_0^2}g_0H_0}{(\omega^2-\omega_1^2)(\omega^2-\omega_2^2)},$$

$$g_0 = \lambda q\hbar^{-1} = e(mc)^{-1},$$

$$\chi_{xx}^{em} = \chi_{yy}^{em} = -\frac{g_0^2P_0H_0(\omega^2+\omega_0^2-g_0^2H_0^2)}{(\omega^2-\omega_1^2)(\omega^2-\omega_2^2)},$$

$$\overline{\omega_0^2} = \frac{q^2}{f\hbar^2} = \frac{e^2}{fv_0^2},$$

$$\chi_{xy}^{em} = \chi_{yx}^{*me} = \frac{i\omega g_0P_0(\omega_0^2+g_0^2H_0^2-\omega^2)}{(\omega^2-\omega_1^2)(\omega^2-\omega_2^2)},$$

$$\omega_0^2 = \overline{\omega_0^2}(C_2 + a_2k^2),$$

$$\omega_{1,2} = \omega_0 \pm g_0H_0,$$

$$\omega_e^2 = \overline{\omega_0^2}(C_1 + a_1k^2). \tag{4}$$

In expressions (4), ω_e is the component of oscillations of the polarization component P_z along the easy axis. The excitations of transverse components P_x and P_y of electric polarization in zero magnetic field are also oscillations having the same frequency ω_0. The magnetic field removes this degeneracy (the Zeeman effect), and as a result the electric dipole moment in the spectral branches ω_1 and ω_2 precesses about the direction of the magnetic field in opposite direction, $P_y/P_x = \pm i$. The order of magnitude of the frequency $\overline{\omega_0} \sim (e^2/mv_0)^{1/2}$ for $v_0 \sim 10^{-22}$ cm^3 and $m \sim m_e$ (m_e is the mass of a free electron) is $\overline{\omega_0} \sim 10^{15}$ rad$\cdot$s^{-1}. Setting $\omega = 0$ in χ_{xx}^e and χ_{zz}^e and taking into account the smallness of g_0H_0 as compared to ω_0, we can easily verify that the constants $C_1^{-1} \approx \chi_{zz}^e(0)$ and $C_2^{-1} \approx \chi_{xx}^e(0)$.

Expressions (4) obtained for the high-frequency magnetoelectric (ME) susceptibility naturally differs from the expressions for the ME susceptibility of magnetically ordered media obtained earlier in the frequency and parametric dependence. This difference is not only due to different conditions of the problem (a ferroelectric crystal in a magnetic field in our case and a magnet in an external magnetic field in earlier investigations), but also due to the fact that the ME interaction in our case is of dynamic rather than static origin. This is the ME energy [the last term in (1)] which is scalar, i.e., does not depend on the crystal symmetry. It can be seen from expressions (4) that a constant magnetic field induces in the ferroelectric the ME susceptibility components

$$\chi_{xx}^{em} = \chi_{yy}^{em} \sim P_0H_0, \quad \chi_{xy}^{em} \sim iP_0,$$

as well as the nondiagonal dielectric susceptibility component $\chi_{xy}^e \sim iH_0$.

It is well known that, in general, the electric (**d**) and magnetic (**b**) inductions are connected with the electric (**e**) and magnetic (**h**) fields through the relations

$$d_i = \varepsilon_{ik}e_k + a_{ik}h_k, \quad b_i = \mu_{ik}h_k + a_{ki}^*e_k.$$

In the case under investigation, $\mathbf{P}_0 \| \mathbf{H}_0 \| z$, and these relations have the form

$$\begin{aligned}
d_x &= \varepsilon_1 e_x - i\varepsilon' e_y - \gamma_2 h_x - i\gamma_1 h_y,\\
b_x &= h_x - \gamma_2 e_x - i\gamma_1 e_y,\\
d_y &= i\varepsilon' e_x + \varepsilon_1 e_y + i\gamma_1 h_x - \gamma_2 h_y,\\
b_y &= h_y + i\gamma_1 e_x - \gamma_2 e_y,
\end{aligned}$$

$$d_z=\varepsilon_2 e_z,$$

$$b_z=h_z, \tag{5}$$

where

$$\varepsilon_1=1+4\pi\chi^e_{xx}, \quad \varepsilon_2=1+4\pi\chi^e_{zz}, \quad \varepsilon'=4\pi i\chi^e_{xy},$$

$$\gamma_1=4\pi i\chi^{em}_{xy}, \quad \gamma_2=-4\pi\chi^{em}_{xx}.$$

We will now consider the properties acquired by light incident from vacuum on a semi-infinite medium with induction given by (5).

Using relations (5), we obtain from Maxwell's equations the following dispersion relation for waves in the medium:

$$n^2[\varepsilon_1(n_x^2+n_y^2)+\varepsilon_2 n_z^2]-2\gamma_1^2 n_x^2 n_y^2-2\varepsilon_2(\varepsilon_1-\gamma_1^2)n_z^2 -(n_x^2+n_y^2)[(\varepsilon_1+\varepsilon_2)(\varepsilon_1-\gamma_1^2)+\varepsilon_1\gamma_2^2-(\varepsilon' -\gamma_1\gamma_2)^2]+\varepsilon_2[(\varepsilon_1-\gamma_1^2)^2-\varepsilon'^2]=0. \tag{6}$$

Here $\mathbf{n}=c\omega/\mathbf{k}$. Equation (6) is a special case of a more general dispersion relation for the ME media.[5]

Let us consider the normal incidence of light on the surface of a ferroelectric crystal ($\mathbf{k}\|\vec{\nu},\vec{\nu}$ is the normal to the surface) in different cases.

1. The vectors $\mathbf{P}_0,\mathbf{H}_0$, and the wave vector of an incident wave are directed along the normal to the surface along the optical axis z. In the case of propagation of light along the optical axis, birefringence is observed only in a magnetic field. Let us assume that the incident wave is polarized linearly, and that its electric field is directed along the x axis and has the amplitude A_0. From Eq. (6) we obtain

$$n^2_{1,2}=\varepsilon_1-\gamma_1^2\mp\varepsilon'. \tag{7}$$

In the reflected wave, the electric field components

$$e_x=A\ \exp(-ic^{-1}\omega z), \quad e_y=B\ \exp(-ic^{-1}\omega z)$$

differ from zero. Taking into account the smallness of γ_i and ε', we obtain the following expressions in the approximation linear in P_0 and H_0:

$$A=-A_0\,\frac{(n_0-1)}{(n_0+1)}\left[1-\frac{2i\gamma_1}{n_0^2-1}\right], \quad n_0=\sqrt{\varepsilon_1},$$

$$B=-\frac{iA_0}{(n_0+1)^2}\left\{\frac{\varepsilon'}{n_0}+2i\left[\gamma_2+\frac{\gamma_1\varepsilon'}{n_0(n_0+1)}\right]\right\}. \tag{8}$$

The fact that a light wave reflected in a magnetic field becomes elliptically polarized is familiar.[6] Moreover, it follows from (8) that the polarization plane of reflected light is rotated relative to the plane of incidence through the angle $\overline{\varphi}$, defined as

$$\overline{\varphi}\approx-\frac{2[\gamma_1\varepsilon'+\gamma_2(n_0^2-1)]}{(n_0^2-1)^2}=-\frac{2g_0^2H_0P_0(3\omega^2+\omega_0^2)}{\overline{\omega_0^2}(\omega^2-\omega_0^2)}. \tag{9}$$

In the case of repeated reflection of light, the angle of rotation is doubled, and so on. It should be noted that the uniaxial form of the crystal is immaterial for the obtained effect (and for subsequent analysis), and an equation of the type (9) remains valid for a crystal of any symmetry.

Lyubimov[5] predicted the rotation of the polarization plane of reflected light for media whose symmetry permits the linear ME effect (ME media). The angle of rotation of the polarization plane is proportional to the ME interaction constant, which differs from zero only in crystals with a definite symmetry. Moreover, reflected light in Ref. 5 preserved a linear polarization. In our case, no limitations are imposed on the crystal symmetry, and the ME properties are created by a constant magnetic field and spontaneous polarization P_0, and reflected light acquires elliptic polarization.

For a wave traversing a path of length L in a ferroelectric crystal, we have

$$\frac{e_y}{e_x}=\tan\varphi=\frac{(n_0+1-i\gamma_1)\tan\varphi_0+\gamma_2-i\Delta/2}{n_0+1-i\gamma_1+i(\Delta/2+i\gamma_2)\tan\varphi_0},$$

$$\varphi_0=-\frac{\Delta\omega L}{2c}, \quad \Delta=\varepsilon'/n_0. \tag{10}$$

It follows from (10) that the rotational angle of the polarization plane at the end of the optical path length L is

$$\varphi=\varphi_0+\varphi_{PH}=-\frac{\Delta\omega L}{2c}+\frac{2\gamma_2(n_0+1)+\Delta\gamma_1}{2(n_0+1)^2}. \tag{11}$$

In this expression, the first term is much larger than the second (φ_{PH} is the ME gyration angle for the transmitted light) and is proportional to the ratio L/λ_0, where λ_0 is the wavelength of light. This term is directly proportional to the magnetic field strength ($\Delta\propto H_0$) and describes the well-known Faraday's magnetooptical effect. The second term is proportional to the product P_0H_0 and does not depend on the optical path length. The latter circumstance means that the rotation of the polarization plane of transmitted light through the angle φ_{PH}, as well as the rotation of the polarization plane through the angle $\overline{\varphi}$ [Eq. (9)] upon reflection, occurs near the crystal surface. If light propagates in the opposite direction, while the chosen system of coordinates as well as the directions of $\mathbf{H}_0$ and $\mathbf{P}_0$ remain constant, the value of φ_{PH} changes its sign, while the angle φ_0 of Faraday's rotation preserves its sign. As a result, the contribution of φ_{PH} to the rotation of polarization plane is compensated for upon double passage through the crystal (in the forward and backward directions). The second term in (11) is apparently associated with ''magnetopolarization gyration.'' [2] The method of its measurement in Ref. 2 involved the determination of the difference between the angle of rotation of polarization plane after a single passage and half the angle of rotation as a result of double passage of light.

2. The vectors $\mathbf{P}_0$ and $\mathbf{H}_0$ lie in the plane of the boundary, $\mathbf{k}\|\vec{\nu}\|y$. In this geometry, from Eq. (6) we obtain

$$n_1^2=\varepsilon_1-\gamma_1^2-\varepsilon'^2n_0^{-2}, \quad n_2^2=\varepsilon_2(1-\gamma_1^2\varepsilon_1^{-1}). \tag{12}$$

In zero magnetic field and in the case of spontaneous polarization in the first wave (with the refractive index n_1), only the electric field component e_x differs from zero, while in the second wave (with the refractive index n_2) the only nonzero component is e_z. Spontaneous polarization induces in the second wave a longitudinal electric component which creates a weak elliptical polarization, $e_y=-i\gamma_1\varepsilon_1^{-1}n_2e_z$.

For $H_0 \neq 0$ and $P_0 \neq 0$, all the three electric field components are present in both waves. In the case of a linearly polarized wave with the vector **e** directed along the x axis, the reflected wave acquires a weak elliptical polarization ($e_y \sim i\overline{H_0} P_0^2$), and its polarization plane is turned through an angle $\overline{\varphi} \approx e_z/e_x$,

$$\overline{\varphi} = \frac{2n_2(\gamma_1\varepsilon' + \gamma_2\varepsilon_1)}{\varepsilon_1(n_2+n_1)(n_2+1)(n_1-1)}. \tag{13}$$

This angle of rotation, as well as the angle $\overline{\varphi}$ [Eq. (9)], is proportional to the product P_0H_0 as in the case 1.

Transmitted light also acquires a weak elliptic polarization. The angle φ of rotation of the polarization plane depends periodically on the optical path length. Over distances $L \gg \lambda_0$, we have

$$\varphi = A_L \cos k_1 L,$$

$$A_L = V\sqrt{1+\xi^2+2\xi\cos(k_1-k_2)L},$$

$$V = \frac{n_1(\gamma_1\varepsilon' + \gamma_2\varepsilon_1)}{(\varepsilon_2-\varepsilon_1)\varepsilon_1}, \quad \xi = -\frac{\varepsilon_2+n_1}{n_1(n_2+1)}. \tag{14}$$

The amplitude A_L is modulated in L and is small, $A_L \sim P_0H_0$.

When the light wave propagates in the opposite direction, the value of A_L changes sign, i.e., no rotation of polarization plane is observed in the transmitted light in the case of double passage (in the forward and backward directions).

Thus, in both cases a rotation of the polarization plane in the reflected light through an angle proportional to the product of the first powers of magnetic field and electrical polarization takes place. In the case of multiple reflection, the rotational angle is multiplied accordingly.

In case 1, the rotation of the polarization plane in transmitted light is determined by the Faraday effect [the first term in (11)] and by the ME effect [the second term in (11)], while in case 2, the Faraday effect does not take place, and gyration depends periodically of the optical path length with an amplitude proportional to the product P_0H_0 (14). The magnetooptical effects [(9) and (14)] and the second term in (11) are proportional to magnetic field as well as spontaneous polarization P_0, i.e., are magnetoelectric. Naturally, these effects should be observed not only in ferroelectrics, but also in an insulator in an external electric field $\mathbf{E}_0$. In the latter case, these effects are proportional to the product E_0H_0. It should also be noted that we do not impose any limitations on the crystal symmetry for manifestations of these ME effects. Let us estimate the order of magnitude of these effects.

In Eq. (9), the gyromagnetic ratio $g_0 = e/(mc) = 1.7\times10^7$ GGSE units. Putting $\omega \sim \overline{\omega_0} \sim \omega_0 \sim 10^{15}\text{rad}\cdot\text{s}^{-1}$, far away from resonance we obtain $\overline{\varphi} \sim 10^{-15} P_0H_0$ (H_0 is the magnetic field strength in gauss). For ferroelectric materials for which $P_0 \sim 10^4$ CGSE units (e.g., for a uniaxial $Pb_5Ge_3O_{11}$ crystal studied in Ref. 2), the value of the angle of rotation [Eq. (9)] of the polarization plane upon reflection is $\overline{\varphi} \sim 10^{-11} H_0$ rad. The angle of rotation φ_{PH} (11) and A_L [Eq. (14)] have the same order of magnitude. In fields $H_0 \sim 10^4$ G, the rotational angle is of the order of 10^{-7} rad. At the same time, the first term in (11) (the Faraday effect) is of the order of $\varphi_0 \sim 10^{-7}H_0(L/\lambda_0)$, i.e., is larger than the ME contribution by a factor of $10^4(L/\lambda_0)$. On the other hand, the values of ''magnetopolarization gyration'' in Ref. 2 are of the order of a percent of Faraday's gyration. Thus, our estimates give a much smaller magnitude of the effect than that given in Ref. 2.

Naturally, the closeness of the frequency ω of incident light to the electron frequency ω_0 permits resonant enhancement of the magnetooptical effects under consideration. The frequency dependence of the ME gyration angle φ_{PH} in transmitted light obtained from Eq. (4), (5), (10), and (11) is rather cumbersome. In the vicinity of resonances, when the value of ω is close to ω_i ($\omega < \omega_1$), the frequency dependence of the ME gyration is the same as for Faraday's gyration, i.e., $\varphi_{PH} \sim [(\omega^2-\omega_1^2)(\omega^2-\omega_2^2)]^{1/2}$.

In order to remove the remaining contradictions, it would be expedient to measure the angle of rotation of polarization plane in reflected light or in the geometry corresponding to case 2, in which the Faraday effect is absent and hence does not mask manifestations of weaker ME effects.

The author is grateful to A. B. Beznosov and N. F. Kharchenko for interest to this research and for fruitful discussions.

This research was financed by INTAS Grant No. 94-935.

*E-mail: chupis@ilt.kharkov.ua

[1] R. V. Pisarev, Zh. Éksp. Teor. Fiz. **58**, 1421 (1970) [Sov. Phys. JETP **31**, 761 (1970)]; B. B. Krichevtsev, V. V. Pavlov, and R. V. Pisarev, Zh. Éksp. Teor. Fiz. **94**, 284 (1988) [Sov. Phys. JETP **67**, 378 (1988)].
[2] O. G. Vlokh, Ukr. Fiz. Zh. **26**, 1623 (1981); O. G. Vlokh, I. S. Zheludev, and V. A. Sergatyuk, Izv. Akad. Nauk SSSR, Ser. Fiz. **48**, 1711 (1984); O. G. Vlokh and V. A. Sergatyuk, Doklady Akad. Nauk SSSR **291**, 832 (1986) [Sov. Phys. Dokl. **31**, 980 (1986)].
[3] R. V. Pisarev, Ferroelectrics **162**, 191 (1994).
[4] L. D. Landau and E. M. Lifshitz, *Field Theory* [in Russian], Moscow (1960).
[5] V. N. Lyubimov, Kristallografiya **13**, 1008 (1968).
[6] L. D. Landau and E. M. Lifshitz, *Electrodynamics of Continuous Media* [in Russian], Moscow (1957).

Translated by R. S. Wadhwa

Electron structure of diborides of 3*d* metals

G. E. Grechnev and N. V. Ushakova

*B. Verkin Institute for Low Temperature Physics and Engineering, National Academy of Sciences of the Ukraine, 310164 Kharkov, Ukraine**

P. D. Kervalishvili, G. G. Kvachantiradze, and K. S. Kharebov

Research Institute of Stable Isotopes, 380086 Tbilisi, Georgia
(Submitted July 10, 1996)
Fiz. Nizk. Temp. **23**, 296–299 (March 1997)

The electron energy spectra of diborides of 3*d*-metals ScB_2, TiB_2, VB_2, CrB_2, and MnB_2 are calculated *ab initio*. Thermodynamic properties and stability of these compounds are investigated at low temperatures. An analysis of the low-temperature heat capacity and magnetic properties of diborides has made it possible to establish a number of parameters of many-particle interactions. © *1997 American Institute of Physics.* [S1063-777X(97)00603-8]

Diborides of transition metals with the crystal lattice of the AlB_2 type form a wide and insufficiently studied class of intermetallic compounds. The mechanical and structural properties and the conditions of stability for diborides[1,2] were studied along with the electric and magnetic properties of these compounds.[3–6] Attempts were made to analyze theoretically the electron spectra of TiB_2,[2,7] CrB_2,[8] and VB_2.[9] The electron structure of diborides is of special interest in connection with the possibility of the emergence of high-T_c superconductivity in a compound whose composition is close to TiB_2 (see Ref. 10).

In this research, self-consistent *ab initio* calculations of the electron structure and magnetic properties of the compounds ScB_2, TiB_2, VB_2, CrB_2, and MnB_2 are carried out under a unified approach. The evolution of electron energy spectra in this series of diborides upon a change in the occupancy of the conduction band is studied, the stability of diborides of transition metals is analyzed, and their binding energies are calculated.

The diborides of 3*d*-metals under investigation have a hexagonal crystal structure of the *C*32 type with two boron atoms and one metal atom in a unit cell; the ratio c/a of lattice constants is close to unity.[1] The energy spectra of diborides were calculated by using the linearized *MT*-orbital method in the atomic sphere approximation taking into account scalar–relativistic effects and so-called combined corrections.[1] The exchange–correlation effects were taken into account in the local approximation of the spin and electron density functional theory.[11,12] In the process of self-conformation, only the wave functions of electrons in the conduction band were varied, the states of ion cores being ''frozen.'' In each iteration, the band structure was calculated on a net comprising 112 points in the irreducible part of the Brillouin zone, and the partial densities of states $N_l^i(E)$ ($i=$B, *d*-metal, $l=s$, p, or d is the orbital quantum number) were calculated by the method of tetrahedra. The convergence of calculations with respect to the calculated electron pressure and the final form of the density of states were refined by terminal iterations on a net with 225 points.

The electron densities of states $N(E)$ calculated by us have similar forms for all diborides of 3*d*-metals and differ only in specific details and in the position of the Fermi level E_F. Figure 1 shows the partial densities of electron states of MnB_2 in the paramagnetic phase. Dashed lines show energies corresponding the occupancy for the compounds under investigation. For all diborides, the density of states at the bottom of the conduction band is formed by *s*-states of boron. These states are separated from $p-d$ bands by a minimum on the $N(E)$ curve. As we move to the region of higher energies, the band structure of diborides exhibits a noticeable hybridization of the *p*-states of boron with *s*-, *p*-, and *d*-states of the transition metal. In the energy range close to E_F, the density of states of diborides has three noticeable peaks. The upper and lower peaks, which correspond to antibonding and bonding states, respectively, are formed by *d*-electrons of the transition metal and *p*-electrons of boron. The middle peak, which corresponds to the nonbonding states and which corresponds approximately to the occupancy of VB_2 in Fig. 1, is mainly formed by the *d*-states of the transition metal.

It can be seen from Fig. 1 and Table I that as we go over from ScB_2 to MnB_2 in the series of diborides under investigation, the Fermi level passes through a deep minimum in the density of states (pseudogap at the occupancy level of TiB_2) and goes over to the region of high values of $N(E_F)$ for CrB_2 and MnB_2, which can be accompanied by a decrease in stability of these compounds. Indeed, according to Table I, the experimental values of binding energy[13] decreases in the series $TiB_2-VB_2-CrB_2$. Our results of direct calculations of the binding energy for diborides of 3*d*-metals in the local electron and spin density approximation, according to the method developed by Skriver,[11] are presented in Table I and are in good agreement with the available experimental data.

Since graphite-like boron layers alternate with metal lay-

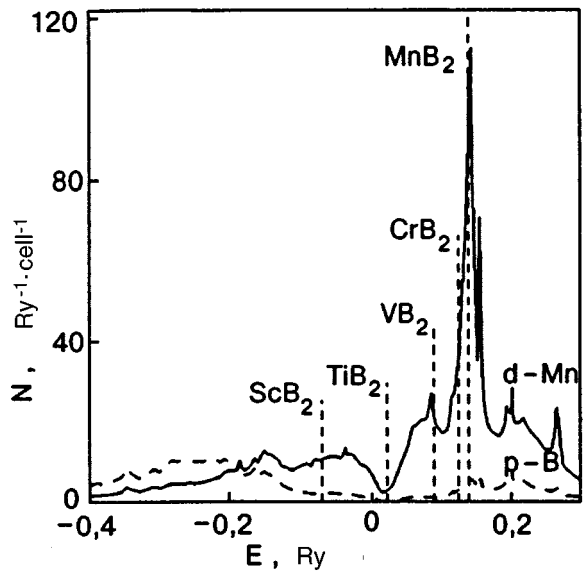

FIG. 1. Partial densities of electron states in the paramagnetic phase of MnB_2: the solid curve corresponds to the *d*-partial density of states of Mn atoms and the dashed curve to the *p*-partial density of states of B atoms. The vertical dashed lines indicate the occupancy levels for the compounds under investigation.

ers in the hexagonal crystalline structure of diborides, it was proposed that the coupling between the layers is weak, and that the crystal lattice stability is determined by the ''metal–metal'' and 'boron–boron'' bonds.[14] However, the results obtained by us and indicating a strong hybridization of the *p*- and *d*-states of the transition metal with the *p*-states of boron show that the coupling between the layers is important for understanding the physical properties of diborides.

According to the current theory, the magnetic properties of transition metals are mainly determined by Pauli paramagnetism χ_P of conduction electrons, which is proportional to $N(E_F)$ to the first approximation. The susceptibility observed for many transition metals is noticeably higher than the Pauli susceptibility, which can be explained by exchange enhancement of spin paramagnetism:

$$\chi_{sp}=S\chi_P=\frac{\mu_B^2 N(E_F)}{1-\alpha}, \tag{1}$$

where $S=(1-\alpha)^{-1}$ is the Stoner factor $\alpha = JN(E_F)/2$; $\chi_P = \mu_B^2 N(E_F)$; and J is the exchange interaction parameter for conduction electrons. In the local electron and spin density approximation, the parameter J can be calculated by using

TABLE I. Thermodynamic parameters of diborides of 3*d*-metals.

	Binding energy, Ry/atom		$N_{exp}(E_F)$	$N(E_F)$	
Compound	exp	theor	state	Ry·cell	λ
ScB_2	–	0.45	–	13.79	–
TiB_2	0.500	0.49	6.25	2.43	1.57
VB_2	0.466	0.48	27.36	18.00	0.52
CrB_2	0.418	0.42	78.32	41.44	0.89
MnB_2	–	0.38	25.62	14.98	0.71

TABLE II. Magnetic susceptibility of diborides of 3*d*-metals (10^{-6} emu/mole) and the values of the Stoner factor $\alpha = JN(E_F)/2$.

Compound	α	χ_{sp}	$\chi_{sp}+\Delta\chi$	χ_{exp}
TiB_2	0.04	6	−44	−40
$(VTi)B_2$	–	22	−28	−28
VB_2	0.37	77	27	21.5
CrB_2	0.91	550	500	455

the computable values of local exchange integrals $J^i_{ll'}$ and partial densities of states at the Fermi level (see Ref. 15):

$$J=\frac{1}{N^2(E_F)}\sum_{ll'i} N^i_l(E_F)J^i_{ll'}N^i_{l'}(E_F). \tag{2}$$

Because of the metal-type conductivity of diborides, we can assume that their susceptibility is also determined by the spin component to a considerable extent. Table II contains the values of spin contribution to magnetic susceptibility calculated from Eqs. (1) and (2) as well as experimental data obtained in Refs. 3 and 5. It can be seen from Table II that the spin contribution to susceptibility is decisive for CrB_2. For other compounds, the discrepancy between the calculated spin contributions χ_{sp} and experimental values χ_{exp} is apparently due to a significant orbital contribution (including ionic contribution) to the magnetic susceptibility. Using the calculated densities of states for TiB_2 and VB_2, we estimated the spin susceptibility for the $(V_{0.5}Ti_{0.5})B_2$ alloy in the virtual crystal approximation: $\chi_{sp}\approx 22\times 10^{-6}$ emu/mole. Since $\chi_{exp}=-28\times 10^{-6}$ emu/mole for this compound, we can estimate the magnitude of the orbital contribution ($\Delta\chi\approx -50\times 10^{-6}$ emu/mole). Taking this value as a rough estimate for TiB_2, VB_2, and CrB_2 and summing up $\Delta\chi$ and the calculated spin contributions, we reach a satisfactory agreement with the experimental values χ_{exp} (see Table II).

According to the results of calculations of the electron structure in the paramagnetic phase, the Stoner criterion of magnetic instability, viz., $\alpha\simeq 1$, virtually holds for the CrB_2 compound [to within the errors in the calculations of the parameters J and $N(E_F)$ in the case where the Fermi level is located on the steep slope of the peak on the density of states; see Fig. 1]. For the paramagnetic phase of MnB_2, the Stoner criterion obviously holds: $\alpha\simeq 3$. In order to determine the possibility of transition of MnB_2 and CrB_2 to the magnetically ordered state, we also calculated the spin-polarized band structure of these compounds by using the local electron and spin density approximation (according to Refs. 11 and 12). For MnB_2, the ferromagnetic ground state with the value $M\approx 2\mu_B$ of spontaneous magnetic moment localized in the atomic sphere of manganese has been established. Strong exchange splitting in the electron spectrum of ferromagnetic MnB_2 leads to a noticeable difference in the densities of states for subbands with ''up'' and ''down'' spins, which are presented in Fig. 2. The total density of states for both spin subbands in this case forms a deep minimum in the vicinity of the Fermi level, leading to a considerable decrease in $N(E_F)$ (see Table I). On the whole, the calculated thermodynamic parameters of ferromagnetic MnB_2 are in accord with the experimental data.[6]

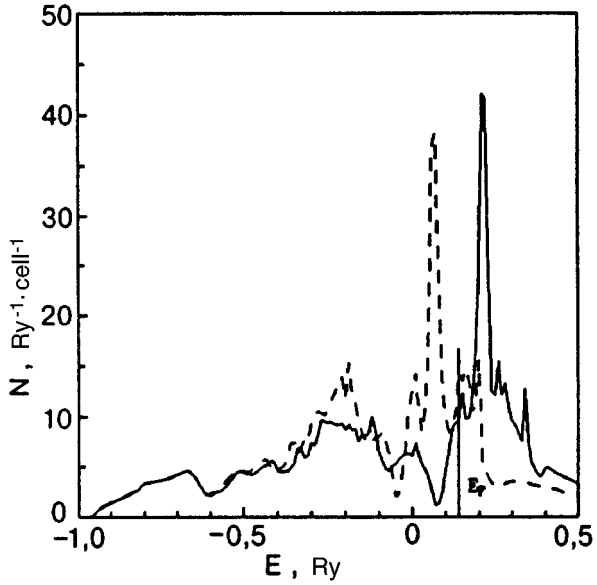

FIG. 2. Electron densities of states in the ferromagnetic MnB_2: the dashed curve corresponds to states with spin ''up'' and the solid curve to states with spin ''down.'' The vertical line indicates the position of the Fermi level.

An analysis of neutron diffraction in a CrB_2 single crystal[6] has made it possible to establish a complex helicoidal magnetic structure at $T<T_N=86$ K with the magnetic moment $0.5\pm0.1\mu_B$, localized at chromium atoms. The analysis of the electron structure for such a noncollinear magnetic phase involves considerable difficulties. Our analysis of the electron structure of the collinear ferromagnetic phase of CrB_2 led to the value $0.8\mu_B$ for the magnetic moment, which is close to that established experimentally.[6]

In conclusion, let us compare the experimental results on the low-temperature electron heat capacity with the theoretical values. The densities of states at the Fermi level calculated by us differ significantly from the corresponding values of $N_{\exp}(E_F)$ determined from the data on electron heat capacity of diborides[3,4] (see Table I). This discrepancy is usually explained by the renormalization of the one-electron spectrum:

$$N_{\exp}(E_F)=(1+\lambda)N(E_F), \tag{3}$$

where the constant λ includes additively the effects of many-particle interaction (the electron–phonon λ_{ep}, the spin-fluctuation λ_{sf}, and the electron–electrons λ_{ee} interactions). Comparing the calculated values of $N(E_F)$ with the values of $N_{\exp}(E_F)$, we can find the corresponding values of the constant λ (see Table I). The large value of λ for TiB_2 can be attributed to a strong electron–phonon interaction in this compound (see Ref. 10). An increase in λ upon a transition from VB_2 to magnetically ordered compounds is apparently associated with increasing contribution of the spin-fluctuation term λ_{sf}.

In this research, we have analyzed the change in the band structure in the series of compounds ScB_2–MnB_2 which differ significantly in their physical properties by using a unified theoretical method based on the local electron and spin density approximation. The analysis shows that the electron structure calculated for diborides of $3d$-metals is in satisfactory agreement with the available experimental data. Such an analysis provides rich information on the electron energy spectrum of diborides, including the parameters of many-particle interactions. The band structure and the estimates of the electron–phonon interaction parameter for TiB_2 do not suggest a peculiar value for the superconducting transition temperature in compounds close in composition to TiB_2.

We with to thank I. V. Svechkarev for interest in this research and for useful discussions.

*E-mail: grechnev@ilt.kharkov.ua

[1] G. V. Samsonov, T. I. Serebryakov, and V. A. Neronov, *Borides* [in Russian], Atomizdat. Moscow (1975).
[2] R. F. Sabiryanov and A. L. Ivanovskii, Metallofizika **14**, 8 (1992).
[3] J. Castaing, R. Caudron, G. Toupance, and P. Costa, Solid State Commun. **7**, 1453 (1969).
[4] B. D. Hanson, M. Mahnig, and L. E. Toth, Z. Naturforschung **26a**, 739 (1971).
[5] J. Castaing, P. Costa, M. Heritier, and P. Legerer, J. Phys. Chem. Solids **33**, 533 (1972).
[6] S. Funahashi, Y. Hamaguchi, T. Tanaka, and R. Bannai, Solid State Commun. **23**, 859 (1977).
[7] De-Cheng Tian and Xiao-Bing Wang, J. Phys.: Condens. Matter **4**, 8765 (1992).
[8] S. H. Lin, L. Kopp. W. B. England, and H. W. Myron, Phys. Rev. **B11**, 3463 (1975).
[9] V. M. Anishchik and N. N. Dorozhkin, Dokl. Akad. Nauk BSSR **33**, 121 (1989).
[10] R. O. Zaitsev, Sverkhprovodimost': Fiz., Khim., Tekhn. **2**, 36 (1989).
[11] H. L. Skriver, *The LMTO Method*, Springer, Berlin (1984).
[12] U. von Barth and L. Hedin, J. Phys. (Paris) **C5**, 1629 (1972).
[13] K. E. Spear, J. Less Common Met. **47**, 195 (1976).
[14] H. Ihara, M. Hirabayashi, and H. Nakagawa, Phys. Rev. **B16**, 726 (1977).
[15] L. Nordstrom, O. Eriksson, M. S. S. Brooks, and B. Johansson, Phys. Rev. **B41**, 911 (1990).

Translated by R. S. Wadhwa

Effect of electron–phonon relaxation on longitudinal electron focussing in metals

Yu. A. Kolesnichenko

*B. Verkin Institute for Low Temperature Physics and Engineering, National Academy of Sciences of the Ukraine, 310164 Kharkov, Ukraine**

Tesgera Bedassa

Kharkov State University, 310077 Kharkov, Ukraine
(Submitted July 4, 1996)
Fiz. Nizk. Temp. **23**, 300–306 (March 1997)

Feasibility of spectroscopy of the electron–phonon interaction (EPI) is substantiated by the method of longitudinal electron focusing (LEF) in thin metal plates. It is shown that the LEF makes it possible to obtain information on the differential function of the EPI characterizing the relaxation of charge carriers with a strictly definite momentum on phonons, which cannot be gained by using other methods.
[S1063-777X(97)00703-2]

In 1965, Sharvin[1] proposed a method for studying the Fermi surface (FS) $\varepsilon_{\mathbf{p}}=\varepsilon_F$ (ε_F is the Fermi energy), which is based on the observation of longitudinal electron focusing (LEF) by a magnetic field **H** in thin metal films whose thickness is much smaller than the mean free path of charge carriers. The LEF experimental geometry is shown in Fig. 1. An electron starting from point E lying on a sample surface can arrive along a ballistic trajectory to point C lying on the same field line on another surface only if the time t_0 of its motion is a multiple to the Larmor period T_H.

In a real experiment, the current-carrying point contact (emitter E) and the measuring potential point contact (collector C) naturally have finite sizes, and electrons arriving from one point contact to the other have the momentum components p_H from a small interval near the value satisfying the equality

$$L=ku_0(\varepsilon_F,p_H)=k\overline{v_H}T_H=\frac{ck}{eH}\frac{\partial S}{\partial p_H},\quad k=1,2,\ldots, \quad (1)$$

where L is the separation between points C and E, $\overline{v_H}$ and p_H are the electron mean velocity and momentum along the direction of the vector **H**, $S(\varepsilon_F,p_H)$ is the area of the FS cross section by the plane $p_H=\text{const}$, and $T_H=(c/eH)\times(\partial S/\partial\varepsilon_F)$.

The signal U being measured obviously has singularities at the values of the magnetic field, for which the phase volume corresponding to the above-mentioned electrons attains its maximum value, i.e., condition (1) is satisfied for charge carriers with an extremal value of the quantity $\partial S/\partial p_H$. The derivative $\partial S/\partial p_H$ has extrema in the cross sections $p_H=p_{\text{extr}}$ corresponding to the extremal displacement $u_0(\varepsilon_F,p_{\text{extr}})$ of an electron along the vector **H** over a period ($\partial^2 S/\partial p_H^2=0$ for $p_H=p_{\text{extr}}$), as well as at the elliptic reference (edge) points $p_H=p_{\max}$, at which $\partial S/\partial p_{\max}=2\pi/\sqrt{K}$ (K is the Gaussian curvature of the FS at the point $p_H=p_{\max}$). Consequently, the observation of the system of LEF peaks periodic in the field **H** makes it possible to determine the Gaussian curvature and extremal values of the derivative $\partial S/\partial p_H$ for the FS.

Although the feasibility of LEF in a metal was demonstrated[2] soon after the publication by Sharvin,[1] this effect has not found an application as a method of fermiology since the same information concerning the FS can be obtained in technologically simpler experiments on observation of Sondheimer oscillations of magnetoresistance of thin plates.[3,4] However, the idea of injection of nonequilibrium electrons with the excess energy eV determined by the applied voltage in a conductor with the help of a point contact proved to be very useful. For example, it was found[5] that LEF can be used to determine the energy dependence of the electron–phonon relaxation length. An analysis of nonlinear current–voltage characteristics of point contacts subsequently led to the development of an extremely effective method of point-contact spectroscopy of the electron–phonon interaction (EPI).[6,7]

The study of phenomena which enable one to take both advantages of this method, i.e., voltage-controlled energizing of electrons and a decisive role of a small region on the FS in the effect, with the help of LEF is undoubtedly promising. We will analyze below the role of the EPI in LEF and will prove that in view of the above-mentioned potentialities, this method can be used for obtaining more detailed (as compared to other methods) information on the interaction of charge carriers with phonon excitations in a metal.

The potential difference U between the collector C and a periphery point of the sample, which is measured by a voltmeter, can be expressed in terms of the semiclassical distribution function for conduction electrons,[8] which must be determined by using Boltzmann's kinetic equation with the corresponding boundary conditions. We will not write here the results of rigorous calculations similar to the calculation of the transverse electron focussing signal[9] and give the final result for the component of the signal ΔU at the collector, which depends nonmonotonically on the magnetic field and is due to electrons moving in strictly ballistic trajectories:

$$\Delta U(\mathbf{L})=(e\langle v_n\Theta(v_n)\rangle)^{-1}\int_{\varepsilon_F}^{\varepsilon_F+eV}d\varepsilon$$

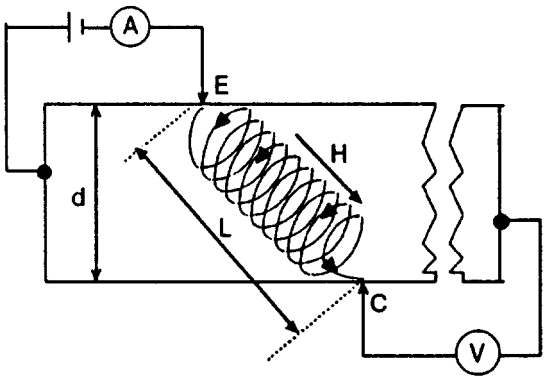

FIG. 1. Schematic diagram of the setup for observation of longitudinal focussing of conduction electrons by a magnetic field **H** in a plate.[1]

$$\left\langle \delta f^* v_n \Theta(v_n)\,\theta(\mathbf{R}-\Delta\mathbf{R}\in S_E) \times \exp\left\{-\int_0^{t_0} \nu_{\mathbf{p}(t')}dt'\right\}\right\rangle_{\varepsilon}, \tag{2}$$

where $eV>0$, the vector $\mathbf{L}=(\mathbf{R},d)$ connects the centers of the contacts, d is the sample thickness, v_n is the velocity component perpendicular to the plane of the aperture S_C of the collector, $\Theta(v_n)$ is the Heaviside (unit step) function, δf^* is the nonequilibrium component of the electron distribution function in the plane of the emitter aperture, $S_E=1/4\pi a^2$ (a is the contact diameter), $\theta(\mathbf{R}\in S_E)$ is the unit function differing from zero for values of $\mathbf{R}$ belonging to S_E, $\Delta\mathbf{R}(\varepsilon,t,p_H)$ is the displacement of charge carriers in a plane parallel to the boundaries over the time $t_0(\varepsilon,t,p_H)$ of motion from contact to contact, t is the ''time'' of motion of an electron in the trajectory,

$$\nu_{\mathbf{p}}(\varepsilon)=\int_0^{|\varepsilon-\varepsilon_F|} g_{\mathbf{p}}(\omega)d\omega \tag{3}$$

is the frequency of electron–phonon relaxation, and

$$g_{\mathbf{p}}(\omega)=\sum_{\alpha}\langle W_{\mathbf{p}-\mathbf{p}',\alpha}\delta(\omega-\omega_{\mathbf{p}-\mathbf{p}',\alpha})\rangle_{\varepsilon}, \tag{4}$$

is the EPI differential function characterizing the interaction of electrons having a momentum $\mathbf{p}$ with phonons. In relation (4), $W_{\mathbf{q},\alpha}$ is the square of the modulus of the matrix element of the EPI, $\omega_{\mathbf{q},\alpha}$ is the frequency of a phonon with the wave vector $\mathbf{q}$, the summation is carried out over the phonon spectrum branches, and $\hbar=1$. The angle brackets denote the averaging over the direction of momentum on the constant-energy surface $\varepsilon_{\mathbf{p}}=\varepsilon$, which is assumed to be closed:

$$\langle\cdots\rangle_{\varepsilon}=\frac{2eH}{N(\varepsilon)(2\pi)^3c}\int_{p_{\min}}^{p_{\max}}dp_H\int_0^{T_H}dt\cdots . \tag{5}$$

Here $N(\varepsilon)$ is the electron density of states.

In order to avoid cumbersome formulas, in the derivation of relation (2) we assumed that the temperature $T=0$. If $T\ll eV$, this leads only to an insignificant broadening of LEF peaks.

Expression (2) for the ballistic component of the LEF signal can be interpreted by using simple physical considerations. The value of U measured by the voltmeter is the electric potential far away from a contact in the bulk of the collector, where the electron distribution function $f_{\mathbf{p}}$ is in equilibrium:

$$f_{\mathbf{p}}=f_0(\varepsilon+eU). \tag{6}$$

The electron distribution function for the emitter acquires a nonequilibrium correction δf^* to the Fermi function $f_0(\varepsilon_{\mathbf{p}})$. In the absence of scattering in the bulk, this nonequilibrium component is transferred by charge carriers along ballistic trajectories to the collector. The distribution function for electrons arriving at the collector (with $v_n>0$) has the form

$$f_{\mathbf{p}}=f_0(\varepsilon_{\mathbf{p}}+e\varphi(\mathbf{L}))+\delta f^*\theta(\mathbf{L}-\Delta\mathbf{R}\in S_E), \tag{7}$$

where $\varphi(\mathbf{L})$ is the value of electrical potential in the plane of the collector aperture, the function θ reflects the fact that the function $f_{\mathbf{p}}$ differs from the Fermi function only for a small group of electrons arriving from the emitter. Assuming that the voltmeter is ideal, we can write the condition of zero current through the contact C by using relations (6) and (7):

$$\int_0^{\infty} d\varepsilon v_n\langle\Theta(-v_n)f_0(\varepsilon_{\mathbf{p}}+e\varphi(\mathbf{L})+eU)+\Theta(v_n)[f_0(\varepsilon_{\mathbf{p}} +e\varphi(\mathbf{L}))+\delta f^*\theta(\mathbf{L}-\Delta\mathbf{R}\in S_E)]\rangle_{\varepsilon}=0. \tag{8}$$

Linearizing the right-hand side of this equation in U and $e\varphi$ under the assumption that eU, $e\varphi\ll\varepsilon_F$ and considering that nonequilibrium electrons belong to the energy interval $[\varepsilon_F,\varepsilon_F+eV]$ for $T\to 0$ and $-\partial f_0/\partial\varepsilon_{\mathbf{p}}=\delta(\varepsilon-\varepsilon_F)$ we obtain Eq. (2), in which the exponential function is the probability of motion of charge carriers in the sample without scattering.

The asymptotic calculation of the mean value (5) in Eq. (2) is based on the smallness (for $\eta=a/L\ll 1$) of the region ''cut'' by the θ-function on the constant-energy surface $\varepsilon_{\mathbf{p}}=\varepsilon$ near the lines $p_H=p_0$ specified by the equations

$$ku_0(\varepsilon,p_H)=\frac{kc}{|e|H_k}\frac{\partial S(\varepsilon,p_H)}{\partial p_H}=L,\quad k=1,2,\ldots . \tag{9}$$

The approximation of the step function $\theta(\mathbf{R}\in S_E)$ by the continuously differentiable function $\exp\{-(\mathbf{R})^2/(a/2)^2\}$ for $a/L\to 0$ makes it possible to find the asymptotic value of ΔU by the Laplace method.[10] Retaining the main term of the asymptotic series, we can write the ballistic component of the LEF signal amplitude in the form

$$\Delta U=\frac{1}{e}\int_{\varepsilon_F}^{\varepsilon_F+eV}d\varepsilon\sum_{k=k_0}^{\infty}A(\varepsilon,p_0) \times\exp\{-kT_H\overline{\nu(}\varepsilon,p_0)\}\delta f^*, \tag{10}$$

where $k(\varepsilon,p_0)=[L/u_0(\varepsilon,p_0)]+1$ and $[x]$ is the integral part of the number x. Here and below, the bar above the letter indicates the value of the corresponding function averaged over the period T_H:

$$\overline{\nu(\varepsilon,p_H)}=\frac{1}{T_H}\int_0^{T_H}dt\,\nu_{\mathbf{p}(t)}(\varepsilon).$$

The function $A(\varepsilon,p_H)$ has the meaning of the partial contribution from electrons with the energy ε and the momentum component p_H to the LEF signal. Its amplitude of the cross section $S(\varepsilon,p_H)$, corresponds to the satisfaction of the focussing condition (9).

If the derivative $\partial^2 S/\partial p_H^2$ and the velocity component $v_\perp$ perpendicular to the vector **H** differ from zero for $p_H=p_0$, we have

$$A(\varepsilon,p_0)=\eta\sqrt{\pi}\,\frac{2m^*\overline{(v_H^2 v_\perp^{-1})}}{\langle v_n\Theta(v_n)\rangle_\varepsilon}\left|\frac{(\partial S/\partial p_H)}{(\partial^2 S/\partial p_H^2)}\right|_{p_H=p_0}. \quad (11)$$

In the case where $p_0=p_{\max}$, the reference point (the boundary point corresponding to the maximum of the derivative $\partial S/\partial p_H$) at which $v_\perp=0$ and $\partial S/\partial p_0=2\pi/\sqrt{K}$, we have

$$A(\varepsilon,p_{\max})=\eta^{2/3}\,\frac{2^{2/3}\pi\Gamma(1/3)\overline{(v_H^2 v_\perp^{-1})}}{\langle v_n\Theta(v_n)\rangle_\varepsilon}\,\frac{\overline{(k_N^{-1/3})}}{KM^{2/3}}. \quad (12)$$

Here $k_N = k_1\sin^2\vartheta + k_2\cos^2\vartheta$; $K=\sqrt{k_1k_2}$, $M=1/2(k_1+k_2)$ are the normal, Gaussian, and average curvatures of the surface $\varepsilon_{\mathbf{p}}=\varepsilon$ at the reference point $p_{\max}$, $R_1=k_1^{-1}$ and $R_2=k_2^{-1}$ are the principal radii of curvature, and $\vartheta=2\pi t/T_H$.

For electrons having the extremal displacement along the magnetic field over a period ($\partial^2 S/\partial p_H^2=0$ for $p_H=p_0=p_{\text{extr}}$), we obtain

$$A(\varepsilon,p_{\text{extr}})=\eta^{1/2}\,\frac{\Gamma(1/4)}{2\sqrt{2}}\,\frac{2m^*\pi\overline{(v_H^{3/2}v_\perp^{-1/2})}}{\langle v_n\Theta(v_n)\rangle_\varepsilon}\times\left|\frac{(\partial S/\partial p_H)}{(\partial^3 S/\partial p_H^3)}\right|^{1/2}_{p_H=p_0=p_{\text{extr}}}. \quad (13)$$

It should be noted that since the parameter $\eta=a/L\ll 1$, the function A, according to relations (11)–(13), has two systems of peaks periodic in the magnetic field. One of these systems is associated with focussing of electrons from reference points at the collector, while the other is associated with electrons corresponding to extremal values of the derivative $\partial S/\partial p_H$ of the cross sections of the surface $\varepsilon_{\mathbf{p}}=\varepsilon$.

The characteristic interval $\Delta\varepsilon$, over which the change in the quantity of A as a function of energy ε is significant, is of the order of $\eta\varepsilon_F$. For $eV<\eta\varepsilon_F$, the amplitude A can be taken on the FS, and its extrema determine the position of the LEF signal peaks on the magnetic field scale. As the nonequilibrium band width eV increases, the difference in the Larmor radii of the trajectories of electrons having different energies, but the same displacement along the vector **H** over a period becomes comparable to the contact diameter a. This is the reason behind the nonlinear dependence of the amplitude of LEF lines on V and the change in their shape as well as the values of the field $H_k(V)$ for which the signal attains its maximum value.[1)] The dependence of the second and third cofactors in the integrand of Eq. (10) on ε associated with the EPI is manifested at energies (eV) of the order of the Debye energy ω_D for phonons.

In real experiments, the inelastic mean free paths for electrons $l_\varepsilon=\min(l_{ep},\sqrt{l_{ep}l_i})$ (l_i and l_{ep} are the mean free paths for elastic and electron–phonon collisions) in the sample and in the contact can differ significantly in view of a strong contamination of the contact region. Accordingly, the contacts with a small elastic relaxation length are characterized by two contributions to the LEF signal, which are nonlinear in V. One of these contributions is associated with the EPI at the contact and the other with inelastic relaxation of electrons moving from the emitter to the collector.

We assume that the current-carrying contact is ballistic, i.e., $a\ll l_i$, and that the value of l_{ep} is comparable with the separation L of the contacts. In this case, the function δf^* can be regarded as independent of energy. Differentiating expression (10) with respect to the emitter voltage, we obtain the following expressions for the ratio of the second and first derivatives of the amplitude $\Delta U_k^{\max}$ of the kth LEF line in the main approximation in the parameter $eV/\varepsilon_F\ll 1$:

$$\frac{(\partial^2\Delta U_k^{\max}/\partial V^2)}{(\partial\Delta U_k^{\max}/\partial V)}=ekT_H\overline{g(}eV,p_e), \quad (14)$$

where

$$p_e=p_{\max}(v_\perp(p_{\max})=0),$$

or

$$p_e=p_{\text{extr}}(\partial^2 S/\partial p_{\text{extr}}^2=0).$$

For the values of magnetic field corresponding to the focussing peaks for electrons from the neighborhood of a reference point of the FS, the quantity $g_{\mathbf{p}_{\max}}(\omega)=\overline{g(}\omega,p_{\max})$ does not depend on the phase on the cyclotron trajectory, and hence expression (14) contains the local value of the EPI function. It should be noted that point-contact spectroscopy can be used to determine the EPI function which is averaged over the FS and which contains the geometrical form factor,[7] and the observation of nonlinear transverse electron focusing makes it possible to determine the function $g_{\mathbf{p}}(\omega)$ (4) integrated along the line connecting the ends of the extremal diameter on the FS.[13]

Relation (14) demonstrates the possibility of reconstructing the EPI differential function by measuring the LEF signal for various mutual arrangement of the contacts. In this connection, it is appropriate to mention the recent experiments[14] on the observation of anisotropy of electron flows in a thin metal plate.[15] In these experiments, a focused laser beam, which could be displaced along one of the surfaces of the plate, was used instead of a point contact for creating a local nonequilibrium state in the electron system, while the measuring conventional point contact located at the other surface remains stationary. It should be noted that although the ratio (14) remains finite for $l_{ep}\to 0$, it can be determined in actual practice as long as $l_{ep}(eV)\leqslant L$. In bismuth-type semimetals, the electron–phonon relaxation length is relatively large ($l_{ep}\approx 10^{-2}$–10^{-3} cm) even for excess electron energies $eV>\omega_D$ (ω_D is the Debye energy of phonons), which makes it possible to use relatively thick plates in such experiments.

In the opposite limiting case, when the EPI on a ballistic trajectory is insignificant ($L/l_{ep}\gg 1$), but the contact size is comparable to the inelastic relaxation length in it, the non-

linearity of the LEF signal is due to the energy dependence $\delta f^*(\varepsilon)$ of the distribution function for charge carriers injected in the metal.

The determination of the nonequilibrium distribution function for electrons in a contact, taking the EPI into account, forms an independent problem which was considered by many authors in connection with the problem of point-contact spectroscopy (see, for example, the spectral atlas in Ref. 16 and the references cited there). Although the explicit form of the function δf^* is sensitive to the emitter geometry, the form of its energy dependence is determined by the relation between the contact size a and the length l_ε. In the case of a weak inelastic electron relaxation, the EPI can be taken into account in the perturbation theory, and the function δf^* can be written in the form[13]

$$\delta f^* = f_1 + f_2 \frac{a^2}{v_F l_i}\left\{ \int_0^{\varepsilon-\varepsilon_F} d\omega g(\omega) + \int_0^{\varepsilon_F+eV-\varepsilon} d\omega g(\omega)\right\}; \quad l_1 \ll a \ll l_\varepsilon, \tag{15}$$

where $g(\omega) = \langle g_{\mathbf{p}}(\omega)\rangle_\varepsilon$; f_1, f_2 = const(ε), and v_F is the Fermi velocity. Setting $\nu = 0$ in expression (10) for $L/l_{ep} \gg 1$, we obtain the following expression for the ''inelastic'' correction δU for the LEF signal:

$$\delta U = f_2 \frac{a^2}{v_F l_i} \int_{\varepsilon_F}^{\varepsilon_F+eV} d\varepsilon \int_0^{\varepsilon-\varepsilon_F} d\omega g(\omega) \times \sum_{k=k_0}^{\infty} [A(\varepsilon, p_0) - A(\varepsilon-\omega, p_0)]. \tag{16}$$

According to this result, the second derivative of the LEF signal amplitude is proportional to the EPI (Eliashberg) function averaged over the FS:

$$\frac{\partial^2 \delta U}{\partial (eV)^2} \approx f_2 \frac{a^2}{v_F l_i}\left(\sum_{k=k_0}^{\infty} \frac{\partial A}{\partial \varepsilon_F}\right) eVg(eV); \quad eV \ll \varepsilon_F. \tag{17}$$

Note the absence of a form factor in the EPI function which is determined by the method of electron focusing, which appears in the point-contact spectroscopy.[7,16] This can be explained by a considerably weaker dependence of the LEF signal on the contact geometry as compared to the contact resistance.

If the electron mean free path in inelastic collisions is comparable with the size of the emitter ($l_\varepsilon \sim a$), the perturbation theory in the electron–phonon collision integral is inapplicable, and it is impossible to obtain an explicit expression for $\delta f^*(\varepsilon)$ under arbitrary assumptions concerning the EPI function $g_{\mathbf{p}}(\omega)$. The model considered in Ref. 13 takes into account the interaction of electrons with phonons having a certain frequency $\omega_{\mathbf{q}} = \omega_0$. Such a model successfully describes, for example, inelastic relaxation of charge carriers by optical and intervalley phonons in semimetals. In this case, the function δf^* has jumps Δf_n for discrete energy values:[13]

$$\delta f^*(\varepsilon) \approx \sum_{n=0}^{N} \Delta f_n(\varepsilon)\Theta(\varepsilon_n - \varepsilon), \tag{18}$$

$$\varepsilon_n = \varepsilon_F + eV - n\omega_0, \quad n = 0, 1, 2, ..., N, \quad eV - N\omega_0 < \omega_0, \tag{19}$$

where $\Delta f_n(\varepsilon) = \delta f^*(\varepsilon_F + eV - 0)$ is the jump in the distribution function at the boundary of the nonequilibrium band. We do not write here cumbersome expressions (see Ref. 13) for the function Δf_n whose explicit form is immaterial for subsequent analysis. It should only be noted that the amplitude of jumps depends on the parameter a/l_ε. In the limit of weak electron–phonon relaxation ($a/l_\varepsilon \ll 1$), the maximum jump of the distribution function is equal to Δf_0, and successive phonon repetitions of this jump are proportional to powers of the parameter $(a/l_\varepsilon)^2$. The highest probability corresponds to one-phonon processes described by the distribution function (15). In the opposite case of strong EPI ($a/l_\varepsilon > 1$), the number of nonequilibrium electrons decreases exponentially upon an increase in their energy, and the magnitude of the jump Δf_n increases accordingly with the number n.

Substituting the function δf^* [Eq. 18] into Eq. (10) and differentiating the result, we obtain

$$\frac{\partial U}{\partial V} = \sum_{k=k_0}^{\infty} \sum_{n=0}^{N} A(p_0, \varepsilon_n)\Delta f_n. \tag{20}$$

In magnetic fields satisfying relation (9), the derivative (20) has peaks for energies ε_n (19). The condition of their observation is the requirement $a/L \gg \omega_0/\varepsilon_F$, under which the separation between neighboring extrema on the magnetic field scale is larger than the linewidth.

Thus, for large emitter voltages V, LEF can serve as a method of EPI spectroscopy. In the case where relaxation at a ballistic trajectory dominates ($a < L \leqslant l_{ep}$), the second derivative of the LEF signal at the maximum formed by electrons from the reference point $\mathbf{p} = \mathbf{p}_{\max}$ on the FS is proportional to the ''differential'' EPI function $g_{\mathbf{p}_{\max}}(\omega)$ (4), which characterizes the interaction of electrons having a momentum $\mathbf{p}_{\max}$ with phonons. By varying the position of one of the contacts and changing the roles of the current-carrying and measuring contacts, we can reconstruct $g_{\mathbf{p}_{\max}}(\omega)$ on the entire FS from the derivative $\partial^2 U^{\max}/\partial V^2$. Similar analysis of nonlinear voltage dependence of the amplitudes of peaks associated with electrons corresponding to FS cross sections with extremal values of the derivative $\partial S/\partial p_H$ makes it possible to determine the function $\overline{g(\omega, p_H)}$ averaged over a cyclotron trajectory. If, however, electron–phonon relaxation directly in the emitter contact dominates ($a/L \ll l_\varepsilon/l_{ep}$), the derivative $\partial^2 \Delta U/\partial V^2$ in the case of weak EPI ($a \ll l_\varepsilon$) contains a correction proportional to the function $g(\omega) = \langle g_{\mathbf{p}}(\omega)\rangle_{\varepsilon_F}$ averaged over the FS, which coincides with the EPI thermodynamic function (Eliashberg function) in the main approximation in the small parameter a/L. It is important that the frequency ω_0 of dispersionless phonons at which electron relaxation leads to the emergence of a system of peaks on the first derivative of the LEF signal for $a/L \ll \omega_0/\varepsilon_F$ can be determined easily with the help of LEF.

The authors are grateful to V. G. Peschanskii for fruitful discussions of the results of this research.

*E-mail: kolesnichenko@ilt.kharkov.ua
**E-mail: tesgera@martin.kharkov.ua

[1)]The effect of ''geometrical'' nonlinearity in transverse electron focusing was predicted theoretically[11] and studied experimentally[12] earlier.

[1] Yu. V. Sharvin, Zh. Éksp. Teor. Fiz. **48**, 984 (1965) [Sov. Phys. JETP **21**, 655 (1965).
[2] Yu. V. Sharvin and L. M. Fisher, Pis'ma Zh. Éksp. Teor. Fiz. **1**, 54 (1965) [JETP Lett. **1**, 152 (1965)].
[3] E. H. Sondheimer, Phys. Rev. **80**, 401 (1950).
[4] V. L. Gurevich, Zh. Éksp. Teor. Fiz. **35**, 668 (1958) [Sov. Phys. JETP **8**, 464 (1958)].
[5] Yu. V. Sharvin and N. I. Bogatina, Zh. Éksp. Teor. Fiz. **56**, 772 (1969) [Sov. Phys. JETP **29**, 419 (1969)].
[6] I. K. Yanson, Zh. Éksp. Teor. Fiz. **66**, 1035 (1974) [Sov. Phys. JETP **39**, 506 (1974)].
[7] I. O. Kulik, A. N. Omel'yanchuk, and R. I. Shekhter, Fiz. Nizk. Temp. **3**, 1545 (1977) [*sic*].
[8] Yu. A. Kolesnichenko and I. O. Kulik, Fiz. Nizk. Temp. **18**, 1005 (1992) [Sov. J. Low Temp. Phys. **18**, 706 (1992)].
[9] Yu. A. Kolesnichenko, Fiz. Nizk. Temp. **18**, 1059 (1992) [Sov. J. Low Temp. Phys. **18**, 741 (1992)].
[10] Yu. A. Kolesnichenko, T. Bedassa, and V. I. Grishaev, Fiz. Nizk. Temp. **21**, 1049 (1995) [Low Temp. Phys. **21**, 806 (1995)].
[11] Yu. A. Kolesnichenko, R. I. Shekhter, and V. A. Buldovskii, Fiz. Nizk. Temp. **14**, 263 (1988) [Sov. J. Low Temp. Phys. **14**, 144 (1988)].
[12] V. V. Andrievskii, E. I. Ass, and Yu. F. Komnik, Fiz. Nizk. Temp. **14**, 253 (1988) [Sov. J. Low Temp. Phys. **14**, 139 (1988)].
[13] Yu. A. Kolesnichenko, I. O. Kulik, and R. I. Shekhter, Zh. Éksp. Teor. Fiz. **94**, 328 (1988) [Sov. Phys. JETP **67**, 834 (1988)].
[14] M. Primke, J. Heil, and P. Wyder, Physica B **218**, 26 (1996).
[15] A. M. Kosevich, Fiz. Nizk. Temp. **11**, 1106 (1985) [Sov. J. Low Temp. Phys. **11**, 611 (1985)].
[16] I. K. Yanson and A. V. Khotkevich, *Atlas of Point-Contact Spectra of Electron–Phonon Interaction in Metals* [in Russian], Naukova Dumka, Kiev (1986).

Translated by R. S. Wadhwa

Surface energy relaxation of conduction electrons in bismuth using transverse electron focusing technique

V. V. Andrievskii, Yu. F. Komnik, and S. V. Rozhok

*B. Verkin Institute for Low Temperature Physics and Engineering, National Academy of Sciences, 310164 Kharkov, Ukraine**

(Submitted July 24, 1996)
Fiz. Nizk. Temp. **23**, 307–312 (March 1997)

The position of the first and second lines of transverse electron focusing on the scale of magnetic fields is analyzed to determine the loss of excess energy of conduction electrons in bismuth as a result of collisions with the crystal boundary upon normal incidence as well as the shape of the functional dependence of this quantity on the initial excess energy. It is found that beginning from relatively low values of excess energy (~ 3 meV), a sharp drop in energy occurs upon reflection of electrons at the boundary. © *1997 American Institute of Physics.*
[S1063-777X(97)00803-7]

INTRODUCTION

The focusing of conduction electrons in metals with the help of a transverse magnetic field[1] was earlier used mainly for studying the interaction[2] of extremely low excitation energy electrons with the surface. This method provides information about the probability of specular[3] or intervalley[4,5] surface reflection of electrons incident normally at the crystal boundary, as well as about the possibility of Andreev reflection of quasiparticles at the normal metal–superconductor interface.[6,7] This information was obtained from the ratio of amplitude of the first two electron focusing (EF) lines for a slight nonequilibrium of carriers.

In this work, we shall show that by using the EF technique in bismuth for a considerable excess energy of electrons injected in the crystal, the position of the first two EF lines can provide information about the magnitude and nature of loss of a part of the excess energy due to interaction of normally incident electrons with the surface.

EF TECHNIQUE

In order to realize transverse electron focusing, two point contacts are formed at the surface of a single crystal in such a way that the separation L between them is smaller than the electron mean free path in the metal. Current is passed between one point contact (emitter) and a distant peripheral contact. The emitter is used for injecting electrons into the metal. The measurable quantity is the potential U_c across the second point contact (collector) relative to another peripheral point. The magnetic field **H** is directed in the plane of the metal surface at right angles to the line connecting the point contacts. The electrons leaving the emitter move in ballistic (cyclotron) trajectories in a magnetic field and some of them reach the collector and create a potential on it. Upon a change in the magnetic field, the potential U_c characterizes the number of electrons leaving the emitter at different angles and reaching the collector. The maximum signal (first EF line) is formed in a magnetic field H_0^{I} in which the electrons belonging to the extremal diameter of the Fermi surface reach the collector. For low excitation energy of electrons, the field H_0^{I} is defined by the expression

$$H_0^{\mathrm{I}}=\frac{2cp_{zF}}{eL}, \tag{1}$$

where p_{zF} is the Fermi momentum component and the z axis is directed at right angles to the surface.

In the EF technique, some electrons injected into the metal have an excess energy $\delta\varepsilon$ (relative to the Fermi energy ε_F) due to the voltage V applied to the point contact. Since the electrons being injected have an energy $\varepsilon_F+\delta\varepsilon$, p_z belongs to the constant energy surface $\varepsilon_F+\delta\varepsilon$, and hence the field $H^{\mathrm{I}}>H_0^{\mathrm{I}}$:

$$H^{\mathrm{I}}=\frac{2cp_z}{eL}, \tag{2}$$

$$p_z=p_{zF}\left(1+\frac{\delta\varepsilon}{\varepsilon_F}\right)^{1/2}. \tag{3}$$

The second EF line is formed by electrons that are reflected once from the surface during their movement along the ballistic trajectory. The peak signal for the second EF line is formed in a field H^{II} in which electrons reach the collector after interacting with the surface upon normal incidence. In the absence of energy losses during reflection at the surface, the following exact relation must be satisfied for such electrons:

$$H^{\mathrm{II}}=2H^{\mathrm{I}}. \tag{4}$$

The ratio of the amplitudes of the second and first EF lines is determined by the coefficient q of specular reflection at the surface. The interaction of an electron with the surface for $q=1$ is assumed to be totally elastic, and the absolute value of the normal component is conserved upon a reversal of its sign.

MEASURING TECHNIQUE

The standard technique of electron focusing by a transverse magnetic field[1] was used for analyzing the position and amplitude of the first and second EF lines in bismuth for different values of the excess electron energy. Sharpened tips of copper wire, attached to the trigonal face of a bismuth single crystal separated by a distance $L\sim 0.2$ mm were used

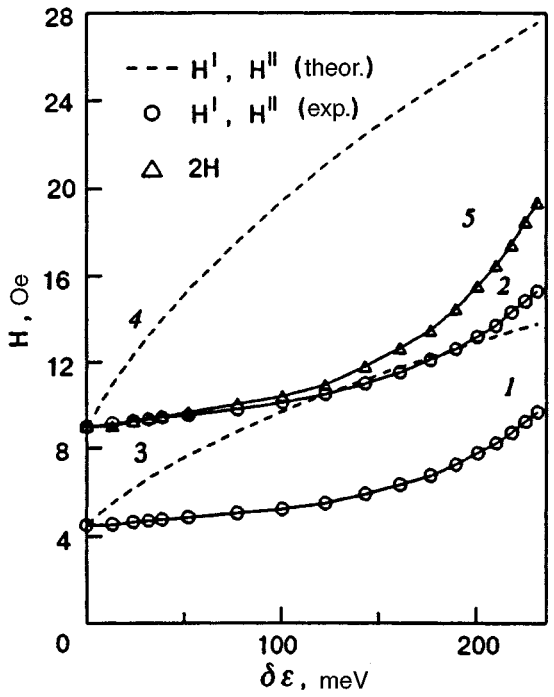

FIG. 1. Change in the position of the peak of the first (*1*) and second (*2*) EF lines on the scale of magnetic fields as a function of the excess electron energy determined by the voltage applied to the emitter point contact. Curves *3* and *4* show the theoretical dependences as per Eqs. (2) and (4). Curve *5* corresponds to the expected variation in the position of the second line when Eq. (4) is satisfied relative to the experimentally observed dependence for the first line.

as the emitter and the collector. Microscopic contact welding of the wires was carried out by using a battery supplying a constant voltage of 100 V across a ballast resistance of 1 MΩ directly in liquid helium. The contact diameter d was determined from Vexler's formula[8] ($d \sim 5\,\mu$m for a point contact resistance $\simeq 1\Omega$). A small value of the ratio d/L ensured a very sharp EF line.[9] The magnetic field was produced by Helmholtz coils, thus ensuring a high uniformity and smoothness of the field being applied. The orientation of the contact line, crystallographic axes, and magnetic field corresponds to the standard recording of the EF lines: $\mathbf{n} \| \mathbf{C}_3$, $\mathbf{L} \| \mathbf{C}_2$, $\mathbf{H} \perp \mathbf{L}$. The EF curves were recorded at liquid-helium temperatures in the interval 1.5–4.2 K, the required temperature was attained by pumping helium vapor.

In addition to the potential $U_c(H)$ across the collector, the potential derivative with respect to the emitter current $dU_c/dI_e(H)$ was also recorded in a number of cases by modulating the emitter current with a low-amplitude alternating current (~ 0.5 mA) and recording the collector signal at the modulation frequency. The $dU_c/dI_e(H)$ recording has the advantage of sharper extrema than on the $U_c(H)$ recording. The displacement of extrema of the first and second EF lines on the $dU_c/dI_e(H)$ relative to $U_c(H)$ can be easily taken into consideration.

EXPERIMENTAL RESULTS

It was found that Eq. (4) is violated as a result of increasing of the excess energy of electrons being injected into bismuth. By way of an example, Fig. 1 shows the dependence of the magnetic field for first (H^{I}) and second (H^{II}) EF lines on the applied voltage V across the emitter (curves 1 and 2). It would appear that this voltage must ensure an excess electron energy eV. The dashed curves show the anticipated variation in the values of the magnetic fields H^{I} and H^{II} as functions of eV in accordance with the focusing condition (2) and relation (4).

However, these relations are violated. First, the experimental curves $H^{\mathrm{I}}(eV)$ and $H^{\mathrm{II}}(eV)$ are lower than the theoretical curves. Second, the experimental curve *2* for the second line lies lower than curve *5* plotted according to relation (4) from the experimental curve for the first line. There is a factor capable of altering the position of the EF line on the scale of magnetic fields upon the passage of strong currents through the emitter. This is the intrinsic magnetic field of the current in the point contact, viz., the region of its maximum concentration. It has its highest value along the perimeter of the point contact and decreases rapidly with increasing distance from the emitter in the plane of the external metal boundary. In the bulk of the metal, the emitter current produces virtually no magnetic field. Thus, the magnetic field of the emitter current can affect the electron trajectory in the initial segment, i.e., the emitter region only, and does not affect the ballistic movement in the bulk of the metal. The displacement of the first EF line toward higher magnetic fields was recorded for currents $\gtrsim 50$ mA. Note that the intrinsic magnetic field of the emitter current must lead to a simultaneous unidirectional displacement of both the first and second EF lines, i.e., it cannot be responsible for a decrease in the separation between them. In order to eliminate the possible effect of the intrinsic magnetic field of the current, we confined our analysis to the position of the first and second EF lines for currents not exceeding 50 mA.

The first peculiarity of Fig. 1, viz., a departure of the dependences $H^{\mathrm{I}}(eV)$ from the theoretical curve described by Eq. (2), was mentioned by us earlier in Refs. 10 and 11. According to our analysis, the most probable explanation for this deviation is that the actual excess energy of the injected electrons is lower than eV. This decrease is apparently due to the relaxation process occurring in the emitter region.[11] The actual excess energy $\delta\varepsilon$ of injected electrons can be calculated by comparing the theoretical and experimental dependences for given values of the magnetic field. The actual excess energy of electrons can be determined analytically. Since, according to (1) and (2),

$$\frac{H^{\mathrm{I}}}{H_0} = \frac{p_z}{p_{zF}},$$

and p_z is determined by Eq. (3), we obtain the dependence of the actual excess energy $\delta\varepsilon_1$ on the position of the first EF line H^{I} for nonequilibrium electrons relative to H_0:

$$\delta\varepsilon_1 = \varepsilon_F \left[\left(\frac{H^{\mathrm{I}}}{H_0} \right)^2 - 1 \right]. \tag{5}$$

The second peculiarity in Fig. 1, viz., the departure of the dependence $H^{\mathrm{II}}(eV)$ from Eq. (4) relative to the experimental curve for the first line, indicates the loss of a part of the excess electron energy during interaction with the sur-

face. Considering that the first part of the ballistic trajectory prior to the collision with the surface is traversed by an electron with an excess energy $\delta\varepsilon_1$, and the second part of flight up to the collector is traversed with an excess energy $\delta\varepsilon$, we obtain a relation for determining $\delta\varepsilon_2$. Indeed, setting $L=L_1+L_2$, we obtain

$$L=\frac{2c}{eH^{\mathrm{II}}}(p_{z1}+p_{z2}), \tag{6}$$

where p_{z1} corresponds to the energy $\varepsilon_F+\delta\varepsilon_1$ and p_{z2} to the energy $\varepsilon_F+\delta\varepsilon_2$. Using Eq. (3) for p_{z1} and p_{z2} as well as Eq. (1), we obtain

$$\delta\varepsilon_2=\varepsilon_F\left[\left(\frac{H^{\mathrm{II}}-H^{\mathrm{I}}}{H_0}\right)^2-1\right]. \tag{7}$$

Figure 2 shows two examples of constructing the dependences of the ratio $\delta\varepsilon_2/\delta\varepsilon_1$ on $\delta\varepsilon_1$ in the range of variation of the initial excess energy up to $\sim$50 meV. The dependence $U_c(H)$ is recorded in one case (a) and the dependence $dU_c/dI_e(H)$ of the derivative in the other case (b). The results were found to coincide in both cases. It can be seen that even for low values of $\delta\varepsilon_1\sim 3-4$ meV, a sharp decrease is observed in the excess energy due to interaction with the surface. The dependences obtained in our experiments can be described analytically by a function of the form

$$\delta\varepsilon_2=A\,\delta\varepsilon_1^k, \tag{8}$$

where $k\simeq 1/2$. For $\delta\varepsilon_1\approx\varepsilon_F$, the excess electron energy $\delta\varepsilon_2$ after interaction with the surface decreases to $\sim(0.25-0.30)\delta\varepsilon_1$. On the whole, the curves presented in Fig. 2 describe the change in the intensity of an inelastic process involving the collision of electrons with the surface upon normal incidence. The probability of inelastic interaction of electrons with the surface can be characterized in terms of the difference $1-\delta\varepsilon_2/\delta\varepsilon_1$ as a function of $\delta\varepsilon_1$.

The coefficient of specular reflection at the surface, obtained from the ratio of amplitudes of the second and first EF lines, decreases with increasing excess electron energy (Fig. 3), but this decrease is not so strong and sharp as the loss of electron energy (cf. Fig. 2). A somewhat unusual picture is observed: the interaction of normally incident electrons with the surface becomes markedly inelastic even for small values of the excess energy, but the high value of the specular reflection coefficient is preserved. It can be assumed that electrons incident normally at the bismuth surface are reflected from the surface potential, and the emergence of tangential components of quasimomentum is obviously not necessary for such a process.

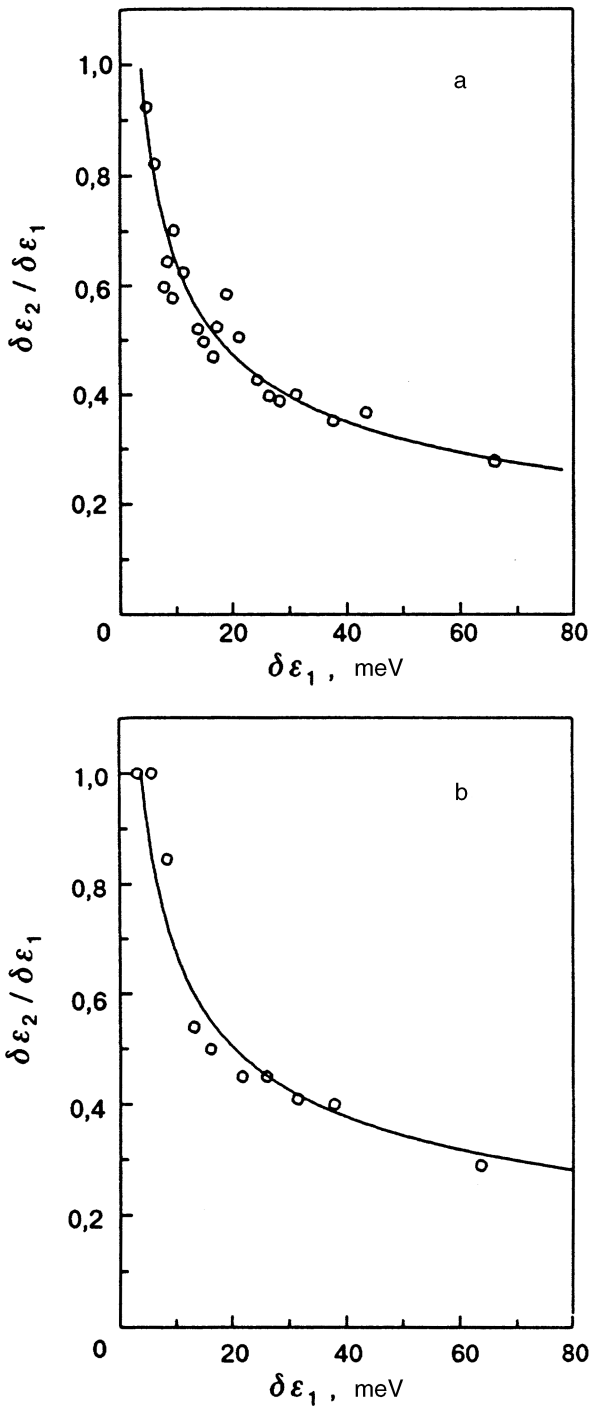

FIG. 2. Ratio of the excess electron energy $\delta\varepsilon_2$ after collision with the surface to the initial excess energy $\delta\varepsilon_1$ as a function of $\delta\varepsilon_1$. The data were obtained by recording the EF signal $U_c(H)$(a) and the derivative $dU_c/dI_e(H)$(b).

DISCUSSION

Beginning from relatively small values of the initial excess energy $\delta\varepsilon_1$, the most probable explanation for the sharp decrease in the ratio $\delta\varepsilon_2/\delta\varepsilon_1$ is the excitation of the surface vibrations of the lattice during reflection of electrons at the surface. The possibility of studying inelastic surface scattering of electrons by electron focusing was mentioned for the first time in Ref. 12, where a relation was obtained between the signal being measured (derivative of the potential across the collector with respect to the emitter voltage) and the corresponding function which characterizes the interaction of electrons with surface vibrations.

Apparently, the interaction of normally incident electrons with the surface may lead to the excitation of a surface elastic wave in which the displacement of atoms occurs in a plane perpendicular to the surface (Rayleigh-type waves). We are not aware of the characteristics of such waves in

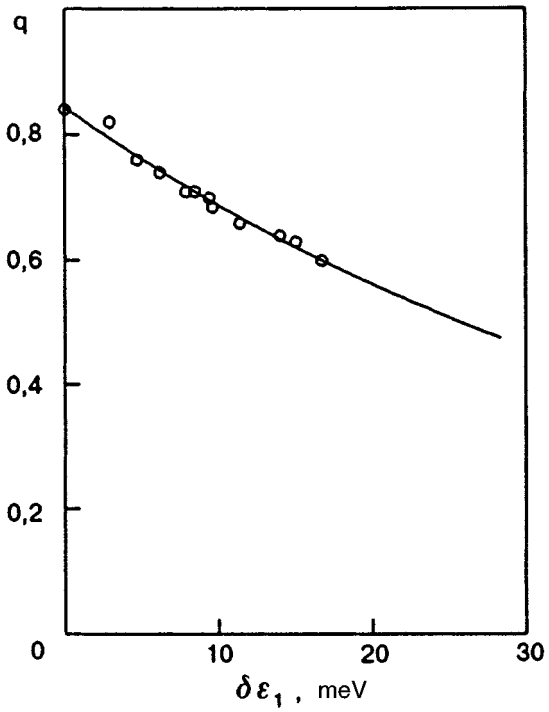

FIG. 3. Change in the specular reflection coefficient q of electrons incident normally at the boundary of the Bi crystal as a function of the excess electron energy.

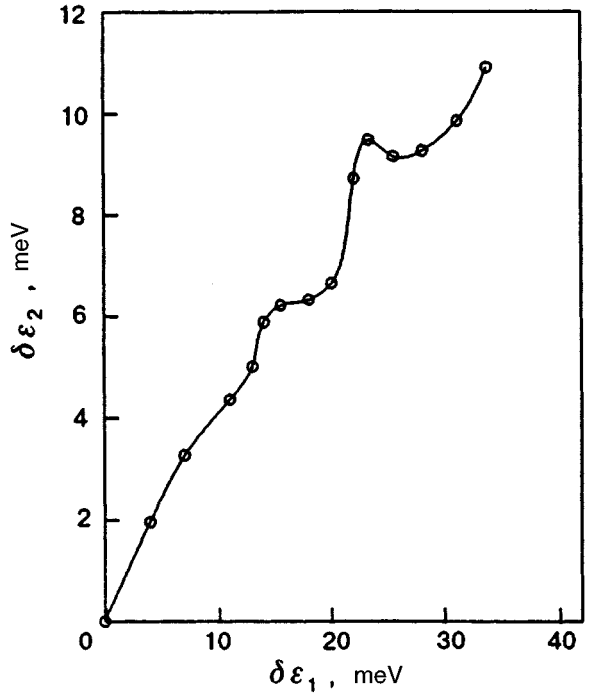

FIG. 4. Dependences of $\delta\varepsilon_2$ on $\delta\varepsilon_1$.

bismuth. In order to evaluate the possible limiting frequency range for surface phonons, we must use the available information on the bulk phonons in bismuth and, above all, phonons with transverse polarization. Transverse acoustic phonons in the bulk of bismuth, propagating along the trigonal axis, are characterized by a limiting energy 4.8 meV, while the longitudinal acoustic phonons have an energy 7.5 meV. The energy of transverse optical phonons lies in the interval 9.2–12.6 meV, while longitudinal optical phonons have an energy 12.6–13.5 meV.[13] Only longitudinal phonons exist in the direction of the binary axis. According to the results of investigations of the phonon spectrum of bismuth using the slow neutron scattering,[14] transverse optical phonons do not give a clearly manifested peak in the phonon density distribution function.

It was shown for the first time in Ref. 15 that surface waves correspond to discrete frequencies that are lower than the limiting frequencies for bulk waves. In the case of bismuth, these frequencies must be lower than the above values for transverse phonons in the bulk. It follows from the experimental data presented in Fig. 2 that there exists a certain threshold value for $\delta\varepsilon_1$ at which the energy loss in electrons commences upon reflection at the surface. However, it is hard to find the exact value of this quantity. An analysis of the dependences presented in Fig. 2 gives $\sim 3-5$ meV for the ratio $\delta\varepsilon_2/\delta\varepsilon_1=1$. An analogous result is obtained by constructing the dependence $\delta\varepsilon_1-\delta\varepsilon_2$ as a function of $\delta\varepsilon_1$. These dependences are found to be straight lines that intersect the abscissa axis at $\delta\varepsilon_1\sim 4$ meV. Note that these estimates are quite rough.

Another result obtained by us from an analysis of the experimental data deserves attention. The dependence of the excess electron energy $\delta\varepsilon_2$ after collision with the surface on the initial excess energy $\delta\varepsilon_1$ is characterized by reproducible nonmonotonicities which are clearly manifested in the dependence of $\delta\varepsilon_2$ on $\delta\varepsilon_1$ (Fig. 4). This dependence reveals slight dips at energies ~ 18 and ~ 25 meV. Hence, in addition to the excitation of surface vibrations as a result of interaction of nonequilibrium electrons with the surface or during their motion in the bulk of the crystal, there exists another relaxation process involving a decrease in the abovementioned characteristic values of energy. We believe that this process is associated with the excitation of plasmon vibrations. According to Ref. 16, the plasmon excitation frequencies in bismuth correspond to the following energy values: 19.6 meV for polarization perpendicular to the trigonal axis C_3 and 23.2 meV for polarization along C_3. The characteristic values of energy corresponding to the dips on the dependence of $\delta\varepsilon_2$ on $\delta\varepsilon_1$ are close to these values.

CONCLUSIONS

An analysis of the relative position of the first two EF lines on the scale of magnetic fields upon a change in the excess electron energy in bismuth has opened new prospects for the transverse focusing technique. This technique has made it possible to detect and determine the drop in excess energy of electrons as they collide with the surface. Such a process begins for low values of the excess electron energy ($\sim 3-5$ meV) and is apparently accompanied by the excitation of surface waves.

*E-mail: komnik@ilt.kharkov.ua

[1] V. S. Tsoi, Pis'ma Zh. Éksp. Teor. Fiz. **19**, 114 (1974) [JETP Lett. **19**, 70 (1974)].
[2] V. S. Tsoi, J. Bass, and P. Wyder, Adv. Phys. **41**, 365 (1992).
[3] V. S. Tsoi, Zh. Eksp. Teor. Fiz. **68**, 1849 (1975) [Sov. Phys. JETP **41**, 927 (1975)].
[4] V. S. Tsoi and Yu. A. Kolesnichenko, Zh. Éksp. Teor. Fiz. **78**, 2041 (1980) [Sov. Phys. JETP **51**, 1027 (1980)].
[5] V. V. Andrievskii, E. I. Ass, and Yu. F. Komnik, Fiz. Nizk. Temp. **11**, 1148 (1985) [*sic*].
[6] S. I. Bozhko, V. S. Tsoi, and S. E. Yakovlev, Pis'ma Zh. Éksp. Teor. Fiz. **36**, 123 (1982) [JETP Lett. **36**, 153 (1982)].
[7] V. S. Tsoi, N. P. Tsoi, and S. E. Yakovlev, Zh. Éksp. Teor. Fiz. **95**, 921 (1989) [Sov. Phys. JETP **68**, 530 (1989)].
[8] G. Wexler, Proc. Phys. Soc. **89**, 927 (1966).
[9] Yu. A. Kolesnichenko, Fiz. Nizk. Temp. **18**, 1059 (1992) [Sov. J. Low Temp. Phys. **18**, 741 (1992)].
[10] V. V. Andrievskii, Yu. F. Komnik, and S. V. Rozhok, Fiz. Nizk. Temp. **22**, 1406 (1996) [Low Temp. Phys. **22**, 1066 (1996)].
[11] V. V. Andrievskii, Yu. F. Komnik, and S. V. Rozhok, Fiz. Nizk. Temp. **22**, 1418 (1996) [Low Temp. Phys. **22**, 1076 (1996)].
[12] Yu. A. Kolesnichenko and R. I. Shekhter, Fiz. Nizk. Temp. **15**, 959 (1989) [Sov. J. Low Temp. Phys. **15**, (1989)].
[13] J. L. Yarnell, J. L. Warren, R. G. Wenzel, and S. H. Koenig, IBM Res. Dev. **8**, 234 (1964).
[14] B. A. Kotov, N. M. Okuneva, and E. L. Plachenova, Fiz. Tverd. Tela **11**, 2003 (1969) [Sov. Phys. Solid State **11**, 1615 (1969)].
[15] I. M. Lifshits and L. N. Rozentsveig, Zh. Éksp. Teor. Fiz. **18**, 1012 (1948).
[16] V. S. Edel'man, Usp. Fiz. Nauk, **123**, 257 (1977).

Translated by R. S. Wadhwa

Photoconductivity of a quantum ballistic contact

V. S. Borovikov and L. Yu. Gorelik

*B. Verkin Institute for Low Temperature Physics and Engineering, National Academy of Sciences of the Ukraine, 310164 Kharkov, Ukraine**

V. Z. Kleĭner

National Science Center ''Kharkov Physicotechnical Institute'', 310108 Kharkov, Ukraine

R. I. Shekhter

Department of Applied Physics, Chalmers University of Technology and Göteborg University, S-412 96 Göteborg, Sweden

(Submitted July 19, 1996; revised September 27, 1996)
Fiz. Nizk. Temp. **23**, 313–318 (March 1997)

The electron transport through a microscopic constriction in a two-dimensional quantum channel in an alternating transverse electromagnetic field is considered. A general expression is derived for the photoconductivity as a function of elements of a multichannel scattering S-matrix. This expression generalizes the Landauer formula for the conductivity of a $2D$ ballistic point contact (BPC) to the case of inelastic processes of interaction of ballistic electrons with alternating electromagnetic field. The relation between the symmetry of the S-matrix of electrons and the transport properties of the BPC in a nonstationary field is considered. The photoconductivity of a BPC with an adiabatic geometry is obtained in the semiclassical approximation. [S1063-777X(97)00903-1]

1. The fundamental concepts concerning the nature of electron transport through narrow ballistic point contacts (BPC) are based on the well-known Landauer concept.[1] The physical assumptions underlying this concept can be formulated as follows:

(1) voltage drop takes place only in the point-contact region;
(2) the motion of electrons in this region is ballistic;
(3) the distribution function for electrons incident on the point contact is determined by only two completely independent reservoirs (''banks'') which are in thermal equilibrium.

These assumptions are apparently valid for the description of narrow channels which connect the reservoirs and have a length smaller than the phonon mean free path for electrons, but a width large enough for the number of transverse quantization modes to be much larger than the number of transverse modes propagating through a channel. Landauer[1] proved that under the conditions formulated above, the problem of determining the steady-state conductivity in the case of elastic scattering at a BPC is essentially reduced to a purely dynamic problem of calculation of the S-matrix of potential scattering of ballistic electrons. The Landauer theory successfully describes the results of numerous experiments on conductivity of point contacts in a $2D$ electron gas of semiconducting heterostructures and is generally accepted. On the other hand, a unified consistent theory for the case of inelastic scatterers in the BPC region has not been developed yet.

This research aims at obtaining a general expression for describing the conductivity of a BPC in the presence of inelastic scattering processes induced by a varying field on the basis of the main assumptions of the Landauer theory. Such an analysis is also important in connection with recent experiments on the measurement of photoconductivity of point contacts in $2D$ semiconducting structures.[2]

2. In order to derive a general expression for the conductivity of a $2D$ BPC, we will proceed from the Schrödinger equation with the time-dependent Hamiltonian

$$H(t)=-\frac{\hbar^2}{2m}\Delta_{x,y}+U(x,y)+V(x,y)\cos\,\omega t,$$

in which $U(x,y)$ is the effective potential which determines the point-contact geometry and which varies along the x axis only in the contact region $-L<x<L$, so that $U(x,y)=U(y)$ for $|x|>L$ (at the same time, the potential increases unlimitedly along the y axis, thus ensuring the finiteness of the motion of a particle in this direction), and $V(x,y)$ is the effective potential of the external alternating field. Because of these conditions, the electron spectrum outside the point contact region in zero alternating field has a well-defined band structure of a multimode one-dimensional system, i.e.,

$$\varepsilon_n(k)=\frac{\hbar^2k^2}{2m^*}+E_n,$$

where ''the transverse'' energies E_n are eigenvalues of the operator

$$H_y=-\frac{\hbar^2}{2m^*}\frac{\partial^2}{\partial y^2}+U(y);$$

k is the wave vector in the direction of the x axis, and m^* is the electron effective mass.

It is convenient to carry out the analysis of the dynamics of a system in a field varying periodically with time in the quasi-energy representation of the wave function

$$\Psi_e(x,n,t)=\sum_l \Psi_\varepsilon(x,n,l)\exp[-i(l\omega t+\varepsilon t/\hbar)], \qquad (1)$$

where the functions $\Psi_\varepsilon(x,n,l)$ are solutions of the time-independent Schrödinger equation $H\Psi_\varepsilon = \varepsilon\Psi_\varepsilon$ with the effective Hamiltonian

$$\hat{H}=\hat{H}_0+\hat{W};$$

$$\hat{H}_0=\left[\left(-\frac{\hbar^2}{2m^*}\frac{\partial^2}{\partial x^2}+E_n\right)\delta_{nn'}-\hbar\omega l\right]\delta_{ll'};$$

$$\hat{W}=\hat{U}+\hat{V};$$

$$\hat{U}=\left[\int_{-\infty}^{\infty}dy\,\varphi_n(y)U(x,y)\varphi_{n'}(y)-E_n\delta_{nn'}\right]\delta_{ll'};$$

$$\hat{V}=\frac{1}{2}\left[\int_{-\infty}^{\infty}dy\,\varphi_n(y)V(x,y)\varphi_{n'}(y)\right](\delta_{l-1,l'}+\delta_{l+1,l'}); \qquad (2)$$

Here $\varphi_n(y)$ are the real-valued eigenfunctions of the operator H_y.

The wave function $\Psi_\varepsilon(x,n,l)$ is multiple-valued due to the quasi-energy representation, which is manifested in the fact that if $\Psi_\varepsilon(x,n,l)$ is an eigenvector of the operator H with the eigenvalue ε, then the function

$$\Psi_{\varepsilon+\hbar\omega l'}(x,n,l)\equiv\Psi_\varepsilon(x,n,l-l') \qquad (3)$$

is also an eigenvector, which, according to Ref. 1, generates the same solution of the time-dependent problem.

In view of the local nature of the perturbation $\hat{W}$ in the coordinate x, the complete set of eigenfunctions of the operator $\hat{H}$ can be constructed on the basis of the scattering states $|\Psi^{(+)}_{NLk}\rangle$ ($N=1,2,\ldots; L=0,\pm1,\pm2,\ldots; -\infty<k<\infty$), which are solutions of the Lippmann–Schwinger equation

$$|\Psi^{(+)}_{NLk}\rangle=|\Phi^{(+)}_{NLk}(n,l,x)\rangle+\hat{G}_0^+(\varepsilon_{NL}(k))\hat{W}|\Psi^{(+)}_{NLk}\rangle, \qquad (4)$$

where

$$\Phi_{NLk}(n,l,x)=(2\pi)^{-1/2}e^{ikx}\delta_{nN}\delta_{lL},$$

$$\varepsilon_{NL}(k)=\varepsilon_N(k)-\hbar\omega L$$

are the eigenstates and eigenvalues of the operator $\hat{H}_0$; $G_0^+(\varepsilon)=(\varepsilon-\hat{H}_0+iv)^{-1}$. Using the explicit expression for the unperturbed Green's function

$$G_0^+(\varepsilon)=i\,\frac{\delta_{nn'}\delta_{ll'}}{v_{nl}}\exp[i\hbar k_{nl}(\varepsilon)|x|];$$

$$v_{nl}=\frac{\hbar}{m^*}k_{nl}(\varepsilon);$$

$$k_{nl}(\varepsilon)=k_{nl}(\varepsilon+\hbar\omega l)=\frac{1}{\hbar}\sqrt{2m^*(\varepsilon-E_{nl}+\hbar\omega l)},$$

we can prove that the asymptotic forms of the solutions of Eq. (4), which are normalized to the δ-function and which describe the scattering of plane waves incident on a BPC, have the following form in the (n,l,x)-representation:

$$\Psi^{(+)}_{NLk}(n,l,x)$$

$$=\frac{1}{\sqrt{2\pi}}\begin{cases}e^{ikx}\delta_{nN}\delta_{lL}+R^{lL}_{nN}(|k|,\sigma)\\ \quad\times\exp[-i\sigma k_{nl}(\varepsilon_{NL}(k))x]; & \sigma x<-L;\\ T^{lL}_{nN}(|k|,\sigma)\exp[i\sigma k_{nl}(\varepsilon_{NL}(k))x]; & \sigma x>L,\end{cases} \qquad (5)$$

where $\sigma=\mathrm{sgn}(k)$. It should be noted that the coefficients R^{lL}_{nN} and T^{lL}_{nN} in expressions (5) are connected directly with the elements of the multichannel S-matrix of scattering

$$\hat{S}\equiv\begin{pmatrix}\hat{r}(|k|,+1) & \hat{t}(|k|,+1)\\ \hat{t}(|k|,-1) & \hat{r}(|k|,-1)\end{pmatrix}; \quad \hat{S}\hat{S}^+=1 \qquad (6)$$

through the expressions

$$t^{lL}_{nN}(|k|,\sigma)=\left[\frac{k_{nl}(\varepsilon_{NL}(k))}{|k|}\right]^{1/2}T^{lL}_{nN}(|k|,\sigma); \qquad (7)$$

$$r^{lL}_{nN}(|k|,\sigma)=\left[\frac{k_{nl}(\varepsilon_{NL}(k))}{|k|}\right]^{1/2}R^{lL}_{nN}(|k|,\sigma). \qquad (8)$$

In accordance with Eqs. (1), (7), and (8), the solutions of the time-dependent Schrödinger equation generated by the states $|\Psi^{(+)}_{N0k}\rangle$ have the form

$$\Psi_{Nk}(n,x,t)=\frac{1}{\sqrt{2\pi}}$$

$$\times\begin{cases}\exp[ikx-i\varepsilon_N(k)]\delta_{nN}+\sum_l R^l_{nN}(|k|,\sigma)\\ \quad\times\exp[-i\sigma k_{nl}(\tilde{\omega})x-i\tilde{\omega}t/\hbar]; & \sigma x<-L;\\ \sum_l T^l_{nN}(|k|,\sigma)\exp[i\sigma k_{nl}(\tilde{\omega})x-i\tilde{\omega}t/\hbar]; & \sigma x>L\end{cases} \qquad (9)$$

and describe inelastic scattering of an electron with the transverse quantum number N and the wave vector k at a microscopic constriction ($\tilde{\omega}=\varepsilon_N(k)+\hbar\omega l$). In this case, the coefficients $T^l_{nN}\equiv T^{l0}_{nN}$ and $R^l_{nN}\equiv R^{l0}_{nN}$ determine the scattering probability amplitudes for an electron in a state with the transverse quantum number n with the absorption of l energy quanta $\hbar\omega$. Obviously, these solutions are important for calculating the nonstationary ballistic transport through a BPC.

3. While deriving a general expression for current through a contact, we will use the generally accepted Landauer approach, according to which the electron distribution function away from a microscopic constriction is in equilibrium and is defined as

$$f_N^{(\pm)}(k)=f_0\left(\varepsilon_N(k)\mp\frac{1}{2}eV\right),$$

where $f_0(\varepsilon)$ is the Fermi function, V is the voltage across the point contact, and the sign $+(-)$ corresponds to the region to the left (right) of the BPC. In this case, the one-particle density matrix $\hat{\gamma}(t)$ which ensures the satisfaction of the boundary conditions, according to which the flux incident on the BPC from the left (right) is determined by the equilibrium function $f_0(\varepsilon_N(k) - 1/2\ eV)$ and on the right by the function $f_0(\varepsilon_N(k) + 1/2\ eV)$, which explicitly takes into account the assumption on the absence of electron correlations of reservoirs, can be constructed on the basis of the wave functions (9) as follows:

$$\hat{\gamma}(t)=\sum_{N,|k|,\sigma} f_N^{\sigma}(k)\Psi_{N,|k|,\sigma}(n,x,t)\Psi^{*}_{N,|k|,\sigma}(n,x,t). \quad (10)$$

The period-averaged current I_{x_0} through the cross section at point x_0 is defined as

$$I_{x_0}=e\,\frac{\omega}{2\pi}\int_0^{2\pi/\omega}dt\sum_n\left[\frac{\hbar}{2m^*i}\left(\frac{\partial}{\partial x}-\frac{\partial}{\partial x'}\right)\times\hat{\gamma}_{nn'}(x,x',t)\right]_{x=x'=x_0} \quad (11)$$

and is naturally independent of the choice of the cross section (this fact follows directly from the continuity equation $[(\partial/\partial x)I_x = \partial/\partial t\Sigma_n\gamma_{nn}(x,x,t)]$. Consequently, the point of observation x_0 can be displaced, for example, to a region separated by large distance from the microconstriction, where the asymptotic expressions (9) are valid. The substitution of these expressions into (11) and simple calculations give[1)]

$$I=\frac{e}{\pi}\sum_{N,k}\sum_{n,l}\left[f_0\left(\varepsilon_N(k)-\frac{1}{2}eV\right)|T^{l0}_{nN}(|k|,1)|^2+f_0\left(\varepsilon_N(k)+\frac{1}{2}eV\right)(|R^{l0}_{nN}(|k|,-1)|^2-\delta_{nN}\delta_{l0})\right]v_{nl}(\varepsilon_N(k)). \quad (12)$$

Taking into account relations (7) and (8), and the equality

$$\sum_{n,l}\left[|t^{l0}_{nN}(|k|,-1)|^2+|r^{l0}_{nN}(|k|,-1)|^2\right]=1$$

(a consequence of the unitary nature of the S-matrix), and also assuming that $\varepsilon_N \gg eV$ and the temperature is equal to zero, after the replacement of summation over the momentum $\mathbf{k}$ by integration with respect to the energy of an impinging electron, we obtain the expression

$$I=\sum_{N,n,l}\left[2\frac{e}{h}\int_0^{\infty}d\varepsilon f_0(\varepsilon)(|t^l_{nN}(\varepsilon,1)|^2-|t^l_{nN}(\varepsilon,-1)|^2)+\frac{e^2V}{h}(|t^l_{nN}(\mu,1)|^2+|t^l_{nN}(\mu,-1)|^2)\right], \quad (13)$$

where μ is the Fermi energy. The quantity $t^l_{nN}(\varepsilon,\sigma) \equiv t^{l0}_{nN}[k_N(\varepsilon,\sigma)]$ is the scattering probability amplitude for an electron with energy ε and the transverse quantum number N to the state with the transverse quantum number n and the energy $\varepsilon+\hbar\omega l$ after its passage through the BPC. The indices N and n label the scattering channels, and the entire process under investigation can be regarded as an inelastic scattering of particles from channel N to channel n.

4. The inclusion of the symmetry factors simplifies Eq. (13) considerably. One of these factors, i.e., the reversibility of scattering in time, is directly connected with the real-valuedness of the operator $\hat{W}=\hat{U}+\hat{V}$. According to definition (3), this operator is real since the functions $\varphi_n(y)$ are real-valued. Under these conditions, the S-matrix is known to be symmetric: $\hat{S}=\hat{S}^T$ (see, for example, Ref. 3). Thus, by definition (6), the matrices $\hat{r}(k,\pm1)$ of the ''backward'' scattering amplitudes are also symmetric. Accordingly, the matrices $\hat{t}(k,\pm1)$ of ''forward'' scattering amplitudes are connected through the relation

$$\hat{t}(k,+1)=\hat{t}^T(k,-1).$$

Taking into account the latter circumstance, it can be easily verified that in zero alternating field, when $t^l_{nN}(\varepsilon,\pm1)=0$ for $l \neq 0$, the first term in the brackets of Eq. (13) vanishes, while the second term coincides with the Landauer formula for static conductivity $G = (2e^2/h)\Sigma_{nn'}|t^l_{nn'}(\mu)|^2$ of a multichannel system. In the general case of inelastic processes, the amplitudes of ''forward'' scattering from left to right and from right to left are connected, according to the detailed balancing principle, by the relation

$$|t^{l0}_{nN}(\varepsilon,-1)=|t^{-l,0}_{nN}(\varepsilon+\hbar\omega l,+1)|.$$

[see Eq. (3)]. Using this relation, the first term in (13) can be reduced to the form

$$I_{\mathrm{ph}}=\frac{2e}{h}\int_0^{\infty}d\varepsilon\sum_l\left[f_0(\varepsilon)-f_0(\varepsilon+\hbar\omega l)\right]\sum_{n,n'}|t^l_{nn'}(\varepsilon)|^2. \quad (14)$$

This expression shows that an alternating field localized in the BPC region generally can induce a steady-state current for zero potential difference applied to the banks. Such a photovoltaic effect was considered in Refs. 4 and 5 for a quantum contact of special geometry.[2)]

5. We will consider below symmetric scattering potential $\hat{W}(-x)=\hat{W}(x)$. In this case, the forward scattering amplitudes satisfy the relation

$$|t^l_{Nn}(\varepsilon,+1)|=|t^l_{Nn}(\varepsilon,-1)|.$$

As a result, of which the photocurrent (14) is equal to zero according to (13), and the conductivity at $T=0$ is defined as

$$G=\frac{2e^2}{h}\sum_l\sum_{n,n'}|t^l_{nn'}(\mu)|^2. \quad (15)$$

This formula generalizes the Landauer result to the case of electron transport through a symmetric BPC, taking into account the inelastic processes in a varying applied field. It should be noted that $t^l_{nn'}$ contains contributions from elastic and inelastic processes for $l=0$ and $l \neq 0$. The contribution from the latter processes can be separated by introducing the T-operator $\hat{\tau}$ of electron scattering by the varying field, which is formally defined as

$$\hat{\tau}=\hat{V}+\hat{V}G_s\hat{\tau},$$

where the Green's function $G_s=(\varepsilon-\hat{H}_s+iv)^{-1}$ describes the scattering at the potential $U(x,y)$; i.e.,

$$\hat{H}_s=(\hat{H}_0+\hat{U}-\hbar\omega l)\,\delta_{ll'}\,.$$

Using the relation between the matrix elements of the scattering operator and the elements of the S-matrix, as well as the universal relations between the scattering operator and the Green's function (see, for example, Ref. 9), we can express the amplitudes t^l_{Nn} in (15) in terms of the matrix elements of the operator $\hat{\tau}$:

$$t^l_{nN}(\varepsilon,\sigma)=t^{\rm st}_{nN}(\varepsilon,\sigma)\,\delta_{l0}-\frac{2\pi i}{\hbar}\,\langle\Phi^{(-)}_{n,\sigma k_n(\varepsilon+\hbar\omega l)}|\,\hat{\tau}\,|\Phi^{(+)}_{N,\sigma k_N(\varepsilon)}\rangle, \qquad (16)$$

where $t^{\rm st}_{nN}$ and $|\Phi^{(+)}_{n,\sigma k_n(\varepsilon)}\rangle$ are the scattering amplitudes and states of the Hamiltonian $\hat{H}_s$, which are determined by the corresponding Lippmann–Schwinger equation. Using (16), we can write expression (15) in the form $G=G_s+G_p$, where G_s is the static conductivity component, and G_p is photoconductivity:

$$G_p=\frac{4\pi e^2}{\hbar^3}\sum_l\sum_{n,n'}|\langle\Phi^{(-)}_{n,\sigma k_n(\mu+\hbar\omega l)}|\,\tau^{(l)}\,|\Phi^{(+)}_{n',\sigma k_{n'}(\mu)}\rangle|^2-\frac{4e^2}{\hbar^3}\,{\rm Im}\left[\sum_{n,n'}[t^{\rm st}_{nn'}(\mu)]^*\langle\Phi^{(-)}_{n,\sigma k_n(\mu)}|\,\tau^{(0)}\,|\Phi^{(+)}_{n',\sigma k_{n'}(\mu)}\rangle\right], \qquad (17)$$

where $\tau^{(l)}=\tau^{l0}_{nn'}$. Equation (17) expresses photoconductivity of a BPC in terms of the matrix elements of the operator $\tau^{(l)}$, calculated from the scattering states in the static potential.

6. We will use the general expression (17) obtained above for calculating photoconductivity in the most important (from the point of view of experimental applications) case of a BPC with an adiabatic geometry, i.e., with a smooth variation of the potential $U(x,y)$ along the x-direction in the scale of the de Broglie wavelength for electron. It is well known[10] that in this case the motion occurs with the conservation of transverse quantum number, and hence the matrix of the amplitudes $t^{\rm st}_{nn'}$ is diagonal and can be presented in the form

$$t^{\rm st}_{nn'}=\theta(\varepsilon-E_n)\,{\rm e}^{i\sigma\chi_n(\varepsilon)}\,\delta_{nn'}\,. \qquad (18)$$

Here $\chi_n(\varepsilon)$ is the phase factor. The states $|\Phi^{(\pm)}_{N,\sigma k_N(\varepsilon)}\rangle$ in the adiabatic case are described by semiclassical wave functions which are related by

$$\Phi^{(-)}_n(\varepsilon,\sigma)=\Phi^{(+)}_n(\varepsilon,\sigma)\,{\rm e}^{-i\sigma\chi_n(\varepsilon)}\,\theta(\varepsilon-E_n)+\Phi^{(+)}_n(\varepsilon,-\sigma)\,{\rm e}^{-i\chi_n(\varepsilon,-\sigma)}\,\theta(E_n-\varepsilon). \qquad (19)$$

In these expressions, the θ-functions for a fixed n separate semiclassical electron states into those propagating through a BPC without reflection $[\varepsilon>E_n=\max E_n(x)]$ and those that are reflected from the BPC completely $(\varepsilon<E_n)$. In zero varying field, this leads to fundamental quantization of conductivity of the adiabatic BPC.[10] Using Eqs. (16), (18), and (19), we can present expression (17) in the form

$$G_p=\frac{4\pi e^2}{\hbar^3}\sum_l\sum_{nN}(A^{(+),l}_{Nn}[\,\theta(E_N-\mu)\,\theta(\mu-E_n+\hbar\omega l)+\theta(E_N-\mu)\,\theta(E_n-\hbar\omega-\mu)]-A^{(-),l}_{Nn}[\,\theta(\mu-E_N)\,\theta(E_n-\hbar\omega l-\mu)+\theta(\mu-E_N)\,\theta(\mu-E_n+\hbar\omega l)]), \qquad (20)$$

where

$$A^{(\pm),l}_{Nn}=|\langle\Phi^{(-)}_{n,\pm k_n(\mu+\hbar\omega l)}|\,\tau^{(l)}\,|\Phi^{(+)}_{N,k_N(\mu)}\rangle|^2.$$

In this case, we have used the relation for the operator $\hat{\tau}$:

$$\langle\Phi^{(+)}_{N,k_N(\varepsilon)}|\,\tau^{(0)*}-\tau^{(0)}\,|\Phi^{(+)}_{N,k_N(\varepsilon)}\rangle=2\pi\sum_{n,l,\sigma=\pm1}|\langle\Phi^{(-)}_{n,\sigma,k_n(\varepsilon+\hbar\omega l)}|\,\tau^{(l)}\,|\Phi^{(+)}_{N,k_N(\varepsilon)}\rangle|^2,$$

which follows from the generalized optical theorem.[3] Estimating the semiclassical matrix elements $A^{(\pm),l}_{Nn}$ in (20), we can verify that in the Born approximation for small amplitudes of the varying field, the contribution to photoconductivity comes only from the first terms in the brackets of Eq.(20):

$$G_p=\frac{4\pi e^2}{\pi^3}\sum_{n,l,N}[A^{(+),l}_{Nn}\,\theta(E_N-\mu)\,\theta(\mu-E_n+\hbar\omega l)-A^{(-),l}_{Nn}\,\theta(\mu-E_N)\,\theta(E_n-\hbar\omega l-\mu)]. \qquad (21)$$

The first term describes the motion of an electron through a BPC, which is induced by its scattering from the reflecting mode to the one propagating after absorption of l field quanta. The second term, in contrast, corresponds to scattering from the propagating mode to the reflected one with the radiation of the field and reduces the value of the conductivity. Expression (21) coincides completely with the result obtained in Ref. 11 in the framework of the consistent theory of perturbations in varying field.

Thus, the general expression (17) obtained for photoconductivity in terms of the matrix elements of a multichannel S-matrix of scattering generalizes the Landauer formula for the conductivity of a $2D$ BPC to the case of inelastic processes of interaction of ballistic electrons with an alternating electromagnetic field. Equation (21) gives the photoconductivity of a BPC with an adiabatic geometry in the semiclassical approximation.

This research was supported, in part, by the INTAS grant No. 94-3862.

*E-mail: borovikov@ilt.kharkov.ua

[1)]Here we also take into account the factor 2 which appears in the summation in the electron spin degrees of freedom.

[2)]It should be noted that in some publications (see Refs. 6 and 7) the formulas for current similar to (12) include, in addition to $f_0(\varepsilon_n-eV/2)$, an additional factor $[1-f_0(\varepsilon_n+\hbar\omega l+eV/2)]$, in analogy with the method of tunnel Hamiltonian, assuming that this factor reflects the Pauli exclusion principle. Such an artificial application of the circuit which is suitable in the limit of small transparency is extremely doubtful in the case of description of ballistic point contacts and was criticized more than once (see, for example, the review by Landauer).[8] In the problem under investigation, the terms linear in the distribution function are omitted completely in the ex-

pression for current as in the case of static scattering at a BPC in view of the above-mentioned symmetry of the *S*-matrix. We especially emphasize this fact since in some publications in which the *S*-matrix is calculated approximately, the inclusion of the ''Pauli'' factors led to the emergence of new effects (e.g., the photovoltaic effect based on the Pauli principle exclusively).[6]

[1] R. Landauer, IBM J. Res. Develop. **1**, 233 (1957): Phil. Mag. **21**, 863 (1970).
[2] Quing Hu, Appl. Phys. Lett. **62**, 837 (1993).
[3] A. I. Baz', Ya. B. Zel'dovich, and A. V. Perelomov, *Scattering, Reactions, and Decays in Nonrelativistic Quantum Mechanics* [in Russian], Nauka, Moscow (1971).
[4] F. Hekking and Yu. V. Nazarov, Phys. Rev. B **44**, 9110 (1991).
[5] L. Fedichkin, V. Ryzhii, and V. V'yurkov, J. Phys. **5**, 6091 (1993).
[6] F. Hekking and Yu. V. Nazarov, Phys. Rev. B **44**, 1156 (1991).
[7] S. Datta, Phys. Rev. B **45**, 1347 (1992).
[8] R. Landauer, Physica Scripta **T42**, 110 (1992).
[9] J. Ziman, *Elements of Advanced Quantum Theory*, Cambridge Univ. Press, Cambridge (UK) (1969).
[10] L. I. Glazman, G. B. Lesovik, D. E. Khmel'nitskii, and R. I. Shekhter, Pis'ma Zh. Éksp. Teor. Fiz. **48**, 218 (1988) [JETP Lett. **48**, 238 (1988)].
[11] L. Yu. Gorelik, A. Grinzwaig, M. Jonson, *et al.*, Physica B **210**, 452 (1995).

Translated by R. S. Wadhwa

Ballistic transport and interband interference in two-dimensional quantum contacts

M. V. Moskalets

93a/48, pr. Il'icha, 310020 Kharkov, Ukraine
(Submitted September 10, 1996; revised September 26, 1996)
Fiz. Nizk. Temp. **23**, 319–326 (March 1997)

A new effect, viz., the oscillatory dependence of the collector current on the diameter of the diagram confining the electron flow from the emitter to the collector, is considered. Such a dependence is due to a change in the position of conducting subbands of the diaphragms upon a change in its diameter. It is also shown that the collector current contains a noticeable interference component (associated with the Aharonov–Bohm effect and corresponding to the mixing of conduction channels of the quantum diaphragm) in the case of a strong mismatching of electron states outside and inside the diaphragm. © *1997 American Institute of Physics.* [S1063-777X(97)01003-7]

INTRODUCTION

Ballistic electron transport in mesoscopic systems[1] has become an object of interest in connection with the possibility of experimental creation of controllable structures whose size is comparable with the electron wavelength λ_F, on the one hand, and due to the fact that the quantum-mechanical (wave) nature of charge carriers is manifested in such structures on the macroscopic level, on the other.

This is manifested most clearly in the conductivity of two-dimensional ballistic point contacts in the form of a narrow bridge (whose width d is comparable with λ_F) connecting two regions in a two-dimensional electron gas (see Fig. 1). It was shown experimentally in Refs. 2 and 3 that the conductance G of such a junction is quantized in the units of $G_0=2e^2/h$. The reason behind this is a restriction in the transverse (relative to the contact axis) motion of electrons in the microscopic constriction region, and consequently the quantization of the transverse momentum of particles.[2–11] Each quantization level $\varepsilon_n=(\pi n\hbar/d)^2/2m$ $(n=1,2,\ldots)$ corresponds to the one-dimensional subband $\varepsilon_n(p_x)=p_x^2/2m+\varepsilon_n$ (the x axis is directed along the contact axis) with the conductance $G_n=G_0$. The number N of conducting subbands is determined by the magnitude of the Fermi energy ε_F of electrons in the banks ($x\to\pm\infty$; the junction coordinate $x=0$) and by the contact width d which limits the separation between transverse quantization levels. The subband is conducting under the condition $\varepsilon_n<\varepsilon_F+e\varphi(d)$ [$\varphi(d)$ is the potential emerging between the junction and the banks].[12] According to the multichannel generalization of the Landauer formula,[13] the conductance of the junction is $G=NG_0$. As the diameter d of the junction is varied, the separation between energy levels, and hence the number of conducting subband changes. Consequently, the $G(d)$ dependence has the shape of a ladder with steps of the same height G_0.

Quantum contacts are usually described by using one of the two models: the model of a junction with a smooth geometry (adiabatic contact)[10,11] or the model of a junction with an abrupt geometry.[4–9] The calculations based on either of these models lead to a step dependence $G(d)$, but the passage of an electron through the contact region differs significantly in these models. For example, in an adiabatic contact a reflectionless matching of electron states in the left and right banks is observed.[10] In this case, each electron state can be unambiguously attributed to a certain conducting subband of the junction. Interband transitions associated with nonadiabaticity of the contact shape at long distances[14] or with the presence of scattering centers in the junction[15] only lead to small corrections for the conductance of the microscopic structure. A different situation takes place for contacts with an abrupt geometry. Mismatching of the electron states in the banks leads to a strong scattering of the electron wave in the regions of conjugation of the junction with the banks. The ''backward'' scattering leads to the multiple passage of the contact region by the electron wave, which is manifested in the form of the resonant structure in the $G(d)$ dependence.[4–9] The ''forward'' scattering leads to the existence of several channels of transition from a certain state $\mathbf{k}$ of the left bank to a certain state $\mathbf{k}'$ of the right bank (via different states in the junction; see Fig. 1b) and (see below) is responsible for the interference term appearing in the expression for the transition probability $|t_{\mathbf{k},\mathbf{k}'}|^2$ ($t_{\mathbf{k},\mathbf{k}'}$ is the element of the transition matrix of the contact). Both these processes lead to a strong interband mixing, It should be noted that no resonant structure on the $G(d)$ dependence was observed in the experiments.[2,3] This is probably due to the fact that the contacts used in these experiments have a smooth shape in view of the electrostatic nature of the potential barrier that forms the microscopic constriction. According to Castano and Kirczenow,[16] the $G(d)$ dependence for nonadiabatic contacts with a smooth shape does not contain a resonant structure either. These authors emphasized a significant role of interband mixing in such contacts.

Among other things, the universal nature of quantization of conductance and its relative insensitivity to details of electron scattering in the contact is due to the fact that conductance G is determined by all electron states of the left and right banks. The expression for G has the form[1]

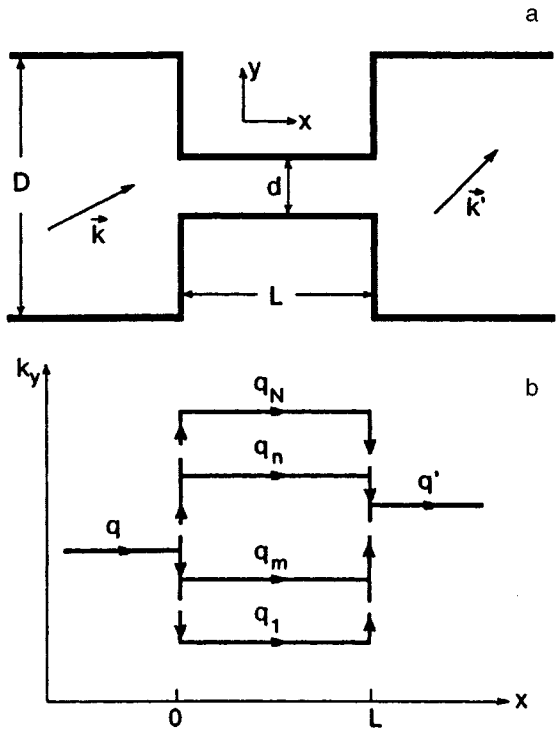

FIG. 1. (a) Model of a quantum contact of length L and width d, which connects $2D$ regions of width D; $\mathbf{k}$ and $\mathbf{k}'$ are the electron wave vectors before and after the passage through the contact, respectively. (b) Phase trajectories of an electron moving through a contact; $q, q_i (1<i\leqslant N)$, and q' are the projections of the electron wave vector on the x axis in front of the contact. in the contact, and behind the contact, respectively.

$$G=\frac{2e^2}{h}\,\mathrm{Tr}(tt^{+})_{\varepsilon_F}=\frac{2e^2}{h}\sum_{\mathbf{k}}\sum_{\mathbf{k}'}|t_{\mathbf{k}\mathbf{k}'}(\varepsilon_F)|^2. \qquad (1)$$

The coefficients of transition matrix $t_{\mathbf{k}\mathbf{k}'}$ themselves contain more detailed information on electron scattering.

In the present paper, we will show that the value of $|t_{\mathbf{k}\mathbf{k}'}|^2$ can be determined by a method similar to the method of transverse electron focusing[17] realized in a two-dimensional electron gas.[18] It was shown theoretically in Ref. 19 that an analysis of the dependence of the collector current I_c on the magnetic field H makes it possible to reconstruct the angular distribution of electrons leaving the emitter. If we place a diaphragm between the emitter and the collector (Fig. 2), the collector current for a fixed value of H is proportional to the transition probability $|t_{\mathbf{k}\mathbf{k}'}|^2$ ($\mathbf{k}$ corresponds to an electron moving from the emitter to the diaphragm, and $\mathbf{k}'$ to an electron moving from the diaphragm to the collector). The collector current $I_c(d)$ in such a situation oscillates depending on the diaphragm diameter d. The peaks on the $I_c(d)$ dependence (Fig. 3) correspond to quantization levels of transverse motion of electrons in the region of microconstriction. Moreover, it is predicted that contacts with a sharp geometry are characterized by a significant interference contribution to I_c, which is associated with the Aharonov–Bohm electrostatic effect.[20]

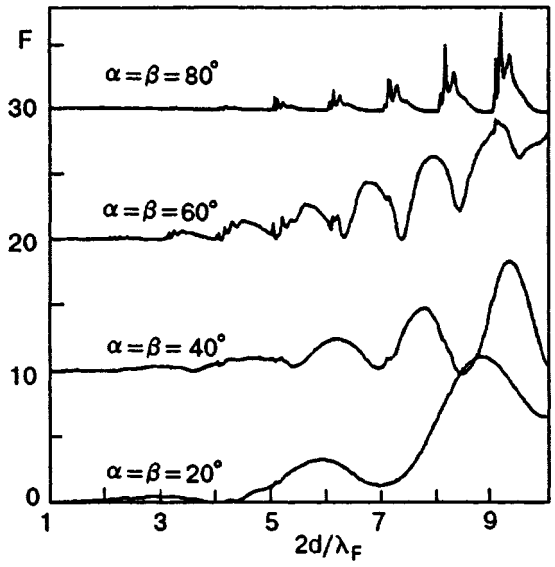

FIG. 3. Dependence of the collector current ($I_c\sim F$) on the diaphragm diameter for various angles of incidence of an electron. The value of $L/\lambda_F=5$. For better visualization, the curves are displaced along the vertical by 0, 10, 20, and 30 rel. units and are compressed along the vertical by a factor of 6.6, 7, 3, and 0.3, respectively.

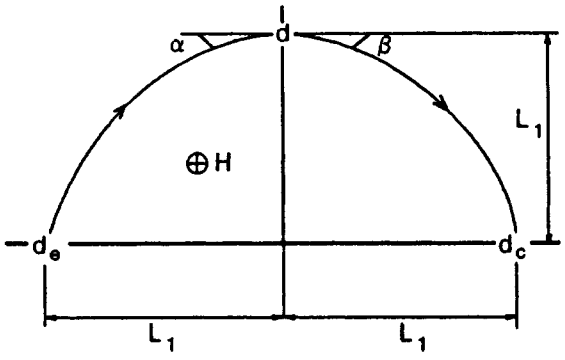

FIG. 2. Schematic diagram of mutual arrangement of the contacts.

1. TRANSITION MATRIX FOR A CONTACT WITH SHARP GEOMETRY

We consider a model of a two-dimensional ballistic contact in the form of a rectangular channel of width d and length L, connecting two broad regions $D\gg d$ (Fig. 1a). The electron mean free path l is assumed to be larger than the characteristic size of the contact ($l\gg L,d$). We will describe the propagation of an electron wave through the contact by the method developed in Ref. 4.

Let us consider an electron having an energy $\varepsilon_{\mathbf{p}}=p^2/(2m)$ and momentum $\mathbf{p}=\hbar\mathbf{k}$ moving through the contact (Fig. 1) from left to right (we denote $k_x\equiv\kappa$ and $k_y\equiv q$). We can write the electron wave function $\Psi_{\mathbf{k}}$ in the form

$$\begin{cases} \Psi_{\mathbf{k}}(x<0)=\chi_q(y)\exp(i\kappa x) \\ \quad +\sum\limits_{\mathbf{k}'} r_{\mathbf{k}\mathbf{k}'}\chi_{q'}(y)\exp(-i\kappa' x), \\ \Psi_{\mathbf{k}}(0<x<L)=\sum\limits_n \varphi_n(y)\left[t_{\mathbf{k}n}\exp(i\kappa_n x)\right. \\ \quad \left.+r_{\mathbf{k}n}\exp(-i\kappa_n x)\right], \\ \Psi_{\mathbf{k}}(L<x)=\sum\limits_{\mathbf{k}'} \tau_{\mathbf{k}\mathbf{k}'}\chi_{q'}(y)\exp(i\kappa' x). \end{cases} \tag{2}$$

Here $\chi_q(y)$ and $\varphi_n(y)$ are the transverse wave functions in the broad band and in the channel, respectively, which are normalized to unity. The summation is extended to all the states satisfying the energy conservation law $\varepsilon_{\mathbf{p}}=\varepsilon_{\mathbf{p}'}=\varepsilon_n+\hbar^2\kappa_n^2/2m$ [in this paper, we do not consider the effect of the electrostatic potential $\varphi(d)$].[12] In addition, $\kappa>0$ and $\kappa'>0$. In order to define the coefficients $t_{\mathbf{k}n}$, $r_{\mathbf{k}n}$, $\tau_{\mathbf{k}\mathbf{k}'}$ and $r_{\mathbf{k}\mathbf{k}'}$, we use the continuity of the wave function (2) and of its derivative for $x=0$ and $x=L$. After simple transformations, we obtain the following system of equations for the quantities $t_{\mathbf{k}n}$ and $r_{\mathbf{k}n}$:

$$\begin{cases} \sum\limits_{\mathbf{k}'}\sum\limits_m \kappa' a_{q'n}a_{q'm}\left[t_{\mathbf{k}m}\exp(i\kappa_m L)\right. \\ \quad \left.+r_{\mathbf{k}m}\exp(-i\kappa_m L)\right]=\kappa_n\left[t_{\mathbf{k}n}\exp(i\kappa_n L)\right. \\ \quad \left.-r_{\mathbf{k}n}\exp(-i\kappa_n L)\right], \\ \sum\limits_{\mathbf{k}'}\sum\limits_m \kappa' a_{q'n}a_{q'm}(t_{\mathbf{k}m}+r_{\mathbf{k}m}) \\ \quad =2\kappa a_{qn}-\kappa_n(t_{\mathbf{k}n}-r_{\mathbf{k}n}). \end{cases} \tag{3}$$

Here $a_{qn}=\int_0^d dy\,\chi_q(y)\varphi_n(y)$ is the overlapping coefficient for transverse wave functions. The solution of this system of equations determines the coefficients $\tau_{\mathbf{k}\mathbf{k}'}$:

$$\tau_{\mathbf{k}\mathbf{k}'}=\mathrm{e}^{-i\kappa' L}\sum_n a_{q'n}(t_{\mathbf{k}n}\mathrm{e}^{i\kappa_n L}+r_{\mathbf{k}n}\mathrm{e}^{-i\kappa_n L}). \tag{4}$$

Calculating the quantum-mechanical current I through a contact with a voltage $eV\ll\varepsilon_F$ applied across the banks in the standard way, at zero temperature, we obtain

$$I=\frac{2e^2}{h}V\sum_{k=k_F}\sum_{k'=k_F}\theta(\kappa)\theta(\kappa')\frac{\kappa'}{\kappa}|\tau_{\mathbf{k}\mathbf{k}'}|^2. \tag{5}$$

Here $\theta(x)$ is the unit step (Heaviside) function. Each term in expression (5) is the current passing through the contact upon a transition of an electron from the state $\mathbf{k}$ in front of the contact to the state $\mathbf{k}'$ behind it. Comparing the expression for the conductance $G=I/V$ obtained from (5) with expression (1), we can determine the relation between the elements of the transition matrix $t_{\mathbf{k}\mathbf{k}'}$ and the coefficients $\tau_{\mathbf{k}\mathbf{k}'}$ defining the amplitude of the wave function after the passage through the contact:

$$t_{\mathbf{k}\mathbf{k}'}=\sqrt{\kappa'/\kappa}\,\tau_{\mathbf{k}\mathbf{k}'}. \tag{6}$$

The quantity $|t_{\mathbf{k}\mathbf{k}'}|^2$ determines the intensity of electron flux in the state $\mathbf{k}'$ after the passage through the contact for a unit intensity of the flux of electron in the state $\mathbf{k}$ incident at the contact.

The solution of the system of equations (3) can be obtained only by numerical methods and requires a considerable computer time. However, Szafer and Stone[4] used similar calculations to substantiate a method of approximate determination of coefficients $t_{\mathbf{k}n}$ and $r_{\mathbf{k}n}$ (the mean-field approximation), lying in the replacement of the exact expression for the coefficients a_{qn} by the approximate expression

$$a_{qn}^2=\frac{d}{D}\left[\theta(q-q_{n-1})-\theta(q-q_{n+1})\right]. \tag{7}$$

In this case, the coefficients a_{qn} must satisfy the completeness condition $\Sigma_q a_{qn}a_{qm}=\delta_{nm}$. It can easily be verified that using definition (7), we can assume to a sufficiently high degree of accuracy that

$$\sum_k \kappa a_{qn}a_{qm}=\delta_{nm}\sum_{q=q_{n-1}}^{q_{n+1}}\kappa=\delta_{nm}(K_n+iJ_n). \tag{8}$$

Substituting (8) into (3), we can determine the coefficients $t_{\mathbf{k}n}$ and $r_{\mathbf{k}n}$. Substituting the obtained expressions into (4), we can find the expression for the coefficients $\tau_{\mathbf{k}\mathbf{k}'}$ in the mean-field approximation:

$$\tau_{\mathbf{k}\mathbf{k}'}=\sum_{n=1}^{N}2\kappa_n\kappa a_{qn}a_{q'n}Z_n^{-1}\exp(-i\kappa' L-\theta_n), \tag{9}$$

where

$$Z_n^2=4K_n^2\kappa_n^2+[(K_n+\kappa_n)^2+J_n^2][(K_n-\kappa_n)^2+J_n^2]\sin^2(\kappa_n L+\varphi_n), \tag{10}$$

$$\tan\varphi_n=2J_n\kappa_n(K_n^2-\kappa_n^2+J_n^2)^{-1}, \tag{11}$$

$$(\tan\theta_n)=\frac{2J_n\kappa_n\cos(\kappa_n L)-(K_n^2+\kappa_n^2-J_n^2)\sin(\kappa_n L)}{2K_n[\kappa_n\cos(\kappa_n L)+J_n\sin(\kappa_n L)]}. \tag{12}$$

Expression (9) shows that the amplitude of transmitted wave ($\tau_{\mathbf{k}\mathbf{k}'}$) consists of N terms corresponding to the existence of N possible channels through a contact, namely, to an electron transition to a certain conducting subband of the contact (see Fig. 1b) (for $L/\lambda_F\gg 1$, the contribution of attenuating modes $n>N$ can be neglected). The contribution from each possible channel of the transition is proportional to the product of the overlapping coefficients $a_{qn}a_{q'n}$. It should be noted that the mean-field approximation (7) and (8) can be applied only for solving the system of equations (3). The quantity θ_n is the phase shift of the electron wave during its passage through the contact in the subband with the number n. For deep energy levels (actually for $n\leqslant N-1$), we have

$$\theta_n=-(1-(n\lambda_F/2d)^2)^{1/2}k_F L. \tag{13}$$

The motion in the subband can be regarded as the motion in the region with the potential energy $\varepsilon_n=(\pi n\hbar/d)^2/(2m)$. Thus, a multichannel analog of the Aharonov–Bohm electrostatic effect is realized in this situation.

While calculating the value of quantities quadratic in $\tau_{\mathbf{k}\mathbf{k}'}$ [such as the current (5)], we encountered interference terms associated with the splitting of the electron wave en-

tering the channel and with subsequent interference of transmitted waves emerging from the channel (see Fig. 1b). Interference is possible in the absence of inelastic processes which destroy the coherent electron state, which we are assuming here.

Further, substituting (9) into (6), we obtain an expression for the quantities $|t_{\mathbf{kk}'}|^2$ in the form

$$|t_{\mathbf{kk}'}|^2=\sum_{n=1}^{N} 4\kappa_n^2\kappa\kappa' a_{qn}^2 a_{q'n}^2 Z_n^{-2}+2\sum_{n=2}^{N}\sum_{m=1}^{n-1} 4\kappa_n\kappa_m\kappa\kappa' \times a_{qn}a_{q'n}a_{qm}a_{q'm}Z_n^{-1}Z_m^{-1}\cos(\theta_n-\theta_m). \quad (14)$$

The first term corresponds to the additive contribution of the conducting subbands to the transition probability, while the second is the interference term. Its sign is determined by the difference in the phase lead in different subbands as well as by the phase jump at the entrance and at the exit of the channel, i.e., by the signs of the quantities a_{qn}.

In the next section, we will consider the schematic diagram of an experiment which makes it possible to determine the coefficients $|t_{\mathbf{kk}'}|^2$ directly.

2. COLLECTOR CURRENT IN THE PRESENCE OF A QUANTUM DIAPHRAGM

Let us consider the ballistic propagation of electrons from the emitter to the collector separated by a diaphragm in a weak magnetic field (see Fig. 2). The diaphragm was in the form of a quantum contact with the elements of transition matrix $t_{\mathbf{kk}'}$, while the collector and the emitter were classical point contacts. When the current I_e was passed through the emitter, a fraction of nonequilibrium electrons scattered by the diaphragm reaches the collector creating the collector current I_c (we assume that electrons cannot move directly from the emitter to the collector). For the mutual arrangement of the contact shown in Fig. 2, the expression for the collector current can be written in the form

$$I_c=I_e\int_{\alpha_2}^{\alpha_1} d\alpha\int_{\beta_2}^{\beta_1} d\beta\,\cos\alpha\,\cos\beta|t(\alpha,\beta)|^2. \quad (15)$$

Here $t(\alpha,\beta)=(D/\lambda_F)t_{\mathbf{kk}'}$;

$$\alpha_{1,2}=\arccos\{[1+(1\mp d/2L_1)^2]^{1/2}L_1/2r_H\}-\arccos\{[1+(1\mp d/2L_1)^2]^{-1/2}\};$$

$$\beta_{1,2}=\arccos\{[1+(1\mp d_c/2L_1)^2]^{1/2}L_1/2r_H\}-\arccos\{[1+(1\mp d_c/2L_1)^2]^{-1/2}\};$$

$2L_1$ is the separation between the contacts, $r_H=cp_F/(eH)$ is the cyclotron radius, and d and d_c are the diameters of the diaphragm and the collector, respectively. We assume that the following conditions are satisfied: $l, r_H > L_1 > d_c, d_e > d \simeq \lambda_F$ (d_e is the diameter of the emitter).

In experiments (see, for example, Ref. 18), the voltage V_c which must be applied to the collector for the total collector current to be equal to zero ($I_c-V_c/R_c=0$, where R_c is the resistance of the collector) is usually measured. It should be noted that in the case of a linear response ($eV_c \ll \varepsilon_F$), the value of I_c does not depend on the voltage across the collector. For a small value of the ratio d/L_1 and d_c/L_1, we can factor $t(\alpha,\beta)$ outside the integral sign in (15) and using (14), we can obtain the following expression for the voltage across the collector:

$$V_c=I_eR_c\,\frac{\lambda_F d_c}{16L_1^2}\left[1+\cot\left(\alpha+\frac{\pi}{4}\right)\right]\left[1+\cot\left(\beta+\frac{\pi}{4}\right)\right]F, \quad (16)$$

where $\alpha=\beta=\arccos(L_1/\sqrt{2}r_H)-\pi/4$. Since $\kappa=k_F\cos\alpha$, $q=k_F\sin\alpha$, $\kappa'=k_F\cos\beta$, and $q'=k_F\sin\beta$, we find that the expression for $F=F_0+F_i$ has the form

$$F_0=\sum_{n=1}^{N} 2\xi\kappa_n^2k_F^2Z_n^{-2}\varphi(n,n). \quad (17)$$

$$F_i=\sum_{n=2}^{N}\sum_{m=1}^{n-1} 4\xi\kappa_n\kappa_m k_F^2Z_n^{-1}Z_m^{-1}\varphi(n,m)\cos(\theta_n-\theta_m), \quad (18)$$

$$\varphi(n,m)=a_n(\alpha)a_m(\alpha)a_n(\beta)a_m(\beta)\cos^2\alpha\,\cos^2\beta, \quad (19)$$

where $\xi=2d/\lambda_F$; $\kappa_n=k_F(1-(n/\xi)^2)^{1/2}$, and

$$a_n(\alpha)=\frac{\sqrt{2}n}{\pi\xi^{3/2}}\,\frac{\sin[\pi\xi(\sin\alpha-\sin\alpha_n)]}{\sin^2\alpha-\sin^2\alpha_n}, \quad (20)$$

where $\alpha_n=\arcsin(n\lambda_F/2d)$.

3. DEPENDENCE OF THE COLLECTOR CURRENT ON THE DIAPHRAGM DIAMETER

Figure 3 shows the dependence of the quantity F which appears in expression (16) and which defines the voltage V_c across the collector (or the collector current $I_c=V_c/R_c$) on the diaphragm diameter d. The presence of peaks on the $I_c(d)$ [accordingly, $V_c(d)$] dependence is mathematically due to the vanishing of the denominator of the overlapping coefficient $a_n(\alpha)$ (20). The physical origin of these phenomena is as follows. The quantity $a_n(\alpha)$ has a peak for $\alpha=\alpha_n$, which corresponds to the coincidence of transverse wave vectors $q_n=\pi n/d$ in the contact (in the nth subband) and $q=k_F\sin\alpha$ outside the contact. A change in the diaphragm diameter d leads to a change in the position of quantization levels in the microscopic constriction, and the condition $q=q_n$ is observed for a certain $d=d_n$. At this instant, the resonant mode of electron passage through the microconstriction is realized in the nth subband, leading to an increase in the collector current. The positions of the peaks are determined by the expression

$$d_n=\frac{\lambda_F}{2}\,\frac{n}{\sin\alpha}. \quad (21)$$

The fine structure of the peaks is associated with two effects: the intraband and interband interference. The interference of electron waves in a conducting subband is associated with ''backward'' scattering at the channel edges, which is responsible for multiple passage of the electron wave through the region of microscopic constriction. This effect is described by the quantity Z_n (10) in expressions (17) and (18) and is manifested in the form of a resonant structure on the $G(d)$ dependence for contacts with a sharp shape.[4–11] A peculiar feature of this effect is that the resonant structure is

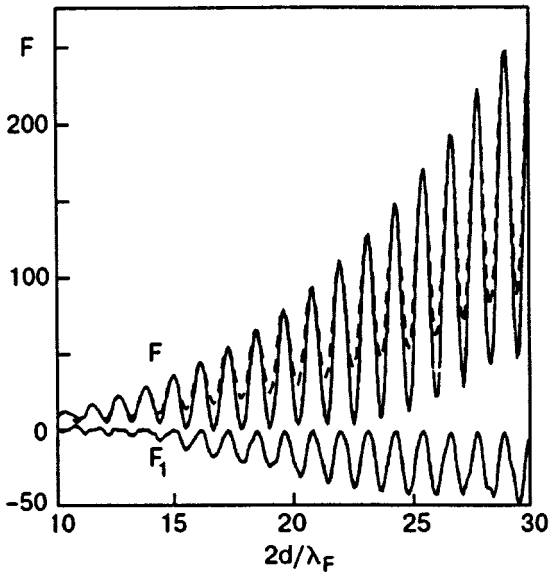

FIG. 4. Collector current ($I_c \sim F$) in the case of large diaphragm diameter for $\alpha=\beta=60°$, $L/\lambda_F=5$. The dashed curve corresponds to the quantity F_0 (17). The curves are compressed along the vertical by a factor of 3.

determined by the contribution from the upper conducting subband alone since the $Z_n(d)$ dependence is smooth for $n<N$. It follows from (21) that the number n of a resonant level is connected with the number $N=[2d/\lambda_F]$ in the contact through the relation $N=[n/\sin\alpha]$ (the brackets indicate the integral part of a number). It can be seen from Fig. 3 that $n=N$ for $\alpha\simeq\pi/2$, i.e., the main contribution to the collector current comes from the upper conducting subband; for this reason, the peak is strongly jagged (for $L/d\gg 1$). As the angle α decreases, the peak is smoothed since the main role is played by deeper energy levels.

The contribution of interband interference to the collector current is defined by Eq. (18). This contribution is significant when a large number of subbands in the microconstriction are conducting. However, for $\alpha\simeq\pi/2$, this contribution is insignificant since the separation between quantization levels in the vicinity of the upper conducting subband (which determines the main contribution to the current in the given case) is large, and the product $a_n(\alpha)a_m(\alpha)(n\neq m)$ is small. Figure 4 shows the dependence of the quantities F, F_0, and F_i on the contact diameter in the region $d\gg\lambda_F/2$. It can be seen that the contribution from interband interference processes considerably affects the shape of the curve.

In the region $d\approx\lambda_F/2$, the peculiarities associated with the two effects are superimposed (Fig. 5a). If, however, we take into account the effect of temperature T, i.e.,

$$|t_{\mathbf{kk}'}(T)|^2=-\int d\varepsilon f'(\varepsilon,T)|t_{\mathbf{kk}'}(\varepsilon)|^2 \tag{22}$$

[$f(\varepsilon,T)$ is the Fermi distribution function], the peculiarities associated with the intraband interferences are smoothed even for $T=0.01\varepsilon_F$ (Fig. 5b).

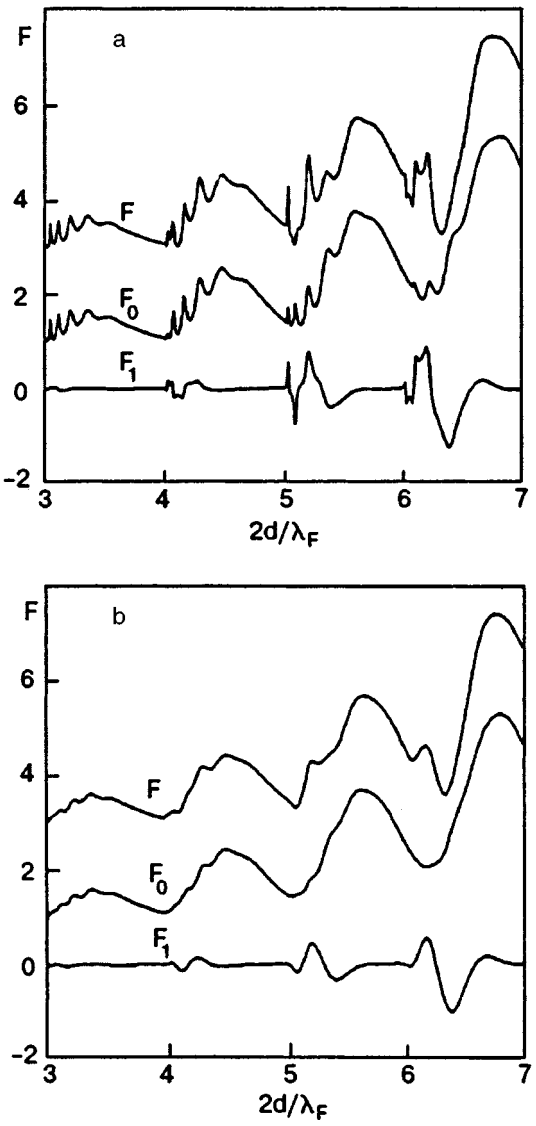

FIG. 5. Dependence of the collector current ($I_c \sim F$) on the diaphragm diameter for $\alpha=\beta=60°$, $L/\lambda_F=5$ at various temperatures: $T=0$ (a) and $T=0.01\varepsilon_F$ (b). The curves are displaced along the vertical by 0.1 and 3 rel. units, respectively, and compressed by a factor of 3.

CONCLUSIONS

We have considered the conductivity of a ballistic microscopic structure consisting of an emitter, a collector, and a quantum diaphragm. It is shown that the current in such a system oscillates with a change in the diaphragm diameter. This is due to the resonant passage of an electron through the microconstriction in the case where the transverse momentum of an impinging electron coincides with the momentum corresponding to one of the quantum energy levels in the microconstriction.

It should be noted that the contribution from electrons reflected from the confining surfaces is not taken into account in expression (15). This contribution is small in weak magnetic fields (is absent for $H=0$) and is manifested in the form of a smooth background on the $V_c(d)$ dependence.

The scattering of an electron wave at the entrance and the exit of the microconstriction (''forward'' scattering)

leads to the emergence of a coherent state corresponding to the passage of the contact over all conducting subbands (see Fig. 1b). The interference of transmitted waves affects the collector current [see (18)]. In this case, the phase shift of the wave $\theta_n \simeq -L(k_F^2-(\pi n/d)^2)^{1/2}$ is different for different subbands and depends on the contact diameter d. This effect is a multichannel analog of the Aharonov–Bohm electrostatic effect.

We have investigated a diaphragm with rectangular edges. Collector current oscillations should be present, however, in the case of an adiabatic contact (playing the role of a diaphragm) also. The only difference lies in the absence of interference contributions, which is manifested in a smoother shape of the peaks.

[1] Y. Imry, in *Physics of Mesoscopic Systems: Directions in Condensed Matter Physics* (ed. by G. Grinstein and G. Mazenco), World Scientific, Singapore (1986).
[2] B. J. van Wees, H. van Houten, C. W. J. Beenakker *et al.*, Phys. Rev. Lett. **60**, 848 (1988).
[3] D. A. Wharam, T. J. Thornton, R. Newbury *et al.*, J. Phys. **C21**, L209 (1988).
[4] A. Szafer and A. D. Stone, Phys. Rev. Lett. **62**, 300 (1989).
[5] G. Kirczenow, Phys. Rev. **B39**, 10452 (1989).
[6] I. B. Levinson, Pis'ma Zh. Éksp. Teor. Fiz. **48**, 273 (1988) [JETP Lett. **48**, 301 (1988)].
[7] L. Escapa and N. Garsia, J. Phys. Condens. Matter. **1**, 2125 (1989).
[8] D. van der Marel and E. G. Haanappel, Phys. Rev. **B39**, 7811 (1989).
[9] A. M. Zagoskin and I. O. Kulik, Fiz. Nizk. Temp. **16**, 911 (1990) [Sov. J. Low Temp. Phys. **16**, 533 (1990)].
[10] L. I. Glazman, G. B. Lesovik, D. E. Khmel'nitskii, and R. I. Shekhter, Pis'ma Zh. Éksp. Teor. Fiz. **48**, 218 (1988) [JETP Lett. **48**, 238 (1988)].
[11] A. Kawabata, J. Phys. Soc. Jpn. **58**, 372 (1989).
[12] M. V. Moskalets, Pis'ma Zh. Éksp. Teor. Fiz. **62**, 702 (1995) [JETP Lett. **62**, 719 (1995)].
[13] M. Büttiker, Y. Imry, R. Landauer, and S. Pinhas, Phys. Rev. **B31**, 6207 (1985).
[14] A. Yacoby and Y. Imry, Phys. Rev. **B41**, 5341 (1990).
[15] A. M. Zagoskin and R. I. Shekhter, Phys. Rev. **B50**, 4909 (1994).
[16] E. Castano and G. Kirczenow, Phys. Rev. **B45**, 1514 (1992).
[17] V. S. Tsoi, Pis'ma Zh. Éksp. Teor. Fiz. **19**, 114 (1974) [JETP Lett. **19**, 70 (1974)].
[18] H. van Houten, C. W. J. Beenakker, J. G. Williamson *et al.*, Phys. Rev. **B39**, 8556 (1989).
[19] M. V. Moskalets, Pis'ma Zh. Éksp. Teor. Fiz. **63**, 604 (1996) [JETP Lett. **63**, 639 (1996)].
[20] Y. Aharonov and D. Bohm, Phys. Rev. **115**, 484 (1959).

Translated by R. S. Wadhwa

Experimental and theoretical study of the optical properties of crystalline and amorphous $TiSi_2$ films

V. N. Antonov, Yu. V. Kudryavtsev, Yu. N. Makogon, V. V. Nemoshkalenko, A. Ya. Perlov, and T. T. Silakova

*Institute of Metal Physics, National Academy of Sciences of Ukraine, 36 Vernadsky str., 252680 Kiev-142, Ukraine**

(Submitted June 17, 1996; revised July 30, 1996)
Fiz. Nizk. Temp. **23**, 327–333 (March 1997)

Optical properties of amorphous and polycrystalline $TiSi_2$ films have been studied experimentally in a wide spectral range (0.5–5.0 eV). The structures in the optical conductivity spectrum of polycrystalline $TiSi_2$ sample are explained on the basis of comparison of the experimental data and the calculated data. Theoretical spectra were obtained within the local-density approximation using the semirelativistic linear-muffin-tin-orbital method (LMTO). It is shown that the transition of crystalline $TiSi_2$ to the amorphous state leads to significant changes in the optical properties. © *1997 American Institute of Physics.* [S1063-777X(97)01103-1]

1. INTRODUCTION

The compound $TiSi_2$ is a representative of refractory metal silicides, which are growing in popularity because of their use in large-scale integrated (VLSI) technology. Because of its high conductivity, high-temperature stability, and resistance to degradation, $TiSi_2$ is a promising material for use as gate electrodes and interconnectors. It would be natural to attribute the unique properties of the silicides to special features of their electronic energy structure (EES).

The first stages of most of the technological processes of growing of the disilicides involve formation of metastable amorphous phases of corresponding compounds. Equilibrium stoichiometric crystalline disilicides are formed as a result of annealing of the metastable amorphous phases. It is interesting to study the influence of the transition of the crystalline phase to the amorphous phase on the EES of titanium disilicide.

It is well known (see., e.g., Ref. 1) that optical spectroscopy is a sensitive tool for study of the EES of solids. The practical use of this experimental technique is complicated by the difficulties in interpretation of the experimental spectra. To reveal the main features in the formation of the optical spectra, *ab initio* calculations of the band structure and optical conductivity spectra of crystalline $TiSi_2$ have been performed using the self-consistent, scalar-relativistic LMTO method within the local spin-density approximation. Such a combination of experimental and theoretical approaches to investigation of the electronic structure of solids also opens new possibilities to study EES of the disordered (e.g., amorphous) solids.

In this paper we study the optical properties and electronic structure of amorphous and crystalline $TiSi_2$, both theoretically and experimentally.

This paper is organized as follows. Theoretical background and methods of calculation of the band structure and frequency dependence of the conductivity tensor are reviewed in Sec. 2. Calculated optical properties of $C54$ and $C49$ phases of $TiSi_2$ are described in Sec. 3. In Sec. 4, the experimental details are briefly described and the measured spectra of the optical conductivity tensor components are presented, discussed, and compared with the calculated ones.

2. CRYSTAL STRUCTURE AND COMPUTATIONAL DETAILS

$TiSi_2$ crystallizes in two different orthorhombic phases: the metastable base-centered structure ($C49$, space group $Cmcm$) and the equilibrium face-centered structure ($C54$, space group $Fddd$). Both phases have two $TiSi_2$ formula units per primitive cell. The lattice constants are $a=3.62$ Å, $b=13.76$ Å, and $c=3.605$ Å (Ref. 2) for the $C49$ phase and $a=8.236$ Å, $b=4.772$ Å, and $c=8.516$ Å for the $C54$ phase.[3] The Brillouin zones (BZ) for $C54$ and $C49$ structures are shown in Figs. 1 and 2, respectively.

We performed first-principles, self-consistent (LDA)[4] calculations of the electronic structure using the LMTO method, including the so-called combined correction term.[5–7] A detailed description of the LMTO method, including its application to the electronic structure of compounds, has been given elsewhere.[8,9] We only give some details of the calculations here. The calculations were semi-relativistic, i.e., all relativistic effects were taken into account except for the spin-orbit coupling. The angular momentum expansion of the basis functions was up to $l=3$ for titanium and $l=2$ for silicon The Ti f orbitals have a minor effect on the energy bands, E_n^k; however, it is necessary to include them, because the $d\rightarrow f$ oscillator strength usually is much larger than that for $p\rightarrow d$ or $s\rightarrow p$ transitions. The k integrated functions were evaluated by the tetrahedron method[10] on a grid of more than 400 k points in the irreducible part of BZ. From the energy bands and the LMTO eigenvectors, we calculated total and orbital (l) projected DOS functions and the optical functions (R, σ, ε_1, and ε_2).

The energy band structures of $TiSi_2$ for $C54$ and $C49$ structures are shown in Figs. 3 and 4, respectively. They agree well with previous results of Mattheiss and Hensel.[3]

3. CALCULATED OPTICAL PROPERTIES

The linear response of a system to an external electromagnetic field in the long-wavelength limit is determined by

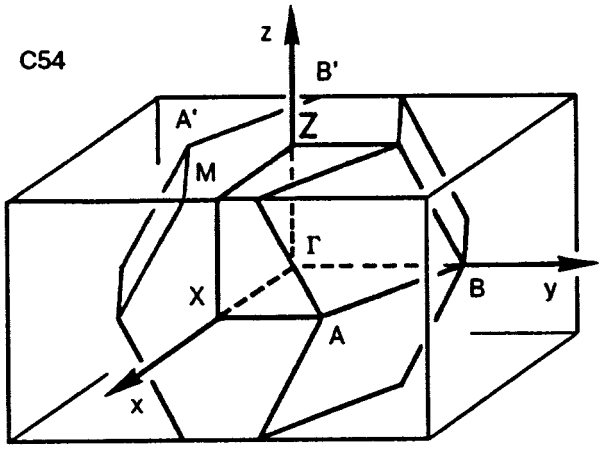

FIG. 1. The Brillouin zone for the $C54$ phase of $TiSi_2$.

the imaginary part, $\varepsilon_2(\omega)$, of the complex dielectric function $\tilde{\varepsilon}$. We have calculated the dielectric function for frequencies well above those of the photons and, therefore, we considered only electronic excitations. We used the random-phase approximation and disregarded local-field and finite life-time effects.[11] The dielectric function is a tensor. However, by an appropriate choice of the principal axes we can diagonalize it, which allows us to consider only the diagonal matrix elements $\tilde{\varepsilon}^{\nu\nu}(\omega)$ with $\nu=x,y,z$. The interband contribution to the imaginary part of the dielectric function is given by

$$\varepsilon_2^{\nu\nu}(\omega)=\frac{8\pi^2\mathbf{e}^2}{m^2\omega^2}\sum_{m\neq n'}^{\text{unocc}}\sum_{n'}^{\text{occ}}\int_{BZ}|P^{\nu}_{nn'}(\mathbf{k})|^2\delta(E^{\mathbf{k}}_n-E^{\mathbf{k}}_{n'}-\hbar\omega)\frac{d^3k}{(2\pi)^3},\tag{1}$$

where $P^{\nu}_{nn'}(\mathbf{k})$ is the projection of the momentum matrix elements $P_{nn'}(\mathbf{k})$ along the υ direction of the electric field $\mathbf{E}$, and $E^{\mathbf{k}}_n$ are the one-electron energies.

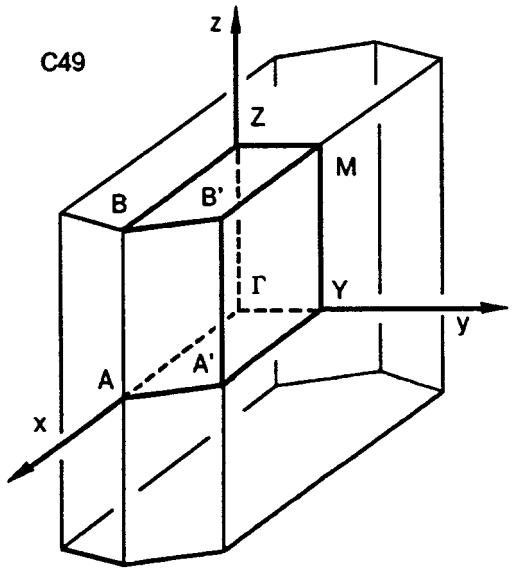

FIG. 2. The Brillouin zone for the $C49$ phase of $TiSi_2$.

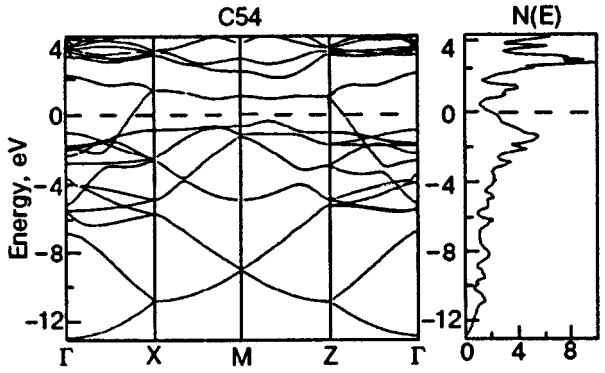

FIG. 3. Self-consistent energy-band structure and total density of states $N(E)$ [number of states/(cell·eV)] for the $C54$ phase of $TiSi_2$.

Having evaluated (1), we calculate the real part of the dielectric function $\varepsilon_1(\omega)$ using the Kramers-Kronig (KK) relation

$$\varepsilon_1^{\nu\nu}(\omega)=1-\frac{(\omega_p^{\nu\nu})^2}{\omega^2}+\frac{2}{\pi}P\int\frac{\varepsilon_2(\omega')\omega' d\omega'}{\omega'^2-\omega^2},\tag{2}$$

where P stands for the principal value. The second term of this equation describes the intraband contribution to the $\varepsilon_1(\omega)$. We disregard this contribution to $\varepsilon_2(\omega)$ according to the perfect-crystal approximation (the defects and lattice oscillations are absent).

The plasma frequency is given by

$$(\omega_p^{\nu\nu})^2=\left(\frac{\mathrm{e}}{\pi\hbar}\right)^2\sum_n\int_{BZ}d^3k[\partial E^{\mathbf{k}}_n/\partial k^{\nu}]^2\delta(E^{\mathbf{k}}_n-E_f).\tag{3}$$

We also calculated the optical conductivity $\sigma(\omega)$ and the reflectivity $R(\omega)$ using Eqs. (1)–(3) and the relations

$$\sigma(\omega)=\frac{\omega}{4\pi}\varepsilon_2(\omega),\tag{4}$$

and

$$R(\omega)=\left|\frac{\sqrt{\tilde{\varepsilon}}-1}{\sqrt{\tilde{\varepsilon}}+1}\right|^2.\tag{5}$$

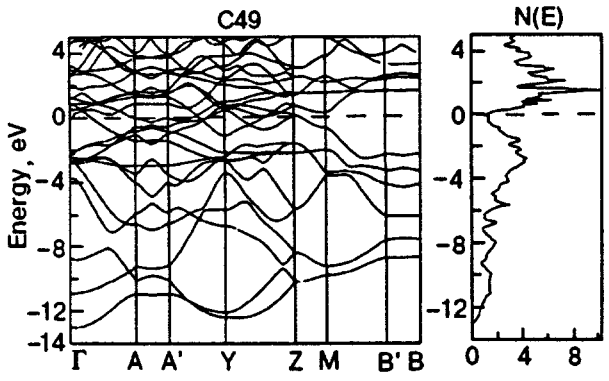

FIG. 4. Self-consistent energy-band structure and total density of states $N(E)$ [number of states/(cell·eV)] for the $C49$ phase of $TiSi_2$.

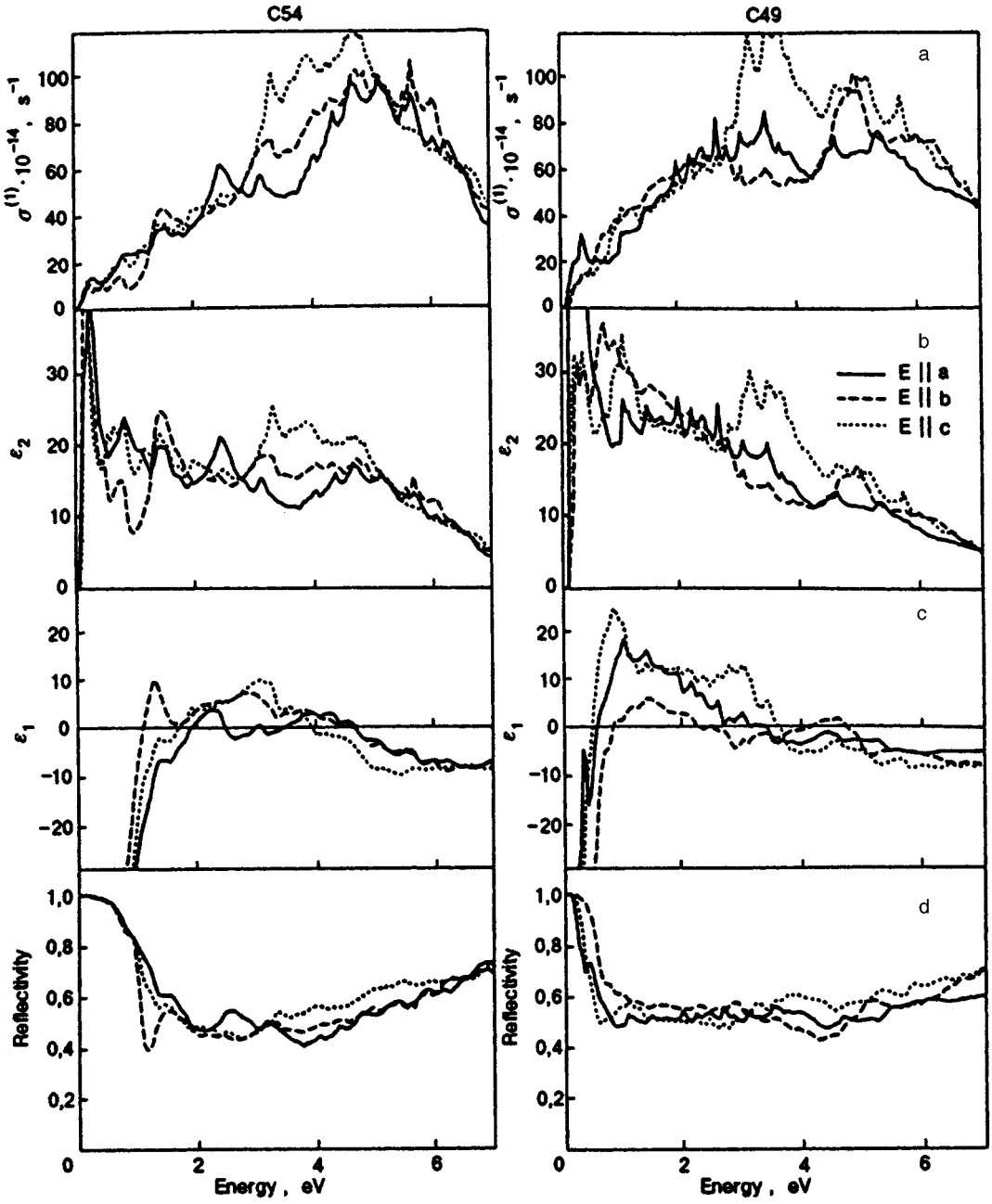

FIG. 5. The calculated $\sigma(\omega)$ (a), $\varepsilon_1(\omega)$ (b), $\varepsilon_2(\omega)$ (c), and reflectivity (d) spectra for the $C49$ and $C54$ phases of $TiSi_2$.

We first calculate directly the imaginary part of dielectric function (1) in a wide energy range from 0 to 30 eV. The real part of the dielectric function and the other optical functions were then calculated using the above formulas. Figure 5a shows the optical conductivity of $TiSi_2$ for three light polarizations $E\|a$, $E\|b$, and $E\|c$ in the energy range from 0 to 7 eV for the two phases. Both phases exhibit strong anisotropy in the main absorption band, which is located in the energy range 2.5 eV$<\hbar\omega<$5.5 eV. This absorption is due to the transitions from the strongly hybridized p states of Si and d states of Ti in the valence band to the unoccupied states, primarily to Ti d-states which have an admixture of p character.

For the $C49$ phase all three polarizations exhibit a noticeable dispersion of $\varepsilon_2(\omega)$ and $\sigma(\omega)$. There is a double peak in the low-energy part of the spectra ($\hbar\omega \approx 0.2$ eV and $\hbar\omega \approx 0.34$ eV). Both maxima originate from the transitions from the 12th to 13th energy band. The maximum at $\hbar\omega \approx 2.2$ eV exists only for $E\|a$ and comes from the $12\rightarrow13$ transitions. There are three peaks in the energy range at $\hbar\omega \approx 3.2$, 3.5, and 4.9 eV. These pronounced peaks for the polarization $E\|c$ are due to the interband transitions $8\rightarrow14$, $7\rightarrow14$ and the superposition of the transitions $8\rightarrow18$, $8\rightarrow17$, $7\rightarrow16$, and $9\rightarrow19$, respectively.

In comparison with the $C49$ phase the optical absorption of $C54$ phase in the infrared range is weaker. The peak (I) at $\hbar\omega \approx 0.2$ eV comes from the transition $11\rightarrow12$. Two broad maxima at $\hbar\omega \approx 0.8$ eV and 1.4 eV (II) are due to the transitions ($12\rightarrow13$, 14), respectively. The peak (III) for $E\|a$ at

TABLE I. Parameters of the heat treatment and structure of $TiSi_2$ samples.

No. of sample	Annealing temperature, K	Gas medium	Film structure according to x-ray analysis
1	293 (as depos.)	-	amorphous
2	770	vacuum	amorphous
3	770	hydrogen	amorphous
4	870	vacuum	amorphous
5	1070	vacuum	crystalline $C49 + C54$
6	1270	vacuum	crystalline $C54$

$\hbar\omega \approx 2.4$ eV comes from the 9, 10→13 transitions. In the energy range $3\text{ eV} < \hbar\omega < 4\text{ eV}$ $\varepsilon_2(\omega)$ for $E \| c$ exhibits a double peak structure. The same peaks may be seen for the other polarizations, but owing to optical transition matrix elements their intensity is weaker. The maximum at $\hbar\omega \approx 3.22$ eV (IV) originates from the transitions 10→16, 9→15, 9→14, 8→14, and 11→14 and one maximum at $\hbar\omega \approx 3.8$ eV comes mainly from the transition 8→15. There is a wide maximum (V) at $\hbar\omega \approx 4.75$ eV for all polarizations originating from the 7→15 and 9→15 transitions.

These structures in $\varepsilon_2(\omega)$ and $\sigma(\omega)$ curves are reflected in a rather complicated way in the $\varepsilon_1(\omega)$ and reflectivity spectra (see Fig. 5c and 5d).

4. EXPERIMENTAL PROCEDURE, RESULTS, AND COMPARISON WITH THE THEORETICAL DATA

$TiSi_2$ films with total thickness of 300 nm have been prepared by magnetron sputtering of the corresponding target onto the ⟨111⟩ monocrystalline Si substrates at 620 K. The target for sputtering of $Ti_{0.333}Si_{0.667}$ content was prepared by means of a powder metallurgy technique—cold pressing with subsequent sintering. The background argon pressure during deposition was $5 \cdot 10^{-1}$ Pa and the deposition rate was 0.33 nm per second. According to structure analyses, the as-deposited films were in the amorphous state. To form the stoichiomentric polycrystalline $TiSi_2$ films, annealing at different (770–1270 K) temperatures was carried out in vacuum or in flowing hydrogen. The duration of the heat treatment was 0.5 hour. In this work we obtained and investigated a series of $TiSi_2$ samples (see Table).

The structure and phase composition of the as-deposited and annealed $TiSi_2$ films were studied using x-ray diffraction in Cu K_α and K_β radiation. It was shown earlier[12] that the gas media influences greatly the kinetics of the amorphous-to-crystalline phase transition and the perfection of the crystalline structure. The common feature of these processes is that annealing in vacuum leads to a total crystallization with a lower rate and at a higher temperature than in the H_2 media. It is necessary to note that after annealing at 1070 K in vacuum (sample 5) the crystalline film consists mainly of equilibrium, orthorhombic face-centered $C54$-phase and a small amount of metastable orthorhombic base centered $C49$ phase. After annealing at 1270 K (sample 6) only $C54$ is presented in $TiSi_2$ films.

The optical properties (the real ε_1 and imaginary ε_2 parts of the dielectric function) of the as-received $TiSi_2$ films and of films annealed under different conditions were studied at room temperature in the spectral range 250–2 500 nm (5.0–0.5 eV) at a fixed incidence angle of 73° by the polarimetric Beattie technique.[13]

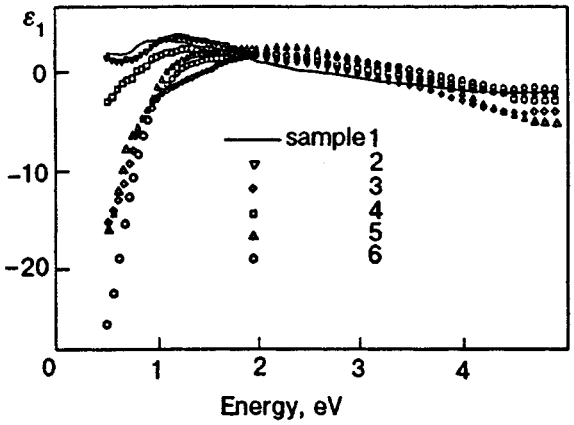

FIG. 6. Experimental $\varepsilon_1(\omega)$ spectra for amorphous (samples 1–4) and polycrystalline (samples 5 and 6) $TiSi_2$ films.

The experimental $\varepsilon_1(\omega)$, $\varepsilon_2(\omega)$, and $\sigma(\omega)$ spectra for polycrystalline and amorphous $TiSi_2$ films are presented in Figs. 6–8. The experimental $\varepsilon_1(\omega)$ and $\sigma(\omega)$ spectra for x-ray amorphous $TiSi_2$ films (samples 1–4) are shown in Figs. 8 and 9. We see that the experimental optical conductivity spectra for the crystalline $TiSi_2$ films, which were obtained by annealing at 1270 K (samples 6), have the same structures, and are situated exactly at the same energies, but they have lower intensities. According to Ref. 12, this decrease of the optical conductivity is caused by surface oxidation. Because sample 5 has a cleaner surface, it will be used as a crystalline sample for further discussion. The experimental optical conductivity spectrum for polycrystalline $TiSi_2$ film exhibits a strong absorption peak with maximum E near 3.9 eV, and some features (absorption peaks) in the low-energy shoulder, which are marked by arrows and letters A, B, C, and D (see Fig. 8). There are two possible explanations for the strong increase in the optical conductivity in the near IR region. A is a shoulder of an absorption peak, whose maximum is situated outside the experimentally in-

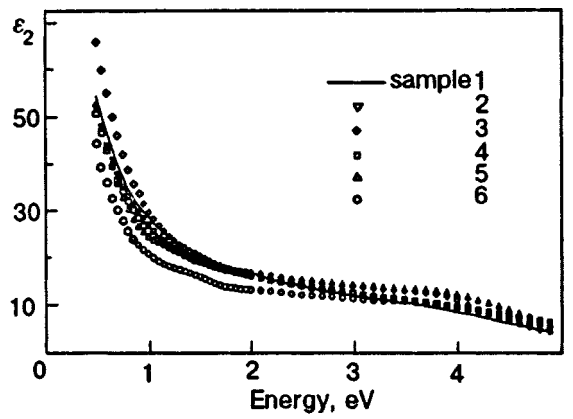

FIG. 7. Experimental $\varepsilon_2(\omega)$ spectra for amorphous (samples 1–4) and polycrystalline (samples 5 and 6) $TiSi_2$ films.

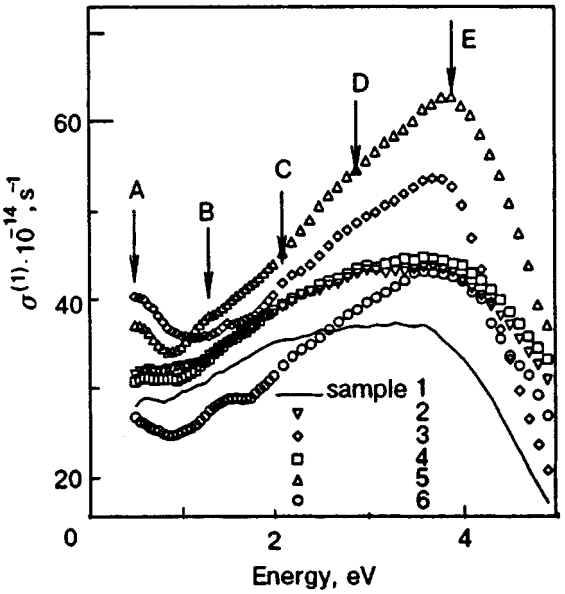

FIG. 8. Experimental $\sigma(\omega)$ spectra for amorphous (samples 1–4) and polycrystalline (samples 5 and 6) $TiSi_2$ films. The curve for sample 5 is shifted up to $5\cdot10^{-14}\,s^{-1}$ and the curve for sample 1 is shifted down to $5\cdot10^{-14}\,s^{-1}$.

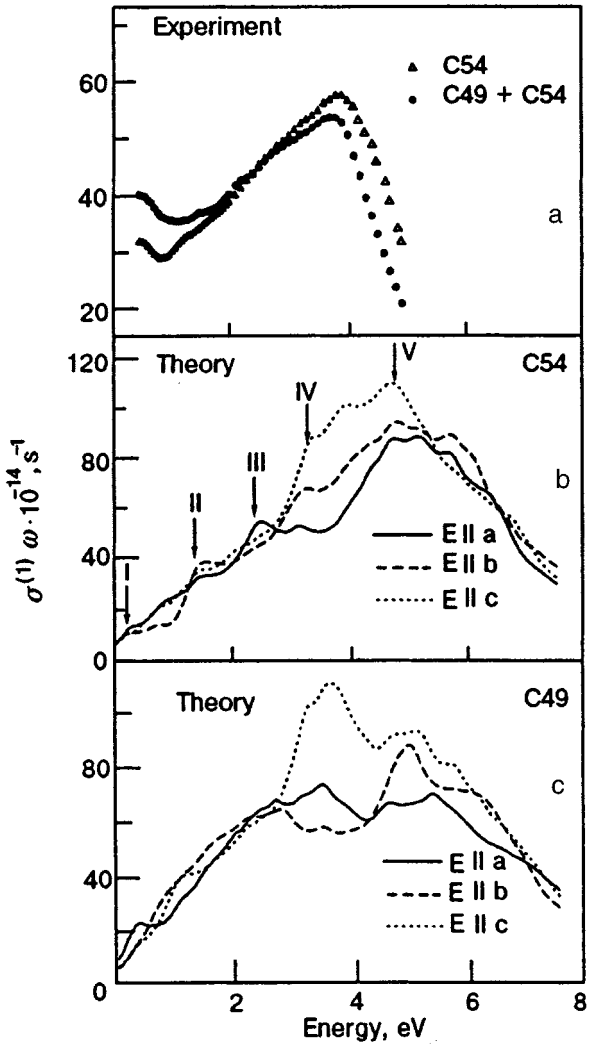

FIG. 9. Comparison of the experimental (a) and calculated (b,c) $\sigma(\hbar\omega)$ spectra of $TiSi_2$.

vestigated spectral range. This conclusion agrees with the results of the theoretical calculations. The other explanation is that *A* is an intraband Drude-like contribution to the optical conductivity spectrum of the crystalline $TiSi_2$. The behavior of the $\varepsilon_1(\omega)$ curve in this region suggests that there exists a considerable intraband contribution to the optical conductivity in the NIR region of the spectrum. This conclusion is confirmed by the results of the resistivity measurements of amorphous and crystalline $TiSi_2$ films[12] and by the absence of a noticeable intraband contribution to $\sigma(\omega)$ for the amorphous as-received film.

The overall shape of the optical conductivity spectrum of the polycrystalline $TiSi_2$ film is in good agreement with the results of the theoretical *ab initio* calculations; however, the experimental spectrum is slightly shifted to the low energies by 0.8 eV (see Fig. 5). We can therefore relate the absorption peak *A* in the experimental spectrum to the absorption band I in the theoretical spectrum, peak *B*—to peak II, peak *C*—to III, peak *D*—to IV, and peak *E*—to V and the corresponding electron transitions.

To compare theoretical and experimental data we simulated the lifetime effects by broadening the calculated spectra with a Lorentzian of width $\delta=0.1$ eV, where δ is the inverse relaxation time. Since the experimental samples are polycrystals, we carry out the averaging of all three polarizations. Naturally, such averaging ignores the possibility that experimental samples may possess some texture.

Figure 9a shows the experimental optical conductivity spectra for the pure *C*54 phase and for the mixture of *C*54 and *C*49 phases. It is easy to see that the admixture of *C*49 phase to the *C*54 phase leads to an increase in the absorption in the IR range of the spectrum. In addition to this increase the main absorption peak diminishes and shifts to the left. These effects are in good agreement with the theoretical data (see Fig. 9b,c).

A noticeable shift of the main theoretical peak from its experimental position (≈ 0.8 eV) may arise from the failure of the local density approximation. Another reason may be the inadequate averaging procedure. Figure 9c shows the theoretical $\sigma(\omega)$ for the $E\|c$. As can be seen, these curves agree much better with the experimental curves.

As was mentioned above, we studied four x-ray amorphous samples (samples 1–4).

The loss of the translation invariance in the amorphous state leads to noticeable changes in the optical properties of $TiSi_2$ (Figs. 6–8): significant decrease in the intensity of peak *E* in the $\sigma(\omega)$ spectrum and its shift to the lower energies side; considerable changes become apparent in the $\varepsilon_1(\omega)$ spectra at $\hbar\omega < 2.0$ eV. It should be noted, however, that all the features which are typical of the optical conductivity spectrum of the polycrystalline $TiSi_2$ films are shown in the $\sigma(\omega)$ spectrum for amorphous as-received $TiSi_2$ film. This means that the short-range order inherent to crystalline *C*54 phase does not change significantly on transition to the amorphous phase.

The heat treatment of amorphous $TiSi_2$ films at 770 and 870 K in vacuum leads to certain changes in their optical properties in the comparison with as-received amorphous sample. These changes are as follows: the high-energy wide maximum in the $\sigma(\omega)$ spectrum located at 3.0–3.4 eV is shifted to higher energies by about 0.5 eV and is split into two distinct maxima, *D* and *E* on curves *2* and *3*. Even more pronounced influence of the heat treatment is manifested by the $\varepsilon_1(\omega)$ spectra, especially in the near IR region (see Fig. 6). Of the $TiSi_2$ amorphous films which we studied sample 3, which was exposed to a heat treatment at 770 K in flowing hydrogen, must be set aside. We recall that this is an x-ray amorphous sample. We see (Figs. 6 and 8), however, that its optical properties strongly differ from the other amorphous samples. Moreover, the overall shapes of the $\sigma(\omega)$ and $\varepsilon_1(\omega)$ spectra of sample 3 are very similar to those of the crystalline samples. This result confirms the conclusion of Ref. 12, that the annealing in the H_2 media allows us to obtain better crystalline structure in $TiSi_2$ films with a shorter annealing time. Thus the amorphous $TiSi_2$ films, which are indistinguishable by the traditional x-ray structural analysis, possess essentially different optical properties. These differences, in our view, are caused by slight differences in the short-range order of different amorphous states, which cannot be determined by the traditional techniques.

5. SUMMARY

1. Polycrystalline-amorphous phase transition in $TiSi_2$ films leads to significant changes of the optical properties.

2. On the basis of the similarity of the main features of the optical conductivity spectra for amorphous and polycrystalline phases of $TiSi_2$ it is concluded that the main features of the short-range order in both phases are conserved.

3. Simultaneous analyses of the $\varepsilon_1(\omega)$ and $\sigma(\omega)$ spectra make it possible to record slight changes in the short-range order in $TiSi_2$ films, which are caused by heat treatment.

4. Gas media influence strongly the kinetics of amorphous-polycrystalline transition and the quality of the surface of the film.

The research described in this publication was made possible, in part, by Grant No. U42200 from the International Science Foundation.

*E-mail: anton@d24imp.kiev.ua

[1] B. P. Voznyuc, R. Gontarz, J. Dubowik, Yu. V. Kudryavtsev, and N. A. Lesnik, Fiz. Tverd Tela **32**, 694 (1990).
[2] W. B. Pearson, *A Handbook of Lattice Spacings and Structures of Metals and Alloys*, Pergamon, New York (1967), Vol. 2.
[3] L. F. Matheiss and J. C. Hencsel, Phys. Rev. B **39**, 7754 (1989).
[4] U. Barth, and L. Hedin, J. Phys. C **4**, 2064 (1971).
[5] O. K. Andersen and O. Jepsen, Phys. Rev. Lett. **53**, 2571 (1984); O. K. Andersen, Z. Pawlowska, and O. Jepsen, Phys. Rev. B **34**, 5253 (1986).
[6] O. K. Andersen, O. Jepsen, and D. Glötzel, in *Highlights of Condensed-Matter Theory*, F. Bassani, F. Fumi, and M. P. Tosi (eds.), North-Holland, New York (1985).
[7] W. R. L. Lambrecht and O. K. Andersen, Phys. Rev. B **34**, 3439 (1986).
[8] O. K. Andersen, Phys. Rev. B **12**, 3060 (1975).
[9] H. L. Skriver, *The LMTO Method*, Springer, Berlin (1984).
[10] P. E. Blöchl, O. Jepsen, and O. K. Andersen, Phys. Rev. B **49**, 16223 (1994).
[11] H. Ehrenreich and M. H. Cohen, Phys. Rev. **115**, 786 (1959).
[12] E. E. Kachurina, Yu. N. Makogon, and S. I. Sidorenko. *Metally*, No 2, 67 (1993).
[13] J. R. Beattie and G. K. Conn. Philos. Mag. **6**, 235 (1955).

This article was published in English in the original Russian journal. It was edited by S. J. Amoretty.

Luminescence and ODMR studies of *X*-traps for triplet excitons in organic crystals

A. A. Avdeenko, L. M. Buravtseva, V. S. Gorobchenko, and V. V. Eremenko

*B. I. Verkin Institute for Low Temperature Physics and Engineering of National Academy of Sciences of Ukraine, 47 Lenin Avenue, Kharkov 310164, Ukraine**

S. V. Izvekov

Kiev University, Department of Theoretical Physics, 6 Glushkov Avenue, Kiev, 252127, Ukraine

A. E. Kravchenko and O. S. Pyshkin

B. I. Verkin Institute for Low Temperature Physics and Engineering of National Academy of Sciences of Ukraine, 47 Lenin Ave. Kharkov 310164, Ukrains

V. I. Sugakov

Institute of Nuclear Research, National Academy of Sciences of Ukraine, 47 Nauki Avenue, Kiev, 252650, Ukraine

(Submitted June 18, 1996, revised August 5, 1996)
Fiz. Nizk. Temp. **23**, 334–337 (March 1997)

The excited triplet states of shallow *X*-traps in neat single crystals of 4,4′-dichlorobenzophenone were studied at liquid helium temperature by luminescence spectroscopy and magnetic resonance with optical detection. The vibrational phosphorescence bands, the polarization of phosphorescence spectra, and the triplet zero-field splitting parameters of these traps have been analyzed. A specific model of the structure defect (a molecule is turned by 180° on its long axis) has been considered in organic crystals of benzophenone type which consist of molecules whose dipole moments compensate each other in a unit cell. The calculated depth of such a dipole *X*-trap for triplet excitons in 4,4′-dichlorobenzophenone crystals at the account of a defect molecule relaxation upon its slewing was found to be comparable with the experimental one.
 [S1063-777X(97)01203-6]

1. INTRODUCTION

The electron excitation energy transfer by excitons in real organic crystals can be interrupted because of the existence of trapping centers. Those centers are formed by the structure defects and impurities.[1,2] In pure crystals the trapping centers, the so-called *X*-traps, are mainly attributable to the lattice imperfections.[3] Of great interest is to study the nature of *X*-traps. In organic crystals consisting of molecules with a large dipole moment the structure defects can induce the appearance of so-called dipole traps.[4]

In the present paper we will examine the nature of *X*-traps of a 4,4′-dichlorobenzophenone (DCBP) molecular crystal (the molecular and crystal structures[5,6] are shown in Fig. 1) by luminescence spectroscopy and magnetic resonance with optical detection (ODMR). We studied the low-temperature phosphorescence spectra and their polarization, as well as microwave transitions between spin sublevels of the excited triplet states of *X*-traps in a zero magnetic field. A particular model of the structure defect is studied in organic crystals which consist of molecules with a dipole moment. The electronic levels of the corresponding *X*-traps are calculated.

2. EXPERIMENTAL

4,4′-dichlorobenzophenone was recrystallized and zone refined. Single crystals were grown by the Bridgman method. Plates about 1 mm thick were cleaved along the bc-plane for measurements. Measurements were carried out in a liquid-helium cryostat at 1.4 and 4.2 K. The crystals were excited with the emission of a 500-W mercury-discharge lamp which was filtered at 366 nm. The phosphorescence was monitored at right angles to the excitation path with a double-grating, 0.8-m DFS-12 scanning spectrometer.

The spectral slit widths of the spectrometer were 0.5 cm^{-1}. Signals were detected by a cooled FEU-79 (S-6) photomultiplier in a standard photon-counting scheme with long signal averaging. A similar optical scheme was used to record the magnetic resonance spectra with optical detection (ODMR) in the zero field. The crystals were placed in a helix which was connected to a microwave sweep oscillator operated at 1–6 GHz, 5 mW, via a coaxial line. The positions of resonance frequencies were determined within accuracy of 3 MHz. For polarization measurements the phosphorescence was analyzed with a film polarizer and a depolarizer was placed in front of the spectrometer entrance slit.

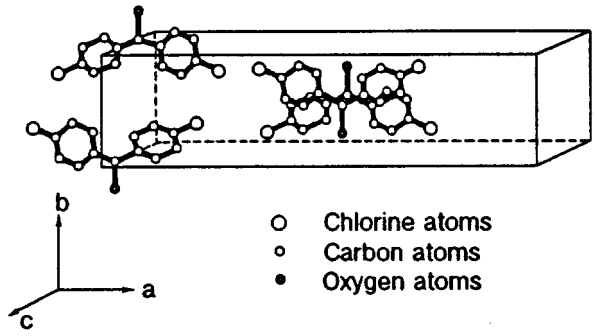

FIG. 1. The arrangement of 4,4′-dichlorobenzophenone molecules in a crystal unit cell C_{2h}^6.

3. RESULTS AND DISCUSSION

Phosphorescence spectra

The DCBP crystal phosphorescence spectra at 1.4 and 4.2 K are shown in Fig. 2. The spectral position of the 0–0 band of the triplet exciton emission is[7] ν=24 245 cm^{-1} (where ν is wavenumber). The exciton origin of the band is confirmed by the temperature measurements: In contrast with the exciton emission, the emission of shallow *A*-traps is absent at 4.2 K due to detrapping to the exciton band (the inset in Fig. 2). The same vibronic structures of the exciton phosphorescence and of the traps (Fig. 3) serve as the most convincing evidence which confirms that the radiating traps for triplet excitons are the *X*-traps.[1] In each case the vibronic mode at 1670 cm^{-1}, which is characteristic of the carbonyl groups,[8] gives rise to the progression. Since the triplet emission is strictly polarized along the carbonyl axis and along the crystal *b*-axis,[9] the polarization of triplet emission bands of *X*-traps were studied in order to define possible deviation of the carbonyl axis of defect molecules from the crystal *b*-axis. A thorough study shows that while measuring

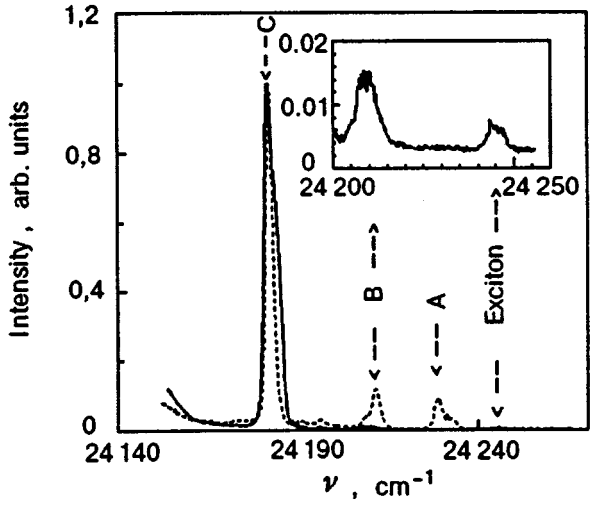

FIG. 2. Phosphorescence spectra of a 4,4′-dichlorobenzophenone single crystal at 4.2 (solid curve) and at 1.4 K (dashed curve). The inset scale up the phosphorescence spectrum at 4.2 K in close vicinity to the 0–0 band of triplet exciton emission.

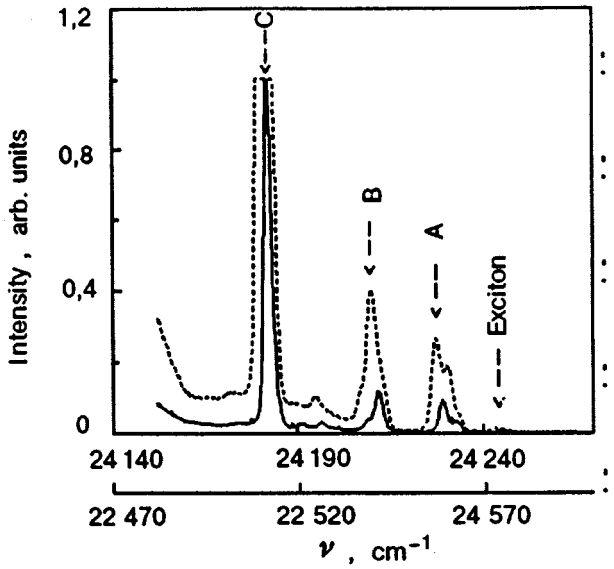

FIG. 3. Phosphorescence spectra of a 4,4′-dichlorobenzophenone single crystal at 1.4 K: 0–0 bands (solid curve, top axis of the abscissa); 0–1 bands (dashed curve, bottom axis of the abscissa).

the polarization within the accuracy of 3° the defect molecule dipoles are directed along the crystallographic *b*-axis.

ODMR spectra in the zero field of excited triplet states of *X*-traps at 1.4 K

Absolute values of the triplet zero-field splitting (ZFS) parameters D and E[8] for different traps (Table 1) were defined using the experimental resonance microwave frequencies (Fig. 4). It can be shown that because of the way in which the molecules are packed in the DCBP crystal lattice, the triplet exciton ZFS parameters nearly coincide with the molecular parameters. Our resonance frequencies for traps are close to those for excitons.[10] As is well known,[8] splitting of the excited triplet in the zero field reflects the electron density distribution over a molecule and therefore is an individual feature of a molecule. As can be seen from Table I, the ZFS parameters for different radiation centers are similar. It can therefore be stated that shallow trapping centers in the crystal under study are *X*-traps. It was shown earlier that ZFS parameters are fairly sensitive to the distortion of the shape of such nonrigid molecules as benzophenones.[11] On the basis of our data it can therefore be inferred that rotation and

TABLE I. Resonance microwave frequencies (ν_1, ν_2) and ZFS parameters (|D| and |E|) in the excited triplet states of 4,4′-dichlorobensophenone single crystal *X*-traps (Δ—trap depth).

X-trap	ν_1	ν_2	|D|	|E|	Δ
	GHz			cm^{-1}	
A	3.687	5.129	0.14843	0.02447	16
B	3.722	5.127	0.14897	0.02365	37
C	3.662	5.060	0.14683	0.02353	65

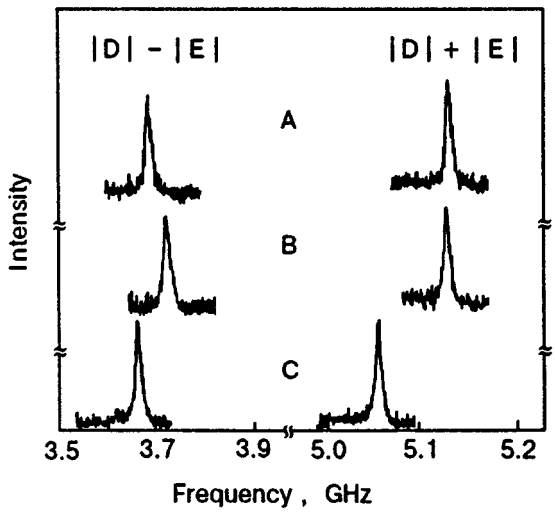

FIG. 4. ODMR signals in the excited triplet states of different *X*-traps in a 4,4′-dichlorobenzophenone single crystal at 1.4 K: $|D|-|E|$ and $|D|+|E|$microwave transitions for A, B, and C traps, where D and E are the ZFS parameters.

displacement of a molecule in a crystal are responsible for the structure defects which lead to the appearance of *X*-traps.

Model of the dipole *X*-trap

The dipole moments of individual molecules in a DCBP crystal are directed along the carbonyl axes. They are compensated for a unit cell (Fig. 1), and the dipole moment of a unit cell is zero.

Let us consider a simple model of a structure defect: A nondefect molecule is turned on the carbonyl axis by 180° and is then reflected in the plane that passes through the centers of molecules phenyl rings and normal to the crystallographic *b*-axis. Thus, the dipole moment of a defect molecule is fixed opposite to that of a nondefect molecule. The reorientation of the defect molecule dipole leads to a change of the interaction energy with the remaining crystal molecules. As a result, *X*-traps for an exciton appear. The structure defects of the above type were detected experimentally in dibenzfuran crystals.[12] The trap depth was calculated in accordance with the theory developed in Ref. 4, taking into account the defect molecule relaxation.

Let us consider the traps for triplet excitons. Bands for such excitations are quite narrow (e.g., the width of one of the triplet exciton bands in a DCBP crystal is[13] 8 cm^{-1}. It can therefore be assumed that the electronic excitation is localized at a separate molecule. Since a DCBP molecule has a dipole moment in the ground state and since the dispersion interaction energy decreases with the distance much faster than the dipole-dipole interaction energy, it is expected that the main contribution to the trap depth is from a change in the energy of the dipole-dipole interaction of a defect molecule with the remaining crystal molecules upon excitation.

Let us label the molecules in a crystal by $n\alpha$, where n is the number of the unit cell, and α is the number of the molecule in the cell. Let us label the defect molecule by $0\alpha^\circ$ ($n=0$, $\alpha=\alpha^\circ$).

The trap depth due to the electrostatic interaction can be calculated as

$$E^{\rm dip}_{0\alpha^\circ}=D_{0\alpha^\circ}-D^{\rm dip}, \tag{1}$$

where $D_{0\alpha^\circ}$ is a change in the energy of the dipole-dipole interaction of a defect molecule with the remaining molecules following electronic excitation, and $D^{\rm dip}$ is a similar value for a nondefect molecule. In the calculation we took into account that the dipole moment is localized at the carbonyl C=O bond and that at the reorientation the dipole position characterized by the vector $\mathbf{r}_{0\alpha^\circ}$ changes to the vector $\vec{\rho}_{\alpha^\circ}$. We can then write

$$D^{\rm dip}=\sum_{m\beta\neq 0\alpha^\circ} V(\Delta\mathbf{P}_{\alpha^\circ},\mathbf{r}_{0\alpha^\circ};\mathbf{P}_\beta,\mathbf{r}_{m\beta}), \tag{2}$$

$$D_{0\alpha^\circ}=\sum_{m\beta\neq 0\alpha^\circ} V(-\Delta\mathbf{P}_{\alpha^\circ},\mathbf{r}_{0\alpha^\circ}, +\vec{\rho}_{0\alpha^\circ};\mathbf{P}_\beta,\mathbf{r}_{0\alpha^\circ};\mathbf{P}_\beta,\mathbf{r}_{m\beta}), \tag{3}$$

where

$$V(\mathbf{P}_1,\mathbf{r}_1;\mathbf{P}_2\mathbf{r}_2)=\frac{1}{\varepsilon}\left[\frac{(\mathbf{P}_1\mathbf{P}_2)}{|\mathbf{r}_1-\mathbf{r}_2|^3} - \frac{3(\mathbf{P}_1[\mathbf{r}_1-\mathbf{r}_2])(\mathbf{P}_2[\mathbf{r}_1-\mathbf{r}_2])}{|\mathbf{r}_1-\mathbf{r}_2|^5}\right]. \tag{4}$$

Here $\Delta\mathbf{P}_\alpha$ is an additional dipole moment which a molecule with a number α gains at the transition to the excited state, ε is the crystal static dielectric constant, and the vector $\mathbf{r}_{m\beta}$ passes through the dipole centers of all the nondefect molecules. The coordinates of nondefect molecules are taken from data of the known crystal structure of DCBP.[5,6]

It can be shown that the calculated values of trap depths are strongly dependent on the relaxation position of a defect molecule. The relaxation position was determined by the atom-atom potentials. To determine the minimum energy, the defect molecule is moved in three directions along the crystallographic **a**, **b**, and **c**-directions and is rotated about the carbonyl axis of the C=O bond. The surrounding molecules are regarded as fixed molecules. In the relaxation position a defect molecule is displaced by the vector **R** with the coordinates $0.1647a$, $0.0647b$, $0.2721c$, where a, b, and c are the lattice constants, and the molecule is rotated about the carbonyl axis by about 3° with respect to the initial position. It was used for the calculations of the distribution of charge for a benzophenone molecule.[14]

The dipole sums (2) and (3) were calculated by the Evald–Kornfeld point dipole lattice summation.[15] Taking into account the relaxation of a defect molecule in a crystal and the specific parameters of the DCBP crystal[16,17] ($|\mathbf{P}_\alpha|=2.7D$, $|\Delta\mathbf{P}_\alpha|=0.8D$, the direction of the vector $\Delta\mathbf{P}_\alpha$ is opposite to $\mathbf{P}_\alpha$, and $\varepsilon=3$), the calculated depth of a dipole trap is 93 cm^{-1}, which is comparable to that of a pronounced *X*-trap (65 cm^{-1}) (Fig. 2, trap C).

The accuracy of calculation of the dipole trap depth can be improved by taking into account the contribution from

the interaction between dipoles, which are located along the C–Cl bonds (the dipole moment of this bond is[18] 1.7 *D*) of a defect molecule, and the remaining molecules of a crystal.

Because the disturbance of the crystal molecules nearest to a defect is weak, the energy spectrum exhibits a set of levels connected with these molecules.[19,20] An energy funnel is therefore formed.[19,20] This energy funnel induces trapping of a triplet exciton by a defect molecule after nonradiative relaxation through the local levels.

The A and B shallow *X*-traps in the DCBP crystal phosphorescence spectra (Fig. 2) therefore do not seem to be associated with the traps induced by the C trap. This assumption is confirmed by the fact that the intensity ratios of different trap bands in the phosphorescence spectra change from one sample to another. It can be assumed that these traps are also the dipole traps. In this case however, a defect is formed due to the rotation of crystal molecules about the carbonyl axis. This leads to a change in the interaction between the dipoles of the C–Cl bond. We plan to continue studies of the nature of shallow *X*-traps.

In conclusion, measurements of the low-temperature phosphorescence spectra, of their polarization, and of the ODMR spectra in zero field in the excited triplet states made it possible to infer that in a 4,4′-dichlorobenzophenone crystal shallow traps are *X*-traps. A particular model of the structure defect, i.e., a model of the dipole trap, is proposed.

The research described in this publication was made possible, in part, by Grants U9J000 and U9J200 from the International Science Foundation and Grant ISSEP SPU 04265 from the Soros Science Education Program of the International Renaissance Foundation.

*E-mail: avdeenko@ilt.kharkov.ua

[1] M. Pope and C. E. Swenberg, *Electronic Processes in Organic Crystals*, Clarendon Press, Oxford, Oxford University Press, New York (1982).
[2] N. I. Ostapenko, V. I. Sugakov, and M. T. Shpak, *Spectroscopy of Defects in Organic Crystals*, Kluwer Academic Publication, Dordrecht–Boston–London (1993).
[3] A. Propstl and H. C. Wolf, Z. Naturforsh. **18a**, 724 (1963).
[4] S. V. Izvekov and V. I. Sugakov, Phys. Status Solidi B **191**, 449 (1995).
[5] K. G. Shields and C. H. L. Kennard, J. Chem. Soc. Perkin Trans. Part II, No. 4, 463 (1977).
[6] M. M. Granger and M. F. Coillot, Acta Cryst. **C41**, 542 (1985).
[7] A. A. Avdeenko, T. L. Dobrovol'skaya, V. A. Kulchitskii, and Yu. V. Naboikin, Phys. Status Solidi **B99**, 909 (1980).
[8] S. McGlynn, T. Adzumi, and M. Kinosita, *Molecular Spectroscopy of the Triplet State*, Prentice-Hall (1969).
[9] C. Dijkgraaf, Spectrochim. Acta **23A**, 363 (1967).
[10] S. B. Singham and D. W. Pratt, J. Phys. Chem. **86**, 507 (1982).
[11] I. Y. Chen and X. Q. Qian, J. Chem. Phys. **92**, 929 (1990).
[12] V. Fischer, C. von Borczyskowski, and M. Schwenter, Phys. Rev. **B41**, 9126 (1990).
[13] P. Peretti, P. Ranson, and Y. Rousset, Chem. Phys. **56**, 135 (1981).
[14] C. Mijole and J. M. Leclercq, J. Chem. Phys. **70**, 2560 (1979).
[15] D. P. Craig and S. H. Walmsley, in *Physics and Chemistry of the Organic Solid State*, D. Fox, M. L. Labes, and A. Weisenberg (Eds.), Vol. 1, New York–London (1965).
[16] L. F. Wojdac and L. J. Noe, J. Phys. Chem. **85**, 2119 (1981).
[17] H. Nakayama, T. Egushi, and N. Nakamura, Z. Naturforsh. **49a**, 267 (1994).
[18] D. Kirin and G. S. Pawley, Chem. Phys. Lett. **85**, 298 (1982).
[19] L. S. Kukushkin, Opt. and Spectr. **15**, 371 (1963) (in Russian).
[20] H. Benk and H. Haken, J. Chem. Phys. **77**, 5730 (1982).

This article was published in English in the original Russian journal. It was edited by S. J. Amoretty.

The structure, slip systems, and microhardness of C_{60} crystals

S. V. Lubenets, V. D. Natsik, L. S. Fomenko, A. P. Isakina, A. I. Prokhvatilov, M. A. Strzhemechny, and N. A. Aksenova

*B. I. Verkin Institute for Low Temperature Physics and Engineering, National Academy of Sciences of the Ukraine, 310164 Kharkov, Ukraine**

R. S. Ruoff

Dept. of Physics, CB 1105, One Brookings Drive, Washington University, St. Louis, MO 63130-4899, USA
(Submitted July 1, 1996; revised September 9, 1996)
Fiz. Nizk. Temp. **23**, 338–351 (March 1997)

The structure and microplasticity of high-purity fullerite C_{60} have been investigated comprehensively. The crystalline structure, lattice parameters, and phase transitions have been studied by x-ray diffractometry in the temperature range 30–293 K. It is found that the temperature corresponding to the orientational order–disorder phase transition is $T_c = 260$ K. A considerable number of regions with stacking faults discovered in the samples leads to blurring of the fcc→sc phase transition in the temperature interval $T_c \pm 3$ K. The $a(T)$ dependences of the lattice parameter display peculiarities at the following characteristic temperatures: T_c at which the lattice parameter jump $\Delta a/a = 3.3\times 10^{-3}$ is observed, and the temperatures $T_0 \simeq 155$ K, and $T_g \simeq 95$ K which are associated with the beginning and end of molecular orientation freezing. It is shown that the formation of orientational glass is accompanied by a considerable increase in the width of x-ray reflections. The slip geometry and the temperature dependence of microhardness H_V are studied in the temperature interval 81–293 K. It is shown that a system of the $\{111\}\langle 110\rangle$ type is the only slip system in the fcc and sc phases. The value of H_V depends on the indentation plane: $H_V^{111} > H_V^{100}$. Below T_c, the microhardness increases abruptly (by approximately 30%). The temperature interval of this anomaly decreases after annealing of the crystal in vacuum. At $T < T_0$, the $H_V(T)$ dependence becomes much stronger. It is shown that the hardness of C_{60} normalized to the elastic shear modulus is higher than the hardness of typical molecular crystals at comparable homologic temperatures. © *1997 American Institute of Physics.* [S1063-777X(97)01303-0]

1. INTRODUCTION

Fullerite C_{60} is a typical simple molecular crystal in which peculiarities of lattice properties such as polymorphism are associated with the thermal activity of rotational degrees of freedom of their molecules. The phase transition observed at $T_c = 260$ K (which is a first-order phase transition according to some indications) does not change the symmetry of spatial arrangement of the centers of gravity of molecules that form the fcc lattice. A decrease in lattice symmetry from $Fm3m$ (fcc) to $Pa3$ (sc) upon cooling is due to partial orientational ordering of molecules.[1–3] Neutron diffraction studies[2,4] have revealed that the molecules in the low-temperature phase are in two orientational states that are nonequivalent from the symmetry point of view, but have close energy values. These states are called pentagonal and hexagonal configurations and correspond to global and local energy minima of the noncentral part of molecular interaction. They are separated by the energy gap of ~0.25 eV. The number of less advantageous hexagonal configurations decreases upon cooling, but so does the rotational frequency of molecules. Hence the orientational glass phase is formed even at a fairly high temperature ~90 K.[2,4–6] Variations in the orientational subsystem must influence the temperature dependence of the structural and other physical characteristics of fullerite crystals.

The high-temperature fcc phase of fullerite, which is dominated by central van der Waals molecular interaction, can be formally treated as a ''plastic crystal'' according to the classification and criteria proposed by Timmermans.[7] A transition to the orientationally ordered SC phase is accompanied by an enhancement of the role of the off-central component in molecular interaction, and must increase the lattice rigidity. Moreover, a change in the lattice symmetry due to such a transition can lead to a change in the crystallography of plastic slip.[8] Hence, in addition to structural studies, investigations of the parameters of plastic deformation and slip systems of C_{60} crystals as well as their variation in the vicinity of the fcc→sc phase transition, orientational glass-formation temperature $T_g = 90$–100 K, and other points on the temperature scale at which anomalies in physical properties have been observed also acquire a considerable significance.

Intense studies of the mechanical properties of fullerite C_{60} are being carried out at present by several groups. Static or dynamic indentation technique are used for mechanical

TABLE I. Values of melting temperature T_m, elastic moduli μ and E, relative microhardness H_V/μ and H_V/E for fullerite C_{60} and materials with other types of bonds in the lattice.

Substance	T_m, K	T/T_m	μ GPa	E GPa	$10^3 H_V/\mu$	$10^3 H_V/E$
C_{60}	1400*	0.08		28.4	32	12.3
	[14]	0.21		20[22]	26	10
Graphite	3770	0.08	20		50	20
	[15]		[17]			
CH_4	90.7	0.22	1.1		3.45	1.3
	[16]		[18]			
Ar	83.8	0.12	1.56		2.37	0.9
	[16]		[19]			
Kr	115.8	0.086	1.83		1.64	0.6
	[16]		[19]			
NH_3	196	0.39	3.04		40.5	15.6
	[16]		[20]			
NaCl	1073	0.27	15.5	38.7	7.3	2.8
	[15]		[21]	[21]		
Au	1336	0.22	27	78	8.3	3.2
	[15]		[15]	[15]		

*The estimate is based on the method of nonsymmetrized self-consistent field;[14] T/T_m is the temperature of measuring the microhardness reduced to the melting point of the material: we assume that the moduli E and μ are connected through the relation $\mu = E/2(1+\nu)$, in which the Poisson coefficient $\nu = 0.3$. The microhardness measurements were made on CH_4,[23] Ar,[24] Kr,[25] NH_3,[26] graphite,[9,10] Au,[27] and NaCl (this publication).

testing in most cases because of the small size of the crystals being grown. The first and only stress-strain curve obtained as a result of compression of a sample with a cross section ~ 0.5 mm^2 at a constant strain rate is given in Refs. 9 and 10.

Weak van der Waals interactions between molecules are responsible for low values of Vickers microhardness H_V and the yield stress σ_0 for fullerite C_{60} crystals. At room temperature, the typical value of $H_V \simeq 0.2$ GPa,[8–12] while the ratio $H_V/\sigma_0 \simeq 20$.[9,10,13] As regards microhardness, fullerite C_{60} crystals are comparable to graphite, plastic fcc metals of the gold type, or NaCl crystals. Table I gives a more detailed information on fullerite hardness as compared to other cryocrystals. It can be seen that for comparable values of homological temperature, the relative microhardness of fullerite is higher than the hardness of typical molecular crystals (except ammonium in which the ordered $P2_13$ structure is preserved up to the melting point), fcc metallic and alkali-halide crystals. The high relative hardness of ammonium and fullerite C_{60} in this series of molecular crystals is obviously due to much larger contribution of the noncentral component of forces to the molecular interaction, leading to the formation of an ordered sc phase of C_{60} below the phase-transition temperature.

The physical and mechanical properties of C_{60} crystals depend significantly on the past history of the samples: the purity of the initial raw material, the method of obtaining (either from solution or from the gaseous phase), the time of holding in the gaseous medium and its composition, and illumination. The crystals grown from the gaseous phase are distinguished by higher purity and structural perfection. At present, high-quality crystals with a mass up to 14 mg (and volume up to 8.5 mm^3),[28] as well as larger crystals with the size $5\times3\times3$ mm,[29] which are suitable for various investigations, can be obtained.

The most interesting effects observed in microplasticity investigations for fullerite C_{60} are associated with low-temperature structural transformations in this crystal. However, x-ray diffraction[30] and acoustic studies[31] proved that the nature of phase transitions is determined to a considerable extent by various defects in real C_{60} crystals, such as the inclusions of C_{70}, amorphous phase, and other impurities inherited during the crystal growth or transformed as a result of thermal treatment. This is mainly manifested in the broadening of the temperature interval of orientational transition and its displacement toward lower temperatures, as well as in a considerable variation of temperature dependences of structural and thermodynamic parameters of C_{60} in the transition region.[30,31] First measurements of the temperature dependence of microhardness of C_{60} (Refs. 8–10 and 12) have also revealed qualitative difference for samples synthesized in different ways. It was found that the value of H_V for polycrystalline samples grown from solution and containing impurities of C_{70} and other phases increases monotonically without noticeable anomalies as the temperature decreases from 600 to 81 K.[10,32] More perfect crystals grown from the gaseous phase clearly manifest the fcc$\rightarrow$sc phase transiton at $T_c \simeq 260$ K,[1–3] while the microhardness of such single crystals displays a discontinuity in the region of T_c (Refs. 8 and 12) and a noticeable kink at $T_0 \simeq 155$ K, which correlates with a weak anomaly on the temperature dependence of the lattice parameter.[12] Above T_c, the hardness of these crystals is virtually constant in the temperature range 260–300 K.[8,10,12] At high temperatures $T > 370$ K, an anomalous growth of the value of H_V with increasing temperature is observed.[8]

Considerable influence of the surrounding medium on the mechanical properties of fullerite C_{60} was noted in Refs. 9, 10, and 32 and investigated partially by the nanoindentation technique in Ref. 33. It was shown that the strain-hardening was the strongest when the crystals were held in argon or oxygen due to implantation of Ar atoms or O_2 molecules in octahedral voids in the fcc lattice of C_{60}.[33] For example, the microhardness and the Young modulus of a crystal placed in Ar atmosphere after 45 h of holding at room temperature increased by a factor of ~ 100. Subsequent annealing led to restoration of the initial characteristics.

Finally, another important phenomenon was observed:[33] a change in microhardness as a result of irradiation of a C_{60} crystal with green light ($\lambda = 514$ nm). The magnitude and sign of the effect were determined by the gaseous medium: the crystal was strain-hardened in oxygen atmosphere, while in argon its hardness decreased. This peculiar photoplastic effect is associated with the formation of apex $C-O_2$ bonds upon the implantation of oxygen molecules in the crystal and with the polymerization of C_{60} molecules in the chains in the argon atmosphere. This effect differs from the photoplastic effects studied comprehensively for semiconducting crystals[34,35] and in irradiated alkali-halide crystals[36] and obviously requires further investigations.

Chemical and thermal etching of the crystal surface in

the vicinity of the indentation revealed that the plastic deformation of fullerite C_{60} crystals is of dislocation origin.[37,38] This means that the peculiarities of the temperature dependence of H_V must be attributed to a change in the mobility of dislocations: the high-temperature anomaly can be due to the interaction of dislocations with impurity molecules that diffuse in the crystal,[8] while the enhancement of the $H_V(T)$ dependence in the sc phase below 155 K is associated with the relaxation of orientational ordering of C_{60} molecules in the elastic field of moving dislocations.[13] However, the slip crystallography as well as the structure of dislocations in these crystals have been studied incompletely.

This research is devoted to (1) a more detailed description of the results of studies of the temperature dependence of the lattice parameters and microplasticity of pure C_{60} crystal, which were briefly discussed in Ref. 12, (2) an analysis of slip crystallography in the fcc and sc phases, (3) the study of microhardness anisotropy, and (4) an analysis of the effect of crystal annealing on the microhardness anomaly in the region of the fcc→sc transition.

2. MATERIAL AND EXPERIMENTAL TECHNIQUE

The samples were obtained from commercial fullerite having a purity of ~99.5% by double sublimation in Ar. The initial material was placed in a quartz boat of the sublimation column; argon was blown under a pressure of ~1 atm in the direction of temperature growth; C_{60} was heated approximately to 920 K during several hours; sublimated fullerite was returned to the column, and the process was repeated. According to the results of high-sensitivity liquid-phase chromatography, the purity of the obtained fullerite was higher than 99.9%. In addition to fine-disperse fraction with a grain size 10^{-1}–10^{-2} mm, the powder contained isolated crystals of size $\sim 2\times 1\times 0.3$ mm. Some of the crystals had a larger plane parallel to the {111} direction, some others were of the {100} type, while the edges, as a rule, had an orientation ⟨110⟩. Because of the uncontrollable growth, the facetting of individual crystals deviated from the crystallographic direction. Islets with specular surfaces of the {111} or {100} type, which are convenient for slip crystallography, were observed at the faces of the crystals.

The morphology of the surface of initial and indented samples was studied with the help of an optical microscope. The microhardness measuring technique in the temperature range 81–300 K was described in Ref. 39. All experiments were made in atmosphere, nitrogen vapor, and in liquid air ($T=81$ K) on the samples not protected from natural illumination. The spread in data was reduced by multiple measurements on the same sample. A thin layer of the surface being indented was removed between measurements by sample polishing with chamois leather impregnated with benzene. The relative error in determining the average value of microhardness did not exceed 2%. Here we present the average values of microhardness calculated from the results of measurements of 10–20 indentations.

In the case of x-ray diffraction studies, the coarse-grain sublimated powder was crushed and annealed in vacuum for 1 h at 500 K. Such a procedure of annealing made it possible to obtain samples free of macrostresses with a crystallite size

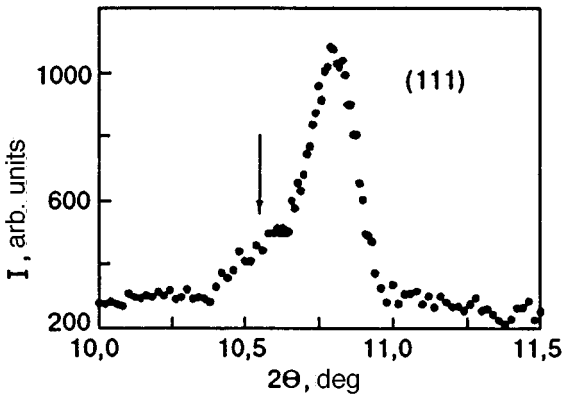

FIG. 1. The profile of the (111) x-ray reflection of fullerite C_{60} at room temperature. The arrow indicates the position of pseudo-Bragg diffraction.

10^{-4}–10^{-5} mm. Sample homogeneity and quality were monitored from the profile and width of diffraction reflexes. In the course of measurements, the samples were permanently in vacuum and were protected from illumination. Structural studies were carried out in Cu-K_α radiation on an automated DRON–type diffractometer in the temperature range 30–293 K by using an original liquid-helium cryostat.[40] The sample temperature was measured with a platinum resistance thermometer. The error in temperature stabilization was ±0.05 K, and the error in determining the lattice parameters did not exceed ±0.001 Å. The errors in determining the linewidth and intensity for x-ray reflexes are presented in the figures.

3. DISCUSSION OF RESULTS

3.1. X-ray studies

An analysis of x-ray diffraction pattern obtained at room temperature has proved that the process of dispersion and subsequent annealing did not lead to contamination of the sublimated material with any impurities. X-ray diffraction patterns contained only reflections from the cubic fcc phase of fullerite C_{60}. The value of the lattice parameter $a=14.161$ Å averaged over several measurements is in good agreement with the data for single crystals.[11,41,42] However, diffraction for the crushed material was characterized by an enhanced general background and by the emergence of additional pseudo-Bragg diffraction in the form of asymmetry or an ''arm'' in the (111) reflection profile (Fig. 1). The latter can be due to violation of the stacking order in atomic layers (111) of the fcc lattice, which lower the symmetry of defective regions of the crystal to the hexagonal symmetry. The effect of various types of stacking faults on the diffraction pattern for fullerite C_{60} crystals is considered in detail by Vaughan *et al.*[43] Such structural inhomogeneities in fullerite crystals can lead to a number of anomalies in the physical properties in the region of orientational phase transition: the formation of the second heat-capacity peak[43] and to a noticeable ''blurring'' of this transition detected by x-ray diffraction technique (see below).

X-ray studies in the temperature range 30–293 K confirmed, in general, the existing concepts concerning struc-

TABLE II. Angles and experimental values of intensities of x-ray reflections in fullerite C_{60} at 32 K.

No.	$2\Theta^{\circ}_{exp}$	I_{exp}	hkl	$2\Theta^{\circ}_{calc}$	$\Delta(2\Theta°)$
			100	6.360	
			110	9.000	
1	11.03	1000	111	11.028	−0.002
			200	12.741	
			210	14.252	
			211	15.621	
2	18.07	925	220	18.056	−0.014
			300	19.161	
			310	20.208	
3	21.21	720	311	21.206	−0.004
4	22.17	200	222	22.161	−0.009
			320	23.078	
			330	27.228	
5	28.02	60	331	27.989	−0.031
6	28.76	75	420	28.731	−0.029
			421	29.456	
			332	30.166	
7	31.53	86	422	31.541	0.011
			430	32.210	
			510	32.865	
8	33.53	76	511	33.510	−0.020
			520	34.767	
			600	38.886	
9	39.48	52	610	39.445	−0.035
			611	39.997	
			620	41.082	
10	41.56	32	540	41.616	0.056
11	42.19	23	541	42.144	−0.046
12	42.65	25	533	42.667	0.017
13	43.21	390	622	43.185	−0.025
			630	43.698	
			444	45.209	
14	45.74	58	632	45.704	−0.036
15	46.17*	35	550	46.195	0.025
16	46.71	95	551	46.681	−0.029
			640	47.164	
			722	49.524	
17	49.93*	74	730	49.987	0.064
18	50.46	280	731	50.446	−0.014
			650	51.355	
			820	54.451	
19	54.86	60	821	54.883	0.023
			653	55.313	
			664	62.723	
20	63.17	29	850	63.120	−0.05
21	63.47*	34	930	63.514	0.044
			931	63.908	
			961	74.121	
22	74.82	57	1042	74.852	0.032
			1100	75.218	

*Structural reflections which belong to a space symmetry group lower than $Pa3$.

tural transformation occurring during the cooling of C_{60} crystals. The fcc→sc phase transition is accompanied by the emergence of superstructural reflexes on diffraction patterns, corresponding to a decrease in the total symmetry of the crystal as a result of orientational ordering of molecules. Most of the observed superstructural reflexes are identified in the space group $Pa3$. A part of experimental diffraction pattern at $T=32$ K is presented in Table II, together with the theoretically calculated reflexes for the lattice parameter $a=14.043$ Å. In addition to the experimental ($2\Theta^{\circ}_{exp}$) and theoretical ($2\Theta^{\circ}_{calc}$) values of the reflection (hkl) angles, Table II also contains the experimental values of the intensities (I_{exp}) of the observed reflections in relative units, normalized to the intensity of the strongest reflections (111). The first column of Table II contains the number of observed reflections, while the last column shows the difference $\Delta(2\Theta°)$ between the theoretical and experimental diffraction angles. For large diffraction angles, several superstructural reflections of the ($hk0$) type with odd h and k (marked by asterisks in Table II), which do not belong to $Pa3$ symmetry and whose intensity is comparable with that of the main structural reflections in this range of diffraction angles,

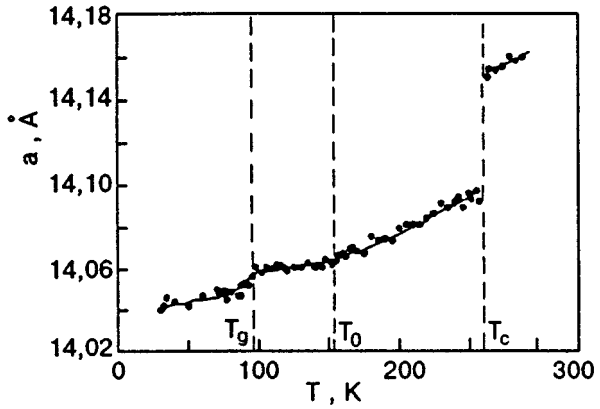

FIG. 2. Temperature dependence of the lattice parameter for the fullerite C_{60}: T_c is the temperature of orientational phase transition fcc→sc, T_0 and T_g are the temperatures corresponding to the beginning and end of the formation of the orientational glass, respectively.

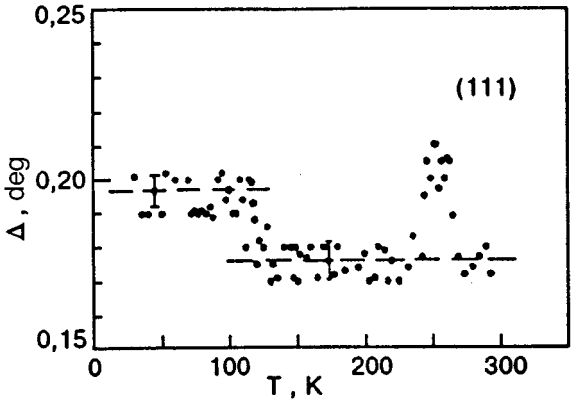

FIG. 3. Temperature dependence of the half-width Δ of (111) x-ray reflection.

are observed. Since powder samples contained a large number of regions with stacking faults with a symmetry lower than that of fcc, it can be naturally assumed that the orientationally ordered structure has a symmetry lower than $Pa3$ in these regions also. This circumstance can be responsible for the emergence of additional superstructural reflections at $T<T_c$. It should be noted that the intensity of such reflections must increase with the volume of defective regions. However, we could not verify much an increase.

The temperature dependence of the lattice parameter a (Fig. 2) contains regions corresponding to three characteristic temperatures. The fcc→sc phase transition is accompanied by a jump in the lattice parameter whose relative decrease ($\Delta a/a \simeq 0.33\%$) as a result of the transition is in good agreement with the results obtained in Refs. 2 and 42. The temperature variation of the lattice parameter in the high-temperature phase corresponds to the available experimental data.[2,5,41,42] The obtained phase-transition temperature $T_c = 260$ K which we obtained virtually coincides with the temperature typical of single-crystal samples.[2,11] Detailed analysis of x-ray patterns revealed the coexistence of the fcc and sc phases in the vicinity of the phase transition temperature $T_c \pm 3$ K. The presence of two phases in such a significant temperature interval during an orientational phase transition is apparently due to dispersion in the values of phase-transition temperature in defective regions of the crystal. The regions of short-range orientational order in the parts of the crystal with stacking disorder near T_c is characterized by a smaller correlation radius of the orientational interaction as compared to the rest of the crystal,[43] and hence by a lower phase-transition temperature T_c. According to the results on inelastic x-ray and neutron scattering,[44] the regions of short-range orientational order in perfect C_{60} single crystal in which translational disorder of the stacking fault type is not observed have a correlation length of the order of 40 Å (at $T = 265$ K).

At $T_g \simeq 95$ K, the $a(T)$ dependence has a clearly manifested kink (see Fig. 2); this anomaly is also well known from previous structural studies.[2,12] The peculiarity in the behavior of $a(T)$, which is observed at $T_0 = 155$ K and about which the information is controversial,[2,6] was detected by us more clearly. It should be noted that some other parameters of fullerite have certain peculiarities just in the vicinity of this temperature (this problem was discussed, for example, in the review in Ref. 6).

The peculiarities on the temperature dependence of some physical parameters at $T<160$ K are associated by David *et al.*[2,4] with the retardation of rotation of C_{60} molecules about $\langle 111 \rangle$ axes, which is manifested in an increase in the lifetime of orientational defects (hexagonal configurations of pairs of neighboring molecules) upon a decrease in temperature. Subsequent cooling leads to virtually complete freezing of the rotational motion and to the formation of orientational glass at $T<95$ K (with a fixed relation between pentagonal and hexagonal configurations of C_{60} molecules). This explains the increase in the half-width of x-ray reflections in the region $T_g<T<T_0 \simeq 155$ K observed in our experiments. The results of measurement of the half-width Δ of the profile of one of the main reflections (which are structural in the case of an fcc lattice) are presented in Fig. 3. As the temperature decreases from 155 K to the glass-transition point, the half-width of the reflection profile undergoes an overall variation of 10–12%. A similar diffraction involving the variation of the reflection profile half-width was observed earlier in solid solutions of simple molecular crystal N_2–Ar[45] and O_2–Ar[46] during the formation of orientational glass in them. However, the glass-formation process in these systems was accompanied by a more significant broadening of reflections (by more than 70%). We believe that the freezing of molecules in random orientations leads to their non-uniform static displacements from lattice cites. The magnitude of displacements, and hence the broadening of diffraction reflections, are determined by the contribution of anisotropic forces to the lattice energy. In contrast to this effect, the noticeable increase in the profile half-width of the (111) reflection near T_c (Fig. 3) is due to the superposition of reflections from two coexisting phases with a small difference in molecular volumes, while the shape of the temperature dependence of the half-width of the (111) reflection in the two-phase region characterizes the change in the concentration of phases upon a transition through T_c.

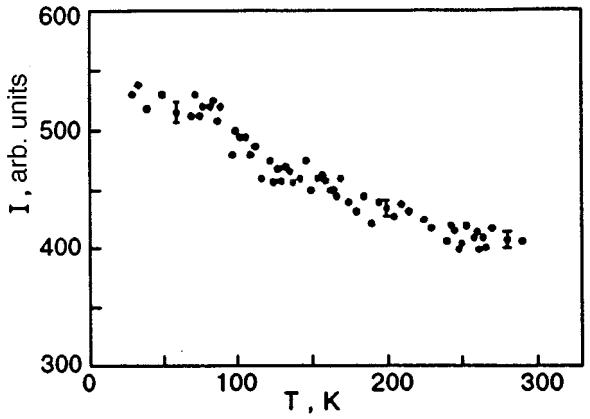

FIG. 4. Temperature dependences of the intensity of (111) x-ray reflections.

We have not discovered any anomalies on the temperature dependences of the intensity of structural reflections in the entire temperature range of investigation. As the temperature decreases, their intensity increases monotonically (Fig. 4) mainly due to a change in the Debye–Waller factor as a result of the decrease in the amplitude of mean-square displacements of the molecules. A decrease in temperature below T_g leads to an anomalous retardation of the growth of intensity $I(T)$ (see Fig. 4). Since the peculiarities on the temperature dependences of the physical properties of fullerites are mainly determined by the behavior of its orientational subsystem, it would be interesting to study the temperature dependence of the intensity of superstructural reflections. Superstructural reflections typical of the $Pa3$ lattice were studied in detail for C_{60} single crystals.[43,47–49] The results described in these publications show that a retardation of the growth of $I(T)$ similar to that shown in Fig. 4 is typical of most of superstructural $Pa3$ reflections upon a transition to a glass-like phase.

3.2. Growth twins and slip crystallography

The polished surface of crystals displayed plane-parallel stripes aligned along the $\langle 110 \rangle$ directions, which were preserved after multiple polishing. One of such stripes observed on the $\{100\}$ plane is shown in Fig. 5. Such stripes are apparently growth twins corresponding to $\{111\}\langle 112 \rangle$ systems typical of fcc crystals. They become visible because of selective etching of twinned planes and their boundaries under the action of benzene. Growth twins are typical defects in fullerite C_{60} crystals.[29] The width of the twins varied from 5–10 μm to tens of micrometers. The effect of growth twins on microhardness was not studied, but it would hardly be significant for a low density of twin boundaries. However, twins do play a noticeable role in the formation of cracks. Indentation in the vicinity of twin boundaries always leads to the formation of cracks along the latter. We did not observe the formation of deformation-induced twins under the action of a concentrated force, but it cannot be ruled out that strongly distorted regions of the crystal can contain a large number of deformation-induced stacking faults in the vicinity of indentations.

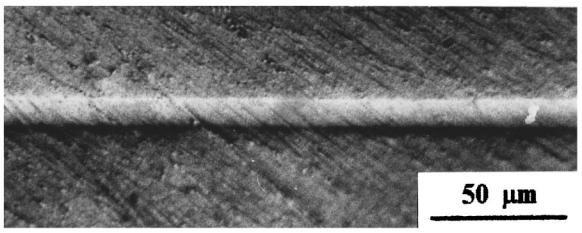

FIG. 5. The growth twin detected on the $\{100\}$ plane of the C_{60} crystal as a result of its mechanical and chemical polishing with chamois leather impregnated with benzene. The direction of twin boundaries coincides with the $\langle 110 \rangle$ direction.

The cubic lattice of fullerite C_{60} as well as the familiar habitus of the crystals make it possible to determine unambiguously the slip systems in the high- and low-temperature phases from an analysis of the pattern of slip traces in deformed regions in the region of indentation (Fig. 6). It is well known that a slight slippage in fcc crystals can easily be realized along the octahedral system $\{111\}\langle 110 \rangle$. For crystals with a sc lattice, the systems $\{100\}\langle 100 \rangle$ or $\{110\}\langle 100 \rangle$ might turn out to be advantageous from the energy point of view.[8] Proceeding from these considerations, let us compare the pattern of slippage stripes on the sample surface with the directions of traces of crystallographic planes $\{111\}$, $\{100\}$, and $\{110\}$ on the habitus planes (111) and (100) of the crystal.

Clearly manifested slippage planes were formed in the vicinity of an indentation for loads exceeding 0.1–0.2 N. The stripes formed on the (111) plane under a loading of 0.2N ($T = 290$ K) can be seen in Figs. 6a and 6b (at $T < T_c$, the pattern is similar). Repeated indentation under the same load (Fig. 6b) only led to a more intense slippage and elongation of the stripes formed as a result of the previous indentation. Figure 6d shows that the traces of the three types of the planes $\{111\}$, $\{100\}$, and $\{110\}$ on the (111) plane of the sample have the same $\langle 110 \rangle$ direction. Planes of the $\{110\}$ type can have the $\langle 112 \rangle$ direction also. These two sets of traces can be identified only if the crystallographic direction of at least one of the crystal edges is known. The triangles of traces turned relative to one another reflect converging and diverging slip systems along which the transfer of matter is accomplished in the vicinity of the indentor to the surface of the sample and to its bulk. This explains different (black and white) contrasts of parallel slippage stripes in Figs. 6a and 6b. In the case of the $\{110\}\langle 100 \rangle$ system, the traces in the $\langle 112 \rangle$ direction correspond to the three slippage planes $(0\bar{1}1)$, $(\bar{1}10)$, and $(\bar{1}01)$ from the $\{110\}$ family, which intersect the (111) surface of the sample at right angles. Naturally, an analysis of the plastic shear pattern (slip steps) on the $\{111\}$ plane alone[38] does not lead to an unambiguous conclusion about slip crystallography (especially at temperatures below the phase-transition point).

Figure 6c shows the microscopic structure of the deformed region of the sample indented at $T = 81$ K at the surface that deviates slightly from the (100) plane. It can be seen from Fig. 6e that the pattern of the traces of the $\{111\}$, $\{100\}$, and $\{110\}$ planes intersecting the (100) plane is extremely simple. Remarkably, only the slippage planes of the $\{111\}\langle 110 \rangle$ can be either converging or diverging, form-

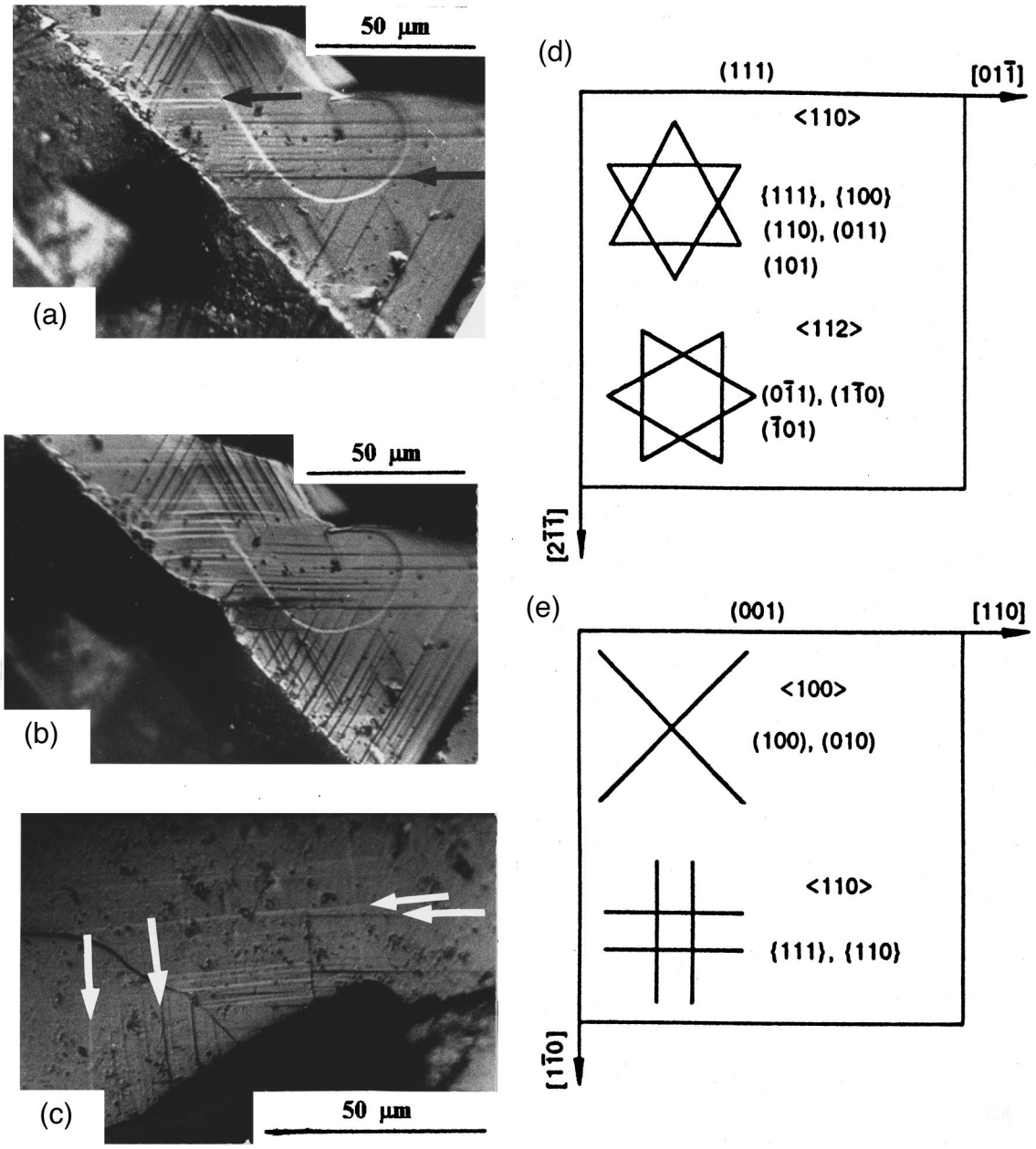

FIG. 6. Slip stripes bear the impression of the indenter on the (111) (a,b) and (100) (c) planes and schematic diagrams of possible slip planes $\langle 111\rangle$, $\langle 100\rangle$, and $\{110\}$ on habitus planes of the C_{60} crystal: the first and repeated indentation at $P=0.2$ N and $T=290$ K(a,b); and indentation at $P=0.35$ N and $T=81$ K(c); the (111) plane, the direction of traces $\langle 110\rangle$ and $\langle 112\rangle$(d), the (001) plane, the direction of traces $\langle 100\rangle$ and $\langle 110\rangle$(e).

ing parallel traces on the (100) plane. The $\{110\}\langle 100\rangle$ system with the Burgers vector lying in the $\{100\}$ plane naturally is not seen. A deviation of the sample surface from (100) leads to the emergence of nonparallel traces (Fig. 6c). Different optical contrasts of steps on the surface and their nonparallelism indicate that the pairs of slippage planes marked by arrows and forming small angles with one another belong to different families $\{111\}\langle 100\rangle$.

Thus, our microstructural observations of slippage stripes and their geometrical analysis lead to the unambiguous conclusion that only the octahedral slip system $\{111\}\langle 110\rangle$ is active at temperatures in the interval 81–300 K. Although such a conclusion was made earlier in Refs. 12 and 38, crystals of two orientations were used only in Ref. 12 and in the present work for its verification.

The conservation of slip in $\{111\}$-type planes during fcc→sc phase transition is a phenomenon that has been studied well in ordered alloys Cu_3Au and Ni_3Mn.[50] It is possible that like in these alloys, slip in $\{111\}$ planes in the ordered sc-phase of C_{60} occurs through the motion of partial dislocations accompanied with the formation of low-energy out-of-phase boundaries.[12] The microscopic nature of conservation of slip systems in C_{60} crystals upon a fcc→sc transition is undoubtedly interesting and deserves further investigations.

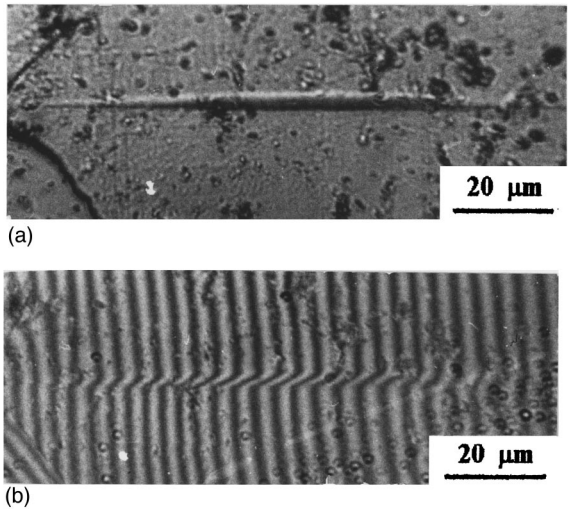

FIG. 7. Lens-shaped shear region formed as a result of indentation of the (100) plane in the C_{60} crystal at $T=290$ K and $P=0.7$ N: metallographic microscope (a) and interference microscope (b).

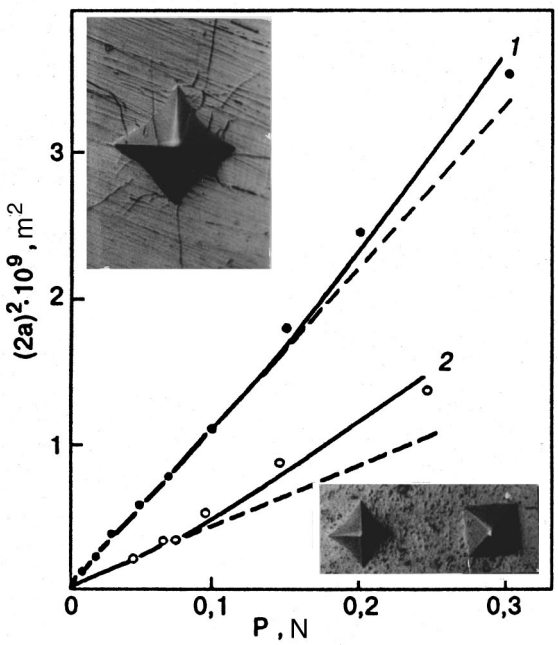

FIG. 8. Dependence of the square of the impression of the indenter on the (100) plane of the C_{60} crystal on the load applied to the indenter at $T=290$ K (curve *1*) and $T=81$ K (curve *2*). The upper inset shows the impression of the indenter on the (100) plane at $P=0.25$ N and $T=81$ K. The diagonal of the impression is directed along [011]. The lower inset shows the impressions of the indenter in the (100) plane for $P=0.05$ N and $T=290$ K; the horizontal direction is parallel to [110].

3.3. Localization of slip

The deformation of C_{60} crystals by indentation is characterized by noticeable localization of plastic shear strains leading to the formation of clearly manifested steps upon the emergence of a slip stripe at the surface (Fig. 7a,b). A lens-shaped shear region is formed as a result of indentation under a large load applied to the indenter. It resembles a twin in shape, but the height of a step at the surface turns out to be smaller than in the case of a twin in the fcc lattice by a factor of 2.5. The lens-like shape is due to deceleration of a slip strip at cracks restricting its elongation on both sides.

It is well known that slip localization upon indentation is enhanced upon an increase in rigidity of the crystal, for example, as a result of doping, irradiation, or cooling.[51] This phenomenon should not be typical of pure molecular crystals (at least in their high- temperature phase).[7] The C_{60} crystals investigated by us were initially saturated with Ar atoms which, according to Haluska *et al.*,[33] can lead to a significant strain-hardening and a decrease in plasticity even in an orientationally disordered state.

3.4. Microhardness of C_{60} crystals

Dependence of H_V on the load applied to the indentor. The dependences of the square $(2a)^2$ of the impression diagonal on load P, obtained on (100) plane at 81 and 290 K, are shown in Fig. 8. The linear relation between $(2a)^2$ and P corresponding to the constancy of $H_V(P)$ was observed only for loads $P \leqslant 0.1$ N at 290 K and $P \leqslant 0.075$ N at 81 K. At higher loads on the indentor, the material was broken. Cracks in the vicinity of impression had no clearly manifested crystallographic direction like in the case of brittle crystals, but the $\langle 110 \rangle$ direction can be indicated as a preferred direction of their propagation. At nitrogen temperatures, crack formation was more intense (see the inset in Fig. 8) and started at lower loads.

The absence of the $H_V(P)$ dependence for the $\{111\}$ plane was observed in Ref. 8 at room temperature for loadings down to ~ 0.14 N, while in Ref. 28 the microhardness for the same plane decreased significantly upon an increase in load to ~ 0.2 N and only after that it remained unchanged up to $P=0.8$ N. The existence of a wide range of loads for which $H_V(P)=\text{const}$ obviously indicates the homogeneity of the crystals under investigation due to favorable conditions of their growth. The reason behind a decrease in microhardness and increasing load (impression depth) observed in Refs. 9 and 10 could be the concentration gradient of impurities diffusing through the sample surface.

Microhardness anisotropy. The anisotropy of plastic slip is manifested in experiments on microindentation of C_{60} crystals in experiments on microhardness first in different values of microhardness for different indentation planes for the same values of P and T, and second, in a dependence of the impression shape on the direction of the indentor diagonal. It can be seen from Fig. 8 that the impressions are concave if the indentor diagonal is oriented along the $\langle 110 \rangle$ direction and convex if the diagonal is oriented along $\langle 100 \rangle$. This is due to the displacement of the material ejected during the intrusion of the indenter in the slip direction as for other cubic crystals[51] (in the case of fullerite C_{60}, this is the $\langle 110 \rangle$ direction; see the schematic diagram in Fig. 6e). It should be noted that the preservation of the shape of the impression upon a change in temperature of indentation is an indication of preservation of the slip system in C_{60} during the phase transition.

At all temperatures, the value of microhardness measured in the (111) plane was higher than that measured in the (100) plane (Fig. 9). The ratio of the values of H_V for these

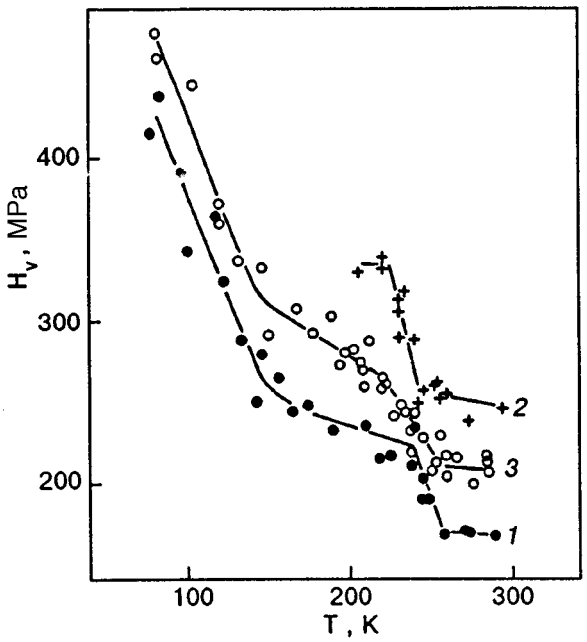

FIG. 9. Temperature dependences of microhardness obtained as a result of indentation of habitus planes (100) (curve *1*) and (111) (curves *2* and *3*) for three different C_{60} crystals.

planes is $\sim 1.25-1.5$ in the region of room temperatures, which is in good agreement with the results obtained in Ref. 11; as the temperature decreases, this ratio becomes smaller and attains the value ~ 1.1 at 81 K. The anisotropy of hardness is probably due to different values of strain hardening of the material under the indentor, whose intensity can depend on the direction of indentation $\langle 111\rangle$ or $\langle 110\rangle$ (see the schematic diagram in Figs. 6d and 6e).

Temperature dependence of microhardness. In order to analyze the temperature dependence of microhardness, we used a load ~ 0.05 N, which ensures the satisfaction of the condition $H_V(P) = \text{const}$ in the entire temperature interval of interest.

Figure 9 shows three $H_V(T)$ dependences obtained as a result of indentation of the (100) plane (curve *1*)[12] and the (111) plane (curves *2* and *3*). The absolute values of microhardness at room temperature ($H_V^{100} = 170$ MPa and $H_V^{111} = 210-250$ MPa) are close to those obtained by other authors.[8,10,11,28] The spread in the values of H_V for different samples of the crystals with the same orientation was $\sim 20\%$. The same spread was also observed in Ref. 8.

The main peculiarities of the temperature dependence of microhardness can be reproduced for all the samples, are insensitive to the orientation of the indentation plane, and are obviously associated with specific structure of fullerite.[8,12,13] The first of these peculiarities is the athermal nature of H_V in the high-temperature phase of C_{60} even when impurity diffusion processes leading to the fixation of dislocations are included.[8] This feature is typical of the mechanical properties of high- symmetry crystals and can indicate that the fcc fullerite belongs to plastic molecular crystals.[7]

Two anomalies (namely, the step-wise variation of microhardness in the region of the fcc→sc transition and the kink on the $H_V(T)$ dependence in the region of $T \sim 155$ K, correlate with the observed anomalies on the temperature dependence of the lattice parameter (see Fig. 2). Note that an increase in microhardness in the sc phase can be partly due to an increase in the elastic moduli for fullerite: the increase in Young's modulus during a phase transition is $\sim 8\%$, while the cooling from room temperature to 6 K causes its increase by 40%.[22] At the same time, the step on H_V in the transition region amounts to 30–50%,[8,12] while the microhardness increases approximately by a factor of two in the temperature range 290–81 K. The main contribution to the increment of H_V during cooling is undoubtedly associated with a considerable effect of thermally activated processes on the slip kinetics (mobility of dislocations). Among other things, an increase in the size of the deformation region with well-developed slip stripes upon an increase in the holding time under loading indicates the activation nature of slip evolution (Fig. 6b).

Two types of relaxation processes occurring in the elastic field of a dislocation moving in the sc phase of fullerite C_{60} were analyzed in Ref. 13. It was shown that these processes are due to dynamic interaction of dislocations with rotational degrees of freedom of C_{60} molecules. Each such process can make a significant contribution to dislocation drag. In the immediate vicinity of T_c, the dominant role is played by the relaxation losses accompanying the interaction of the elastic field of dislocations with the field of the order parameter which corresponds to this transition. According to the estimates obtained in Ref. 13, the proposed mechanism can explain the stepwise increase in H_V below T_c. In the temperature range of ~ 160 K, the main role is played by dynamic losses of the dislocation, which are associated with the thermally activated relaxation in the system of pentagonal and hexagonal molecular configurations, whose equilibrium is violated by the elastic dislocation field. This drag mechanism can be used to explain the beginning of a significant increase in H_V upon a decrease in temperature in the region of orientational vitrification of fullerite.

It should be observed that the relaxation of the order parameter as well as the activation transitions in the system of pentagonal and hexagonal configurations affect the acoustic properties of the fullerite C_{60} quite significantly. Hence the acoustic anomalies must be closely related physically to the $H_V(T)$ anomalies below T_c.[13]

Effect of impurities on the microhardness anomaly in the fcc→sc *transition region.* The stepwise increase in microhardness associated with the phase transition occurs over a fairly wide temperature interval between 10 K (Refs. 8 and 12) and 20 K or more (Figs. 9 and 10). The $H_V(T)$ dependences obtained during cooling and heating of the sample are identical to within the measuring error. It is known from structural,[30,52,53] acoustic[31,54,55] and NMR studies,[56,57] as well as the data on heat capacity[58,59] that the width of the phase transition ΔT and the behavior of thermodynamic properties of fullerites in the vicinity of T_c depend significantly on the presence of impurities in the sample. A significant concentration of the interstitial impurities of the C_n-type molecular fragments, N_2 or O_2 molecular components or other components of air may not only lower the superconducting transi-

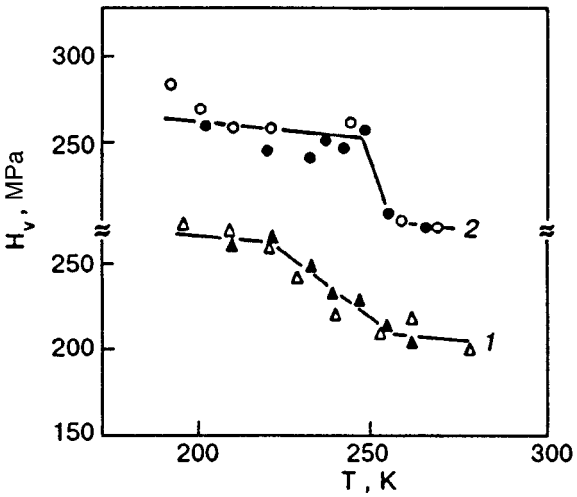

FIG. 10. Temperature dependences of microhardness in the region of the fcc→sc transition obtained on the same C_{60} crystal subjected to different treatment: the initial crystal polished before the measuring microhardness (curve *1*, light triangles), the same crystal polished after annealing in vacuum (the annealing mode is given below) and holding in air for five days (dark triangles); the crystal polished and annealed in a 10^{-3} Torr vacuum for 24 h at 400 K (curve *2*; the symbols ○ and ● correspond to different experiments).

tion temperature T_c, but also considerably increase the interval ΔT (up to ~10 K or more).[30]

The extended step on the $H_V(T)$ dependence during a transition through T_c may also be due to the molecular impurities trapped by the sample surface from the surrounding air or during mechanical and chemical polishing. In order to verify this assumption, we annealed a sample in a vacuum of 10^{-3} Torr at 400 K for 24 h. Figure 10 shows that annealing leads to an abrupt narrowing of the temperature interval of variation of microhardness.

In our opinion, atmospheric oxygen is the most probable trapped impurity. In contrast to noble gases, oxygen molecules affect significantly the intermolecular forces in fullerite[28] and determine the peculiarities of the fcc→sc phase transition to a certain extent.[60,61] The high mobility of oxygen in C_{60}, which is due to a low diffusion activation energy of 0.24 eV,[62] is a factor facilitating the saturation of the surface layers of the sample with oxygen as well as their purification in a moderate vacuum at a low temperature ($T \sim 400$ K). The details of the effect of impurities on the phase transition in C_{60} require further investigations.

CONCLUSIONS

1. The crystal structure, the lattice parameters, the half-width and intensity of x-ray reflections of fullerite C_{60} are studied by the method of x-ray diffractometry in the temperature range 30–293 K. It is shown that the temperature corresponding to the orientational phase transition in high-purity fullerite is $T_c = 260$ K and that it nearly coincides with the value typical of single crystals.

2. It is found that the samples under investigation contain a noticeable number of regions with stacking faults. A two-phase region with an interval of blurring of ±3 K due to dispersion of the of transition temperatures in defective regions of the crystal is detected in the fcc→sc transition. Along with superstructural reflections typical of $Pa3$ lattice, a number of $(hk0)$ reflections with odd h and k corresponding to a lower symmetry of the orientational ordering of molecules are observed in the low-temperature phase of fullerite. This symmetry can be realized in crystal regions with stacking faults.

3. The temperature dependence of the lattice parameter a manifests three distinct features: the jump $\Delta a/a = 3.3 \times 10^{-3}$ in the parameter at the phase-transition temperature T_c, weakening of the $a(T)$ dependence at $T_0 \lesssim 155$ K, and a kink at $T_g \simeq 95$ K, which are associated with the beginning and termination of molecular orientation freezing. It is shown that the formation of orientational glass is accompanied by a considerable increase in the half-width of structural reflections. Anomalous deceleration of the increase in the intensity of structural reflections with decreasing temperature is observed in the region corresponding to orientational glass ($T < T_g$).

4. Microscopic observations of the surface and crystallographic analysis of the patterns of plastic shears in the (111) and (100) planes lead to the unambiguous conclusion concerning the activity of the only slip system of the $\{111\} \times \langle 110 \rangle$ type in the fcc and sc phases.

5. The temperature dependence of microhardness H_V of C_{60} crystals is studies in the temperature range 81–293 K. The hardness of the fcc phase normalized to the elastic modulus turns out to be higher than the hardness of typical molecular crystals at comparable homological temperature values. This fact as well as considerable localization of slippage indicates that the crystals studied in this research cannot be classified as plastic crystals in view of the presence of hardening impurities in them.

6. The microhardness increases stepwise by approximately 30% upon a transition through T_c, while at $T < 160$ K the $H_V(T)$ dependence becomes stronger. These anomalies are regarded as consequences of dislocation drag due to relaxation losses during the interaction of the elastic field of dislocations with the field of the orientational order parameter (the T_c region) and with the system of pentagonal and hexagonal configurations of C_{60} molecules whose equilibrium is violated by a moving dislocation (the region of $T \simeq 160$ K).

7. The increase in the value of H_V during the fcc→sc transition is observed in the temperature interval larger than 10 K. The width of this interval decreases as a result of annealing in vacuum, which is apparently due to the purification of surface layers from gaseous impurities saturating the crystal during its storage in air.

8. Plastic deformation in C_{60} crystals is anisotropic, which is manifested, for example, in the dependence of the value of H_V on the direction of the indentation plane: $H_V^{111} \simeq (1.25-1.5) H_V^{100}$ at $T = 293$ K.

This research was carried out under financial support of the Ukrainian State Committee on Science, Engineering, and Industrial Policy (project No. 09.01.01/033-92 ''Material'') and was supported in part, by the Soros International Science Foundation.

*E-mail: lubenets@ilt.kharkov.ua

[1] P. A. Heiney, J. A. Fischer, A. R. McGhie *et al.*, Phys. Rev. Lett. **66**, 2911 (1991).
[2] M. I. F. David, R. M. Ibberson, T. J. S. Dennis *et al.*, Europhys. Lett. **18**, 219 (1992).
[3] V. M. Loktev, Fiz. Nizk. Temp. **18**, 217 (1992) [Sov. J. Low Temp. Phys. **18**, 149 (1992)].
[4] W. I. F. David, R. M. Ibberson, and T. Matsuo, Proc. Roy. Soc. London **A442**, 129 (1993).
[5] J. E. Fischer and P. A. Heiney, J. Phys. Chem. **54**, 1725 (1993).
[6] J. D. Axe, S. C. Moss, and D. A. Neumann, in *Solid State Physics* (ed. by H. Ehrenreich and F. Spaepen), Acad. Press, New York (1994), vol. 48.
[7] J. Timmermans, Phys. Chem. Sol. **18**, 1 (1961).
[8] M. Tachibana, M. Michiyama, K. Kikuchi *et al.*, in *Crystal Growth of Organic Materials*, ACS Conference Proceedings Series (ed. by A. S. Myerson, D. A. Green, and P. Meenan), American Chemical Society (1996).
[9] Yu. A. Ossipyan, V. S. Bobrov, Yu. S. Grushko *et al.*, Appl. Phys. **A56**, 413 (1993).
[10] V. S. Bobrov, R. A. Dilanyan, L. S. Fomenko *et al.*, in *Solid State Phenomena* **35–36** (ed. by J. Rabier, A. George, Y. Brechet, and L. Kubin) (1994).
[11] J. Li, S. Komiya, T. Tamura *et al.*, Physica **C195**, 205 (1992).
[12] L. S. Fomenko, V. D. Natsik, S. V. Lubenets *et al.*, Fiz. Nizk. Temp. **21**, 465 (1995) [Low Temp. Fiz. **21**, 364 (1995)].
[13] V. D. Natsik, S. V. Lubenets, and L. S. Fomenko, Fiz. Nizk. Temp. **22**, 337 (1996) [Low Temp. Fiz. **22**, 264 (1996)].
[14] V. I. Zubov, N. P. Tretiakov, J. N. Teixeira Rabelo, and J. S. Sanches, Phys. Lett. **A194**, 223 (1994).
[15] J. Kay and T. Lebi, *Tables of Physical and Chemical Constants* [Russian transl.], Gos. Izd. Fiz. Mat. Lit., Moscow (1962).
[16] *Cryocrystals* [in Russian] (ed. by B. I. Verkin and A. F. Prikhot'ko), Naukova Dumka, Kiev (1983).
[17] J. Friedel, *Dislocations* [Russian transl.], Mir. Moscow (1967).
[18] S. W. Marx and R. O. Simmons, J. Chem. Phys. **81**, 944 (1984).
[19] *Rare Gas Solids* (ed. by M. L. Klein and J. A. Venables), vol. 1, Acad. Press, London (1976).
[20] D. N. Bol'shutkin and A. I. Prokhvatilov, Fiz. Tverd. Tela (Leningrad) **8**, 248 (1966) [Sov. Phys. Solid State **8**, 198 (1966)].
[21] I. N. Frantsevich, F. F. Voronov, and S. A. Bakuta, *Elastic Constants for Metals and Nonmetals* (A Handbook) [in Russian], Naukova Dumka, Kiev (1982).
[22] S. Hoen, N. G. Chopra, X.-D. Xiang *et al.*, Phys. Rev. **B46**, 12737 (1992).
[23] D. N. Bol'shutkin, A. V. Leont'eva, V. G. Snigerev, and V. I. Startsev, Fiz. Tverd. Tela (Leningrad) **7**, 2607 (1965) [Sov. Phys. Solid State **7**, 2110 (1967)].
[24] C. Trepp, Schweizer Archiv **24**, 230 (1958).
[25] F. P. Bouden and G. W. Rove, Proc. Roy. Soc. **A228**, 1 (1955).
[26] A. I. Prokhvatilov, V. V. Pustovalov, T. V. Sil'vestrova, and V. I. Startsev, Ukr. Fiz. Zh. **10**, 1127 (1965).
[27] G. P. Upit and S. A. Varchenya, in: *The Science of Hardness Testing and Its Research Applications* (ed. by J. H. Westbrook and H. Konrad), USA (1971).
[28] M. Haluska, M. Zehetbauer, H. Kuzmany *et al.*, Mol. Matter **4**, 73 (1994).
[29] J. Li, T. Mitsuki, M. Ozawa *et al.*, J. Crystal Growth **143**, 58 (1994).
[30] N. A. Aksenova, A. P. Isakina, A. I. Prokhvatilov *et al.*, in *Fullerenes. Proc. Symp. on Recent Advances in the Chemistry and Physics of Fullerenes and Related Materials* (ed. by K. M. Kadish and R. S. Ruoff), The Electrochemical Society Inc., Pennington (1994), vol. 94–24.
[31] X. D. Shi, A. R. Kortan, J. M. Williams *et al.*, Phys. Rev. Lett. **68**, 827 (1992).
[32] V. S. Bobrov, R. A. Dilanyan, L. S. Fomenko *et al.*, J. Supercond. **8**, 1 (1995).
[33] M. Haluska, M. Zehetbauer, M. Hulman, and H. Kuzmany, in *Materials Science Forum*, vols. 210–213, Part. 1 *Nondestructive Characterization of Materials II* (ed. by A. L. Bartos, R. E. Green, Jr., and C. O. Ruud), Transtec Publ., Switzerland (1966).
[34] G. C. Kuczinski and R. F. Hochman, Phys. Rev. **108**, 946 (1957); Phys. Rev. **30**, 669 (1959).
[35] Yu. A. Osip'yan, V. F. Petrenko, A. V. Zaretskii, and R. W. Withwort, Adv. Phys. **35**, 115 (1986).
[36] J. S. Nadeau, J. Appl. Phys. **35**, 669 (1964).
[37] V. I. Orlov, V. I. Nikitenko, R. K. Nikolaev *et al.*, Pis'ma Zh. Éksp. Teor. Fiz. **59**, 667 (1994) [JETP Lett. **59**,704 (1994)].
[38] M. Tachibana, H. Sakuma, M. Michiyama, and K. Kojima, Appl. Phys. Lett. **67**, 2618 (1995).
[39] B. Ya. Farber, N. S. Sidorov, V. I. Kulakov *et al.*, Sverkhprovodimost': Fiz., Khim., Tekh. **4**, 2393 (1991).
[40] A. I. Prokhvatilov, I. N. Krupskii, L. D. Yantsevich, and A. S. Baryl'nik, Pribory Tekh. Eksper. No. 3, 261 (1981).
[41] R. Moret, P. A. Albouy, V. Agafonov *et al.*, J. Phys. (Paris) **2**, 511 (1992).
[42] H. Kasatani, H. Terauchi, Y. Hamanaka, and S. Nakashima, Phys. Rev. **B47**, 4022 (1993).
[43] G. B. M. Vaughan, Y. Chambre, and D. Dubois, Europhys. Lett. **31**, 525 (1995).
[44] L. Pintschovius, S. L. Chaplot, G. Roth, and G. Heger, Phys. Rev. Lett. **75**, 2843 (1995).
[45] H. Klee, H. O. Carmesin, and K. Knorr, Phys. Rev. Lett. **61**, 1855 (1988).
[46] A. S. Baryl'nik and A. I. Prokhvatilov, Fiz. Nizk. Temp. **15**, 971 (1989) [Sov. J. Low Temp. Phys. **15**, 536 (1989)].
[47] R. Moret, Phys. Rev. **B48**, 17619 (1993).
[48] K. Sakaue, N. Toyoda, H. Kasatani *et al.*, J. Phys. Soc. Jpn. **63**, 1237 (1994).
[49] N. Toyoda, K. Sakaue, H. Terauchi *et al.*, J. Phys. Soc. Jpn. **63**, 2025 (1994).
[50] J. Hirt and I. Lote, *Theory of Dislocations* [Russian transl.], Atomizdat, Moscow (1972).
[51] Yu. S. Boyarskaya, D. Z. Grabko, and M. S. Kats, *Physics of Microindentation* [in Russian], Shtiintsa, Kishenev (1986).
[52] J. Q. Li, Z. X. Zhao, Y. L. Li *et al.*, Physica **C196**, 135 (1992).
[53] H. Werner, M. Wohlers, D. Herein *et al.*, in *Fullerenes and Atomic Clusters, Proc. Intern. Workshop*, St. Petersburg, Russia (1995).
[54] W. Schranz, A. Fnith, P. Dolinar *et al.*, Phys. Rev. Lett. **71**, 1561 (1993).
[55] I. O. Bashkin, N. P. Kobelev, A. P. Moravskii *et al.*, in *Fullerenes and Atomic Clusters, Proc. Intern. Workshop*, St. Petersburg, Russia (1993).
[56] P. Bernier, I. Luk'yanchuk, A. Belahmer *et al.*, in *Mat. Res. Soc. Symp. Proc.*, vol. 359 (1995).
[57] S. A. Myers, R. A. Assink, J. E. Schirber, and D. A. Loy in *Mat. Res. Soc. Symp. Proc.*, vol. 359 (1995).
[58] T. Atake, T. Tanaka, and H. Kawaji, Chem. Phys. Lett. **196**, 321 (1992).
[59] E. Grivei, M. Cassart, J.-P. Issi *et al.*, Phys. Rev. **B48**, 8514 (1993).
[60] J. E. Schirber, R. A. Assink, G. A. Samara *et al.*, Phys. Rev. **B51**, 15552 (1995).
[61] H. Warener, D. Bublak, U. Gobel *et al.*, Angew. Chemie **31**, 868 (1992).
[62] K. Matsuishi, K. Tada, S. Onari *et al.*, Phil. Mag. **B70**, 795 (1994).

Translated by R. S. Wadhwa

Theory of magnetoelastic vibrations in spin glass

I. A. Akhiezer,[1)] D. P. Belozorov, and Z. A. Spol'nik

National Science Center ''Kharkov Physicotechnical Institute,'' 310108 Kharkov, Ukraine
(Submitted November 15, 1996)
Fiz. Nizk. Temp. **23**, 352–354 (March 1997)

The spectra of magnetoelastic vibrations in spin glass are determined in the absence and in the presence of an external magnetic field. Various cases of magnetoacoustic resonance are considered. © *1997 American Institute of Physics.* [S1063-777X(97)01403-5]

Magnetoelastic oscillations and magnetoacoustic resonance (see Ref. 1) were studied in detail for substances with a long-range spatial magnetic order (such as ferromagnets, antiferromagnets, and ferrimagnets). In this communication, we consider magnetoacoustic phenomena in magnetically ordered substances without any long-range spatial magnetic order, viz., spin glasses.[2)]

We will describe excitations of spin glass proceeding from the well-known hydrodynamic model which characterizes spin glass as a nondissipative continuous medium whose state is determined by three angles of spin rotations specified at each point.[3,4] Such a description of spin glass is apparently valid only for low temperatures and small characteristic times (high frequencies), which is primarily due to the structure of the phase space of spin glass, namely, due to the presence of a large number of valleys which are separated by high barriers and which correspond to different metastable states of the spin system. At low temperatures, the system exists in the vicinity of a given metastable state for a long time, experiencing only small deviations; this forms the basis for a hydrodynamic description of spin glass as a nondissipative system. It should be noted, however, that a decrease in temperature leads to a further factorization of the phase space of the spin system into smaller and smaller valleys,[5] the factorization process continuing down to absolute zero temperature. In this case, the dynamics of the system at low temperatures is determined by the existence of degrees of freedom which make the main contribution to thermodynamics.

Assuming that spin glass is a continuous medium, we will proceed from the Lagrangian

$$L=L_m+L_a+L', \tag{1}$$

where L_m is the Lagrangian of the magnetic subsystem:[6–8]

$$L_m=\frac{2\chi}{\gamma^2}\int\left\{\dot{\vec{\varphi}}^2-s_m^2\left(\frac{\partial\varphi_i}{\partial x_j}\right)^2+\gamma\dot{\vec{\varphi}}(\mathbf{H}+[\mathbf{H},\vec{\varphi}])-\omega_0^2\varphi^2\right\}d^3x, \tag{2}$$

L_a is the Lagrangian of the acoustic subsystem:

$$L_a=\frac{\rho}{2}\int\{\dot{\mathbf{u}}^2-\lambda_{iklm}u_{ik}u_{lm}\}d^3x;$$

$$\lambda_{iklm}=\{(s_l^2-2s_t^2)\delta_{ik}\delta_{lm}+s_t^2(\delta_{il}\delta_{km}+\delta_{im}\delta_{kl})\}; \tag{3}$$

and L' is the Lagrangian describing the interaction of the subsystems. Here $\vec{\varphi}$ is the angular variable, $\mathbf{u}$ is the displacement vector, u_{ij} is the strain tensor, $s_{l,t}$ are the velocities of longitudinal and transverse sounds, χ is the static magnetic susceptibility, $\mathbf{H}$ is the magnetic field strength, γ is the gyromagnetic ratio, s_m^2 is the rigidity of the spin system, ρ is the density, and ω_0^2 is the local magnetic anisotropy constant. The magnetization is related to the angular variable $\vec{\varphi}$ by the standard relation

$$\mathbf{M}=\chi\left(\mathbf{H}+\frac{2}{\gamma}\dot{\vec{\varphi}}\right). \tag{4}$$

Let us first consider a crystal without an inversion center. In this case, L' can be chosen in the form

$$L'=\frac{\xi\sqrt{\rho\chi}}{\gamma}\int A_{ijlm}\frac{\partial\varphi_i}{\partial x_l}\frac{\partial u_j}{\partial x_m}d^3x, \tag{5}$$

where ξ is the dimensionless magnetoelastic coupling constant, and A_{ijlm} is a tensor (for simplicity, we henceforth assume that $A_{ijlm}=\alpha\delta_{ij}\delta_{lm}$). In the order of magnitude, $\alpha\propto s_m^2\propto s_l^2\propto s_t^2\propto 10^{11}(\text{cm/s})^2$; as regards the parameter ξ, it must be proportional to $(v/c)^4$ in the case of ideal spin glass like the magnetic anisotropy constant (here v is the electron velocity, and c the velocity of light).[6] By varying (1), we can easily obtain coupled equations for the vectors $\vec{\varphi}$ and $\mathbf{u}$ and determine the spectra of magnetoelastic waves. We will give here only the final results.

In the absence of magnetic anisotropy and external magnetic field, spin glass can transmit coupled magnetoelastic waves with the linear energy–momentum relation $\omega=s_t'k$ and $\omega=s_m'k$, where $s_t'=s_+$, $s_m'=s_-$, and

$$s_\pm^2=\frac{s_t^2+s_m^2}{2}\pm\frac{1}{2}\sqrt{(s_t^2-s_m^2)+\xi^2\alpha^2}. \tag{6}$$

We note that the velocity of spin waves and velocity of sound have the same order of magnitude; the velocity s_m depends significantly on the magnetic impurity concentration c_m and temperature T (vanishing at the spin-freezing point). The resonant relation $s_m=s_t$ (or $s_m=s_l$) can hold in principle for certain values of c_m and T. In resonance, the coupling between the magnetic and elastic systems increases sharply (the coupling constant is proportional to ξ instead of ξ^2).

According to Eq. (6), the resonance sets in not for a certain value of the wave vector, but for all values of k (the situation is similar to that studied in Refs. 9 and 10 for antiferromagnets).

In the presence of an external magnetic field (and also in the case where magnetic anisotropy is taken into account, i.e., for $\omega_0 \geqslant s_m k$), spin waves have the frequencies $\omega_{l,t}$ (for the longitudinal and transverse waves, respectively) in accordance with Ref. 6, where

$$\omega_l^2 = \omega_0^2 + s_m^2 k^2,$$
$$\omega_t^2 = \sqrt{\omega_l^2 + (\gamma H/2)^2} \pm \gamma H/2. \tag{7}$$

In this case, magnetoacoustic resonance accompanied by an abrupt increase in the coupling between the magnetic and elastic subsystems is also possible. However, the resonance sets in not for all values of k, but for certain values of the wave vector which is defined by one of the equations

$$\omega_l = s_l k, \quad \omega_t = s_l k, \quad \omega_l = s_t k, \quad \omega_t = s_t k. \tag{8}$$

If we disregard, following Ref. 6, magnetic anisotropy, the invariants appearing in L' in the presence of an inversion center in the crystal always contain higher-order derivatives as compared to Eq. (5), and the magnetoelastic coupling turns out to be very weak (proportional to $\xi a^2 k^2$, where a is the lattice constant). At the same time, Rusek[11] chose the invariant

$$U_{\text{int}} = \Lambda \vec{\varphi} \ \text{curl}\ \mathbf{u} \tag{9}$$

as the energy density of the magnetoacoustic interaction, which leads to a significant coupling between spin waves and elastic waves for crystals with an inversion center. Such a choice appears as doubtful. Indeed, let us consider a homogeneous state characterized by a constant value of the angular variable $\vec{\varphi} = \vec{\varphi}_0$. Going over to a coordinate system rotated relative to the initial system through an infinitely small angle $\vec{\omega}$ and noting that such a rotation corresponds to the strain tensor $\partial u_i / \partial x_j = \varepsilon_{ijl} \omega_l$, we find that the energy of the system is supplemented with the quantity $2\Lambda \vec{\varphi}_0 \vec{\omega}$. On the other hand, a transition to the rotated system of coordinate does not change the energy of the system; i.e., $\Lambda = 0$.

In summary, the magnetoelastic interaction can play a significant role, as was demonstrated above, only in crystals without an inversion center, where it leads to the emergence of a magnetoacoustic resonance and the formation of coupled magnetoelastic waves for all values of the wave vector k in the absence of magnetic anisotropy and in zero magnetic field.

[1)] This article was written on the basis of I. A. Akhiezer's archives.
[2)] The magnetoelastic interaction in disordered media is considered in Ref. 2.

[1] A. I. Akhiezer, V. G. Bar'yakhtar, and S. V. Peletminskii, *Spin Waves* [in Russian], Nauka, Moscow (1967).
[2] V. V. Men'shenin, I. F. Mirsaev, and G. G. Taluts, Fiz. Metal. Metalloved. **54**, 451 (1982).
[3] A. F. Andreev and V. I. Marchenko, Usp. Fiz. Nauk **130**, 39 (1980), [Sov. Phys. Uspekhi **23**, 21 (1980)].
[4] K. Binder and A. P. Young, Rev. Mod. Phys. **58**, 801 (1986).
[5] V. S. Dotsenko, Usp. Fiz. Nauk **163**, 1 (1993) [Phys. Usp. **36**, 155 (1993)].
[6] A. F. Andreev, Zh. Éksp. Teor. Fiz. **74**, 786 (1978) [Sov. Phys. JETP **47**, 411 (1978)].
[7] D. V. Volkov, A. A. Zheltukhin, and Yu. P. Bliokh, Fiz. Tverd. Tela (Leningrad) **13**, 1668 (1971) [Sov. Phys. Solid State **13**, 1396 (1971)].
[8] D. V. Volkov and A. A. Zheltukhin, Fiz. Nizk. Temp. **5**, 1359 (1979) [Sov. J. Low Temp. Phys. **5**, 643 (1979)].
[9] V. G. Bar'yakhtar, M. A. Savchenko, and V. V. Tarasenko, Zh. Éksp. Teor. Fiz. **49**, 94 (1965) [*sic*].
[10] I. A. Akhiezer, A. È. Ginzburg, L. N. Davydov, and Z. A. Spol'nik, Zh. Éksp. Teor. Fiz. **63**, 1444 (1972) [*sic*].
[11] P. Rusek, J. Phys. **C16**, 1687 (1983).

Translated by R. S. Wadhwa

Positive Hall effect in a transition-metal-free amorphous alloy

V. M. Kuźmenko and V. I. Melńikov

National Science Center ''Kharkov Physicotechnical Institute,'' 310108 Kharkov, Ukraine
(Submitted October 17, 1996; revised December 4, 1996)
Fiz. Nizk. Temp. **23**, 355–357 (March 1997)

The Hall effect of homogeneous amorphous Be films of thickness 25–100 nm stabilized with hydrogen impurity is investigated at $10\ \mathrm{K} < T < 50\ \mathrm{K}$. The value of Hall coefficient estimated as $R_H = +(1.1 \pm 0.2) \times 10^{-10}\ \mathrm{m^3/C}$ is found to be independent of temperature and sample thickness. This is the first consistently repeatable observation of positive Hall effect in a homogeneous nontransition amorphous metal. The observed effect contradicts the predictions of the theory that the Hall effect in nontransition amorphous metals must be negative.
 [S1063-777X(97)01503-X]

We investigated the Hall effect in the amorphous beryllium–hydrogen [a-(Be(H)] system. Homogeneous a-Be(H) amorphous films of thickness 125–100 nm were obtained by low-temperature condensation in ultrahigh (in all components of air) vacuum under a partial hydrogen pressure of 4.67×10^{-5} Pa.[1] According to our estimates, the films contained ~1 at.% of hydrogen. The superconducting transition temperature T_c for these films was ~10 K.[1)] The transition width ΔT_c determined from the change in electrical resistance from 10 to 90% of its value in the normal state was 0.1–0.3 K. The transition of a-Be(H) to the stable hcp phase occurs as a result of sample heating to the temperature $T_{\mathrm{cr}} = 60$–70 K and is virtually completed at $T \simeq 100$ K.

Among amorphous metal alloys not containing a transition metal, a-Be(H) films possess one of the highest values of resistivity $\rho = 250 \pm 30\ \mu\Omega \cdot \mathrm{cm}$ (at 13 K). In the classical theory, this value corresponds to the electron mean free path l of the order of atomic spacing a.[3] With such a strong scattering, strong deviations from the theory of the Hall effect based on Boltzmann's concepts should be expected.

We analyzed the Hall effect according to classical technique. The magnetic field with induction B up to 1.6 T was created by a superconducting solenoid and was applied at right angles to the plane of a rectangular film ($\mathbf{B} \perp \mathbf{j}$, where $\mathbf{j}$ is the measuring current density). The polarity of the electric field potentials in the direction of the vector $\mathbf{j}$ and the Hall electric field $\mathbf{E}_H$ (in the direction perpendicular to the vectors $\mathbf{j}$ and $\mathbf{B}$) was determined directly on each sample with the help of a tester. In all the cases, the vectors $\mathbf{j}$, $\mathbf{E}_H$, and $\mathbf{B}$ form a right-handed system of rectangular coordinates (Fig. 1), which corresponds to the positive sign of the Hall coefficient R_H (since $\mathbf{E}_H = R_H[\mathbf{B},\mathbf{j}]$). The Hall voltage U_H was measured with the help of a potentiometer P-363. The values of the Hall coefficient was calculated from the formula $R_H = U_H d/(BI)$, where d is the film thickness, and I the measuring current.

It was found that for homogeneous a-Be(H) films the value of $R_H = +(1.1 \pm 0.2) \times 10^{-10}\ \mathrm{m^3/C}$ and does not depend on temperature (in the interval from T_c to T_{cr}), magnetic field (from 0 to 1.6 T), and layer thickness (in the interval 25–100 nm. In the course of crystallization at $T = T_{\mathrm{cr}}$, the value of R_H increases more than fourfold, while $R_H \approx 7 \times 10^{-10}\ \mathrm{m^3/C}$ (at 13 K) after sample heating to $T \approx 650$ K and is close to the value of R_H for a bulk polycrystalline beryllium.[4]

According to modern concepts,[3] the wave vector k_F is still a good quantum number and the Fermi surface can still be determined if the electron mean free path l in an amorphous metal is large enough so that $k_F l \gg 1$. Since the amorphous metal has no preferred symmetry axes, the Fermi surface must be spherical, and the properties of the metal must be described by the theory for free electrons. In this case, the Hall coefficient must be determined by the classical expression

$$R_H = \frac{1}{ne}, \tag{1}$$

where e is the electron charge, $n = z/\Omega$, z is the valence, and Ω is the atomic volume.

Indeed for nontransition low-resistivity ($\rho < 50\ \mu\Omega \cdot \mathrm{cm}$), liquid and solid amorphous metals (alloys), the experimentally determined Hall coefficients are negative and correspond to Eqs. (1) almost exactly.[5,6] Deviations are observed only for liquid[5] or solid amorphous[6] metals, for which the value of l is comparatively small (the smaller the value of l, the stronger the deviations observed). If the scattering is so strong that $l \approx a$, and the Fermi level is in the pseudoband gap (pseudogap), the Hall coefficient can be successfully described in some cases by the Friedman formula (see Ref. 3):

$$R_H = \frac{0.7}{neg}, \tag{2}$$

where $0.3 < g < 1$ characterizes the depth of the pseudogap in an amorphous semimetal. However, all the corrections introduced into the classical expression for the Hall coefficient alter only its value, but do not change its negative sign.

At present, the positive Hall effect, which was first observed in liquid[7] and amorphous[8] transition metals, and sub-

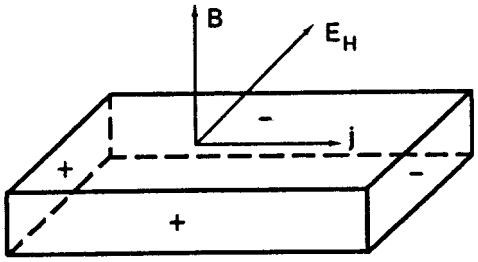

FIG. 1. Arrangement of vectors **j**, **B** and $\mathbf{E}_H$ in the *a*-Be(H) film, corresponding to the emergence of positive Hall effect in it.

sequently was also detected in most of high-resistivity amorphous alloys containing a transition metal,[9] has received the following explanation.

The Hall coefficient for nonmagnetic metals with a spherical Fermi surface and isotropic scattering can be described by the formula[10]

$$R_H=\frac{\alpha}{ne}, \tag{3}$$

where

$$\alpha=\frac{\partial E}{\partial k}\left|\frac{\partial E}{\partial k}\right|^{-1}. \tag{4}$$

Here E is the electron energy, and k is the wave vector. According to Eqs. (3) and (4), the sign of the Hall coefficient for free electrons is opposite to the sign of the group velocity for electrons.

The explanation of the positive Hall effect in the case of liquid and amorphous transition metals was obtained from an analysis of *s*-*d* hybridization of the electron structure.[9] Most of successful explanations of the positive Hall effect were obtained by taking into account the effect of *s*-*d* hybridization on the dynamics of a modified *s*-band. It was shown[9] that *s*-*d* hybridization must lead to an *S*-shaped energy–momentum relation $E(k)$ for modified *s*-states so that the velocity of an electron group is negative for the Fermi energy E_F, and hence the Hall coefficient is positive according to (3) and (4). However, such an explanation is not valid for explaining the positive Hall effect in *a*-Be(H) films that do not contain a transition metal. For this reason, the mechanism of the positive Hall effect in high-resistivity nontransition amorphous metals (homogeneous amorphous *a*-Be(H) films are the first example of such metals) remains unclear and calls for further evolution of the theory.

In the one-band model, the averaged value of the Hall coefficient for *a*-Be(H) films ($+1.1\times10^{-10}$ m^3/C) corresponds to about 0.5 charge carrier per beryllium atom, and a density of states $N(E_F)_{R_H}\approx1.0\times10^{47}$ $J^{-1}\cdot m^{-3}$ (for both directions of spin). This value is the ''bare'' density of states[11] obtained when the electron–phonon coupling is disregarded. The electron–phonon coupling increases the density of states at low temperatures by a factor of $(1+\lambda)$, where λ is the electron–phonon coupling parameter. This is the ''dressed'' density of states.[11] Since $\lambda\approx0.5$ for *a*- Be(H),[12] the ''dressed'' density of states will be about 1.5×10^{47} $J^{-1}\cdot m^{-3}$. This is close to the value 1.63×10^{47} $J^{-1}\cdot m^{-3}$, obtained earlier by us[1] for the same *a*-Be(H) films from the upper critical magnetic field [in the Ginzburg-Landau–Abrikosov–Gor'kov (GLAG) theory].[2)] The closeness of the values of the density of states obtained from two independently determined physical parameters, viz., the Hall coefficient and the upper critical magnetic field, apparently speaks in favor of the one-band model [and Eqs.(3) and (4)] for the amorphous beryllium–hydrogen system. So far, a proper explanation for the negative value of the electron group velocity for E_F has not been obtained in this system.

In conclusion, it should be noted that the positive value of Hall effect for pure low- temperature beryllium condensates was observed earlier also.[13,14] However, these condensates were inhomogeneous and contained, in addition to the amorphous phase, hcp beryllium whose concentration increased with film thickness. Hence the value of the Hall coefficient for such films increased sharply with thickness, approaching the value of R_H for hcp beryllium. In this case, the positive value of R_H can be explained easily and is not of much interest.

[1)]For crystalline hcp beryllium, $T_c\simeq0.026$ K.

[2)]For such a definition of density of states, the electron–phonon coupling is taken into account, in contrast to $N(E_F)_{R_H}$.

[1] V. M. Kuzmenko, V. I. Melnikov, T. P. Chernyaeva, and V. V. Bryk, Fiz. Metal. Metalloved. No. 8, 41 (1990).
[2] R. L. Falge, Phys. Lett. **A24**, 579 (1967).
[3] N. Mott and E. Davis, Electron Processes in Noncrystalline Materials, vol. 1 [Russian transl.], Mir, Moscow (1982).
[4] E. S. Borovik, Zh. Éksp. Teor. Fiz. **23**, 83 (1952).
[5] V. A. Alekseev, A. A. Andreev, and V. Ya. Prokhorenko, Usp. Fiz. Nauk **106**, 393 (1972).
[6] G. Bergmann, Z. Phys. **255**, 76 (1972).
[7] G. Busch, H.-J. Güntherodt, H. U. Künzl *et al.*, J. Phys. (Paris) **35**, Suppl. No. 5, C4-329 (1974).
[8] V. M. Kuzmenko, B. G. Lazarev, V. I. Melnikov, and A. I. Sudovtsov, Zh. Éksp. Teor. Fiz. **67**, 801 (1974) [Sov. Phys. JETP **40**, 396 (1974)].
[9] M. A. Howson and B. L. Gallagher, Phys. Rept. **170**, 265 (1988).
[10] J.-P. Jan, J. Phys. **30**, 497 (1962).
[11] G. Bergmann, Phys. Rev. **B7**, 4850 (1973).
[12] V. M. Kuzmenko, D.Sc thesis, Kharkov, Ukraine (1992).
[13] B. G. Lazarev, V. M. Kuzmenko, A. I. Sudovtsov, and V. I. Melnikov, Fiz. Metal. Metalloved **33**, 984 (1972).
[14] K. Yoshihiro and R. E. Glover, in *Abstracts of Papers to XIII Int. Conf. Low Temp. Phys.*, Colorado, USA (1972).

Translated by R. S. Wadhwa